



University  
of Glasgow

Ravji, Shabir Hussein (2015) *Mechanisms of water vapour transport in polyimide thin films for applications in humidity sensing*.  
PhD thesis.

<http://theses.gla.ac.uk/7034/>

Copyright and moral rights for this thesis are retained by the author

A copy can be downloaded for personal non-commercial research or study

This thesis cannot be reproduced or quoted extensively from without first obtaining permission in writing from the Author

The content must not be changed in any way or sold commercially in any format or medium without the formal permission of the Author

When referring to this work, full bibliographic details including the author, title, awarding institution and date of the thesis must be given

**Mechanisms of Water Vapour Transport in Polyimide  
Thin Films for Applications in Humidity Sensing**

**Shabir Hussein Ravji B.Sc**

Submitted in fulfilment of the requirements for a Doctorate of Philosophy

School of Physics and Astronomy

College of Science and Engineering

University of Glasgow



**Declaration** This thesis is a record of the work carried out by myself in the Materials and Condensed Matter Group of the Department of Physics and Astronomy at the University of Glasgow during the period 2011 - 2015. Unless otherwise stated, the work described herein is my own. However, much of the work has been carried out with assistance and in collaboration. Notably, Dr Andrew Glide constructed the QMC comparator circuit and the vapour pulsing system presented in Chapter 5. Instrument scientists Dr Erik Watkins (ILL) and Dr Maximilian Skoda (ISIS) aligned the reflectometer instruments, and were a point of contact during the data reduction. Dr Andrew Glide also led the data acquisition at both neutron facilities with myself playing a junior role. Dr Brian Moffat from Honeywell recorded much of the Thunder Chamber QCM data, shown in Chapter 3, as he was based on site. Mr William Smith produced some of the TEM sample cross sections (using FIB). Mr Colin How (EF-TEM) and Dr Damien McGrouther (Diffraction Patterns) were also on hand to assist in the acquisition some of TEM images. Dr Ian Maclaren acquired Figure 4.11. Dr Gary Patterson provided much advice on equipment and set up to measure capacitance in a variety of devices. Permporometry was carried out by Dr Yvonne Jüttke to whom thanks is due. The text herein has been proofread by Mr David Keddilty.

Some of the work shown has been at Conference in 2013 in a talk by myself entitled: *Water transport in Polyimide Thin Films for applications in Humidity Sensing* .

This thesis has not previously been submitted for a higher degree.

*“There are some enterprises in which a careful disorderliness is the true method.*

*The more I dive into this matter of whaling, and push my researches up to the very spring-head of it so much the more am I impressed with its great honourableness and antiquity; and especially when I find so many great demi-gods and heroes, prophets of all sorts, who one way or other have shed distinction upon it, I am transported with the reflection that I myself belong, though but subordinately, to so emblazoned a fraternity.”*

**Herman Melville - *Moby Dick* (Chapter 82)**

## Acknowledgements

There are many people who I would like to thank for their input into this work. Firstly, Dr **Damien McGrouther**, for his constant encouragement, and the academics who work in the **MCMP group** who created the conditions for a collegiate atmosphere. It's been a great place to work, much of which is due to my fellow PhD students, research assistants, technical staff, and visiting students. Particularly, Mr **Colin How** (who I will beat at squash), Dr **Gary Paterson**, Dr **Francisco Trindade**, Dr **Pedro Parreria** (Bunk), Dr **Ciaran Ferguson** (McNulty), Mr **Scott Smith**, Ms **Kirsty Annand**, Dr **Aaron Naden**, and Dr **Marco Bigatti**. I will remember the help, advice and conversations, both technical and non-technical, I have had with each of you.

I would also like to thank some of my friends for cups of tea, long hillwalks, and great chats; Mr **Thomas Fay**, Dr **Bryan Jackson**, Dr **Zishan Jiwa**, Mr **Steven Gray**, Mr **Narciso Baldo**, Mr **Brendan Mckeown**, and Dr **Catriona Macleod**.

A very special thanks must go to my parents; Mr **Anwar-Ali** and Mrs **Tazim Ravji**, for having a constant and sometimes baffling faith in me. Especially, for my Mum who, had she had the opportunity, would have undoubtedly been a chemistry genius.

My older siblings; **Sheni & David**, **Ali & Fatemah** and **Kaniz & Kareem**, who I have known that I can rely on. My nephews; **Elias**, **Qaim-Ali**, **Abid-Hassan**, **Faris & Ammar**; and niece, **Zaina**, have always reminded me to enjoy the simple things; I am very proud of you.

Finally, I want to thank Dr **Pollie Humberstone** for being a better partner than I could imagine or deserve. You're my *3am* person.

My life has been better for having all of you as a part of it, and I thank you. As *hope is purest form of prayer*<sup>1</sup>; I hope the very best for each of you.



<sup>1</sup>Paraphrased from a quote attributed to Mahatma Gandhi.

## Abstract

Polyimides are ubiquitous in the electronics, space science, and research industries due to their thermal stability, ease of use, lifetime, and high dielectric strength. These properties, along with the propensity of polyimides to absorb water vapour, has led to both their use as a common sensing element in humidity sensors, and additional challenges when utilising polyimides in solid state electronic devices. Consequently, a substantial amount of literature has been produced regarding the transport properties of water vapour in polyimide films. This has been found to be a complex process dependent on the morphology and chemistry of the particular polyimide in question. Accordingly, as part of an industrial collaboration with Honeywell Inc. several tools and probing techniques were developed to map and quantify the transport properties and characteristics of such materials.

The material of focus is a particular form of polyimide which is used as a sensing element by Honeywell in their capacitance based humidity sensors. The cure procedures and preparation have been varied to understand the relationship between water transport and processing procedure.

Importantly, methods and equipment have been developed to measure and characterise the subtle difference in water transport resulting from variations in the preparation procedure. *in-situ* techniques to characterise transport have included the use of capacitance measurements, Attenuated Total Reflectance Infra -Red spectroscopy (ATR-FTIR), Quartz Crystal Microbalance (QCM), and Neutron Reflectivity. Other techniques to characterise the polymer have included Transmission Electron Microscopy(TEM) and Atomic Force Microscopy(AFM).

The use of Attenuated Transmission Reflectance Infrared Spectroscopy (ATR-FTIR) has indicated a chemical interaction between the polar elements of polymer backbone and the water molecule. Permporometry and an analysis of the TEM images indicate a transport length scale  $\sim 0.2nm$ , similar to the size of a water molecule.

Density profiles fitted to Neutron Reflectivity measurements reveal a dense skin layer on the surface of the polymer, the characteristics of which vary with the sample curing procedure. The neutron reflectivity technique was then used in time of flight mode (ToF) to map the ingress of vapour into the polymer, pushing the time resolution further than has previously been achieved. However, the box-car averaging technique which was used to gain sufficient counts of neutrons was found to obscure the longer timescale transport effects. The QCM procedures outlined have provided Honeywell with a cost effective method of raw material measurements of transport properties for a range of materials. QCM measurements indicate dual diffusion coefficients, skin, and bulk, when Fickian transport models are applied to the system. The transport timescales were found to be thickness independent in the range studied (60nm-1.1 $\mu m$ ), consequently diffusion is not the rate limiting factor in this system.

Thus, the key factors such as time and length scales of this diffusion system have been characterised with the customisation of a host of techniques. The distribution of water vapour within the samples is shown to be uniform in the bulk layer of the sample, and the rate limiting step in the transport of water vapour is demonstrated to be constant on all polyimide thin films. It is also indicated that oxygen plasma etching can be used to reduce the hysteresis effect in this form of polyimide with some indication that such treatment impacts on the chemical interactions between the polyimide films and water vapour.

# Contents

<b>1</b>	<b>Introduction</b>	<b>7</b>
1.1	Humidity . . . . .	10
1.2	Humidity Sensing Methods . . . . .	13
1.3	Polyimide . . . . .	14
1.4	Diffusion . . . . .	16
1.5	Summary . . . . .	24
<b>2</b>	<b>Measurement Techniques and Instrumentation</b>	<b>26</b>
2.1	Impedance Measurements . . . . .	26
2.2	Quartz Crystal Microbalance . . . . .	28
2.3	Neutron Instruments and Facilities . . . . .	30
2.4	Electron Microscopy . . . . .	38
2.5	Atomic Force Microscopy . . . . .	51
2.6	The Thunder-chamber . . . . .	53
<b>3</b>	<b>QCM: A Probe for Mass Transport in Soft Matter</b>	<b>56</b>
3.1	Quartz Crystal Microbalance . . . . .	57
3.2	Measuring the Impedance of a QCM . . . . .	60
3.3	A method of detecting Hysteresis . . . . .	67
3.4	Measurements of Density, Water Uptake and Hysteresis in polyimide Films . . . . .	71
3.5	The effect of Humidity on the viscoelasticity of polyimide . . . . .	74
3.6	Capacitance based Polymer Studies . . . . .	81
3.7	Summary . . . . .	88

<b>4</b>	<b>Transport Characterisation</b>	<b>90</b>
4.1	Interpreting Diffusion . . . . .	90
4.2	Applying Models of Mass Transport . . . . .	99
4.3	Transport Length Scales . . . . .	105
4.4	Summary . . . . .	113
<b>5</b>	<b>Acquiring concentration profiles - In-Situ Neutron Reflectivity</b>	<b>115</b>
5.1	Neutron Reflectivity Theory . . . . .	116
5.2	Experimental Methods . . . . .	124
5.3	Fitted Neutron Reflectivity Profiles . . . . .	132
5.4	Time Resolved Neutron Reflectivity . . . . .	145
5.5	Summary . . . . .	163
<b>6</b>	<b>Conclusions and Future Work</b>	<b>165</b>
6.1	Summary of Results . . . . .	165
6.2	Future Works . . . . .	169
6.3	Evaluation . . . . .	171
<b>A</b>	<b>Appendix</b>	<b>173</b>
A.1	Spin Coating polyimide Calibrations . . . . .	173
A.2	Roughness probed with AFM . . . . .	177
A.3	Evidence of polyimide Charging . . . . .	177
A.4	Diffusion coefficient Measurements . . . . .	178
A.5	QCM sweep measurements . . . . .	181
A.6	QCM: A test bed for materials . . . . .	181
A.7	Raman Spectroscopy to Probe Polyimide-Water Interactions . . . . .	187
A.8	Bright Field image of Neutron 150nm Hard Cured Neutron Sample . . . . .	191
A.9	Time Resolved SLD Profile fit . . . . .	191
	<b>Bibliography</b>	<b>209</b>

# Chapter 1

## Introduction

Sensing or monitoring humidity has proved to be vital for a wide range of scientific, engineering, and medical applications. Consequently, significant research has been performed to service the needs of the automotive[1], food[2], and health[3, 4] industries, with a further range of applications which have been discussed in literature[5, 6]. Scientifically; humidity also plays a significant role in many biological[7], horticultural[8], and environmental processes[1], leading to a desire to monitor humidity in a range of environments.

Relatively recent improvements in manufacturing driven by high-speed, low-power, low-cost microelectronics, and the growth of micro-electromechanical (MEMs) technologies[9], have led to an increase in the use of humidity sensors. Recent market research has forecast that the non-military open market for sensors is to grow from €119.4 billion in 2011, to €184.1 billion in 2016[10]. The anticipated growth in the market has led to government research councils prioritising funding for research into sensing solutions by establishing organisations to coordinate research and exploit market opportunities[11]. Recently developed humidity sensors include low cost humidity sensors for intelligent packaging (potentially to monitor pharmaceuticals and food[12]), for in-situ monitoring of the human body[13] and to detect trace moisture content in natural gas pipelines[14]; three varied environments and applications with different sensitivity requirements. This wide range of products aimed at specific markets require factors such as, cost, processability, size, and accuracy to be balanced to create a product with the correct qualities for the target application.

Honeywell International Inc. are a worldwide market leader in the provision of humidity sensors. Device engineers at Honeywell have exhaustively made improvements in the manufacturing processes to optimise yield, accuracy and throughput, with each incremental improvement resulting in large benefit due to the massive scale of their operation.

However, an understanding of the fundamental processes which underpin the humidity sensing mechanisms of the sensing material is lacking, along with the tools to make fast and cost effective material assessments. This has become the limiting factor in the progress of these products. Therefore, the role of this study is to provide both an understanding of, and the tools to probe, the water transport properties of the sensing material in these Honeywell sensors, in order to provide the awareness required for an improved operation of the sensor.

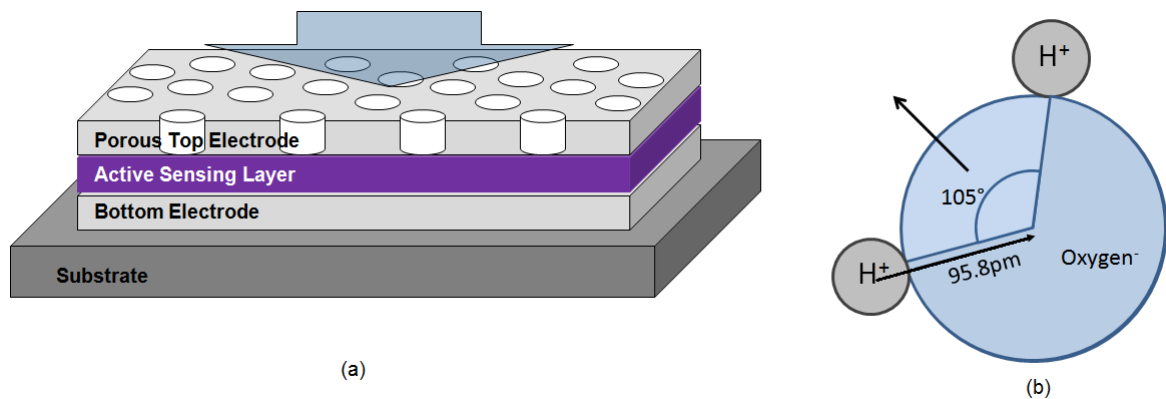


Figure 1.1: (a) An illustration of the structure of a sandwich type humidity sensor (b) A schematic of the water molecule showing the origins of the intrinsic polarity.

The sensors of interest are capacitance based, in which measurements of the dielectric properties of a hygroscopic sensing material are read. The structure of the water molecule is shown in Figure 1.1(b), showing the origin of the intrinsic dipole resulting from an asymmetric distribution of charge, which leads to its high dielectric constant. Therefore, as water absorbs into the sensing layer, the measured dielectric properties of the sensing material shift.

The structure of the sense dye is either a sandwiched structure as shown in Figure 1.1(a), with two electrode surfaces on each side of a sensing element, or an interdigitated structure. The sensing material used is a polyimide, which is easily integrated into the CMOS type manufacturing process. For the sandwich-type structure, a water vapour permeable upper electrode is required which is often coated by an additional layer that is also permeable to water molecules to provide some protection from the environment. The sensing element requires a level of environmental protection without compromising the device properties. The finished product includes a low power application specific integrated circuit, ASIC, in order to convert the measured capacitance into a DC voltage using the circuitry described by Silverthorne et al.[15].

Capacitive type sensors are very cost effective and are consequently the most common types of humidity sensors[5]. The main factor in the performance such sensors is the transport properties of the water

vapour into and out of the sensing element, which is a function of the material itself as well as the device structure[5].

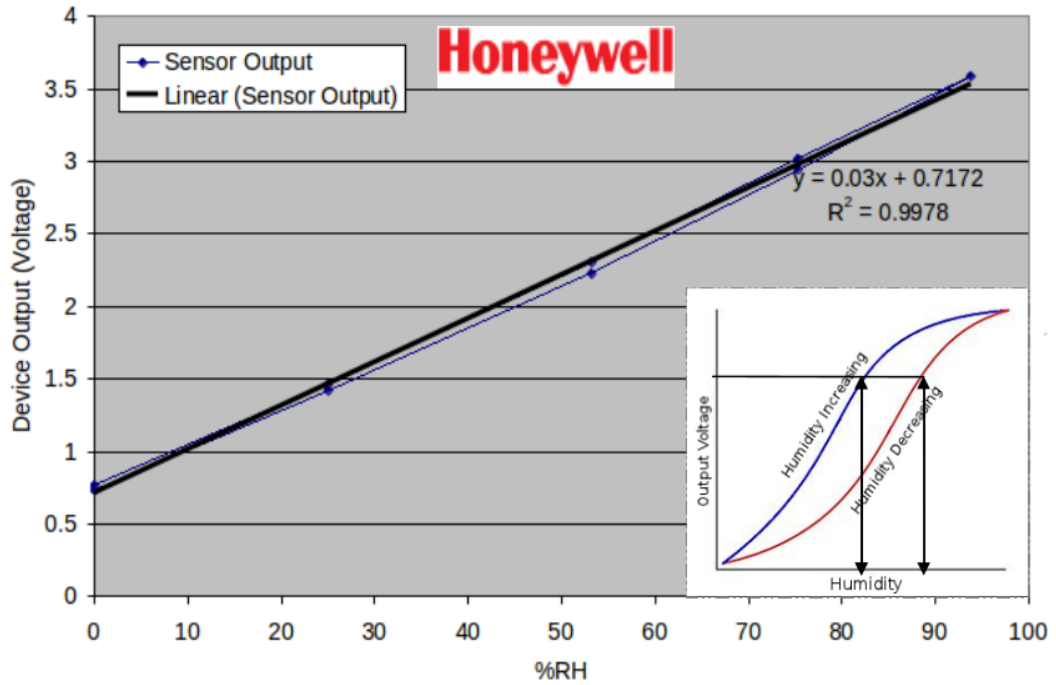


Figure 1.2: A graph provided by Honeywell of the output from a humidity sensor. The sensor exhibits the hysteresis effect. An illustration is added in the bottom right hand corner to depict the sensors hysteretic behaviour.

One of the key areas of interest is the repeatable and consistent hysteresis effect in capacitance based humidity sensors, which is evident as the ambient humidity is cycled from a lower to a higher humidity; as demonstrated in Figure 1.2. This issue is ubiquitous in humidity sensors and is generally addressed by researchers on a case by case basis[5]. The level of the hysteresis varies from product to product, depending on the sensor architecture and the sensing element. A computational correction would require the entire history of the material to be logged, and so is an implausible solution. This leads to the conclusion that the device architecture and/or material transport properties must be improved.

The goals of this project are threefold. Firstly, to provide an accurate and cost effective tool with which to perform assessments of the transport properties of possible sensing materials, which is addressed in chapter 3. Secondly, to identify the important processes and provide any insight into their time and length scales, which is discussed in chapter 4. Finally, to characterise the type of water uptake in the existing sensing material (adsorption or absorption), which is addressed in chapter 5. As mentioned previously, even a small improvement in the process and function of the humidity sensor can lead to a significant impact.

In this chapter the goal is to provide a succinct summary of the wealth of literature and background physics which is relevant to the work presented in later chapters. This encompasses a large body of literature from chemical, manufacturing, and computational backgrounds, dealing not only with water transport but also the array of measurands which can be used to detect the presence and quantity of water vapour. Therefore, a focus in this chapter is placed on four key areas: defining humidity (section 1.1), understanding measurement principles (section 1.2), the sensing material of choice (polyimide, section 1.3), and diffusion in polymers (section 1.4). Literatures covering other topics, such as chemical interactions between water and polyimide, are discussed as relevant throughout this document.

## 1.1 Humidity

Humidity refers to the presence of water vapour in the atmosphere. There are several ways in which humidity can be quantified; absolute humidity, specific humidity, and relative humidity.

The amount of water vapour present in a given volume, generally in  $\frac{g}{m^3}$  or in PPM, parts per million ratio, is referred to as the absolute humidity; somewhat akin to the concept of number density as commonly used in chemistry. Equation 1.1 shows the absolute humidity relationship mathematically:

$$AH = \frac{M_{water}}{V}, \quad (1.1)$$

where;  $AH$  is the absolute humidity,  $V$  is the volume, and  $M_{water}$  is the mass of water vapour.

$$SH = \frac{M_{water}}{M_{water} + M_{gas}}, \quad (1.2)$$

The specific humidity,  $SH$ , is the ratio of the mass of the water vapour,  $M_{water}$ , to the mass of the water and to the mass of the containment gas,  $M_{gas}$ . Practical measurements of the specific humidity are difficult as a knowledge of the specific composition of the containment gas is required.

Furthermore, absolute humidity and specific humidity do not account for the effects of temperature and pressure on many important processes. For example, the rate at which water evaporates is a function of the temperature, pressure, and the atmospheric humidity. For such a process the degree to which the atmosphere is saturated with water vapour is important.

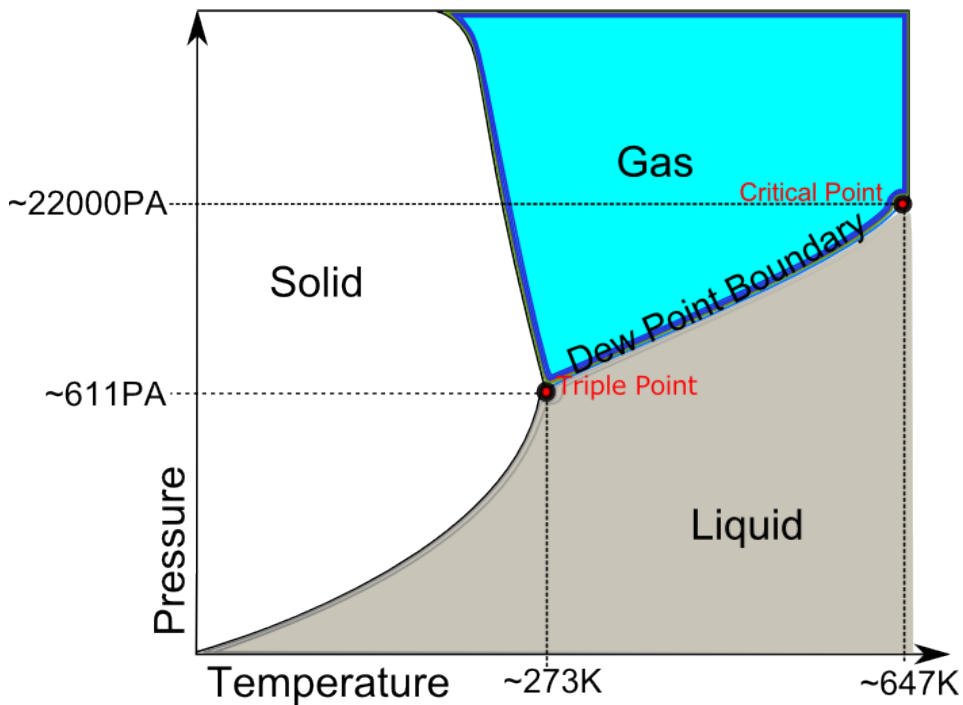


Figure 1.3: A illustration of the phase diagram for water showing the dew point or 100%RH boundary, which is highlighted. The triple point and critical points of water are marked.

Therefore, a useful measure is the temperature (at a constant pressure, normally one atmosphere) at which the condensation of water begins, which is often referred to as the dew point. The dew point is important as it provides a repeatable measuring standard for humidity which can be derived from theory. Consequently, the dew point (which is also known as 100%rh,) is also defines the most commonly used scale of humidity, relative humidity which is discussed later in this section. Due to its importance in defining the relative humidity scale, a brief summary of the theoretical underpinning of the dew point is provided here.

The dew point can be calculated by considering the Gibbs energy,  $g(P,T)$ , of water vapour and liquid gas[16]. According to Gibbs, for which the Gibbs energy is named, the Gibbs energy,  $g(P,T)$ , is a thermodynamic potential that quantifies “*the greatest amount of mechanical work which can be obtained from a given quantity of a certain substance in a given initial state, without increasing its total volume or allowing heat to pass to or from external bodies*” in reversible manner[17]. Gibbs had shown that this potential is defined as,  $g(P,T) = U + PV - TS$ , where;  $U$  is the internal energy of the system,  $P$  is pressure,  $V$  is the volume,  $T$  is the temperature, and  $S$  is the entropy.

At the dew point the Gibbs energy of liquid and vapour are equal as both states coexist in thermodynamic equilibrium,  $g_{liquid}(P,T) = g_{vapour}(P,T)$ , which is the line marked in Figure 1.3 between the liquid and vapour phase of water. Considering the rate of change of pressure with respect to tem-

perature along the phase boundary in the PT diagram (Figure 1.3), and using the first order Taylor expansion, it is possible to arrive at the Clapeyron-Clausius Equation[16].

$$\frac{dP}{dT} = \frac{L}{T(sV_2 - sV_1)} \quad (1.3)$$

Where,  $L$  is the latent heat of the phase change,  $sV_1 - sV_2$  is the change in the specific volume,  $P$  is the pressure, and  $T$  is the temperature. Assuming that the specific volume, which is the volume to mass ratio (the inverse of density) of water in the liquid phase ( $\sim 0.001 \frac{m^3}{kg}$ ), is much greater than volume than the gas phase ( $\sim 1 \frac{m^3}{kg}$ ) yields the approximation,  $sV_{Vapour} - sV_{Liquid} \approx sV_{Vapour}$ . It has been shown that the ideal gas law reduces Equation 1.3 to  $\frac{dP}{dT} = \frac{LP}{T^2R}$  where  $R$  is the gas constant. Integrating gives,  $\ln P = -\frac{L}{RT} + c$ , setting the conditions for the dew point [16].

The dew point is important as it is the point at which a given space<sup>1</sup> is saturated with water vapour, providing a theoretically calculable point that has the factors of pressure and temperature implicitly taken into account. The total absence of water vapour can be considered 0% relative humidity, and the dew point, 100%rh, is the space at saturation; with these two points the relative humidity scale is defined. In summary, the relative humidity, %rh, scale measures of the degree to which the given space is saturated.

$$\%RH = \left( \frac{P_{vapour}}{P_{saturated}} \right) 100 \quad (1.4)$$

Conventionally, relative humidity is defined as shown in Equation 1.4. At a constant atmospheric pressure and temperature, the absolute humidity is proportional to the partial pressure of the water vapour and hence it is proportional to the relative humidity.

Figure 1.4 shows the relative humidity as a function of the absolute humidity on the (left hand side axis) and also shows the dew point temperature, also as a function of the absolute humidity (on the right hand side axis); both at a pressure and temperature of 1 ATM and 20°C. In Figure 1.4 the dew point data is for a constant relative humidity at 100%RH; all lines of constant relative humidity are similarly non-linear with absolute humidity.

---

<sup>1</sup>This does not refer only to the saturation of air, but to any composition of gases.

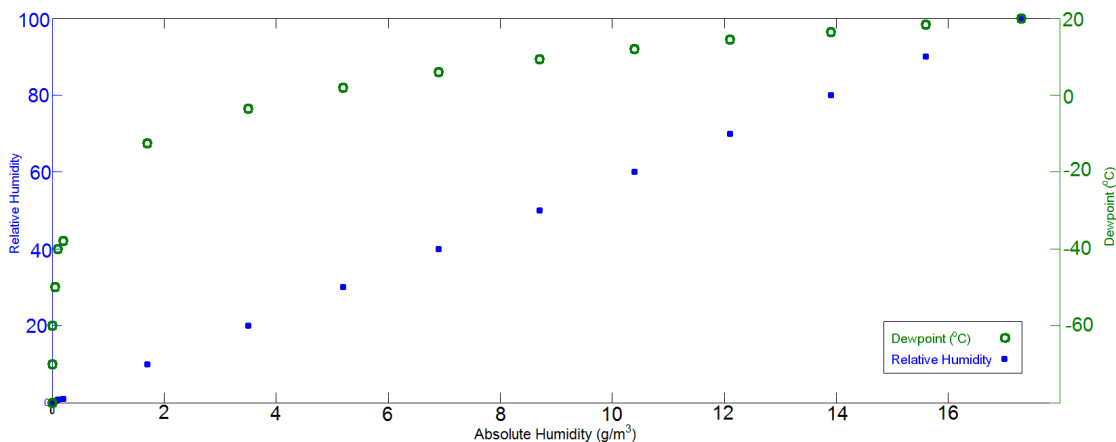


Figure 1.4: A comparison between the relative humidity(linear) and dew point temperature as a function of absolute humidity at 1atm and  $20^{\circ}C$ . Data is taken from Noor et al. [18].

Relative humidity gives an important measure of the humidity for human comfort as the evaporated cooling used by the human body is unable to function at the dew point of 100%RH, leading to condensation on the skin. Similarly, for many chemical processes the relative humidity is a more significant indicator than other measures, such as absolute humidity, as it quantifies the affects of the water vapour in the air which effects evaporation rates. As a consequence most commercial sensors focus on measuring the relative humidity. Absolute humidity is normally used for scientific purposes in low humidity environments. As relative humidity is proportional to the partial pressure of the water vapour in the atmosphere, this also makes relative humidity easier to measure than absolute humidity, which requires a range of pressure, temperature, and gas composition sensors to calculate accurately.

## 1.2 Humidity Sensing Methods

There are a number of methods to reliably detect water vapour and measure humidity which are well reviewed elsewhere[5, 19, 20]. Such methods rely on reading, for example, the EM absorption[13], resistance[9, 21], capacitance[8, 22, 15], and mass[23] of a sensing element.

As discussed in the previous section, the measurement of the dew point is appealing due to its repeatability and relationship with theory. The most common type of dew point hygrometer has a scheme which consists of a cooled metal ‘mirror’ integrated with a temperature feedback loop to maintain the mirror at the dew point temperature. The temperature of the surface of the mirror is maintained to keep a consistent film of water vapour on the surface of the mirror, as measured by the attenuation of a laser which is reflected from the mirror surface. Therefore, the mirror temperature is the dew point

temperature. The main advantage with this technique is the inherent accuracy to which the temperature can be determined as a result of a well-defined dew point, although this has been questioned when such sensors are used in atmospheres of varying pressure and composition[20]. Conventionally, these sensors are relatively large and weigh a few grams, however, more recently systems have been miniaturised by using a peltier based cooling system to reduce the temperature of the mirror[13]. Such sensors are commonly used for high end applications due to the cost.

QCM, piezoelectric resonators<sup>2</sup> have been used to monitor the dew point using gravimetric measurements[23].

A range of sensors which rely on light attenuation are also available. Typically, IR hygrometers use the dual-wavelength absorption technique, taking measurements at two wavelengths with a strong and negligible optical radiation absorption which can then be compared using Beers law as detailed elsewhere[24, 25]. Commonly, these types of sensors come in two categories: evanescent and spectroscopic. The latter relies on evanescent waves in a sensing element as the sensing element absorbs water<sup>3</sup>. This can come in a variety of architectures which determine the robustness of the sensor[18]. However, such sensors are clearly only as good as the sensing element material through which the evanescent wave passes, and tend to have a high cost due to the fiber optics involved. Spectroscopic measurements have also been used to good effect using specific light emitting diodes (LEDs), operational in the near IR band[26].

In this study, the focus is on a particular type of polyimide deployed by Honeywell as their sensing element in their capacitance based humidity sensors. Polyimide is a good candidate to form a sensing layer as it has a low dielectric constant relative to water, as well as other properties which are discussed in the next section of this chapter.

### 1.3 Polyimide

Polyimides are a class of high performance polymer materials defined by the imide functional group, shown in Figure 1.5(a). Since the synthesis of the first polyimide in 1908 applications and interest in this class of materials has grown[27]. The imide group is commonly combined with a benzene ring to produce aromatic polyimides. One such common example is Kapton, the structure of which is shown in Figure 1.5. Such polyimides have been shown to have a high thermal stability, as well as high radiative and solvent resistance[27, 28]. These properties quickly led to the commonplace use of many different type of polyimides synthesised for a range of technical applications with characteristics such as photo sensitivity[29], penetrant selectivity[30], and a range of charge transfer properties[31]. The key properties of thermal stability and chemical resistance arise from the structure of the polyimide

---

<sup>2</sup>QCM will be discussed in great detail in section 2.2.

<sup>3</sup>Evanescent waves are a concept discussed further in section 4.2.1.

backbone while the mechanical strength of polyimides is a consequence of both the imide structure, and the aromatic ring present in particular polyimides[30]. Moreover, electro negativity also results in lower likelihood of oxidation[32]. The strong heat resistance and chemical resistance can also lead to processing difficulties such as a lack solubility, leading to other materials commonly being integrated into the polymer matrix.

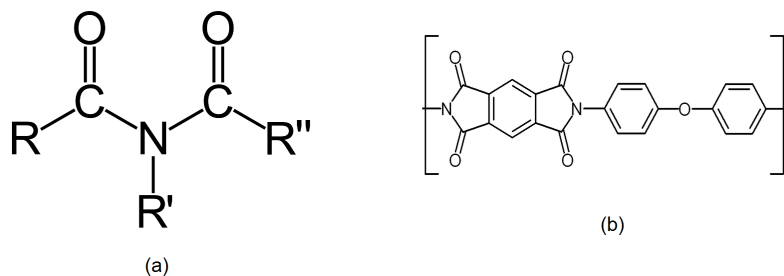


Figure 1.5: (a) The functional group of polyimide. R, R and R refer to any kind of side chain attached to the functional group. (b)The chemical structure of Kapton (*DuPont™* [33]), a common form of polyimide.

The range of polyimides available has led to it being used as the most common class of organic polymers employed for synthesis of membranes for gas separation and solvent resistant nanofiltration (SRNF), for which its mass transport properties are key[30]. According to the diffusion model introduced by Graham in 1866, membrane permeation follows three stages driven by a difference in the chemical potential across the membrane sorption of molecules on the side, with the higher partial pressure, diffusion of the absorbed molecules through the membranes, and desorption of these molecules to the lower partial pressure side. As different penetrants permeate at different rates, separation is achieved; for example oxygen transport occurs at a rate two to seven times faster than nitrogen[30].

One important factor in determining the transport properties of the given polyimide are the annealing regime, commonly used to depress plasticisation<sup>4</sup> which results in a loss of performance[30]. Thermal annealing below the glass transition temperature,  $T_g$  ( $\approx 400^\circ C$  for most polyimides), results in charge-transfer complexes (CTCs); a type of molecular bond in which charge is transferred in an intra or inter molecular fashion to create attractive forces, resulting in weak bonds. Fluorescence spectroscopy has shown that thermal annealing below  $T_g$  enhances the number of CTC bonds and leads to greater gas selectivity and less chain mobility in polyimides[31] which, in turn, can lead to a loss in permanence[35]. Different annealing regimes are designed to create different effects in polymers, and it has even been shown that raising the temperature above  $T_g$ , followed by rapid cooling, generates more free volume;

<sup>4</sup>Plasticisation a process that changes the properties of the Polymer well covered elsewhere [34].

as opposed to cooling the polymer down slowly[36]. Another possibility arising from thermal annealing is cross linking, a stronger chemical bond formed between polymer chains that results in an increasingly rigid polymer, although this is conventionally achieved using either a chemical reaction or EM radiation(UV) to provide the energy required to form the bond[30]. Yet cross linking results in the imide bonds turning into amide bonds, increasing the hydrophilicity of the polymer [37]. Therefore in this investigation annealing is a key parameter of interest.

Commercially, polyimides are available in a range of chemistries which can further be tailored to enhance their performance by annealing and/or cross-linking the polymer, broadening the number of applications. However, despite its common use, the interaction of water vapour and polyimides is still not well understood on a molecular level[38] as the diffusion properties of polyimides depend of the solubility and diffusivity of the penetrant solvent and the specific treatment as well as the chemistry of the given polyimide. Furthermore, it has also been suggested that certain types of polyimide have a tendency to age due to their out-of-equilibrium state[39] yet very little information is provided about the aging of polyimides in the presence of an interacting penetrant.

As water is a polar molecule, the polarity of sites on the polyimide backbone is of interest. The polyimide used by Honeywell as a sensing element is a fully imidized non-fluorinated polyimide, conventionally used as a passivation coating for electronics. The manufacturer's quoted glass transition temperature is  $\approx 310^{\circ}C$ , with a thermal decomposition temperature of  $\approx 510^{\circ}C$ ; temperatures which are important to consider when evaluating the impact of the curing regimes on the water transport properties (which are discussed in sections 3.4 and 5.3). Various sites on the polyimide backbone are polar as they comprise of C=O and C-N bonds. The polyimide being studied is sold in a  $\gamma$ -Butyrolactone (GBL) solution for spin casting and it is designed to produce a  $1\mu m$  thick layer when spun at 5000RPM. GBL itself is a polar molecule which contains a C=O site and a C-N-C site.

The focus of this study is not only the chemical properties of polyimides but rather, to develop an understanding of the water transport mechanisms of an existing propriety form of the pre-imidized non-fluorinated polyimide used by Honeywell Sensing and Control to manufacture humidity sensors.

## 1.4 Diffusion

Diffusion is transport of mass by random molecular motions. The diffusion characteristics of polymers is an area of interest from both a technological and theoretical perspective[40] due to its wide range of applications. Despite an accurate description of diffusion on a macro scale, provided by Fick in the middle of the 19th century, details about the fundamentals of the processes vary from system to system, leading to a great deal of system specific literature.

Polymer penetrability can be tailored for a specific applications, while other materials such as ceramics, metals, and glasses are generally impenetrable and require free volume to enable mass transport. This flexibility has led of a host of new polymers created for distinct applications, for example site-specific targeting for medicines[41] and the use of polyimide membranes for gas filtration[30], as discussed in the previous section.

Mass transfer through polyimide films depends on a wide range of factors, including the diffusivity of the penetrant into the polymer, free volume, and the ambient conditions. Polymers with a high degree of cross linking are usually less penetrable due to a higher density through which penetrant may permeate[30, 42]. In this section an overview of the models used to understand penetrant ingress into polyimide are presented.

### 1.4.1 Fickian Diffusion

Diffusion phenomena is well described by the laws described by Adolf Fick in 1855 after considering the analogies between diffusion phenomena and Fourier’s heat conduction equations[43]. Both processes result in some form of transport as a consequence of random molecular motions. Fick’s first law, equation 1.5, is a statement that the flux,  $J$  ( $\frac{mol}{m^2s}$ ) through a given cross section, is proportional to the concentration profile  $\frac{\partial C}{\partial x}$  ( $\frac{kgm^{-3}}{m}$ ) across that section. This is a statement that a substance tends to move from a high concentration to a low concentration with a flux proportional to the gradient of the concentration, described by the concentration profile. Fick’s first law accurately describes a situation with a fixed concentration on both sides of the film, a steady state in an isotropic medium.

$$J = \frac{dm}{dt} = -D \frac{dC}{dx} \quad (1.5)$$

The properties of the material are accounted for within the diffusion coefficient,  $D$ . The units of the diffusion coefficient represent an area in a time frame i.e. ( $\frac{m^2}{s}$ ), and the sign sets the direction of the flux, showing that diffusion occurs in the opposite sign of an increasing concentration gradient.  $D$  varies as a function of the material used, as well as concentration itself, temperature, molecular weight, and numerous other factors. The physical meaning of the diffusion coefficient on a macro scale is clear: it sets the speed at which the penetrant ingresses into the film. The atomic level description of  $D$  is material dependent, and is discussed further later in this section.

While Fick’s first law describes a static state, in most practical cases the concentration gradient will change with time as the flux drives mass to a low concentration zone. Assuming mass conservation, the rate of change of the concentration  $\frac{dC}{dt}$ , is equal to the rate of the flux in space,  $\frac{d}{dx} J$ . Substituting in for  $J$  from Fick’s first law gives Equation 1.6; Fick’s Second Law. This provides a description of

how the concentration gradient changes in time during a diffusion process. This is applicable when the system is not in a steady state, but rather in a transient state.

$$\frac{d^2C}{dt^2} = \frac{d}{dx} \left( -D \frac{dC}{dx} \right) \quad (1.6)$$

When  $D$  is constant, generally a reasonable assumption in an isotropic medium, equation 1.6 reduces to  $\frac{dC}{dt} = -D \frac{d^2C}{dx^2}$  in one dimension. This shows that if the concentration profile changes rapidly in space then the concentration will change rapidly in time.

When Equation 1.6 is set equal to zero, a steady-state solution for Equation 1.6 can be obtained and can then be integrated with respect to  $x$ . Assuming a constant diffusion coefficient, and introducing the boundary conditions that at  $x = 0$ ,  $C = C_1$  and at  $x = l$ ,  $C = C_2$ , yields  $J = \frac{D(c_1 - c_2)}{l}$ , with  $l$  being a distance into the film. As the concentration is not always known a common form of steady state Equation is  $J = \frac{Pr(p_1 - p_2)}{l}$ , where  $Pr$  is a constant known as the permeability and  $p_n$  is the pressure at site  $n$ .

If the concentration below the surface of the film is proportional to the surface pressure then Henry's law is valid, as  $p = k_h C$  where  $k_h$  is a temperature dependent constant. Henry's Law can also be written as  $C = Sp$  where  $S = \frac{1}{k_h}$  is the solubility. It follows that the relationship between the constants is  $P = DS$  as  $J = \frac{D(c_1 - c_2)}{l} = \frac{Pr(p_1 - p_2)}{l}$ . This treatment is not always valid as the permeability,  $Pr$ , is not independent of the concentration but holds for low values of solvent in the film, and is a convenient way to show where models of solubility and diffusion converge[44].

There are several ways in which to interpret the diffusion coefficient. Statistical considerations of a random walk through various potentials can yield a value for the diffusion coefficient linking microscopic to macroscopic behaviour, such as with the Einstein-Smoluchowski relationship which describes Brownian motion[45]. When applying Fick's laws to a penetrant moving into dense crystalline structures, such as the oxidation of silicon[46],  $D$  is assumed to have an Arrhenius like form;  $D = D_0 \exp \frac{E_A}{k_b T}$  where  $E_A$  is the energy of activation for the process,  $D_0$  is the equilibrium diffusion coefficient,  $k_b$  is the gas constant, and  $T$  is the temperature.  $E_A$  is commonly interpreted to be the energy of vacancy formation in the material added to the energy of molecular migration for penetrant. Such a relationship is not necessarily valid in polymer thin films where free volume and chain mobility play an important role. However, an Arrhenius like form can be appropriate to describe many processes which are energetically activated and so, many still provide some insight into the energetics of molecular level transport.

## 1.4.2 Diffusion in Polymer Thin Films

When Fick's laws are applied to polymers semi-analytical solutions for the diffusion coefficient are required. Crank[47] developed a range of such solutions in the 1950s by assuming that  $D$  is a function of both the kinetics of solute transport and the polymers reaction to strain. This model is shown in Equation 1.7, where,  $\alpha$  is the rate parameter controlling the approach to equilibrium and  $D_i$  is the instantaneous part of the change. The first term of Equation 1.7 accounts for the changes in the kinetics of the system, which may include the occupation of free volume, and the second term in Equation 1.7 represents the mechanical reaction of the polymer to strain:

$$\left(\frac{dD}{dt}\right)_x = \left(\frac{dD_i}{dC}\right) \left(\frac{dC}{dt}\right)_x + \alpha(D_0 - D) \quad (1.7)$$

At lower concentrations,  $\alpha$  is too small and the second term can be neglected. The analytical nature of this form of  $D$  implies two independent time scales in this process; the polymer's mean relaxation time at the conditions of interest in response to strain,  $\lambda_m$ [42], and secondly the characteristic time of penetrant diffusion,  $\theta_D = \frac{l^2}{D}$ , where  $l$  is the polymer film thickness. Both numbers are normally summarised in a ratio, the Deborah number,  $\frac{\lambda_m}{\theta_D} = (DEB)_D$ [48]. The Deborah number is a way of comparing these two important time scales for diffusion, characterising if the material behaves more like a solid or a liquid. As  $\lambda_m$  depends on the concentration and temperature of the penetrant and  $\theta_D$  depends on the thickness of the material,  $(DEB)_D$  is a function of concentration, temperature, and thickness of the material. If the polymer chains are very flexible,  $(DEB)_D \ll 1$ , as is the case above the glass transition temperature, or the Polymer chains take a long time to equilibrate  $(DEB)_D \gg 1$  the diffusion is Fickian. This is well summarised in Figure 1.6 adapted from Vrentas et al.[48, 49]. It is shown that for a fixed penetrant concentration well beneath  $T_E$ , the temperature beneath which pure polymer acts like an elastic solid, and above  $T_V$ , the temperature above which pure polymer acts like a viscous fluid, the diffusion is Fickian. In both cases the polymers response to strain does not affect the diffusion, as in the former case the polymer response to strain is very slow, and in the latter it is very fast when compared to diffusion timescales. Should the two time scales be similar i.e.  $(DEB)_D \sim 1$  non-Fickian diffusion is observed.

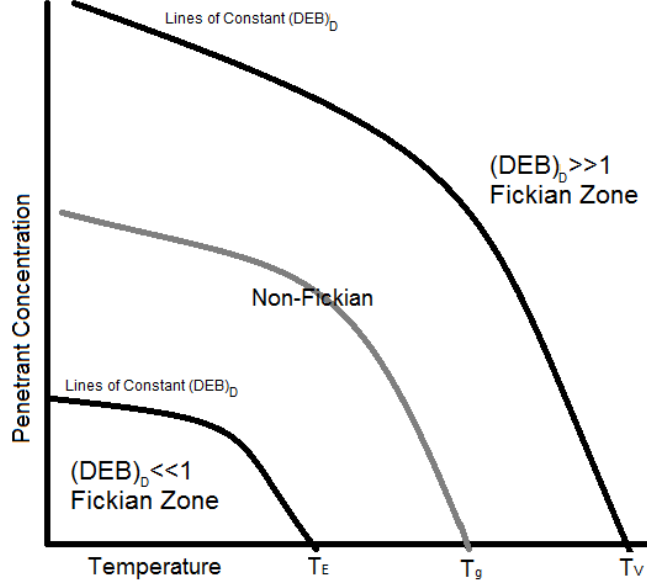


Figure 1.6: A diagram to show the non-fickian diffusion conditions in which  $(DEB)_D \sim 1$ . Diffusion is non-Fickian when the material acts like a fluid  $(DEB)_D \ll 1$  or an elastic solid  $(DEB)_D \gg 1$ .

If the polymer sample has a well defined thin-film geometry Crank has produced several solutions for  $D$ ; all of which neglect edge effects. In these solutions the total mass uptake of penetrant is described by Equation 1.8, which converges at longer time scales and equation 1.9 which converges at shorter timescales the derivation for which is covered elsewhere[50].

$$\frac{M_t}{M_\infty} = 1 - \frac{8}{\pi^2} \sum_{n=0}^{\infty} \frac{1}{(2n+1)^2} \exp \left[ \frac{-(2n+1)\pi^2 Dt}{l^2} \right], \quad (1.8)$$

$$\frac{M_t}{M_\infty} = \frac{4}{l} \left( \frac{Dt}{\pi} \right)^{0.5} + \frac{8}{l} (Dt)^{0.5} \sum_{n=1}^{\infty} (-1)^n \operatorname{ierfc} \left( \frac{nl}{2(Dt)^{0.5}} \right) \quad (1.9)$$

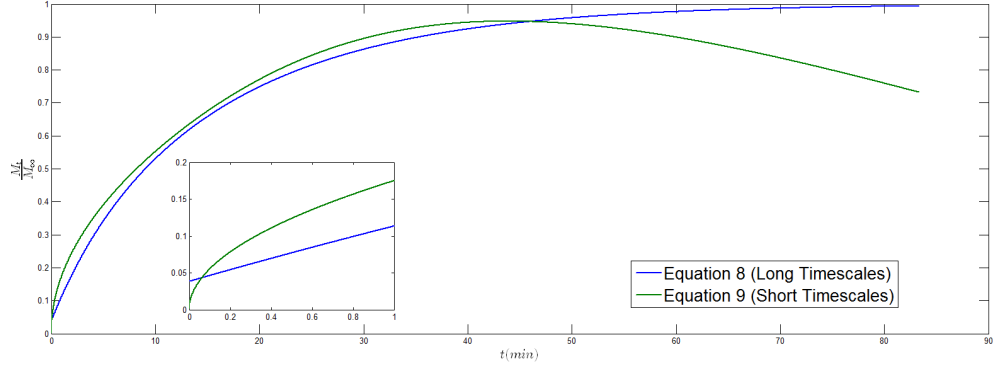


Figure 1.7: Plots of three term approximations for Equations 1.8 and 1.9 for a  $1\mu m$  film with a diffusion constant of  $10^{-12}cm^2s^{-1}$ . For the three term approximation shown, the impact of losing the higher terms means that Equation 1.8 never reaches zero and Equation 1.9 reduces.

Where  $M_t$  is the mass of penetrant absorbed at time  $t$ ,  $M_\infty$  is the mass absorbed at  $t = \infty$  and  $l$  is the polymer film thickness. This leads to two methods used in this study to extract diffusion coefficients. Firstly, from Equation 1.8, the diffusion coefficient can be approximated to two terms, giving Equation 1.10, where  $t_{0.5}$  is the time taken for the normalised mass change of the film to reach half its final value, a mass half life, and  $D_a$  is the apparent diffusion coefficient.

$$t_{0.5} = \frac{0.04914l^2}{D_a} \quad (1.10)$$

Secondly, at short times Equation 1.9 is well approximated by one term giving Equation 1.11 [51].

$$\frac{M_t}{M_\infty} = \frac{4}{l} \left( \frac{Dt}{\pi} \right)^{0.5} \quad (1.11)$$

Therefore fitting a line to earlier part of a plot of  $\frac{M_t}{M_\infty}$  against  $\sqrt{t}$  allows the diffusion coefficient to be deduced.

### 1.4.3 Sigmoidal Diffusion

Equations 1.8 and 1.9 converge when diffusion is Fickian, however, as discussed earlier, this is only valid when the flux is proportional to the concentration gradient, and so  $D$  is constant. More broadly, absorption into polymers is often divided into four categories: Fickian which is proportional to  $\sqrt{t}$ ; anomalous diffusion which is sigmoidal with respect to  $\sqrt{t}$ ; Case II, which is proportional to  $t$ ; or Super Case II, which occurs at an accelerating rate with respect to  $t$ . There are a wide variety of suggested interpretations for each of these behaviours that are well reviewed elsewhere[52].

Fickian behaviour has already been discussed and here a focus is placed on explaining the anomalous sigmoidal behaviour. This is generally attributed to an early stage effect in which Fickian diffusion of the penetrant is initially slowed, resulting in an early exponential diffusion coefficient. Clearly, if initial effects play a major role then Equation 1.10 becomes invalid as it accounts for two diffusion coefficients, and so results in a lower diffusion coefficient than the true coefficient.

There are two physical reasons why the initial mass uptake can be lower than a constant diffusion coefficient would imply; the ambient conditions, or film penetrant surface. The diffusion models discussed here depend on the assumption that the ambient conditions change instantaneously or much faster than the polymer can respond. However, if the time scale for the atmosphere to change its vapour content is similar to the time scales of diffusion, then sigmoidal diffusion is observed. The other common cause of sigmoidal diffusion is a higher surface diffusion coefficient, for example an adsorbed layer, reducing the speed at which the penetrant can enter the bulk of the film initially.

Both cases are well modelled by an initial exponential diffusion coefficient. In desorption experiments, it has been suggested that a temporary change in the heat conduction properties of a local area of the film can lead to a stagnant surface-air boundary layer, explaining sigmoidal desorption[52]. Permeation cups have historically been used to test the water transport. This method involves covering a cup of a penetrant, in this case water, with a thin sample film and weighing the cup periodically to measure the water escaping into a vacuum pumped atmosphere. In these studies it was found that the distance away from the desiccators that pump the ambient atmosphere, determines the diffusion coefficient by up to three times, implying that the ambient conditions just above the thin film were very important[44, 52]. However, sigmoidal diffusion has also been attributed to the properties of the film itself, rather than the ambient conditions. Sigmoidal diffusion has been found for water when ingressing into poly(vinyl acetate)[53] and the diffusion coefficient has also been found to be an exponential function of the concentration for water permeating at steady state through Nylon 6 at 35 °C, and that the surface concentration varied in the film[54] which has been found in systems of cellulose acetate–water and dioxane in polyethylene[52]. In these systems; water permeating through Nylon 6, p-dioxane permeating through Nylon 6, and p-dioxane permeating through polyethylene, the authors attribute the behaviour to a depth dependent permeability coefficient for the system, not the ambient conditions. It is implied that a thin surface layer of higher resistance to diffusion than in the bulk exists for these systems[55]. These studies are also performed at steady state, therefore the observed phenomenon is not related to stress relaxation. Grayson et al.[56] studied methylene chloride in poly(aryl-ether-ether-ketone) using energy dispersive X-ray analysis. The surface treatment and annealing are said to strongly affect the transport, which is not reversible, with the penetrant advancing as a sharp front. In other studies, the molecule size is correlated with activation energetics for the diffusion process

by looking at diffusion rates at a range of temperatures. Considerations of chain mobility led to theories emphasising relative free volume<sup>5</sup> as being the key factor in mass transport in polymers[57, 58], especially in systems in which the polymer swells in the presence of the solvent, such as acetone and PMMA. These studies emphasised the use of a volume fraction to study absorption, rather than mass fraction[52], as the diffusion coefficient was a function of the free volume fraction. For example, the activation energies were found to be a function of the molar volume of the penetrant in polyvinyl acetate[59]. Therefore a diffusion coefficient can vary as a function of free volume, if a denser surface layer on the films is present and several penetrants are studied.

Abbott et al. directly measured concentration profiles in polymer thin films in a system with sigmoidal diffusion by carefully picking a solvent-film system which induced swelling[60]. The swelling was then monitored using NMR. Their measurements show that anisotropic diffusion occurred as a result of a *“highly orientated skin layer being resistant to solvent penetration”*. The hypothesis of the skin layer effect was tested by simply scratching the surface and imaging the swelling in the presence of the solvent; a greater degree of swelling was observed around the scratch. Such cases are particularly important when molecules are transported away from the surface into the polymer faster than they can be adsorbed on the surface[61].

All of the studies discussed here point to the importance of free volume in penetrant polymer absorption. However, direct measurements of density profiles of films linked to the absorption has not been noted in any of these studies, and many of the conclusions seem system specific. Regardless, the factors which are likely to effect the free volume, such as annealing, must be studied carefully in the polyimide-water system, with attention given to the diffusion type which may reveal a density profile.

#### 1.4.4 Water Specific Considerations

Water molecules are particularly small and highly polarised when compared to other organic solvents. Such characteristics give rise to specific considerations when dealing with the transport of water vapour in polymers. In principle, Fickian diffusion can still explain water transport, but such effects need to be taken into account. This has led to recent modelling alongside experiments to investigate the water transport in polymers[62, 63].

Such investigations have provided information about various water specific effects, for example the tendency at high partial pressures of water to increase its diffusion rate because the water separates into separate regions called clusters leading to more free volume[52, 62]. Experimentally and computationally, hydrogen bonds between the polymer and the water vapour have also been shown to be important in certain polymers with hydroxyl, ether, and amines groups, most notably using dielectric

---

<sup>5</sup>Relative to the size of the penetrant molecule.

relaxation spectroscopy and Fourier transform near-infrared spectroscopy to monitor the polar parts of the polymer backbone[64]. Simulations have also shown the importance of this hydrogen bonding with polar groups as it leads to a portion of the absorbed water remaining unbound, free water, and the remainder being bound water via hydrogen bonding[63, 62]. Furthermore, both water monomers and water dimers are formed[65, 62] and, at higher concentration, clusters of water also start to form, as the number of bonding sites on the polymer backbone available to interact with the polar water molecule decline, leading to polymer plasticisation[62]. Pandiyana et al. gave a good description of the plasticisation process based on simulations of epoxy polymer networks[62]. Firstly, initial hole filling absorption which involves no swelling takes place. This is followed by *“the re-arrangement of the small micro-voids... leading to an increase in the partial molar volume of the water molecules. Further increase in the water fraction leads to a sharp change in the volume and the formation of bigger water clusters”*. The large clusters of water lead to a difference in the mechanical properties of the polymer. It would be anticipated that swelling would not occur in every polymer due to a varying degree of cross linking. Simulations, such as Pandiyana’s allow observations at a macro level to be associated with changes at the molecular scale. Such considerations are important when interpreting experimental results presented in this study.

## 1.5 Summary

This chapter began by pointing out the importance and applications of humidity sensing, providing a clear motivation to understand and improve existing humidity sensors. The hysteresis effect in Honeywell capacitance based humidity sensors was then described, and this is one of the catalysts behind this project. The goal of understanding the important factors and mechanisms of water transport in polyimide was outlined.

The various scales of humidity were then discussed such as; dew point, absolute humidity, and relative humidity, in section 1.1. Section 1.2 outlined the working principles of various humidity sensors which rely on measurements of particular properties of water vapour, and many of which rely on the absorption/adsorption of water molecules into a sensing element.

A brief summary of the literature focusing on two key areas was then presented on polyimide, section 1.3, the sensing element material used in Honeywell humidity sensors, and on water diffusion in polymers, section 1.4. This encompassed a large body of literature from a chemical, manufacturing, and computational background. A focus was placed on sigmoidal diffusion and its potential causes. It was suggested that the diffusion type can reveal information about the structure of the polymer thin film as a function of depth, especially a thin skin layer on the surface.

All of these themes are explored in this document. The next chapter outlines the instrumental techniques referred to throughout this study, to allow an interpretation of the results presented.

## Chapter 2

# Measurement Techniques and Instrumentation

Throughout this study, a range of experimental techniques have been used to obtain the data necessary to test hypotheses and develop an understanding of the water vapour/polyimide system. The principles which underpin the instrumentation used during these experiments is outlined in this chapter.

Section 2.1 outlines the concepts and principles used by the instruments which perform the capacitance measurements which are presented throughout this study. Section 2.2 will show how measuring impedance can lead to inferring the mass of thin films that are deposited on quartz crystals.

Three sections outlining methods of structural characterisation are then presented; neutron reflectivity, NR; transmission electron microscopy, TEM; and atomic force microscopy, AFM. The principles of NR are discussed in section 2.3 and the characteristics of the specific instruments used in this study are considered. The operational modes of the TEM for mapping; film structure and elemental distribution in a samples are then presented. Atomic Force Microscopy, AFM, is then described in section 2.5. In each case, the type of data which can be obtained using the given technique is emphasised.

The final section, 2.6, summarises the operation and use of a humidity generating thunder chamber, a controlled environment test chamber in which samples have been probed.

### 2.1 Impedance Measurements

In this section a brief overview is provided of the methods deployed to measure impedance by the instruments used.

### 2.1.1 Auto balancing bridge method

Capacitance measurements of humidity sensors and prototype devices were performed using the Agilent E4980A LCR meter and E4981A capacitance meter. Both instruments use the same method of measuring the impedance via the auto balancing methods, and then converting the measurands into values for the series capacitance and parallel capacitance as required[66].

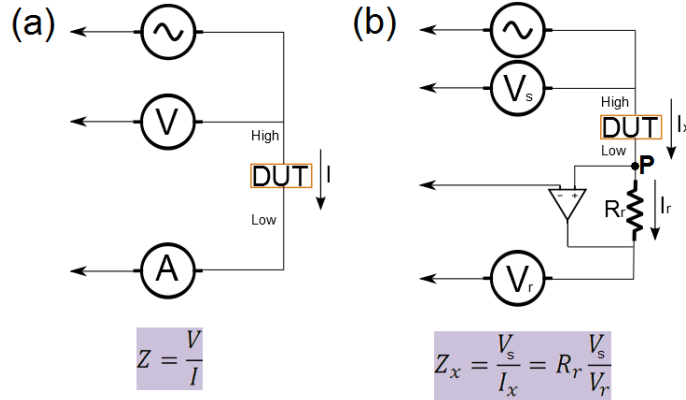


Figure 2.1: Two methods for the measurement of impedance (a) The simplest form, an alternating potential is placed across the device and the resulting current wave is measured. (b) A known resistor is placed in series with the device under test (DUT) and the ratio of the voltages across the DUT and the device allows the characteristics to be inferred.

Figure 2.1(b) shows the use of the auto balancing bridge method. The potential at the point P is kept at zero volts, as the current through R is maintained to be equal to the current flowing through the device under test, DUT. The impedance is calculated using the two voltages  $V_s$  and  $V_r$ . The value of  $R_r$  sets the measurement range. The scheme shown in Figure 2.1(b) has the added advantage over Figure 2.1(a) in that calibration errors can be avoided, as the same voltmeter is used in the measurement of  $V_s$  and  $V_r$  with a switch between them. The two voltages are then fed into a vector ratio detector, which splits the imaginary and real components of the signal. The impedance is calculated by comparing the two voltages. The E480A and E481A both provide the operating frequency required, which is same as the frequency of measurement of a Honeywell device(1Mhz)[15].

### 2.1.2 Measuring Capacitance

In this project, the Agilent 16048A 4-terminal test leads have been used to take all the measurements presented. The instrument was calibrated for each setup by storing an open, and a short, measurement at the point of the device under test(DUT). This allows the measurement box to store the residual impedance and to apply the necessary corrections before presenting a final measurement.

These measurements were then fed into an equivalent circuit model for a capacitor which was used by the instrument to interpret the impedance measurement as a capacitance.

## 2.2 Quartz Crystal Microbalance

Quartz Crystals Microbalance, QCM, has been used throughout this body of work as an in-situ monitor. The specific models used are discussed as appropriate throughout this study; here the principle of QCM as a mass monitor is introduced.

### 2.2.1 Piezoelectric Effect

Piezoelectricity, from the Greek word *piezo* which means pressure, refers to the electric potential formed in a material upon the application of mechanical stress. Materials of this kind were originally postulated by Coulomb, however this effect was first reported by the Curie brothers in the 19th century[67]. The application of mechanical stress results in an asymmetric distribution of electrons with respect to the ions within the crystal lattice, due to the displacement of ions as the crystal experiences strain. As a result of the displaced ions, a potential is formed within the material; in effect a mechanical force is turned into a potential difference.

This occurs specifically in some crystals with ions on crystal lattice sites with asymmetric charge around them, and which lack inversion symmetry. The application of stress in such cases results in a reconfiguration of the asymmetric charge or a reorientation of the molecular dipoles within the material. Likewise, upon the application of a potential across the crystal, the lowest energy configuration for the system changes, and a mechanical deformation of the crystal becomes energetically favourable. This is the inverse piezoelectric effect, that is, the application of potential should result in changes to mechanical properties of the crystal.

A steady alternating potential, applied across a thin crystal with such properties, results in a mechanical oscillation. At the natural resonant frequency of the crystal, stable oscillation occurs forming a standing wave between the electrodes; shown in Figure 2.3. At that resonance frequency the crystal presents a reduced impedance to the applied potential. The resonant frequency modes for such a crystal can then be measured by incorporating the crystal into a feedback loop of an oscillating circuit. The mode of oscillation is a function of; the angle at which the crystal was cut to the major axis of growth of the crystal,  $Z$ , its physical size, and the specifics of the crystalline structure. Furthermore, a

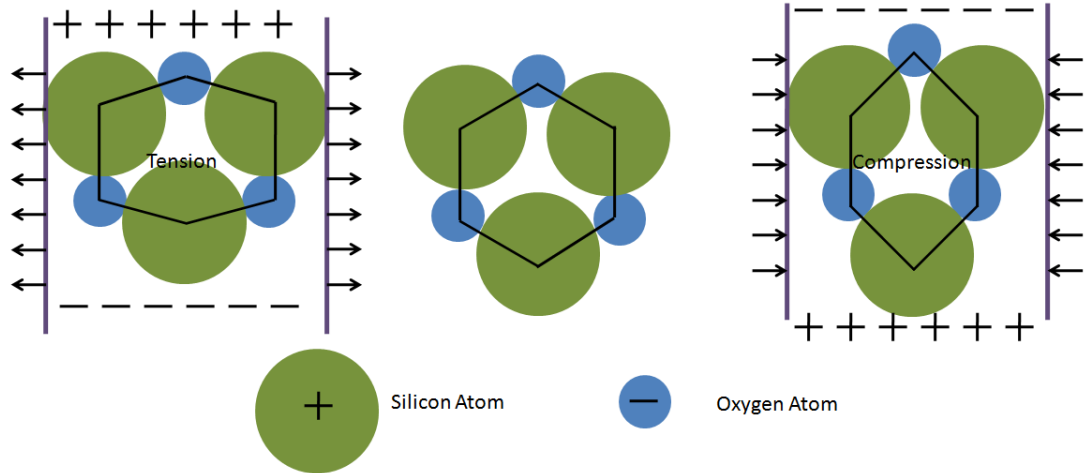


Figure 2.2: Quartz under mechanical stress. It is shown that under tension and compression a potential is generated in the quartz.

given crystal's tendency to deform within an external electric field can be calculated from the density of dipoles and their polarisability, allowing the control and calculation of the resonance frequency.

Quartz,  $SiO_2$ , is the most common place such material used in for applications requiring piezoelectricity due to its economic advantages; it is commonly used for such applications as watches and timers. When cut at  $35^\circ 15'$ , AT-cut, or  $-49^\circ$ , BT-cut, the thermal coefficient is zero giving a high thermal stability[68]. The size of the crystal can then be determined to produce the desired resonant frequency.

### 2.2.2 Piezoelectricity as the basis of a mass sensor

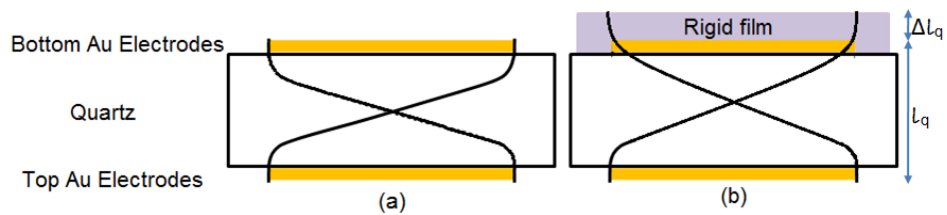


Figure 2.3: The shear mode oscillation in (a) an uncoated QCM (b) a rigid film.

The application of an electric field across a quartz crystal will result in a mechanical deformation. An alternating voltage at the resonant frequency across the crystal leads to resonant standing wave. Upon the addition of mass, the mechanical wave will propagate into any material in contact with the quartz. Therefore to a good approximation, the thickness of the added material will increase the resonant

frequency linearly, providing the viscoelastic properties of the added material are similar to those of quartz.

$$f_q = \frac{V_q}{\lambda_q} = \frac{V_q}{2l_q}$$

Where,  $f_q$  is the resonant frequency of the quartz,  $V_q$  is the velocity of the wave in quartz,  $\lambda_q$  is the wavelength of the resonant wave and  $l_q$  is the length between the two plates. Therefore, as the length, and hence wavelength, of the resonant condition increases, the resonant frequency of the quartz crystal decreases. For a uniform species of deposited material, the increase,  $\Delta l_q$ , is directly proportional to an increase in mass,  $\Delta M_q$ , as shown in Equation 2.1

$$\frac{\Delta f_q}{f_q} = -\frac{\Delta l_q}{l_q} = -\frac{\Delta M_q}{M_q} \quad (2.1)$$

Equation 2.1 can be rewritten into a more useful form as the mass,  $M_q$ , of the quartz crystal in between the electrodes and can be re-written as  $A\rho_q l_q$  where;  $A$  is the active area and  $\rho_q$  is the density of quartz. Substituting in  $l_q = 2f_q$  yields the Sauerbrey equation 2.2 [69]:

$$\Delta f_q = -\frac{2f_q}{V_q A \rho_q} \Delta M_q = -C \Delta M_q \quad (2.2)$$

The linear nature of this equation has led to its use in quartz crystal based film thickness monitors. However, the intrinsic assumption is that the deposited material has similar mechanical properties to those of quartz and hence there are no boundary effects of mechanical losses as the wave passes into the deposited material. This has been shown to be a reasonable assumption in most metals within a material specific mass limit[70, 71].

When used in this manner, as a rigid film deposition monitor, QCM can be considered a mature technology. However, Chapter 3 will probe the veracity of such assumptions for polyimide thin films, outline methods of monitoring the resonant frequency, and discuss other models of QCM behaviour extensively.

## 2.3 Neutron Instruments and Facilities

Neutrons with no net electric charge are capable of penetrating matter to a greater extent than charged particles, such as electrons. In addition, neutrons interact with matter via nuclear forces which operate on the order of femtometers. Hence, to the neutron, solid matter is not particularly

dense. In aluminium for example, a neutron beam is attenuated at  $\sim 1\%$  per millimetre as opposed to  $\sim 99\%$  per millimetre for x-rays[72].

Consequently, neutron reflectivity has commonly been used to assess the structure of thin films for both liquid interfaces[73, 74] and polymer thin films[75, 76]. More recently neutron reflectometry has probed the properties of polymer thin films undergoing dynamic changes[77, 78], such as the diffusion of water into the polymer matrix[79, 80].

However, neutron beams require large energies to be produced, and the mean lifetime of a neutron in the atmosphere is about 15 minutes. Consequently, neutron reflectometers suitable for performing such experiments are located at large scientific facilities, often international collaborations. As a result, beam time is highly coveted. In this study neutron reflectivity has been used for a variety of experiments.

In this section, the use of neutrons as a probe for matter is outlined. Following this, a brief description of the features and requirements of neutron facilities is given, with particular attention paid to the two reflectometers used to collect data during this study.

### 2.3.1 Neutron Scattering

Neutron scattering by matter can occur by either interactions with an unpaired electrons via their spin magnetic moment, or by interactions with the atomic nucleus. For simplicity, magnetic moments are neglected here as this effect is minimal for an un-polarised neutron beam[75].

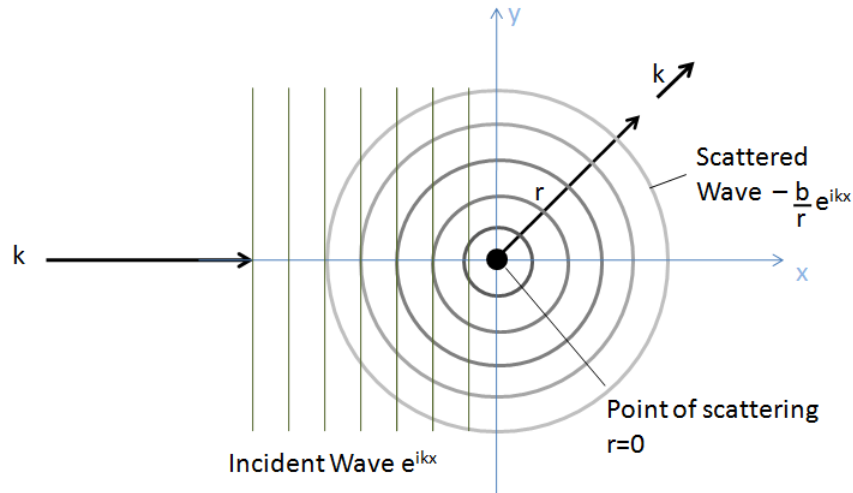


Figure 2.4: The scattering of a neutron wave by a single nucleus. The scattered wave will have amplitude  $\frac{b}{r}$ . The plane wave fronts from the left denote the neutrons which are scatter radially from the nucleus as shown. Adapted from Pynn et al.[72].

The scattering cross section,  $\sigma$ , of a nucleus is the size of the interaction area of the nucleus in square meters, effectively giving a probability of interaction. Typically, neutrons have a wavelengths of a few angstroms,  $\lambda = 10^{-10}m$ . This is much greater than the cross sections (which will be discussed later in this section) of most elements, which are of the order  $\sigma \approx 10^{-14}m^2$ . Consequently, most nuclei can be reasonably approximated as a point scatterer assuming  $\lambda \gg \sigma$ . As a result incident neutrons interacting with the nucleus scatter isotropically[72].

The wavevector,  $k = \frac{1}{\lambda}$ , can be calculated from the de Broglie relationship,  $\lambda = \frac{h}{p} = \frac{h}{mv}$  where:  $h$  is Planck constants,  $v$  is the velocity of the neutron,  $m$  is the mass of the particle (a neutron here) and  $p$  is the momentum.

$$|\vec{k}| = \frac{2\pi mv}{h} \quad (2.3)$$

Equation 2.3 shows the wavevector of the incident neutron. The incident neutron beam is well represented as a plane wave with a wave function,  $\psi_{incident} = e^{i\vec{k}\vec{x}}$ , with unit amplitude as shown in Figure 2.4. Assuming that  $|\vec{k}|_{incident} = |\vec{k}|_{scattered}$ , i.e. elastic scattering, the wave function of the scattered wave can be written as  $\psi_{scattered} = -\frac{b}{r}e^{i\vec{k}\vec{x}}$  where  $r$  is the distance away from the point scatterer. The reduction of the scattered waves amplitude,  $\psi_{scattered} \propto \frac{1}{r}$ , is a consequence of isotropic scattering such that the intensity of the neutrons is given by  $\psi_{scattered}^2 \propto \frac{1}{r^2}$ , in accordance with the inverse square law.

If the cross section,  $\sigma$ , is an area then  $b$  is the radius of such an area, known as the scattering length. It is specific to each nucleus and is a measure of the strength of the scattering as shown,  $\sigma = 4\pi b^2$ . This is generally measured experimentally, however it can be calculated using simulations which consider the interactions of the nuclear force[72]. The minus sign at the front of the amplitude constant accounts for the potential being negative, while  $b$  is generally considered positive. Electromagnetic interactions may result in asymmetric scattering from a single nuclei. However, over a large sample with many non-polarised neutrons such effects are averaged out.

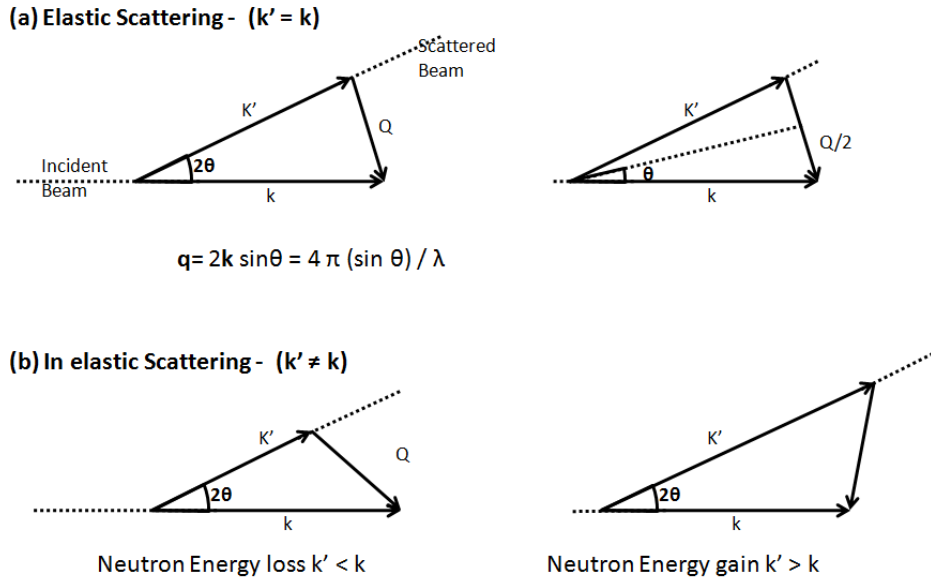


Figure 2.5: (a) Elastic scattering ( $k = k'$ ): Shows an elastic scattering process where there is no transfer of energy between the neutron and the sample. (b) Inelastic scattering ( $k \neq k'$ ): Shows the possibilities for inelastic scattering where energy is transferred between the neutron and the sample. Adapted from Pynn et al.[72].

Scattering is not necessarily elastic as the atoms in matter are able to recoil under the neutron beam resulting in inelastic interactions. The vectoral difference in the wave vectors  $k - k'$  of the scattered and the incident neutron is characterised by  $q$ , the quantity shown in Figure 2.5, for elastic scattering  $q = \frac{4\pi}{\lambda} \sin\theta$ . This is the scattering vector and indicates the strength of a given scattering event.

In this project, neutron reflectivity has been used. Neutron reflectivity is designed to probe interfaces and thin films with appropriate modelling of results[74, 81], which will be discussed as required<sup>1</sup>.

In this section the principles underpinning the production, collimation, and detection of neutrons at the two facilities used in this investigation are outlined, without considering the data interpretation methods. The two facilities are the D17 beam at the Institut Laue-Langevin, ILL[82], and the INTER beam at Rutherford Appleton Laboratories, RAL [83, 84] which will now be considered alongside each other.

### 2.3.2 Neutron Sources

There are three common sources of neutrons: **Electron Linear accelerators**, **Reactor sources**(D17), and **Spallation sources** (INTER). To probe soft matter a good neutron spectral bandwidth and high

<sup>1</sup>Mostly in section 5.1.

flux are desirable in order to probe a wide range of scattering events[83], thus allowing a more accurate representation of the film to be modelled during post processing.

At the ILL the **reactor source** employs nuclear fission, a chain reaction of Uranium 235 in which neutrons of 1-2MeV are a product, see Figure 2.6. The neutrons have a Maxwell-Boltzmann distribution with the most likely velocity being  $v \sim 3000ms^{-1}$  or a wavelength centred on  $1.4\text{\AA}$ .

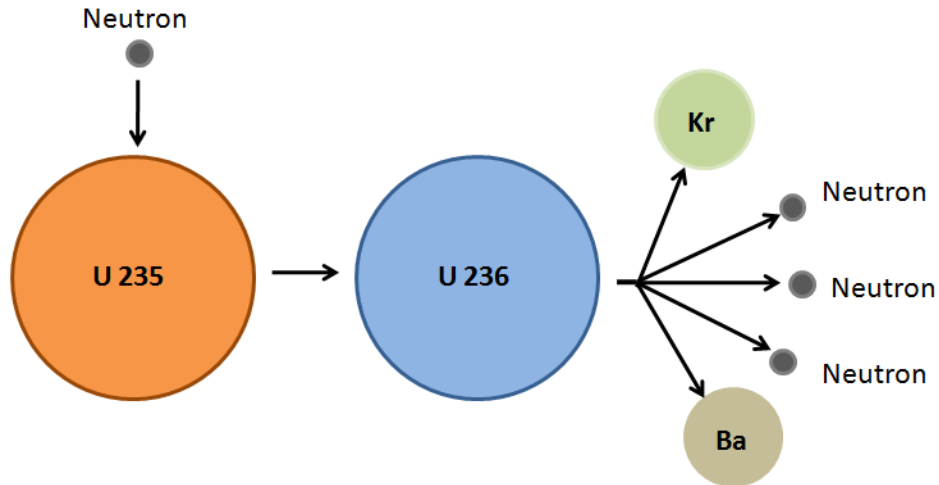


Figure 2.6: The chain reaction causing the production of neutrons. Firstly, an incident particle causes the Uranium 235 to become an unstable isotope Uranium 236. Uranium 236 then break down into krypton (36) and Barium(56) releasing neutrons.

Generally such reactors run continuously, for a period of a few weeks, 50 days at the ILL, before shutting down for a few days in order to have the fuel replaced and to allow maintenance. The flux at the sample site depends not only of the source but on the characteristics of moderators and neutron guides.

The role of moderators is to control the wavelength and pulse timing. This is achieved by using a hydrogenous medium, such as water, so the neutrons are cooled to the desired speed with a Maxwellian distribution. A greater degree of the moderation requires more interaction between the neutrons and the moderator and so a greater variance in the energies of the resulting neutrons. Therefore a balance must be struck between the wavelength and how synchronised in time the resulting pulse is required to be.

**The Spallation source** at ISIS involves the collision of high energy protons with nuclei. The energy required of protons is the order  $800MeV$  and so the incident proton must undergo significant acceleration, in this case via a linear accelerator and a proton synchrotron. Although this is possible in a

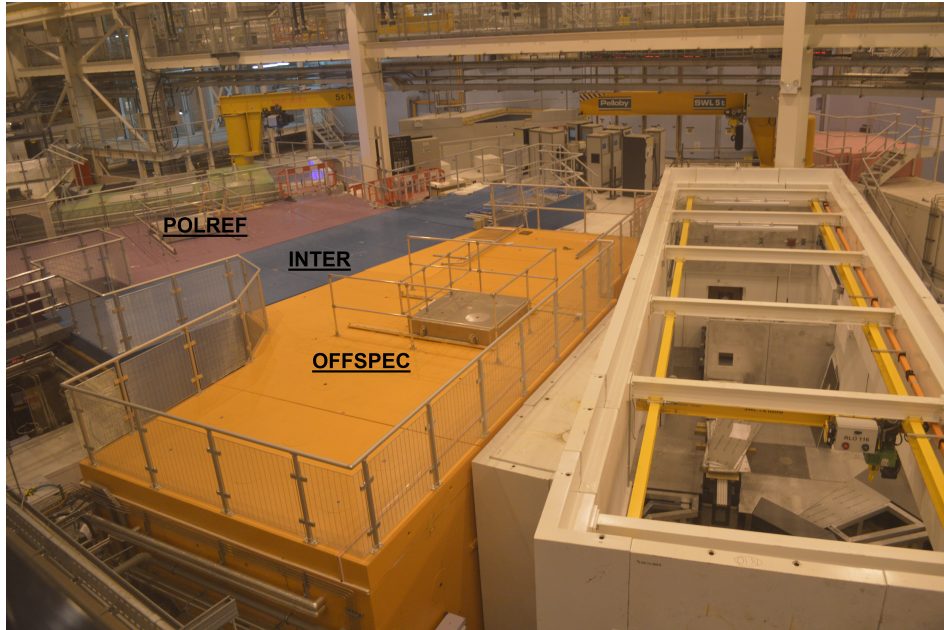


Figure 2.7: A photo showing the various instruments in the main hall of the second target station at the ISIS neutron facility. There is capacity for a total of 18 instruments, and building is ongoing with the three operational instruments labelled. Additionally, the Larmor instrument, on the right hand side, is commissioning. As a result, spatial restrictions are significant.

linear accelerator, a synchrotron is more spatially efficient. However, the proton current is much higher if the protons enter into the synchrotron at a high energy, and therefore a common configuration is a combination; linear acceleration followed by a synchrotron.

At ISIS production begins with an ion source and a linear accelerator consisting of copper drift tube electrodes accelerating the protons to  $0.37c$ , where  $c$  is the speed of light. After 10,000 revolutions around a 163m synchrotron, the protons have been separated into two bunches moving at  $0.84c$ . A tungsten target is then bombarded with these bunches of protons to produce neutrons at target station two which supplies the INTER reflectometer[83]. The repetition rate of proton pulses at 10hz, allowing 100ms for each pulse, this enables wavelengths up to  $20\text{\AA}$  to be used at a good resolution.

### 2.3.3 Neutron transport

As the decrease in the flux of neutrons follows the inverse square law from the source it is clearly desirable to transport the neutrons to the given instrument with as little flux loss as possible. Therefore, in neutron facilities space is at a premium, see Figure 2.7. Neutron transport away from the target to the reflectometer (or other instrument) is achieved with the use of neutron guides. Neutron guides rely on total internal reflection of neutrons. The refractive index of neutrons can be calculated as:

$$\nu = 1 - \frac{\lambda^2 p_b}{2\pi}$$

where  $p_b$  is the scattering length density. This behaviour somewhat like fiber optic cables and can be tailored as such. Most of the epithermal neutrons<sup>2</sup>, undergo little or no moderation and can cause background counts in the detector. Well designed neutron guides can also act as a preliminary filter for the wavelength range as the total external reflection is a function of the neutron wavelength. Locating the instrument away from the source of neutrons with sufficient space to place the required shielding between instruments acts to reduce the background radiation[75].

### 2.3.4 The D17 Reflectometer

Ideally, a beam has both a high flux and well defined wavelength characteristics. In the design of most reflectometers these two attributes are balanced depending on the purpose of the instrument. The D17 reflectometer is designed to allow a high flux such that the widest resolution required to resolve the sample can be selected: this is user defined. As a result, relatively low reflectivities can be measured with a wide  $q$ -range[82]. The reflectometer has two modes of operation, time-of-flight (TOF) and monochromatic. No results using the former mode (TOF) from this reflectometer are presented in this study, but the details of this mode are well covered Cubitt et al.[82].

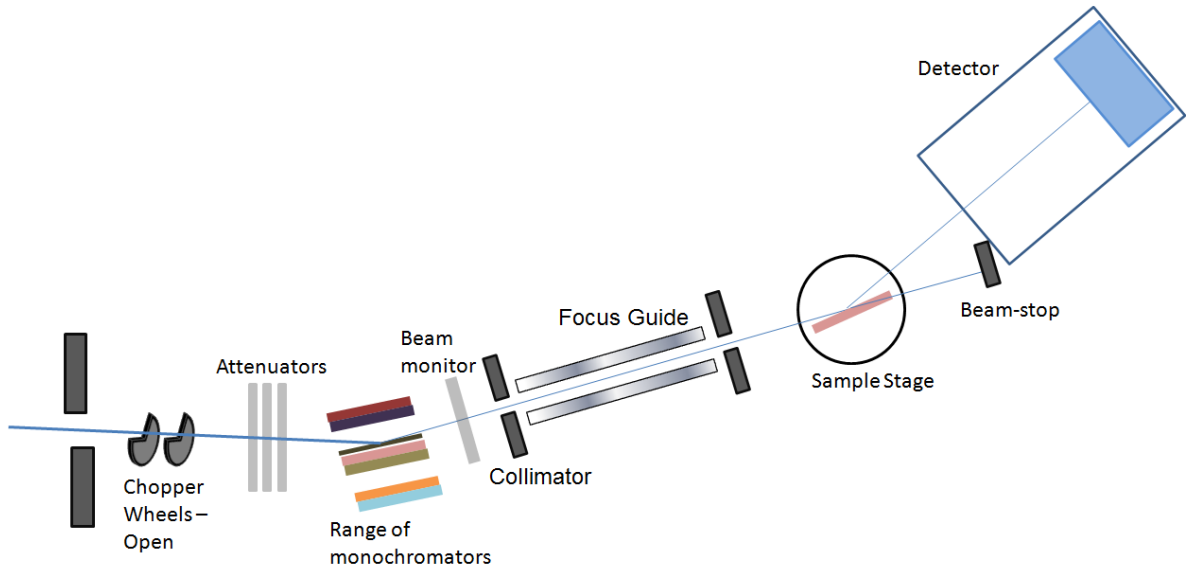


Figure 2.8: The layout of D17 in monochromator mode. Adapted from Cubitt et al.[82].

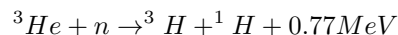
The layout of the D17 in monochromator mode is shown in Figure 2.8 which was adapted from Cubitt et al.[82]. The **chopper wheels** are used in time of flight mode and remain open while the reflectometer operates in monochromator mode.

<sup>2</sup>Neutrons with an energy in the range 0.025–0.4 eV.

**Monochromation** can be achieved either by means a crystal Monochromator, using Bragg diffraction to selected the desired wavelength. In this instrument, a range of crystal monochromator are available allowing the wavelength selection vs beam flux to be controlled. An Fe/Si monochromator can act to polarise the incident beam for experiments in which the magnetic properties of the sample with a wavelength of  $5\text{\AA}$  and a 5% error. Here, the wide range monochromator was used to enable a high flux and probe a wide range of scattering events. The white beam flux at the sample position is  $9.6 \times 10^9 s^{-1} cm^{-2}$  [82].

The incident beam can be monitored by detecting the neutron flux before the sample. A neutron **monitor** consists of a thin layer, a few atoms thick, of  $^{235}U$  on a glass surface of a flat gas detector. The role of the monitor is to react with very few neutrons to produce a signal in proportion to the beam such that the flux can be inferred.

Efficiency in neutron detection is key as it can be used to give the counting time required to acquire a spectrum with good statistics. Typically neutron detection is accomplished by either scintillation or via gas detection. A detector should be able cover a wide range of angles and so a wide range of  $q$  values, which can be achieved by having a broad range of pixels. Gas detectors exploit the effect of neutron absorption into a nucleus and measure resulting ions. The D17 instrument used in this project utilised a reaction of the neutron with Helium 3 in which a neutron is absorbed to produce a proton and tritium nucleus.



The fast ions produced are then detected via the secondary radiation. The detection chip itself is 2D  $250 \times 500mm$  and resolution  $2.3 \times 3.5mm$  type[82] made by A. Gabriel et al.[85]. The wide  $q$  range,  $0.005-0.3\text{\AA}^{-1}$  and high flux from D17 make it a suitable instrument to probe polymer samples<sup>3</sup>.

### 2.3.5 The INTER Reflectometer

The second target station at ISIS was built in order to increase the spectral bandwidth of the neutron beams resulting in neutron wavelengths up to  $20\text{\AA}$ , typically  $1.5 \leq \lambda \leq 17\text{\AA}$ . INTER is a non-polarised vertical scattering plane beam line which is located alongside two other beam lines; POLREF and OFFSPEC, in a crowded hall as shown in Figure 2.7. It has been optimised for liquid surfaces, meaning it has a high flux to detect low reflectivities.

---

<sup>3</sup>The implications and importance of a wide  $q$  range is discussed further in section 5.1.2 in which experiment design is discussed.

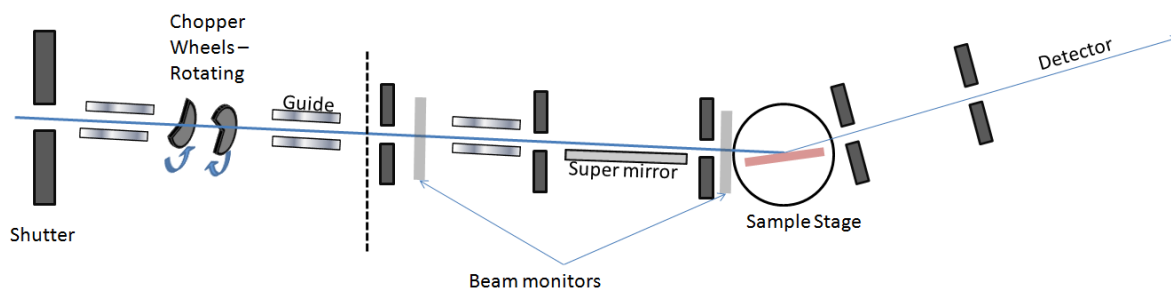


Figure 2.9: The layout of the Inter beam line adapted from Webster et al. [84].

The static mode setup is somewhat similar to the one discussed for the D17 reflectometer. Inter uses a super mirror to define the angle of the beam, a straight wave guide, and a chopper wheel system to act as a monochromator, as shown in Figure 2.9, which is adapted from Webster et al.[84]. The neutrons are moderated partly by a grooved composite moderator before arriving at the dual chopper system. The first chopper is a 400mm thick nimonic blade<sup>4</sup> rotating at 20hz. The second chopper is a disk counter rotating to the first blade; this system defines the bandwidth of the beam at the sample. The monitors are able to monitor the wavelength distribution of the neutrons.

The detector has a variable distance to the sample, from 2-8m, with an identical detector to measure the background[84]. In essence the machine is optimised to measure weak signals across a wide range of  $q$ . In this study, INTER has been used in both static and time of flight modes.

The chopper wheels are vital *to realising* the time of flight mode. Varying the rotation speeds and phasing the two chopper wheels allows the selection of neutrons of a given velocity/wavelength[87]. The undeflected incident beam is at  $2.3^\circ$  the sample stage by default, which gives a peak  $q$  value of  $0.18\text{\AA}^{-1}$  corresponding to a real space thickness which would be anticipated for an adsorbed layer ( $\sim 35\text{\AA}$ ).

The selection criteria for a reflectometer for this project are to have a sufficiently high flux and a wide enough range in  $q$  to allow full reflectivity profiles with good statistics to be acquired in as little a time as possible<sup>5</sup>. The wide  $q$  range and high flux make both of the reflectometers used in this project suitable to probe polymers and adsorbed layers, the materials of interest in this project.

## 2.4 Electron Microscopy

The versatility of Transmission Electron Microscopy (TEM) to provide elemental maps, and as an imaging tool for small samples, has led to its frequent use during this investigation. The use of TEM

<sup>4</sup>Nimonic is a Ni-Cr-Co-Ti-Al super alloy renowned for its mechanical properties [86].

<sup>5</sup>Simulations presented in section 5.1.2 will confirm the  $q$  range required.

requires an understanding of the different imaging modes and contrast generating mechanisms, such that the images obtained can be interpreted accurately. The purpose of this section is to provide a very brief overview of the mechanics of TEM, the origins of the contrast, and different modes in which it can be operated.

### 2.4.1 TEM - Probing a sample

In 1872 Ernst Abbe showed that, given a lens with sufficient angular acceptance, the smallest distance that can be resolved,  $\delta$ , by a given wavelength,  $\lambda$ , is approximated by  $\delta \sim \frac{\lambda}{2}$  for a far field image. Consequently optical light, with a maximum resolution the order of hundreds of nanometres, cannot map atomic distances. The work of de Broglie on wave-particle duality in the 1920s provided a theoretical basis to consider imaging using a wide range of particles. The de Broglie wavelength, defined as,  $\lambda = \frac{h}{p}$ , shows the inverse relationship between a particle's momentum,  $p$ , and wavelength with Planks constant,  $h$  acting as the constant of proportionality.

The electron proved itself to be the immediate particle of choice due to its mass, charge, and ease of production; all of which make it well suited to atomic resolution microscopy. This is demonstrated when considering that a wavelength of  $10^{-10}\text{m}$  is required to probe atomic distances, which corresponds to electrons with an energy  $>30\text{KeV}$ , which are easily produced. Additionally, electrons interact strongly with matter via the EM force. Equation 2.4 shows the de Broglie wavelength where the electrons momentum when accelerated by a potential difference,  $V$ , is  $\sqrt{2m_0eV}$ ; where,  $m_0$  and  $e$  are the rest mass and charge of an electron respectively.

$$\lambda = \frac{h}{\sqrt{2m_0eV}} \quad (2.4)$$

At near relativistic speeds, which are common in modern electron microscopes, the classical Equation  $p = \sqrt{2m_0eV}$  is no longer applicable. Therefore, a relativistic correction is required yielding Equation 2.5, where  $c$  is the speed of light in a vacuum.

$$\lambda = \frac{h}{\sqrt{2m_0eV(1 + \frac{eV}{2m_0c^2})}} \quad (2.5)$$

This theory was put into practice by Ruska and Knoll who built the first working electron microscope in 1932[88].

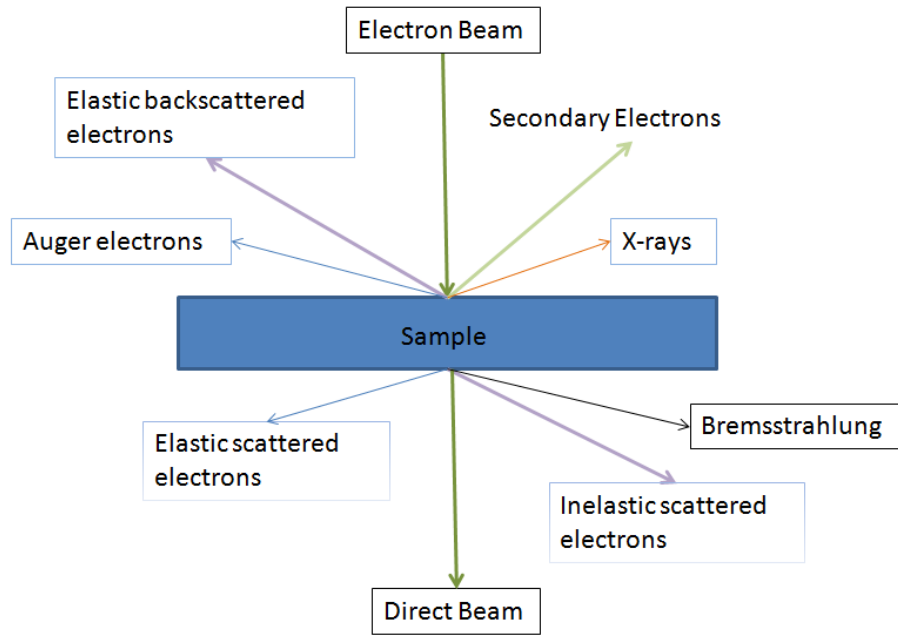


Figure 2.10: The various signals emitted from a thin sample when illuminated by an electron beam, each signal can provide different information about the sample.

For a 200kV electron the wavelength is approximately 2.51pm, much smaller than atomic distances, therefore the limiting factor is no longer the diffraction limit, but rather the quality of electron lenses. In addition to superior resolution, electron-matter interactions also produce a range of signals from a given sample, as shown in Figure 2.10. Depending on the purpose of the experiment, and the sample, it may be preferable to analyse any number of these signals in addition to the direct beam.

Firstly, it is useful to understand the anatomy the TEM as shown in Figure 2.11. In this section each component of the TEM will be considered in turn prior to a general discussion regarding the contrast generating mechanisms from samples relevant to this study, with specific reference to the instruments used.

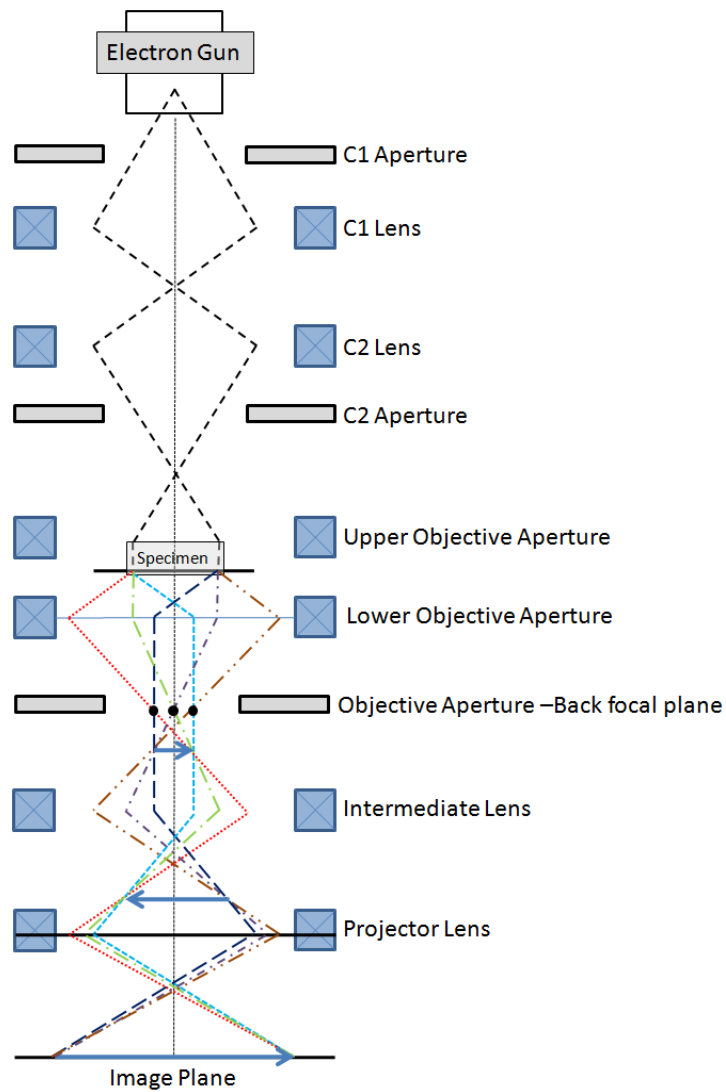


Figure 2.11: Layout of a typical TEM column in bright field mode. This shows the electromagnetic lenses and apertures used to generate an image. The diffraction lens and selected area aperture are not shown. Adapted from Williams and Carter[89].

The overwhelming majority of the TEM work presented has been carried out using a conventional FEI Tecnai T20 transmission electron microscope (T20)<sup>6</sup>.

### The Electron Source

Electron sources for TEM can be categorised under two categories; **thermionic emitters**, and **field emitters**. The brightness and spatial coherence of the beam produced are characteristic of the given emitter.

<sup>6</sup>Some results presented have been obtained using the JEOL ARM200cF transmission electron microscope (ARM) which will be noted.

Thermionic emission is achieved by sufficiently heating an appropriate material, typically tungsten or Lanthanum hexaboride,  $LaB_6$ . The heat generated provides sufficient energy to electrons to overcome the work function of the given material. The heat required is generated by placing a negative potential on the filament and grounding the anode plate, generating electrons. Emission is controlled by the Wehnelt cylinder, which is held at a high negative potential, normally a few hundred volts less than the filament, acting as a convergent lens. An anode is placed further down the column in order to accelerate the electrons[89]. The T20 uses a  $LaB_6$  element with an accelerating voltage of 200KeV.

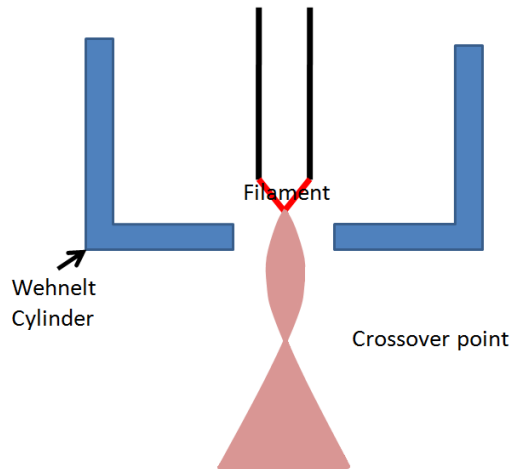


Figure 2.12: The Electron Gun. The cross over point can be considered the source, and the angular divergence is determined by both of the characteristics of the Wehnelt.

Field Emission Guns(FEGs) tend to have current densities three orders of magnitude higher than thermionic emitters. This is achieved by holding a sharpened tungsten tip at a large negative potential and placing it inside a potential such that an intense electric field gradient is produced at the tip. This leads to generation of electrons via quantum tunnelling through the potential barrier. A second anode is then used to further accelerate the electrons and focus them to the cross over point.

The beam current, angular convergences and diameter at the cross over point all determine the brightness of the beam further down the column. The angular convergence, of the order of ten of milliradians, must be optimised for the given imaging setup and so the beam is passed through a system of electron lenses as shown in Figure 2.11.

**Electron Lenses** The simplest type of electron lenses which can be envisaged is an electrostatic lens, which consists of a cylindrically symmetric conducting coil held at a negative potential, centered about the optic axis of the electrons, generating an electric field. An electron passing along the optical

axis experiences no net force. An off-axis electron is deflected towards the optical axis. In such a system, the electron displacement from the optical axis is proportional to the force experienced. The voltage required for electrostatic lenses are comparable to that of the accelerating voltage and so high voltage insulation is required.

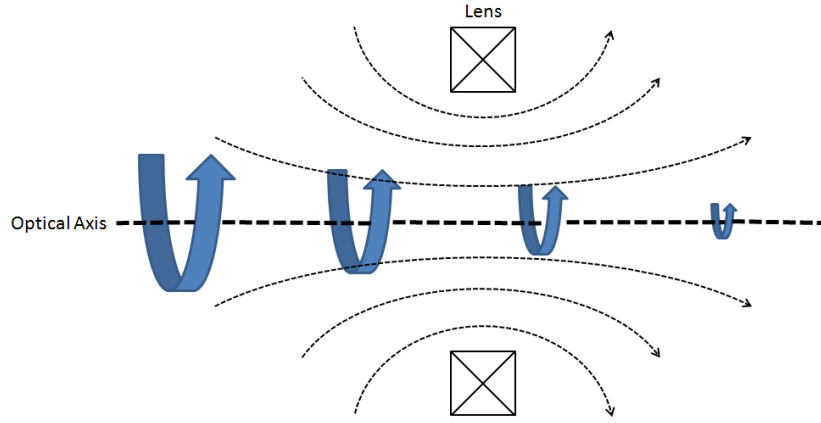


Figure 2.13: 2D depiction of magnetic flux lines (dashed) from a short coil in cross section.

An electromagnetic lens is almost always used (including in the T20). This relies on the Lorentz force,  $\vec{F}$ , experienced by the electrons in a magnetic field,  $\vec{F} = -e(\vec{v} \times \vec{B})$  to provide a focusing action, where;  $e$  is the charge of an electron and  $(\vec{v} \times \vec{B})$  is the cross product of velocity vector of the electrons and the magnetic field. The magnitude of the force,  $F$ , is given by  $F = evB\sin(\phi)$ , where  $\phi$  is the angle between  $v$  and  $B$ . Consequently,  $\vec{F}$  has no component along the optic axis i.e. when  $\phi = 0$ , and so electrons travelling along the optical axis experience no force. This is the direction of most of the field. The use of the Lorentz force results in the electrons experiencing a radial force, and radial focusing resulting in a helical trajectory. Magnetic lenses tend to have lower aberrations for the same focal length than any alternative. Detailed comparisons between the two types of lenses alongside an analysis of the ray path of the electrons are well presented elsewhere[90, 91].

The consequence of the use of electromagnetic lenses is that the beam path is helical resulting in image rotation. Spherical aberrations are a consequence of a lens field having a different effect on off-axis electrons. The lens causes the wavefront from a point source to be spherically distorted as the off-axis ray path is bent more than the on-axis ray path. Practically, this limits the resolution of the microscope. The result is that a point feature in a sample is imaged as a region of high intensity with a surrounding halo (in bright field mode).

**The Condenser Lens System** Prior to interactions with the sample, the source electrons are

shaped into a probe by the condenser system. This consists of: a C1 lens, a C2 lens, and a C2 aperture. The C1 lens acts to de-magnify the first cross over point using a number of predefined excitation levels which determine the degree of demagnification or beam diameter, referred to as the spot size, typically this is of the order of tens of nanometres. The C2 lens is used to form the desired intensity by controlling the angular convergences via a user defined lens current. The C2 lens controls the angular convergence of the beam at the sample, and the aperture selects the current density and coherence of the beam. This provides a flexible range of imaging conditions and magnifications, for example a parallel beam can be formed resulting in sharp diffraction in the back focal plane, which is discussed later.

**The Objective lens system and Sample stage** The objective lens system forms a high magnetic field, of the order of 1 Tesla, around the sample. Here the samples sit in between the upper and lower objective lenses. The upper lens, along with the condenser system, determines the nature of the beam, parallel or convergent, on the sample. The beam then interacts with the sample, which scatters electrons both elastically and in-elastically, forming a diffraction pattern in the back focal plane.

After this lens system, the electrons are passed through another aperture, the objective aperture, allowing control over the contrast. The resulting diffraction pattern is focused by the lower objective in the back focal plane.

## 2.4.2 TEM Contrast and Imaging Modes

Before considering the manner in which the electrons are formed into an image, mechanisms of interaction are considered, a summary of the signals resulting from such interactions was presented in Figure 2.10. Following this, the modes of operation used in this investigation will then be discussed.

**Electron-Sample Interaction and Bright Field Imaging** Electron scattering with a sample can be divided into two broad categories; **elastic scattering** and **in-elastic scattering**. The former describes electron-sample interactions in which there is no net change in the energy of the electron. This can again be sub-divided into interactions between the incident electron & the electron cloud and incident electron & nuclei. Due to the relative size of the electron cloud and the nucleus, most of the incident electrons interact with the electron cloud resulting in small deflections, typically a few degrees in the electron path of travel. Alternatively, a minority of electrons will be elastically scattered by the positive charge of the atomic nuclei. This is referred to as Rutherford scattering, showing that such scattering was proportional to the logarithm of the atomic number,  $Z$ . Rutherford scattering results in the incident electron being scattered elastically over a much broader range of angles and therefore a

detector placed at high angles, above two degrees or greater, will have undergone nuclear interactions. The degree of scattering can be approximated to be proportional to  $Z^2$ , however the exponent can vary depending on the degree to which the nucleus is shielded by the orbital electrons.

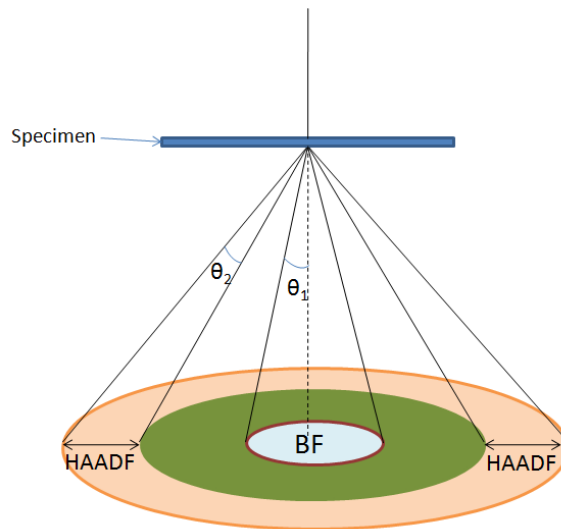


Figure 2.14: Various detectors are required to pick up signals scattered through different scattering vectors. The bright field detector, BF, has a high electron count and is therefore required to be more robust. The high angle dark field detector is designed to pick up fewer electrons and is therefore more sensitive.

Contrast is generated from the difference in the intensity of the electrons as a function of position on the viewing screen or detector. All diffraction patterns consist of a bright central spot and are surrounded by periodic peaks in the brightness. With the use of the objective aperture it is possible to select the electrons at a given scattering vector window with which an image is formed. An image which uses the electrons from the central spot is referred to as a bright field image. A dark field image is formed using off-axis electrons which can be selected using the objective aperture, which sits below the objective lens system.

Contrast in all TEM images is the result of the scattering characteristics of the sample; in a bright field image the scattered electrons are absent and therefore areas with a high electron scattering cross section appear darker. In the dark field image the inverse is true, only electrons which have undergone scattering in the range of  $q$  values selected will be present. Therefore, dark field imaging is a preferable technique with elements with a higher scattering cross section.

In this study, bright field imaging has been deployed as the elements of interest tended to be lighter with a lower electron scattering cross section. Therefore, some images have been acquired using the objective aperture to restrict the electrons which have undergone a greater degree of scattering. Additionally,

off-axis electrons are electrons which have deviated away from the optical axis and so have undergone a greater degree of spherical aberration.

### Phase Contrast

The bright and dark spots in a given diffraction pattern are the product of constructive and destructive interference of the electron beam caused by a path difference. While diffraction contrast is the product of scattered electrons, phase contrast is ever present when two out of phase beams are imaged and results in features such as Moire patterns and Fresnel fringes. When low atomic mass elements are imaged, of which polymers are generally composed, the result is phase contrast dominated images, as mass scattering is proportional to the logarithm of the atomic number. The contrast in such an instance is a result of differences that are present in the phase of the electron as the beam leaves the sample. This is sensitive to many factors such as thickness, making the phase contrast images hard to interpret. The variation in the phase of the beam is a consequence of variations in the electrostatic potential in the polymer, giving rise to Fresnel fringes.

$$\epsilon_0 = -\frac{\Delta V}{E} |k| \quad (2.6)$$

Any voids, cavities, or free volume in the polymer are of interest in this investigation and can be enhanced by defocusing the electron beam, causing a boost in the Fresnel contrast. When the image is under focused high contrast objects are surrounded by a dark fringes and when the image is over focused the fringe is bright[89]. The difference in the inner potential,  $\epsilon_0$ , of such cavities can be considered by thinking of an electron wave moving through a cavity. This is shown in Equation 2.6, where,  $k$  is the wave vector,  $E$  is the energy of the electron beam, and  $\Delta V$  is the potential difference between the inner potential of the polymer and that of the cavity in the direction of the beam [89]. The use of this effect on TEM images of these polymer samples is discussed during the course of this study<sup>7</sup>.

To understand the impact of de-focusing an image, a brief overview of the important concepts are provided; a more vigorous description is given elsewhere[89, 92]. A given point in a sample described by a sample function  $f(x, y)$  is transformed by the optical system of the TEM into a disk in the image described by a function  $g(x, y)$ . For example, two points in the sample,  $a$  and  $b$ , will result in two extended regions in the image;  $g_a$  and  $g_b$ , as shown in Figure 2.15. Extending this out to many points means that the contrast at a given pixel in the resulting image is a consequence of several points in the specimen. Mathematically this can be written as shown in Equation 2.7 where the position  $(x, y)$

---

<sup>7</sup>Particularly in section 4.3.

is described by the vector  $r$ .

$$g(r) = \int f(r')h(r - r')dr' = f(r) \otimes h(r - r') \quad (2.7)$$

Ultimately, Equation 2.7 states that the resulting bright field image is a convolution of the sample and some characteristic function  $h(r - r')$ . As  $h(r)$  accounts for how spread out the information from a given point in the sample is as a result of the imperfect optics in the TEM, it is called the point spread function. When the specimen is de-focused this results in an angular distribution of the electrons which interact with a given point in the sample. Consequently, the phase contrast is enhanced and resolution is decreased.

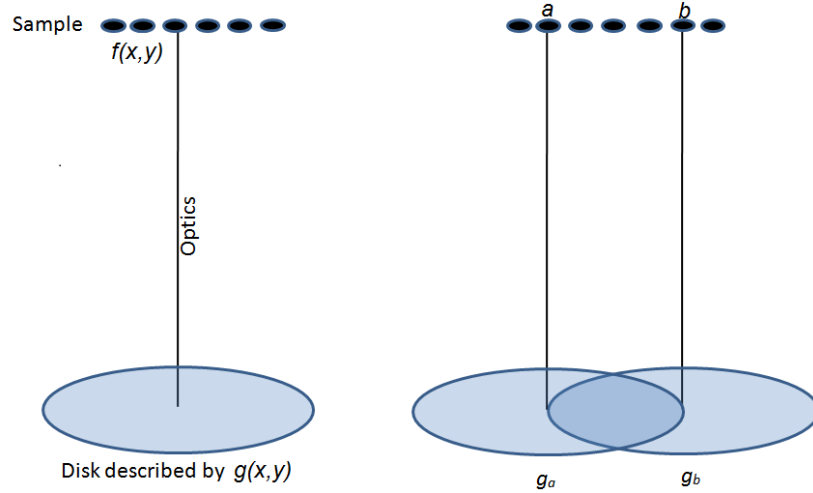


Figure 2.15: The optics results in each point on the sample,  $f(x,y)$ , being represented by an extended disk,  $g(x,y)$ .

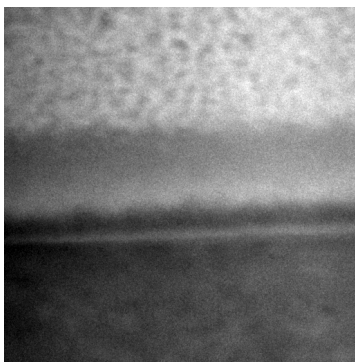
As a convolution in real space corresponds to a multiplication in Fourier space, Equation 2.7 can be written as;  $G(q) = F(q)H(q)$  where  $G(q)$ ,  $F(q)$ , and  $H(q)$  are the Fourier transforms of  $g(r)$ ,  $f(r)$ , and  $h(r)$  respectively. This allows the point spread function contributions from the apertures, attenuation, and lens aberrations to be considered individually as a function of  $q$ , the scattering vector. The spherical aberrations from the lenses are commonly the limiting factor in TEM resolution, and these aberrations are normally represented as a function,  $B(u) = \exp(i\chi(q))$ , in which  $\chi(q)$  is given by Equation 2.8 as an oscillatory function indicative of the phase shifts caused by the spherical aberration, where;  $C_s$  is the spherical aberration constant and  $\Delta f$  is the amount of defocus[89].

$$\chi(q) = \pi\Delta f\lambda q^2 + \frac{1}{2}\pi C_s\lambda^3 q^4 \quad (2.8)$$

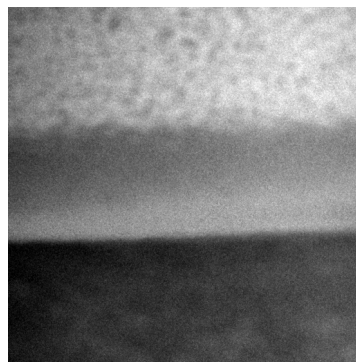
When the microscope is defocused, the second term in Equation 2.8 is normally negligible as the wave length,  $\lambda$ , of the electron is very small, i.e. for a 200keV microscope 2.51pm, and  $q$ , which is also generally small, is raised to the fourth power. When the microscope is in focus, the first term is zero as the de-focus is zero, i.e.  $\Delta f = 0$ . As  $\chi(q)$  is indicative of the phase shift of the electron wave as a function of  $q$  resulting from the spherical aberrations; when it is equal to  $\pi$  radians the condition for destructive interference is met. Therefore, the extent of the de-focusing can be approximated as  $\Delta f = \frac{1}{\lambda q^2}$  at the first  $q$  value at which destructive interference is observed. The same  $q$  value also indicates the de-focus at which the interference effects degrades the image quality, making the image contrast generated hard to interpret.

### Energy Filtered TEM

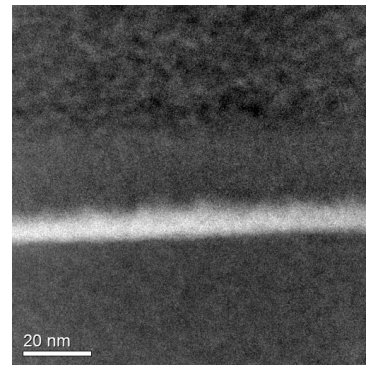
**Inelastic scattering** of electrons occurs due to a number of different interactions such as, sample ionisation, sample damage, the excitation of plasmons and the production of x-rays via atomic excitations. All of these processes will a minimum characteristic energy loss from the incident electrons and therefore an analysis of the energy spectra of the electron beam after its interaction with the sample can provide an insight into the chemical make up of a sample. Electron energy loss spectrometers are capable of separating out the electron beam by applying a magnetic field perpendicular to the direction of travel, resulting in a net Lorentz force on the electron as a function of the electron energy. The electrons corresponding to a particular energy loss can then be used to form an image.



(a) An image with a 20eV window taken **before** the oxygen 532eV edge.



(b) An image with a 20eV window taken **after** the oxygen 532eV edge.



(c) The oxygen map produced from the two previous images showing the SiO layer on top of the silicon substrate in white.

Figure 2.16: Showing the Pre, Post, and final images in producing an oxygen Map. The sample is polyimide spun onto a silicon wafer, here the oxide layer is mapped.

It is also possible to present the collected electrons as a plot of intensity vs energy. Energy filtered electron spectroscopy, EF-TEM, is a method of producing elemental maps of samples using this principle.

The electrons in the energy range which corresponds to those at an immediately lower electron energy loss event are used to form two images (Figure 2.16(a)) in order to characterise the background. An image using the electron immediately after the loss event is then captured (Figure 2.16(b)). The images can then be compared to produce an elemental map (Figure 2.16(c)). This is known as the three window EFTEM technique and is well detailed elsewhere[93]. It must be ensured that the energy windows are well centered and of a suitable energy width in the loss spectrum. Furthermore, the images must be aligned such that each pixel in all three images corresponds to the same point in the sample and the electron counts must be sufficiently high to produce an image with reasonable statistics. In this study this has been used to identify various layers which consist of different atomic species in the sample and their relative locations.

### TEM- Diffraction Mode

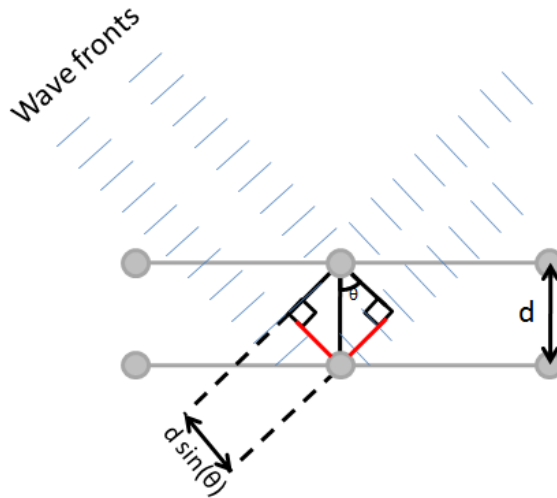


Figure 2.17: illustration diagram showing beam path of Bragg scattered beam and the path difference generated.

When operating in Bragg field mode the electrons scattered from the sample are focused by the lower objective to form a diffraction pattern in the back focal plane as shown in Figure 2.11. Diffraction mode allows the diffraction pattern formed in the back focal plane to be magnified and imaged. This is achieved by varying the strength of the imaging system, normally the intermediate lens projects the back focal plane of the objective lens onto the image plane.

For an ordered crystal, the Bragg condition, Equation 2.9 makes the constructive and destructive interference effects of the electron wave easy to visualise in terms of; the wavelength of the electron,  $\lambda$ , and of the path difference,  $2d\sin\theta$ , between two wave fronts, as shown in Figure 2.17.

$$n\lambda = 2d\sin(\theta_B) \quad (2.9)$$

The form of Equation 2.17 shows that for a fixed wavelength and distance between atoms, the incident angle determines the path difference. When the Bragg condition (for constructive interference) is met the angle  $\theta$  is said to be the Bragg angle,  $\theta_B$ , for the particular wavelength and atomic spacing.

However, diffraction effects occur whenever a path difference is generated between two or more wave fronts, which can be visualised by thinking of the classic Young's double slit experiment. By considering a simple situation, diffraction from two atoms, Von Laue provided a mathematical description of the manner in which the diffraction pattern relates to the sample structure more generally, in terms of the scattering vector<sup>8</sup>,  $q$ .

The scattering vector is the vectoral difference between the incident,  $k_i$ , and diffracted,  $k_d$ , wavevectors<sup>9</sup>. For elastic scattering the magnitudes of the incident and diffracted wave vectors are equal i.e.  $|k_i| = |k_d| = \frac{1}{\lambda}$ . By considering the vectoral difference of the magnitude of the waves vectors it can be shown that  $|k_i| - |k_d| = |q| = \frac{2\sin\theta}{\lambda}$ , where  $\theta$  is the angle of incidence between the plane of the atoms and the incident wave. Equation 2.9, the condition for constructive interference, can be rewritten for  $|q|$ , giving Equation 2.10.

$$|q| = \frac{n}{d} \quad (2.10)$$

Equation 2.10 gives the condition for constructive interference conditions in terms of the reciprocal space between two atoms. For a three dimension crystal, with miller indices  $(hkl)$ , the vector  $g_{hkl}$  gives the reciprocal lattice vector, the vectoral addition of the reciprocal lattice parameters. Therefore constructive interference happens when  $q = g_{hkl}$ .

In a crystalline material elastic scattering of electrons occurs at well defined spatial frequencies in potential, characterised by the reciprocal lattice vector  $g_{hkl}$ . This, in turn, results in a redistribution of intensities into well ordered spots, called reflections, with each reflection corresponding to a reciprocal lattice vector characteristic of the crystal. In a polycrystalline sample the variation of the orientation of each crystal grain results in the same spots arising from periodic variations in the sample potential, rotated to form a series of continuous concentric rings, as shown in Figure 2.18(a). For an amorphous

<sup>8</sup> $q$  was discussed in the context of neutron scattering. The convention in TEM literature is to call it,  $K$ , however for consistency it is referred to as  $q$  here.

<sup>9</sup>See Figure 2.5.

material, there is similar spacing but random orientations and distributions in the potential resulting in a diffuse ring. Therefore, the spacing between the rings corresponds to common spatial frequencies in the distribution of potential, which may correspond to molecular or intra molecular distances.

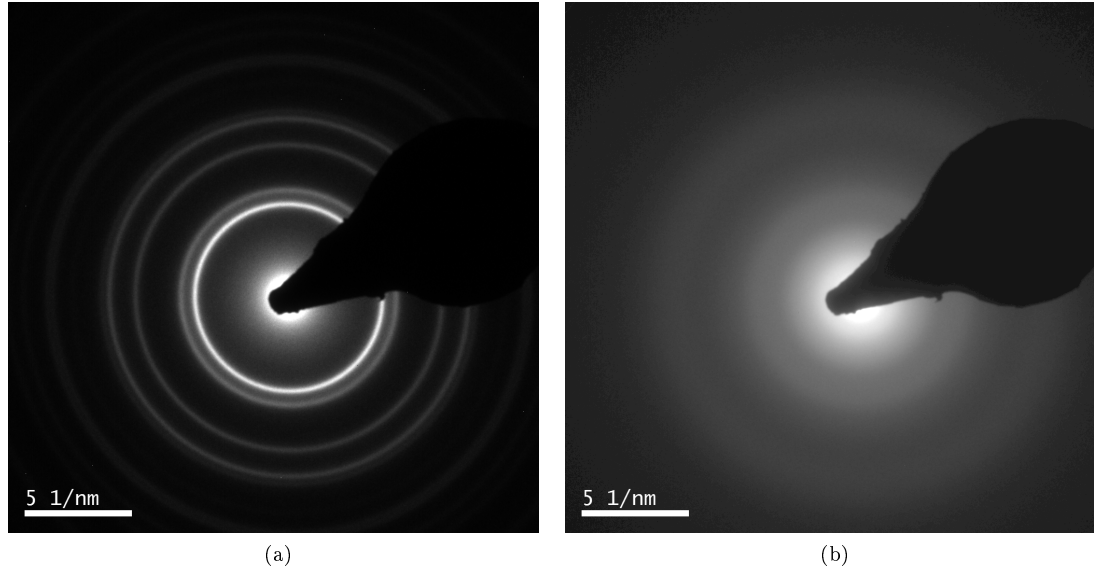


Figure 2.18: Two diffraction patterns. (a) A gold cross grating with well defined common spatial frequencies, and (b), for amorphous polyimide with more diffuse rings corresponding to less well defined spatial frequencies.

As such, the TEM in diffraction mode can map the common spatial frequencies in a given sample.

**TEM- Imaging Electrons** Two lenses in the lower column, the intermediate and projector lenses, project the image onto the image plane. At the image plane, the electrons are detected with either a phosphor screen for direct viewing, or using a scintillator material which converts the electrons signal into light which is then imaged on a CCD chip.

## 2.5 Atomic Force Microscopy

In this study atomic force microscopy has been used in order to measure sample thicknesses and map surface roughness. The working principle is outlined in Figure 2.19. A tip scans across the surface of the sample and deviations are detected using a photo-diode and laser system allowing the formation of a map of the surface topography. Additionally, the needle can be forced to oscillate at a resonance frequency, tapping on the surface. A deviation in the phase of the oscillation of the tip can provide

information about the elasticity of the material, known as phase imaging. Shifts in the phase of the oscillation of the tip are generally indicative of the dissipative properties of the sample.

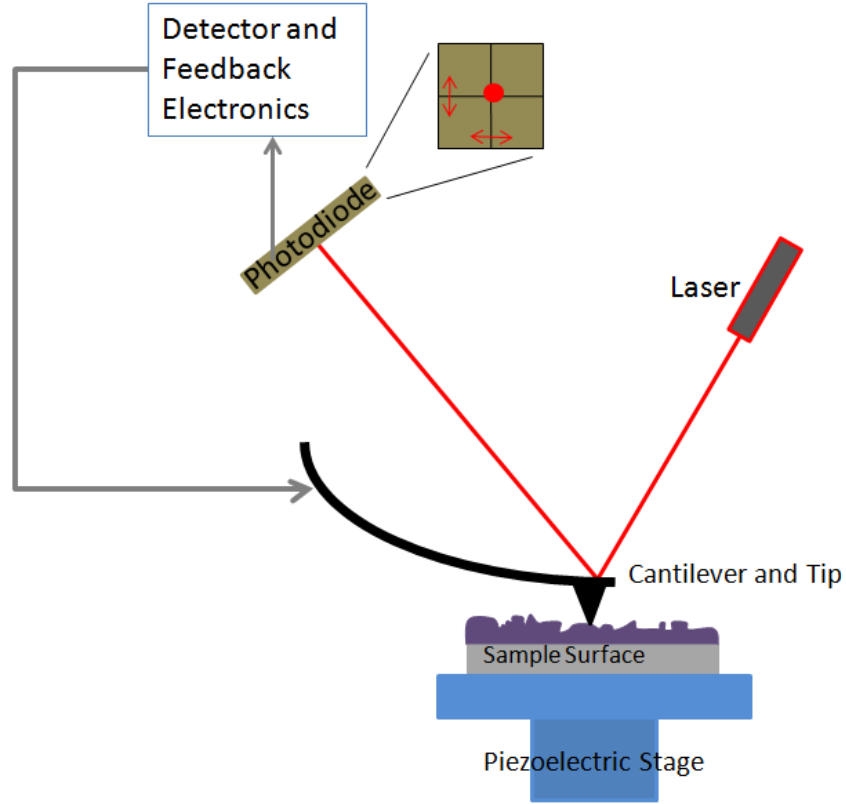


Figure 2.19: Showing the working principles of the NT-MDT Solver NEXT AFM. Deflections in the laser are detected to map the surface properties.

The interaction potential arises as a result of the van der Waals forces between the tip and the surface [94]. This can be approximated by the Lennard-Jones Jones potential:

$$U_{LD}(r) = U_0 \left\{ -2 \left( \frac{r_0}{r} \right)^6 + \left( \frac{r_0}{r} \right)^{12} \right\}$$

Where  $U_{LD}$  is the net potential at the given distance,  $U_0$  is the minima in the Lennard Jones Potential,  $r_0$  is the distance at which the net force is a minimum, and  $r$  is the distance the tip is away from the sample.

The Lennard-Jones potential has two terms; an attractive term, based on the van der Waals forces arising from dipole-dipole interactions, and secondly a repulsive force based on the Pauli exclusion principle. Therefore depending on the tip surface-distance the AFM can operate in either an attractive or a repulsive mode, depending on the interaction distance.

Modes of contact can be sorted into three varieties: contact, semi-contact, and non-contact mode. Contact mode involves the tip being in direct contact with the sample. Here the cantilever of the AFM tip is generally soft, such that the measurement does not influence the sample.

In non-contact mode, the tip undergoes a forced oscillation and change in the phase of the oscillations are mapped. Semi-contact mode allows the acquisition of both phase and topographical information. A piezoelectric oscillator drives the cantilever at its resonant frequency, while the AFM feedback system keeps the oscillation amplitude and a user defined value. The voltage required to do this is recorded and hence topographical information is inferred. Here the measurements presented were taken in semi-contact mode. The AFMs used were either a Veeco Dimension 3100 Scanning Probe Microscope or a NT-MDT Solver NEXT.

Following the acquisition of the data, corrections were applied to the data for artefacts generated in the resulting image. In this study three post processing steps were commonly applied using the software Gwyddion. These were a plane subtraction to correct for any non perpendicularity of the plane of the sample to the tip, a second order polynomial background subtraction, and a median line height matching performed as detailed elsewhere [95].

## 2.6 The Thunder-chamber

In order to test samples in a range of environmental conditions access to a Thunder-chamber 2500 Two-Pressure Two-Temperature Humidity Generator were provided by Honeywell [96]. This consists of three main parts: a test chamber, a saturator producing nitrogen at 100%RH, and an expansion valve between them. As expected, the mechanisms and operations for varying environmental parameters, such as humidity and temperature, leave artefacts in the acquired data, particularly on shorter timescales. Therefore an understanding of the working principles of the Thunder-chamber are required to identify any artefacts in the data.

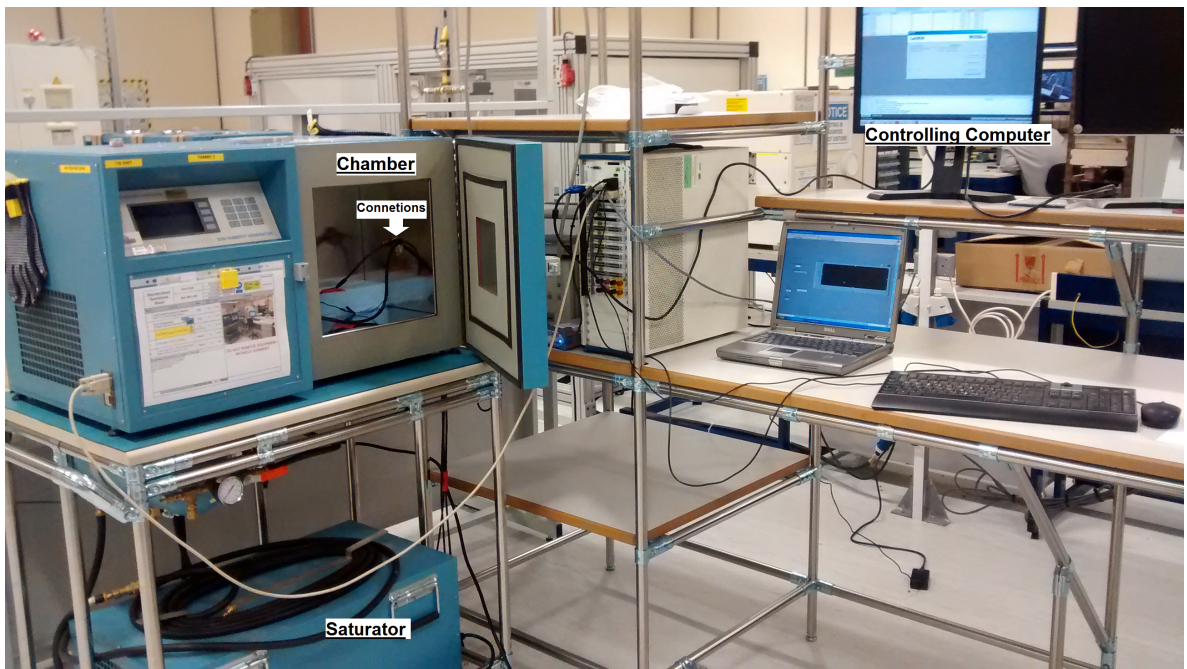


Figure 2.20: A photograph of the thunder scientific thunder chamber Model 2500 Benchtop/Mobile "Two-Pressure" Humidity Generator setup before a calibration run.

### 2.6.1 Temperature Control

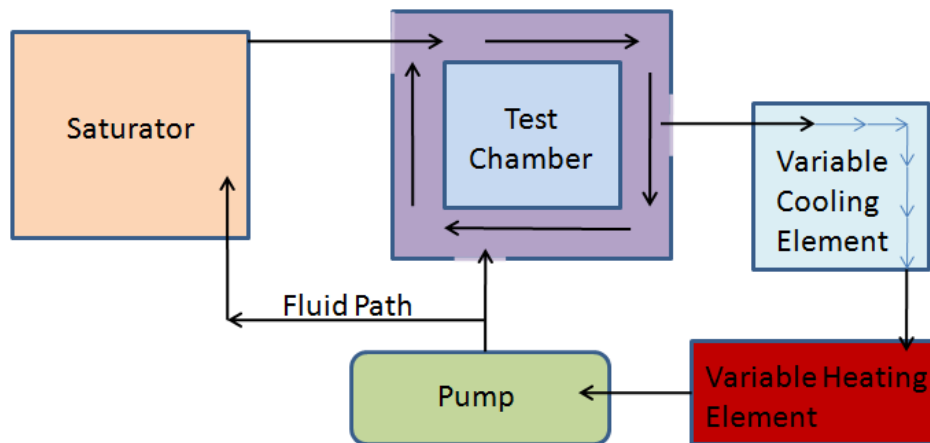


Figure 2.21: The flow diagram showing the movement of heating fluid in the Thunder chamber.

A temperature control fluid, 30-40% water and 60-70% propylene glycol, is circulated around the test chamber and the reservoir at 4.5litres/minute by a pump. The rate of flow and the quantity of the fluid allows a well maintained, uniform temperature in the chamber from  $0^{\circ}\text{C}$  to  $70^{\circ}\text{C}$ . Within the test

chamber the temperature is monitored using a balance circuit to measure the four  $10K\Omega$  thermistors which are spatially distributed within the chamber to give an average. The chamber is made from high grade stainless steel to prevent rust and all seams are welded hermetically. The fluid is able to take two paths though the system to the saturation system or the test chamber, both paths of which pass a 500W heater contained in copper housing, and a refrigerator as shown in Figure 2.21. The refrigerator uses a pulsed flow of a patented liquid refrigerant which expands into a gas as it is heated by the fluid in a *tube in shell type* of cooler.

## 2.6.2 Humidity Generation

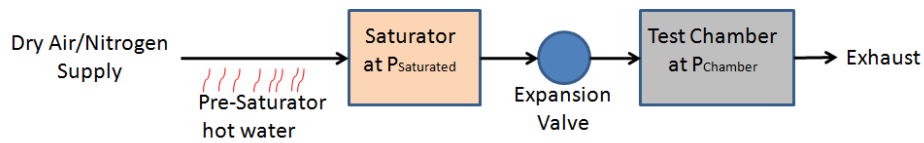


Figure 2.22: The flow of dry air in the Thunder-chamber.  $P_{Saturated}$  is the pressure of saturated water vapour at the set temperature.  $P_{Chamber}$  is controlled by the expansion valve.

Using Dalton's Law of partial pressure, in which the total pressure is the sum of the partial pressure of the gases, a two pressure system can generate and hold the chamber at any relative humidity. Firstly, the temperature in all three component areas is set to the desired temperature. A source of dry nitrogen can be used to lower the relative humidity. The flow of the nitrogen is controlled by a system of solenoid valves which are controlled by the onboard computer.

To raise the relative humidity, a reservoir filled with saturated water vapour at the test chamber temperature must be maintained. This is achieved by passing the dry nitrogen over a water surface at an elevated temperature, about  $15-20^{\circ}C$  higher than required in the chamber, maintained by two 250W stainless steel immersion heaters. The water flow is maintained by a control computer and a solenoid valve. The water vapour saturated nitrogen vapour is cooled and excess condensed water is removed, leaving saturated nitrogen vapour which is stored in the reservoir. The ratio of the pressure in the test chamber to the reservoir is a measure the relative humidity, as described in section 1.1. An expansion valve allows the ingress of saturated vapour or dry nitrogen to flow into the test chamber as desired.

## Chapter 3

# QCM: A Probe for Mass Transport in Soft Matter

The hysteresis effect reported by Honeywell is key in this investigation. In order to understand the factors which govern this effect, a method of measuring and quantifying the water interaction in such films is required. Understanding the extent to which the sensor properties are determined by the material, and not the device architecture, requires the material to be probed directly. Therefore, QCM measurements are shown to be a valid method of assessing the properties of materials directly. Firstly, the principles of the QCM technique, as applied to polymer thin films generally, are discussed in section 3.1. Section 3.2 then presents the construction and proof of sensitivity of a QCM system. This shows QCM to be a valid technique to monitor the mass of these thin films.

The design of a standard test to probe the mass transport of the polyimide-water system is then discussed in section 3.3. This test was then used to standardise the quantification of the hysteresis for this study. The transport characteristics of five thin films of varying thickness were then investigated. Each crystal was measured before (soft cure), and after (hard cure), the films were fully annealed. Following this, the crystals were measured again after an oxygen plasma etch. This was undertaken to investigate the impact of both the film thickness, and each film treatment, on the transport characteristics of water vapour in such films.

The impact of the viscoelastic properties of polyimide thin films on QCM measurements is discussed in section 3.5. This was undertaken to both understand the impact of the viscoelastic properties of the thin films on the mass measurements, and with a view to possible future use of QCM measurements to probe the dissipation properties of thin films.

In the final section of this chapter, the mass measurements presented using the QCM are contrasted

with measurements of a simplified capacitance humidity sensor. QCM is shown to be a good tool for device engineers to quantify the limitations of sensors arising from the material properties of a sensing element in gas sensors.

### 3.1 Quartz Crystal Microbalance

The QCM is a well established method of measuring mass fluctuations[70] and has been used in a wide range of investigations involving adsorption[97], electrochemical analysis[98], and the viscoelastic properties of thin films[99]. The most common scientific use of the QCM technique, as film thickness monitor in deposition systems, is outlined in section 2.2. Such applications depend on the Sauerbrey equation, Equation 3.1, which describes a linear relationship between the shift in resonance frequency of the crystal and the mass incident on the crystal surface[69]. This model is obtained by considering the frequency of mechanical waves when a quartz crystal is excited at its resonance frequency by an AC voltage in its shear mode, as discussed in section 2.2. The Sauerbrey equation is:

$$\Delta f_q = -\frac{2f_o^2}{N\mu_q\rho_q}\Delta M_q = -\frac{S}{N}\Delta M_q \quad (3.1)$$

where,  $\Delta f_q$  is the shift in the resonant frequency of the crystal,  $f_o$  is the base frequency of the crystal,  $\Delta M_q$  is the additional mass on the surface of the quartz,  $N$  is the harmonic described by  $f_0(n=1)$ ,  $\mu_q$  the shear modulus, and  $\rho_q$  is the density of quartz. In section 5.4, QCM results are interpreted using this model, to monitor the ambient humidity in the test cell. A circuit designed to output a voltage proportional to the resonant frequency shift in the crystal is used[100]. In this section, the validity of the assumptions underpinning Equation 3.1 are examined.

The Sauerbrey equation is considered valid if the system meets three criteria; the deposited mass is rigid, it is uniformly deposited, and the shift of the resonance frequency,  $\Delta f_q$ , is less than 2% of the fundamental resonance frequency,  $f_o$ , [70]. These conditions arise by considering the degree to which the generated mechanical wave can propagate from the quartz into film without impediment. The latter two conditions for the thin film; the film uniformity and the film mass, can be controlled by the conditions of the spinning process. However, the viscoelastic properties of the film are unknown.

The effect on the resonance frequency of the QCM resulting from both viscoelastic films and a fluid atmosphere has historically been characterised as an impediment to accurate mass measurement. However, more recently such effects have been a subject of active research as additional information can be gleaned from such techniques[101, 102, 103]. The versatility of the QCM technique as more than a mass measure relies on accurate measurements and modelling of the dissipation and energy storage

properties of the system. A range of modelling techniques for the behaviour of a QCM have been introduced. The primary focus in this study is to gain accurate measurements of the mass uptake of the polyimide thin film in a range of humidity settings. However, at a higher humidity viscous coupling of condensed water to the film surface on the QCM has been shown to decrease the central resonant frequency and to damp the oscillating wave[102]. The extent of the damping is a function of the ratio of the liquid thickness to the decay length of the radiated shear wave[71]. Therefore, a model capable of decoupling the contributions of mass and viscoelasticity of the film to resonance characteristics is required.

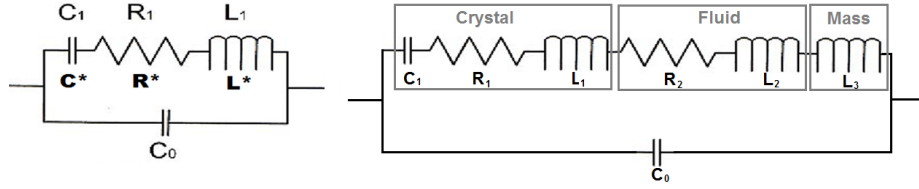


Figure 3.1: (a) A Butterworth Van Dyke circuit representing a blank QCM [70]. (b) A possible circuit representing a QCM loaded with a viscoelastic film presented by Parlak et al.[71].

The fundamental physics of piezo electric resonators in contact with a viscoelastic medium was discussed extensively as early as 1948 by Mason et al.[104]. A Mason equivalent circuit model of a QCM contains two acoustic arms, connected via a transmission line, to model the behaviour of a QCM. However, the Mason circuit can be simplified to a Butterworth–van- Dyke (BvD) circuit if only one side of the crystal is loaded[99]. The BvD circuit models a QCMs characteristic properties of energy storage, dissipation, and inertia as; a capacitor, a resistor, and an inductor in series, respectively, as shown in Figure 3.1(a). An additional capacitance,  $C_0$ , is added in parallel, to account for the static capacitance of the crystal between the electrodes. This equivalent circuit models the impedance characteristics at frequencies close to resonance, allowing the various contributing influences of the QCMs behaviours to be distinguished. The resonance frequency,  $f_s$ , is conventionally defined as the point at which the impedance is at a minimum.

Equation 3.2 models a QCM with a rigid film in a solution. It shows two terms which contribute to the resonant frequency, the first representing the coupled rigid mass contribution,  $\Delta f_q$ , and the second representing the properties of the solution[71, 102, 105]. The second term alters frequency in proportion to  $\sqrt{\eta\rho}$ , where  $\eta$  is the viscosity and  $\rho$  is the density of the surrounding fluid[105].

$$\Delta f_s = \Delta f_q + \Delta f_{solution} = -\frac{2f_o^2}{N\sqrt{\mu_q\rho_q}} \left[ \Delta M_q + \left( \frac{\rho\eta}{4\pi f_o} \right)^{1/2} \right] \quad (3.2)$$

Importantly, this model allows the equivalent rigid film mass to be obtained. However, distinguishing between the two contributions with a measurement of the resonance frequency alone is not possible as there are too many unknown quantities. The admittance, the inverse of the impedance, of an uncoated QCM is shown in Figure 3.2 as a function of the frequency of the exciting AC voltage. When considering the imaginary component of the impedance, the reactance,  $X$ , it is possible to define two other important frequencies  $f_1$  and  $f_2$  occurring at  $X_{max}$  and  $X_{min}$  respectively, marked on Figure 3.2. Both Equation 3.2 and Equation 3.3 are derived from the same model of a rigid film in a fluid medium accounting for both the central frequency shift,  $\Delta f_s$ , and the broadening of the peak  $\Delta(f_1 - f_2)$  respectively.

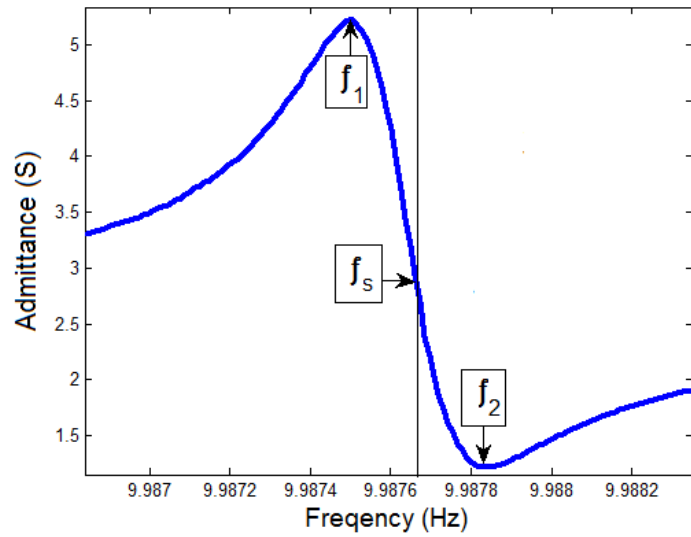


Figure 3.2: Admittance sweep of a blank QCM showing the various admittance at frequencies close to resonance.

Itoh et al. showed that  $f_2$  remains unaffected by the properties of the surrounding medium[106]. This is because  $f_2$  is the frequency at which the fluid resistance and fluid inductance cancel out[71, 106]. Therefore, the mass of water vapour in polyimide films can be directly obtained via linear conversion of the shift in  $f_2$  from Equation 3.1.

The QCM mass measured in this chapter have been calculated from a linear conversion of  $f_2$  to mass via Equation 3.1. A wide range of models have been developed to account for QCMs loaded with rigid solids, viscoelastic media, and Newtonian or Maxwellian fluids, which are summarised well by Bandey et al.[103]. Such models have also been combined to account for the dissipative properties of the given system, for example, for the analysis of metals in a solution[107].

$$\Delta(f_2 - f_1) = -\frac{2N^{\frac{1}{2}}f_o^{\frac{3}{2}}}{\sqrt{\pi\rho_q\mu_q}}(\rho\eta)^{\frac{1}{2}} = k(\rho\eta)^{\frac{1}{2}} \quad (3.3)$$

Equation 3.2 is one such model which was used to decouple mass adsorption from fluid viscosity and density and is outlined by Parlak et al.[71]. It is based upon a rigid film in an ambient fluid, and implies that the broadening of the resonance peak can indicate a condensed layer of water on the rigid film. The simplicity of this model is advantageous over the numerous models of a QCM for which the viscoelastic properties are not easily separated from the mass contribution, as they are in the same term, rather than separated as in Equation 3.2. To decouple the various contributions to the impedance for more complex models measurements of the frequency at more than one overtone are required[101]. Such data has not been collected in this investigation as this would require equipment to measure the impedance at a range of frequencies, which was not available for this investigation.

### 3.2 Measuring the Impedance of a QCM

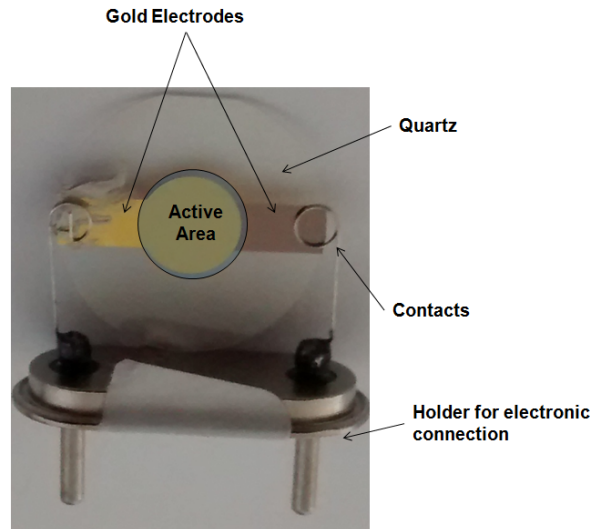


Figure 3.3: A photograph of a 10MHz AT cut crystal in the holder which was used for this project. These crystals were ordered with deposited electrodes on either side of the crystal (10nm/100nm, Ti/Au), mounted inside the holder and unbonded to the holders from International Crystal Manufacturing Inc. (Product# 151218-10) [108]. The diameter of the electrode is 0.51cm, the total crystal diameter being 1.36cm. On this crystal, a polyimide has been spun later (as detailed in section A.1) over the centre electrode and the crystal has then been attached to the holder using conductive silver paint (which can be seen on the left hand side).

In this section a system for measuring the impedance as a function of frequency of the crystals is introduced along with experimental tests of Equation 3.1 at atmospheric conditions. The work presented

in this section was performed as a proof of concept for the QCM impedance sweep technique to probe polyimide thin films prior to investing in a more robust system.

According to the Sauerbrey equation, quartz crystals with a base frequency of 10Mhz provide sensitivity on a nanogram scale, as the constant  $S = 4.426 \times 10^{-9} gcm^{-2} Hz^{-1}$ [70]. The base frequency is a function of both the mechanical properties of quartz, and the spatial dimensions of the crystals, as it is a shear mode resonator. Crystals of a higher frequency are thinner and mechanically more frail. Hence, crystals with a higher sensitivity provide additional challenges when attempting to use standard spin casting methods to deposit the polymer thin film. The choice of crystal is therefore a balance between the crystals sensitivity and robustness. Additionally, the choice of crystal resonance frequency is often dictated by the operating frequencies of the equipment available.

In this project crystals from International Crystal Manufacturing (ICM)[108], with a base frequency of 10Mhz and electrodes predeposited (10/100nm Ti/Au) on both sides of a thin disk of AT-cut quartz crystals were used. The active area of the crystals, which is defined by the electrode area, is  $\approx 0.0951cm^2$  as shown in Figure 3.3. These electrodes lowerd the frequency of the crystal from the base frequency of 10Mhz. The diameter of the crystal is much greater than the diameter of the electrodes such that edge effects play a minimal role. Conveniently, for such crystals a 1hz frequency shift corresponds to 1.1ng of coupled mass incident upon the surface.

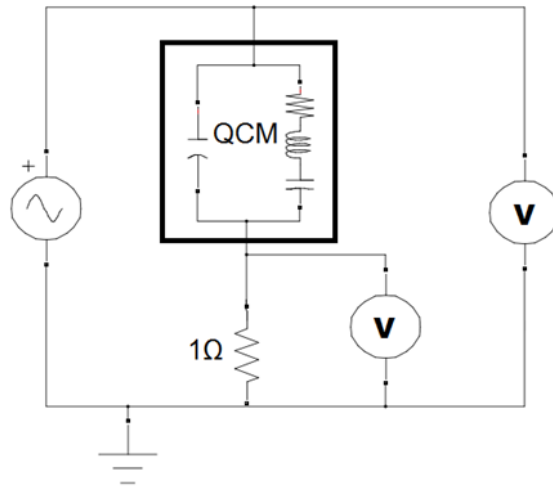


Figure 3.4: A circuit diagram showing the method of measuring the impedance of the QCM which was discussed by Shirazi[109]. The QCM is represented here by its equivalent BvD circuit.

A circuit capable of conducting an impedance sweep was constructed for this project, the circuit diagram of which is shown in Figure 3.4. The voltage between the terminals of the AC waveform generator was measured, along with the voltage across a 1Ω resistor placed in series with the QCM to give a

current wave. The Picoscope 6000 when connected to a control computer is capable of both, creating an AC output sweeping between frequencies in the range 0-10Mhz, and acting as an oscilloscope with a dual input. Both the voltage and the current were then measured using the Picoscope. The maths channel was used to compare the two wave forms producing an instant calculation of the magnitude of the phase shift between the two waves. This is as the product of two wave forms;  $v_1(t) = V_1 \cos(\omega t + \theta_1)$  and  $v_2(t) = V_2 \cos(\omega t + \theta_2)$  where  $t$  is time,  $\omega$  is the angular frequency,  $\theta$  is the phase, and  $V$  is the amplitude, can be shown to be  $v_{product}(t) = \frac{V_1 V_2}{2} [\cos(\theta_1 - \theta_2) + \cos(2\omega t + \theta_1 + \theta_2)]$ [110]. The phase difference then determines the dc offset of  $v_{product}(t)$  and so  $v_{dc}(t) = \frac{V_1 V_2}{2} \cos(\theta_1 - \theta_2)$  where  $v_{dc}$  is the dc difference between the two waves. Therefore, the phase difference  $\theta_1 - \theta_2$  can be measured by monitoring the amplitude of the two waves, taken as the RMS voltage and the dc offset between the two waves. The inverse cosine used to extract the phase change results in a less precise measurement as the phase offset tends towards  $0^\circ$  as  $\cos\theta$  is not as sensitive to  $\theta$ , see Figure 3.5.

The waveforms of voltage, current, and phase for a particular frequency were output in a text file containing five columns; time, RMS source voltage, RMS voltage across the resistor or current, and phase measurement. The result was a folder of hundreds of text files with each file corresponding to a given frequency. A script was then produced in MatLab to read in and interpret all of the files in a given folder. The columns in each file were then averaged, and impedance was calculated by dividing the mean RMS source voltage by the mean current giving the impedance. This was performed on all the crystals as received from the manufacturer to gain an understanding of the crystal impedance when unloaded.

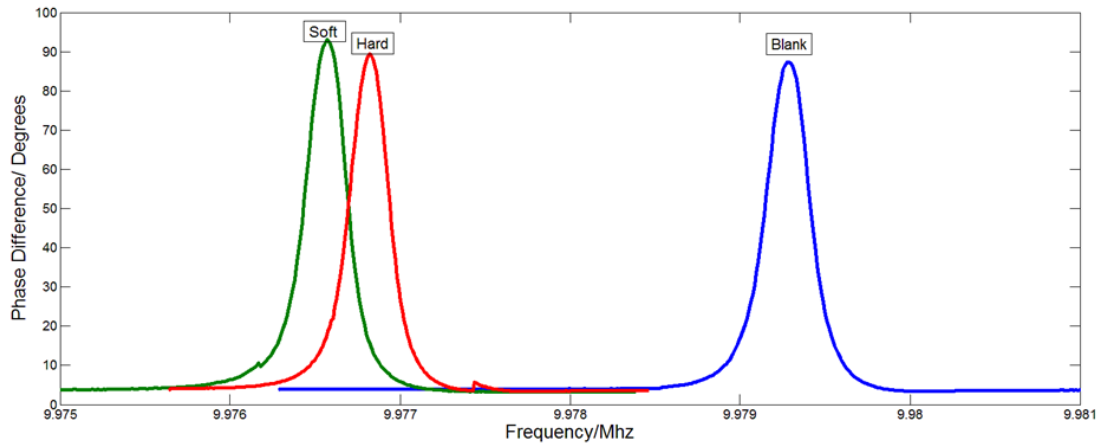


Figure 3.5: The phase shift from the starting positions for the 70nm crystal when it is unloaded, after the deposition of a polyimide film (soft cured), and after a longer anneal (hard cure).

Polyimide thin films were then deposited using spin casting methods with a range of spin speeds and

solution viscosity, as shown in Figure A.2. However, a direct measurement of the thickness of the films on the crystal was difficult to obtain without risking damage to the uniformity of the film coating on the sample. Therefore, alongside the crystal, polyimide was also spun onto a witness sample. The witness sample was prepared to reflect the surface properties of the active area of the crystals by depositing a metal layer (10/100nm Ti/Au) on a glass side. A step height was then created on the witness samples by masking off a section of the polyimide and oxygen plasma etching away the remaining exposed area. These step heights were then measured by AFM to give the estimated thicknesses of the polyimide films on the QCM. The AFM measurements were repeated along the film to account for any local variation, and the standard deviation of these measurements are the error of the thickness measurement.

Figure 3.5 shows a characteristic plot of the phase output of this system for a QCM under various loads, as a function of frequency<sup>1</sup>. The various samples show a shifted frequency with no noticeable effect on  $(f_1 - f_2)$  of the spectra. This implies a constant mechanical loss for the 70nm thin films under different annealing regimes. A decreased mass is indicated after the hard cure, which highlights that perhaps not all the polymer solvent, GBL, is entirely driven off in soft cure, a theme discussed later on in this chapter. According to Equation 3.3 the impedance spectrum broadens out as the dissipative properties of the film increase. Figure 3.6 shows impedance sweeps from crystals with a range of thicknesses. There is no significant change in the characteristics of the impedance sweep for films of up to about  $2\mu\text{m}$  indicating that film dissipation is not significantly changed as the film thickness increases.

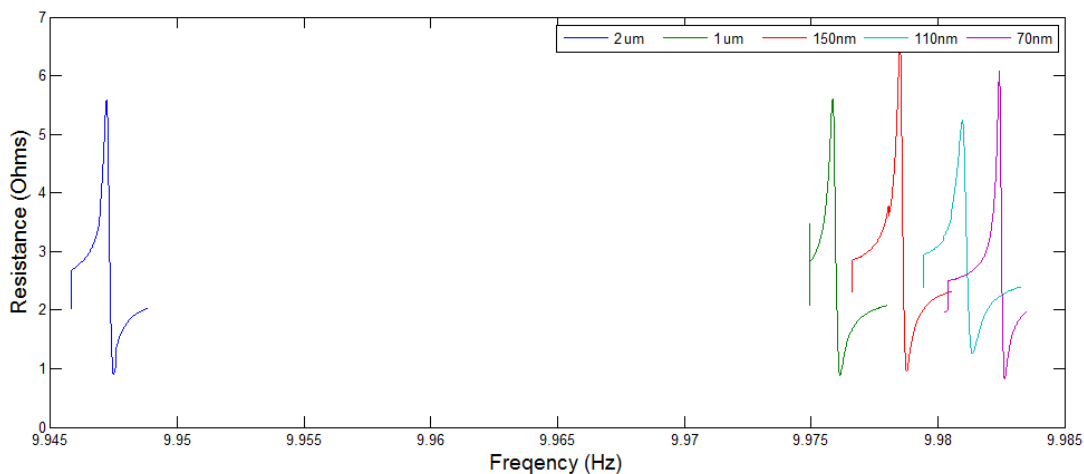


Figure 3.6: Shows the Impedance of crystals of various thicknesses of soft cured polyimide. The raw frequency, not the shift in frequency, is shown.

Figure 3.6 shows two points of inflection in the impedance spectrum. This is similar in an LCR circuit,

<sup>1</sup>The corresponding impedance data is in the appendix, Figure A.8.

in which the circuit properties are dominated by the capacitance at lower frequencies reaching the series resonant frequency with a minimal magnitude of impedance.

To read the resonance frequency from this data, a Gaussian function was fitted to the magnitude of the phase shift between the voltage and current waves when plotted as a function of frequency; an example fit is provided in the appendix(Figure A.7). Figure 3.7 shows the frequency,  $\Delta f_s$ , as a function of thickness; each reading was repeated on different crystals spun under the same conditions. A linear relationship between the assigned thicknesses and frequency shift is evident, and so, the Sauerbrey equation is valid for these films at atmosphere.

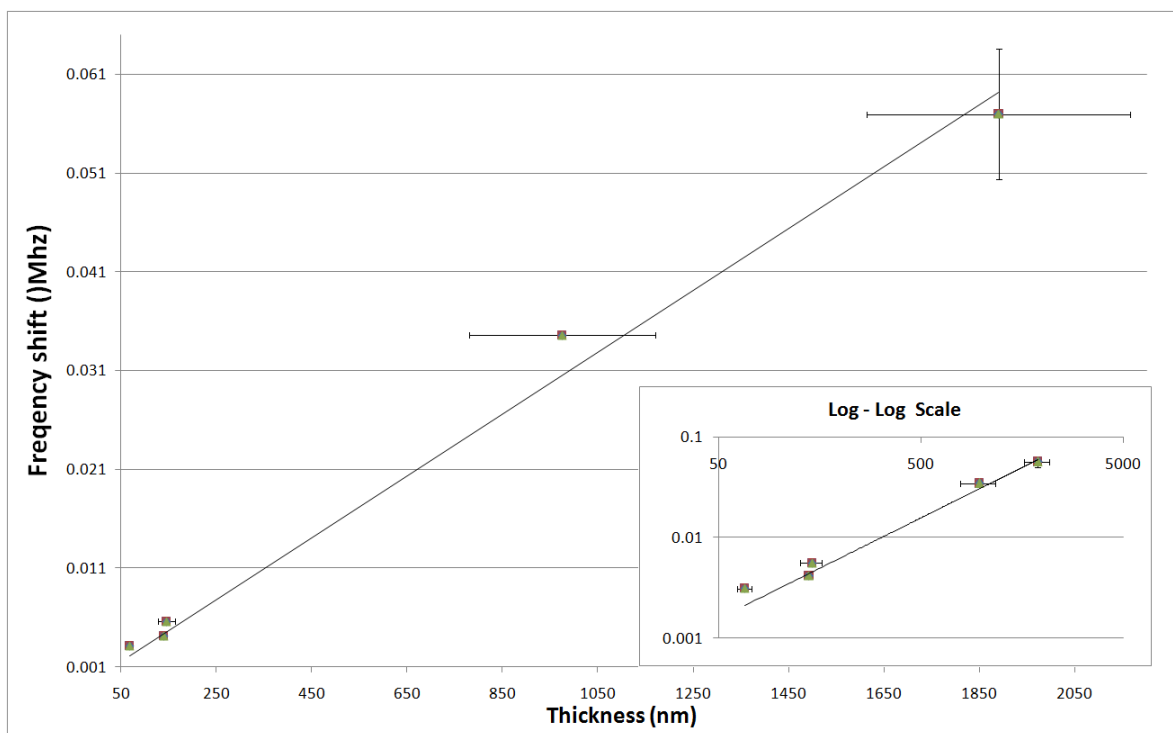


Figure 3.7: Frequency shift as a function of thickness for polyimide thin films on QCM. The thickness measurements are taken from the AFM scans performed on witness samples, and the frequency readings are read from the fitted Gaussian function to the relative phase shift of the voltage and current waves as discussed.

The results presented in Figure 3.7 have shown that the QCM technique is a suitable analytical approach for attaining measurements of the mass of polyimide thin films. Therefore, our industrial partners at Honeywell sought a developed robust QCM measurement solution for industrial measurements. This led to the purchase of a Gamry eQCM 10Mhz impedance sweep box with software. The system conducts an impedance sweep between two frequencies then fits a broken rational function enabling the fitted frequencies,  $f_1$  and  $f_2$  to be read.



Figure 3.8: A screen shot of the Gamry resonator software. Two increases in humidity were generated to check the response of the system. The top graph shows the data and fit of the current reading. The bottom graph shows the measured frequencies as a function of time.

The Gamry resonator box is normally integrated as part of a larger electrochemical system, designed to detect interfacial phenomena such as binding events[111]. The output is shown on the bottom half of Figure 3.8 as  $f_1$  and  $f_2$  resonance frequencies of the system are plotted as a function of time. The frequency resolution quoted by the manufacturer is 0.02hz[111]. This does not take into account the quality of the fit but shows the limits of the system when operating optimally. Importantly, the Gamry system has been constructed with long term stability, allowing the assessment of the polymer on a longer timescale.

## QCM Temperature Response

The timescales of diffusion and the activation energies involved in transport processes are both a function of temperature. Therefore, collecting data at a range of different temperatures would be

desirable to help to test the models discussed. QCMs have a well understood cubic dependence on temperature[70] with the crystals used in this study designed to work optimally at  $25^{\circ}\text{C}$ [108]. Familiar pseudo calibration profiles were collected at three temperatures;  $5^{\circ}\text{C}$ ,  $25^{\circ}\text{C}$  and  $50^{\circ}\text{C}$ , on the same QCM with  $1\mu\text{m}$  polyimide film as shown in Figure 3.9. The  $5^{\circ}\text{C}$  data shows a systematically lower frequency in the desorption when compared with the absorption, and  $50^{\circ}\text{C}$  data showing the inverse trend. This demonstrates the unsuitability of QCMs to take temperature varying data and is caused by internal stresses due to temperature changing the elastic constants in the QCM with the precise characteristics of the frequency-temperature relationship resulting from the resonator cut, overtone measured, frequency, diameter, and mounting technique[112].

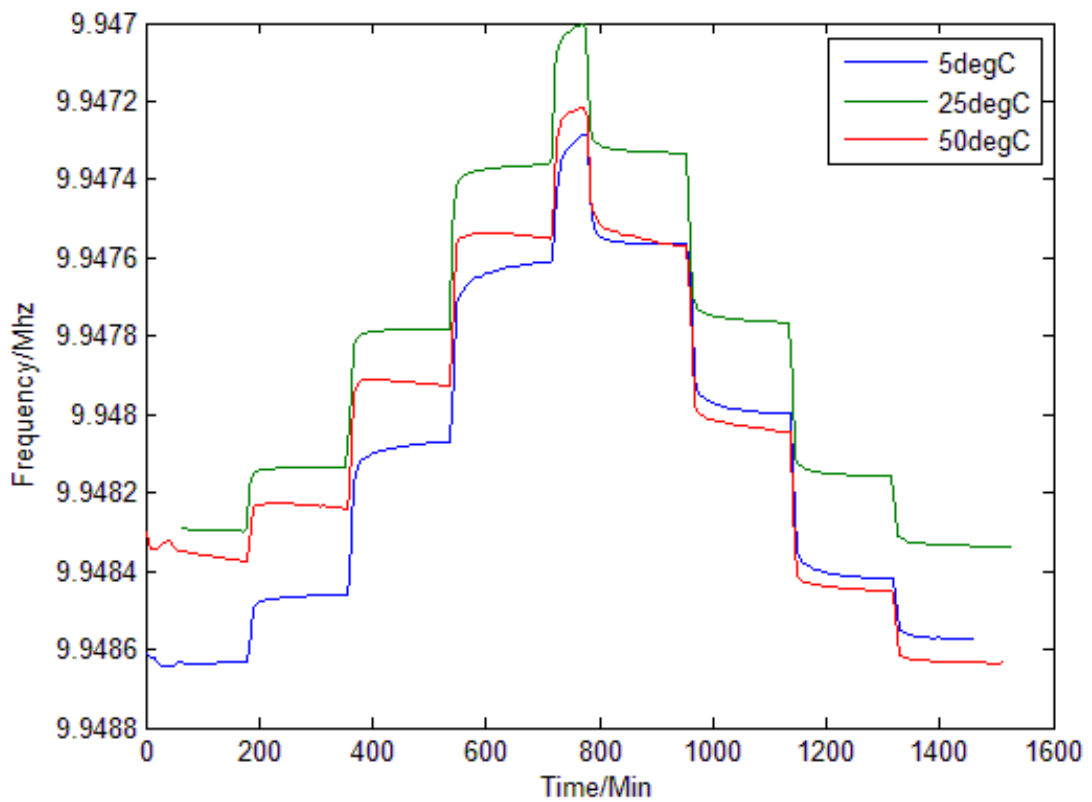


Figure 3.9: The frequency readout for the same film on a QCM at three different temperatures as the humidity is varied.

The temperature-frequency relationship for these crystals was investigated by studying an uncoated crystal in the thunder chamber and the temperature was varied from  $5^{\circ}\text{C}$  to  $65^{\circ}\text{C}$  in two hour steps to allow the readings to stabilise, as shown in Figure 3.10 (a). The stabilised frequency was plotted as a function of temperature and the results reveal a cubic relationship plotted and fitted in Figure 3.10 (b).

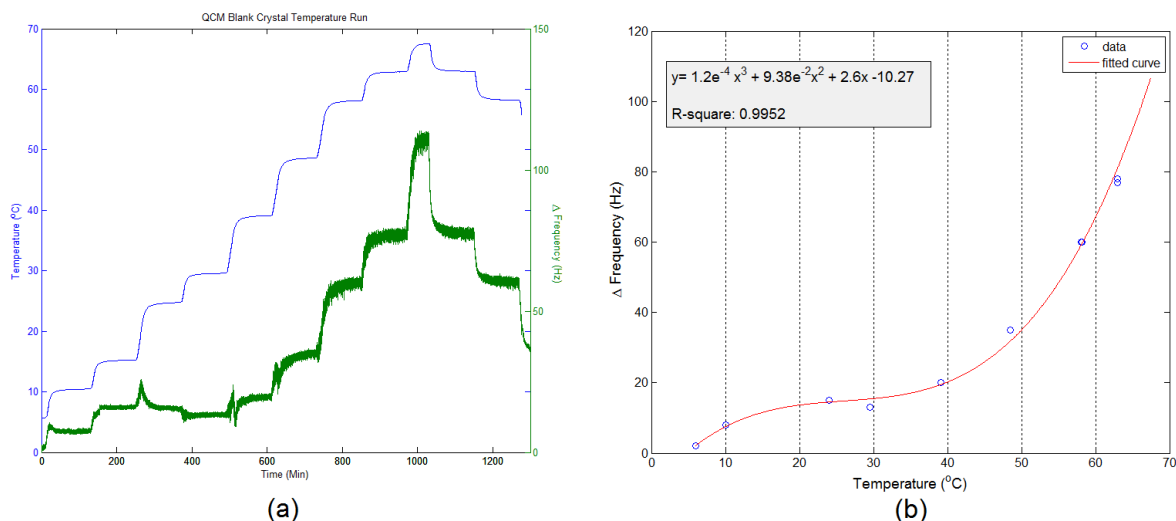


Figure 3.10: (a): The Temperature (green), and frequency (blue), readout of a blank crystal as a function of time. (b): Frequency as function of temperature showing a cubic fit.

This polyimide has a thermal coefficient of expansion of  $\approx 54ppm/^{\circ}C$ , large when compared to that of materials similar to this quartz (fused silica) of  $\approx 0.5ppm/^{\circ}C$ . As the film was spun at ambient conditions, variations in the atmospheric temperature caused stress to the crystal, changing the mechanical properties of the film-crystal system and hence the measured frequency, with no change in mass. This lead to a non-linear relationship between measured frequency and set humidity point for any temperature away from  $\approx 25^{\circ}C$ , as demonstrated in Figure 3.9. To avoid such complications all QCM dynamic data presented was acquired at  $25^{\circ}C$ .

### 3.3 A method of detecting Hysteresis

The objective of this section is to outline a method of defining and measuring the hysteresis. The hysteresis effect has been reported as being observed when film is cycled from a high humidity to a low humidity state while allowing the film to reach equilibrium at each humidity set point. Therefore, in this chapter, the wetting and drying process is probed over several hours. This is of great interest as observations of the hysteresis in commercial humidity sensors have been reported on these timescales. Measurements on longer timescales of days require both the atmosphere and the measuring equipment of the film to have long term stability. The QCM technique has been shown to be a robust and stable method of detecting the raw mass of thin polyimide films to an accuracy on the order of a nanogram. The thunder chamber(discussed in section 2.6) is the industry standard for sensor calibration. It is designed to provide a highly stable controlled atmosphere in which to perform long timescale device

tests.

Figure 3.11, shows the temperature, absolute humidity, and relative humidity readings of the thunder chamber over a test cycle, the form of which is discussed later. Crucially, the thunder chamber measures the relative humidity by feeding data from a series of pressure and temperature sensors into Equation 1.4. This provides an independent verification of the chamber relative humidity which is not reliant on any absorption process. The accuracy of the output is regularly calibrated against a dew point hygrometer.

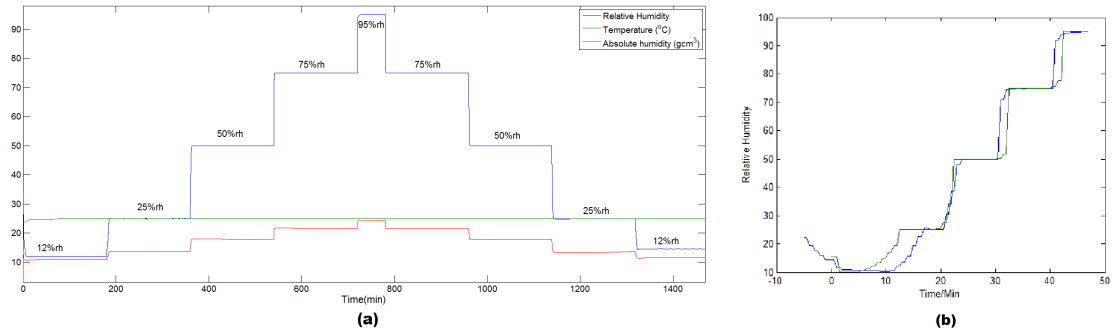


Figure 3.11: (a) Output from the thunder chamber sensors on a test cycle (pseudo calibration) run. The temperature is held at  $25^{\circ}C$  and the humidity is well controlled. (b) Shows no hysteresis in the chamber.

The temperature stability is an important factor as diffusion processes, QCM measurements, and any chemical bonding processes are a function of temperature.

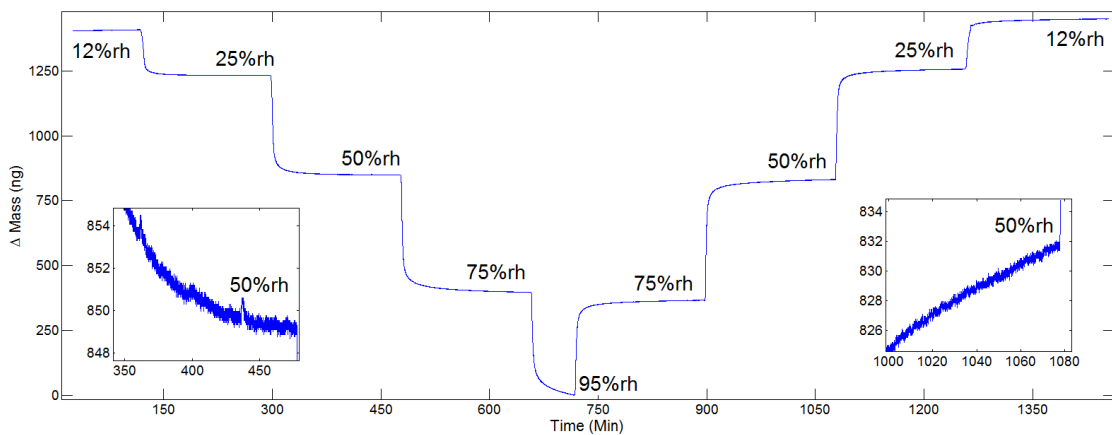


Figure 3.12: The change in mass as a function of time for a soft cured polyimide film. The 50%rh point is zoomed in on for both wetting and drying showing a small mass flux on a nanogram scale after 3 hours.

Calibration cycles are used to test each humidity sensor in a controlled environment like that of the thunder chamber, such as the cycle shown in Figure 1.2. Such cycles involve raising the humidity from a base line to near dew point and back down to the base line again[113, 114]. For example; the relative humidity is raised from 10%rh to 90%rh in 10%rh increments followed by a rise to 95%rh and back down in symmetrical fashion, with the film being allowed to equilibrate at each set point. This results in the observation of hysteresis. The time taken for the films to reach equilibrium means that calibration cycle takes several days to perform.

In this project a calibration cycle has been designed to provide a test for material behaviour. The calibration cycle is shown for a  $\approx 1.1\mu\text{m}$  thick soft cured polyimide film in Figure 3.12, which consists of a 12%rh-25%rh-50%rh-75%rh-95%rh set points. This calibration cycle does not have the same number of set points used when calibrating commercial sensors, and hence the time taken to perform a materials test is reduced. The mass output on Figure 3.12 shows that mass transport is still active after three hours at the 50%rh set point on the order of a few nanograms, with the total mass change per set point being  $\sim 300\text{ng}$ . Therefore, the time at each set point is set to three hours.

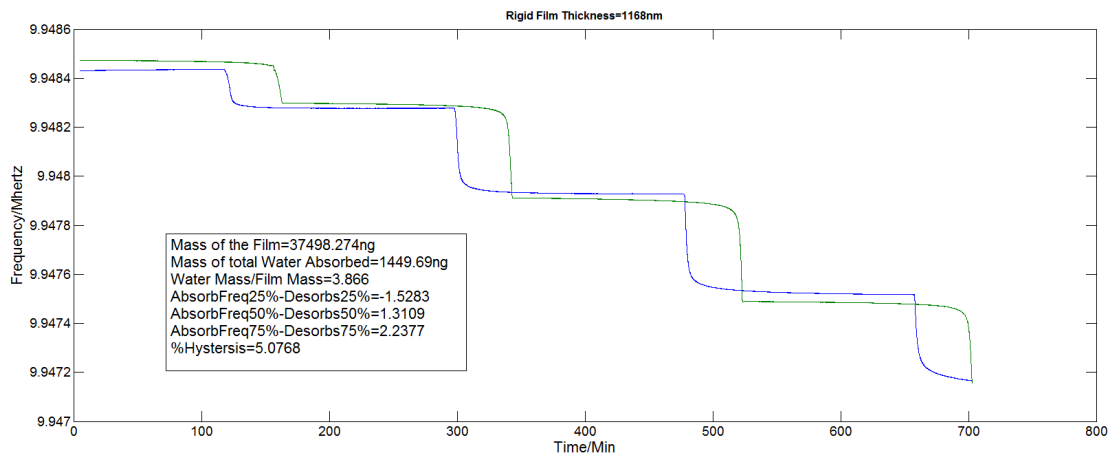


Figure 3.13: The data shown in Figure 3.12 flipped and plotted to show the existence of hysteresis as measured by a MatLab script.

Hysteresis in the data presented in Figure 3.12 is visualised in Figure 3.13 that was produced by script which flipped the profile about the minimum mass point as shown.

Plotting the mass as a function of humidity gives Figure 3.14(a). A comparison of the absorption and desorption curves indicates the characteristics of hysteresis. The measurement of the hysteresis as a material, and not a device property proves that the hysteresis is intrinsic to the polyimide material and not just an electrical feature resulting from the device architecture or the integrated circuit.

Consequently, QCM provides a means to measure this property in materials without fabricating a device.

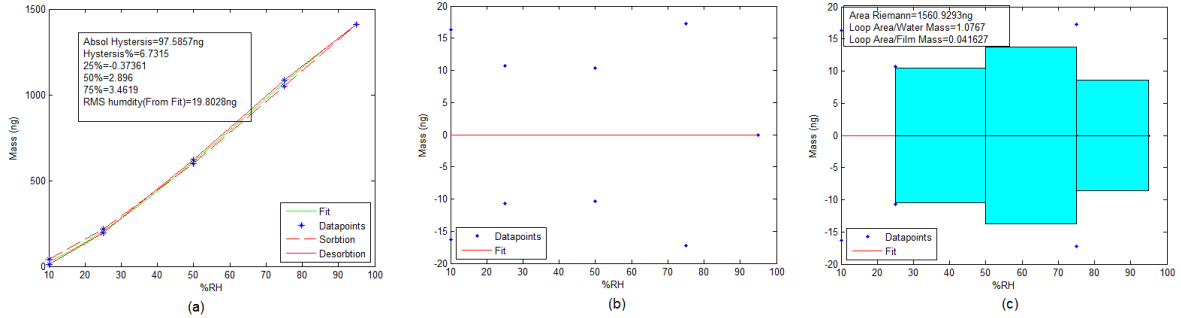


Figure 3.14: Shown are the methods of measuring the hysteresis. (a) The mass of the film as a function of %rh. (b) Residuals of the fit with the fitted line in the middle. (c) Showing the measurement of the area of the hysteresis loop.

There are several methods of quantifying the hysteresis. Conventionally, sensor vendors quote the hysteresis as the ratio of the difference between the readings at 50%rh and the total change in the measurand though a calibration cycle. However, Figure 3.13 shows that the hysteresis also affects readings at other humidity set points, and in some cases more so than at 50%rh.

An ideal sensor with no hysteresis effect may have a characteristic absorption curve or line of the measurand as a function of relative humidity. The characteristics of this ideal curve can be estimated by fitting a function to the data as shown in Figure 3.14(a). The fitted function is dependent on the type of sensor, in this case a fourth order polynomial is sufficient to model the behaviour of the QCM. The residuals of such a plot are indicative of the hysteresis characteristics as shown in Figure 3.14(b) and discussed elsewhere[113].

The approach used in this investigation provides multiple methods of quantifying the hysteresis; a goodness of fit test for the fitted ideal function, a Riemann sum of area between the absorption and desorption curves, Figure 3.14(c), and the difference at 50%rh. Conveniently, estimations of the area between the absorption and desorption curves are in units of mass and so can then be normalised by dividing this by either, the film mass, or the total mass of the water absorbed, giving a dimensionless ratio measuring the hysteresis. Such a method can also be applied to data with any measurands of humidity, i.e. capacitance, and so is advantageous when comparing this work to both past and future studies.

### 3.4 Measurements of Density, Water Uptake and Hysteresis in polyimide Films

The polyimide thin films that constitute the sensing element in Honeywell commercial sensors undergo several processing steps after their initial deposition. An understanding of the impact of each step on both the hysteresis and the material performance as a sense dye is vital when considering improvements to the manufacturing process. The previous sections in this chapter have shown QCM to be a suitable technique to quantify the mass of a polyimide thin films using the Sauerbrey linear conversion as applied to the frequency shift,  $\Delta f_2$ .

In this section a series of measurements from five films of varying thickness are presented. The transport characteristics of films were measured after each of the process steps: soft cure, hard cure, and plasma etching. This was achieved by reading the mass of films throughout a humidity calibration cycle.

The polyimide are first *soft* cured and then *hard* cured. The former curing regime is designed to solidify the polymer after the spinning process; this consists of an oven bake in an  $80^\circ C$  oven for 1 hour. The *hard* cure regime is designed to allow the polyimide film to reach the most energetically favourable configuration by raising the polyimide film above its glass transition temperature of  $350^\circ C$  over the course of 18 hours. Plasma etching is used by Honeywell to bring the thickness of the films within the tolerance level, so the same films had been etched after the hard cure.

Firstly, both the QCM and AFM were used in conjunction to measure the density of films. The density measurement is of use as it allows an understanding of the relationship between the mass, hence thickness, and frequency. The QCM can then measure the thicknesses of the deposited films, similar to a traditional QCM thickness monitor used in film depositions systems.

The dry state mass of the each film was calculated by measuring the frequency of the crystal when it was unloaded, and frequency when it was loaded while in an atmosphere controlled at 12%rh. The volume was calculated as a cylinder, with the area of the circular face assigned as the active area of the QCM and a height equal to the thickness of the film, as measured on the witness sample using an AFM. Figure 3.15 shows the calculated densities as the gradient of the fitted line.

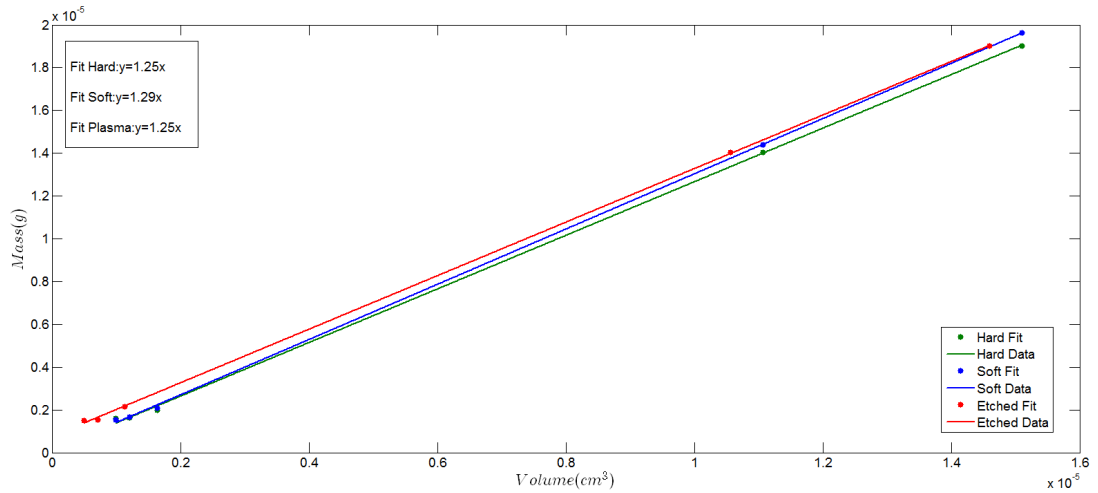


Figure 3.15: Density measurements of the polyimide thin films at different process stages, across a range of thicknesses.

The fitted lines shown in Figure 3.15 indicate that the soft cured films have a density  $\rho_{soft} = 1.29 \pm 0.027 gcm^{-3}$ <sup>2</sup>, slightly denser than the hard cured equivalent at  $\rho_{hard} = 1.25 \pm 0.04 gcm^{-3}$ . The most likely cause of this discrepancy is that a small quantity of the polymer solvent, gamma-Butyrolactone, GBL, which has a boiling point of  $204^{\circ}C$ , may remain in the thin film after a soft cure (maximum temperature of  $90^{\circ}C$ ). The remaining GBL increases the mass of the soft cured thin films when compared to the hard cured film. GBL is also highly soluble in water[115]. This, in turn, leads to the soft cured films to have a greater affinity for water vapour, which is demonstrated in Figure 3.16.

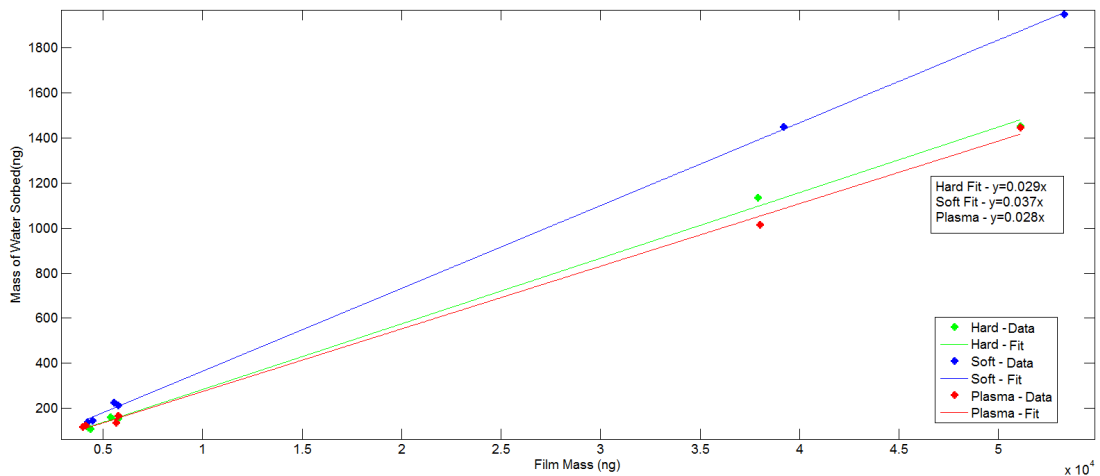


Figure 3.16: The mass of water absorbed as a function of film weight for five polyimide thin films of different thicknesses deposited on a QCM. Three data sets are shown for the same set of crystals after a soft cure, after a hard cure, and a oxygen plasma etched.

<sup>2</sup>The error quoted is the fitting error at the 95% confidence interval.

The mass of the water absorbed into the film was calculated by a script which was written for the purpose. The script found the maximum (at 12%rh) and minimum (at 95%rh) frequencies, and performed the necessary linear conversion to yield a measurement of the mass of water in the film. The total water absorbed is plotted as a function of dry film mass in Figure 3.16 which indicates that the soft cured films have an increased water absorption of  $\approx 3.7\%$  as compared to  $\approx 2.9\%$  for the hard cured films. This result agrees well with the SLD profiles (see Figure 5.12) which show a denser hard cured film, with less free volume for water<sup>3</sup>.

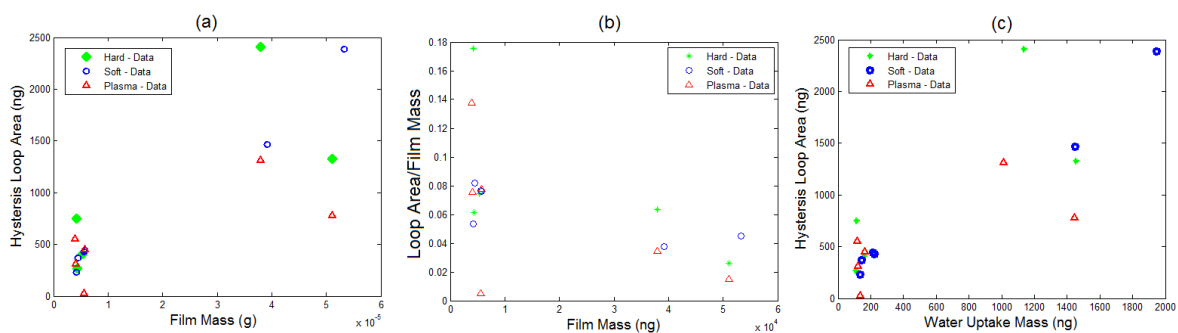


Figure 3.17: (a) The hysteresis loop area as a function of film mass. (b) The hysteresis loop area/Film mass as a function of film mass. (c) The hysteresis loop area as a function of water uptake in each film.

It is important to understand if the hysteresis is bulk, or an interface, effect. Figure 3.17(a) shows a measurement of the hysteresis, the area between the absorption and desorption curve, plotted as a function of the film mass. Should the hysteresis be a function of an interface, the hysteresis would be uniform irrespective of the film thickness and mass, a weak positive correlation is observed implying that the hysteresis is a bulk effect. The hysteresis can then be divided by film mass as shown Figure 3.17(b) to obtain data on each film at a given processing stage.

The cause of the hysteresis is not fully understood, however two possible chemical interactions may contribute; water-water and/or water-polyimide interactions. Figure 3.17(c) shows the hysteresis as a function of the water mass uptake. Should water-water interactions be the source of the hysteresis, then Figure 3.17(c) should present a linear correlation irrespective of film treatment, this is not the case, which demonstrates that the hysteresis is not solely a function of the water absorbed.

<sup>3</sup>An increased absorption in the soft cured films was also observed in the neutron reflectivity experiments.

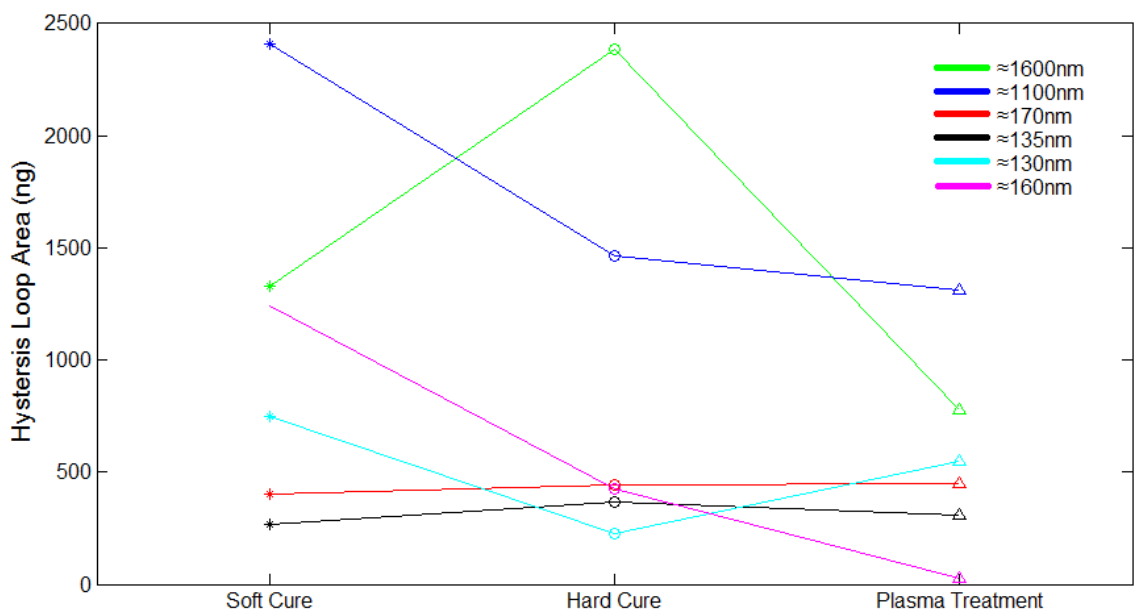


Figure 3.18: The Hysteresis loop area for each film deposited on a QCM is shown in a different colour. The x-axis is divided to show the three processing stages sequentially.

To gain a better insight into the impact of each processing step, the hysteresis of each crystal at each processing step is presented in Figure 3.18. Oxygen plasma etching is used in manufacturing to control the thickness of polyimide layers. Here, all but one of the crystals show a reduction in the hysteresis after the plasma etching. The polyimide in question is similar to Kapton (Figure 1.5) and it is possible the polar sites (C=O) on the polymer backbone are bonded to oxygen from the plasma<sup>4</sup>. Regardless, oxygen plasma etching appears to reduce the level of the hysteresis in this polyimide.

In this section the effects of film process steps on the density, water uptake, and hysteresis have been discussed. It was found that the density of the soft cured films was greater, and this was attributed to polymer solvent remaining in the thin film. The water absorption was found to be greater at the soft cured stage than after hard cure. It was proposed that this was a result of the remaining polymer solvent attracting more water vapour. Finally, the hysteresis was confirmed as a bulk, and not a surface, effect, with oxygen plasma etching reducing the hysteresis.

### 3.5 The effect of Humidity on the viscoelasticity of polyimide

The Sauerbrey equation considers the mass added to the quartz crystal to be an extension of crystal into which the resonant mechanical wave can oscillate with an increased wavelength and hence lower

<sup>4</sup>Bonding will be explored in Section 4.2.1

frequency. However, a change in the material through which the wave passes leads to both boundary effects, and a change in the impedance experienced by the mechanical wave. While using the QCM as a mass measure, this has been addressed as the properties of energy storage and inertia, the capacitive and inductive properties of the thin film cancel at a certain frequency,  $f_2$ . As a result,  $\Delta f_2$ , the shift in  $f_2$ , is the best to use when calculating the mass using the Sauerbrey equation. Consequently, complications arising as a result of the viscoelastic properties of the thin film for mass measurements have been avoided in this study[106]. This section explores the manner in which the viscoelastic properties of the thin film on the quartz surface are reflected in the impedance spectrum and how these properties change with humidity.

One approach is to fit the impedance spectra of a QCM to its equivalent circuit (Manson et al.[104]). This links each mechanical property to the characteristics of an ideal equivalent component. This requires the full impedance spectrum to be saved and fitted, taking a lot of memory and computer processing power with no guarantee of the quality of the fit. Furthermore, this approach would require a different instrument as the native Gamry software did not allow the extraction of numerical data but rather saved two frequencies;  $f_1$  and  $f_2$  shown as  $f_s$  and  $f_p$ , read by fitting a rational function to the impedance sweep, shown in Figure 3.19.

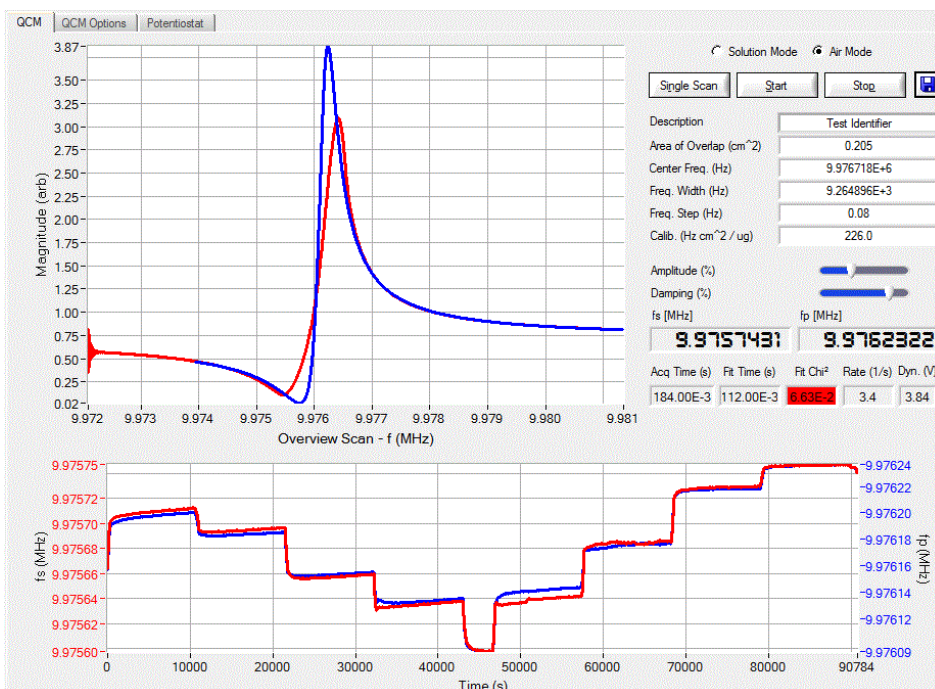


Figure 3.19: A screen shot of Gamry software showing the measurement of  $f_s$  and  $f_p$  using a fitting function. The data is shown in red and the fit is shown in blue. This is not a good fit and so can lead to an error in frequency measurement of  $f_p$  of tens of hertz.

Here, the simple model, discussed in section 3.2, of a rigid film in a fluid medium is applied to this system, a viscoelastic thin film in a changing atmosphere. This approach assumes that the resulting frequencies of this system can be represented by two components to give a qualitative understanding of the changing viscoelastic properties of the film. The two contributions to the impedance spectra being; the lossy film properties represented by the density, and viscosity of the hypothetical surrounding fluid, and the mass of the rigid thin film. This model is advantageous as only two measurements;  $f_1$  and  $f_2$ , are required.

The model shows that for such a case,  $\Delta(f_2 - f_1) = k(\rho\eta)^{\frac{1}{2}}$  where;  $\rho$  and  $\eta$  are the density and viscosity of the surrounding fluid respectively,  $k = -\frac{2N^{\frac{1}{2}}f_o^{\frac{3}{2}}}{\sqrt{\pi\rho_q\mu_q}}$  and  $\Delta(f_2 - f_1)$ .

Johannsmann et al. detailed that the bandwidth,  $\Delta(f_2 - f_1)$ , can probe dissipative processes on the quartz surface in a vacuum[101]. It was also shown that quantitative information can be obtained directly from the correct model by driving the crystal at multiple overtones under the same conditions to solve for the density/viscosity parameter. A graph of frequency shift as a function of overtone allows the viscoelastic constants to be inferred[101]. Doing so in a dynamic atmosphere is problematic as it reduces the time resolution and would involve developing more equipment capable of driving the crystal at higher frequencies. Furthermore, for a film located close to a node of the mechanical standing wave (thin films where  $t \lesssim 50nm$ ), Johannsmann et al. question the availability of this information[101]. Regardless, the  $\Delta(f_2 - f_1)$  parameter can still be used to qualitatively assess the dissipative processes on the quartz surface.

In this section a qualitative interpretation is presented using the model shown in Equation 3.3. An understanding into the variation of the mechanical properties of the thin film provides valuable information for device engineers, such as stresses exerted by the film and expands the functionality of the QCM.

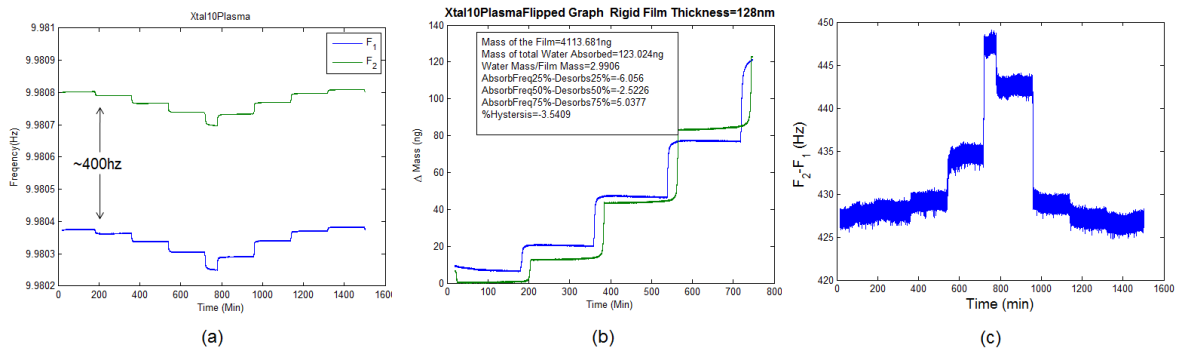


Figure 3.20: The viscoelastic properties of a 130nm plasma treated film through a humidity cycle. (a) The  $f_1$  and  $f_2$  of a QCM with a polyimide film on the surface. (b) The mass calculated from  $\Delta f_2$  using the Sauerbrey equation. (c)  $f_2 - f_1$  reflecting the viscoelastic properties of the film and surrounding medium as discussed.

Figure 3.19 shows a screen shot of the Gamry software at a low humidity, in contrast to Figure 3.8 taken under ambient conditions, in which the fit was better. Figure 3.20(a) shows both frequencies plotted as a function of time during the calibration profile running from 12%rh to 95%rh and back up, with a gap of around 400hz. Figure 3.20 (b) shows the mass of the film, which exhibits hysteresis, and Figure 3.20 (c) shows  $f_2 - f_1$ , which shows asymmetry. Both Figure 3.20(b), and Figure 3.20(c), show an increased hysteresis at the 75%rh point. The correlation between  $\Delta(f_2 - f_1)$ , and the hysteresis level is evident and ubiquitous on the data acquired on all films.

$\Delta(f_2 - f_1)$  for a crystal at each stage of treatment; unloaded, with a  $1\mu\text{m}$  soft cured film on the surface, after a hard cure and after plasma treatment, is shown in Figure 3.21(a). It is clear that the film treatment impacts the  $\Delta(f_2 - f_1)$  parameter and the dissipation qualities of the film. Additionally, the  $\Delta(f_2 - f_1)$  is approximately constant on films with the same treatment, irrespective of the thickness of the film, in the range investigated

Interestingly, the unloaded crystal which would be expected to be constant throughout a humidity calibration cycle shows a small increase implying a greater dissipation on the quartz surface, as shown in red on Figure 3.21(a). This is attributed to the condensation of water vapour between 75%rh and 95%rh. This may be impacted by the orientation of the flat surface of the crystals which was not monitored or controlled and may have influenced the growth of a condensed layer of water. However the unloaded crystal can still be used as a standard, as it should exhibit minimum dissipation. The plasma etched film appears less dissipative when compared to the other two films. The soft cured film exhibits the most dissipation when compared with the other crystals which may be due to the presence of the solvent in the thin film.

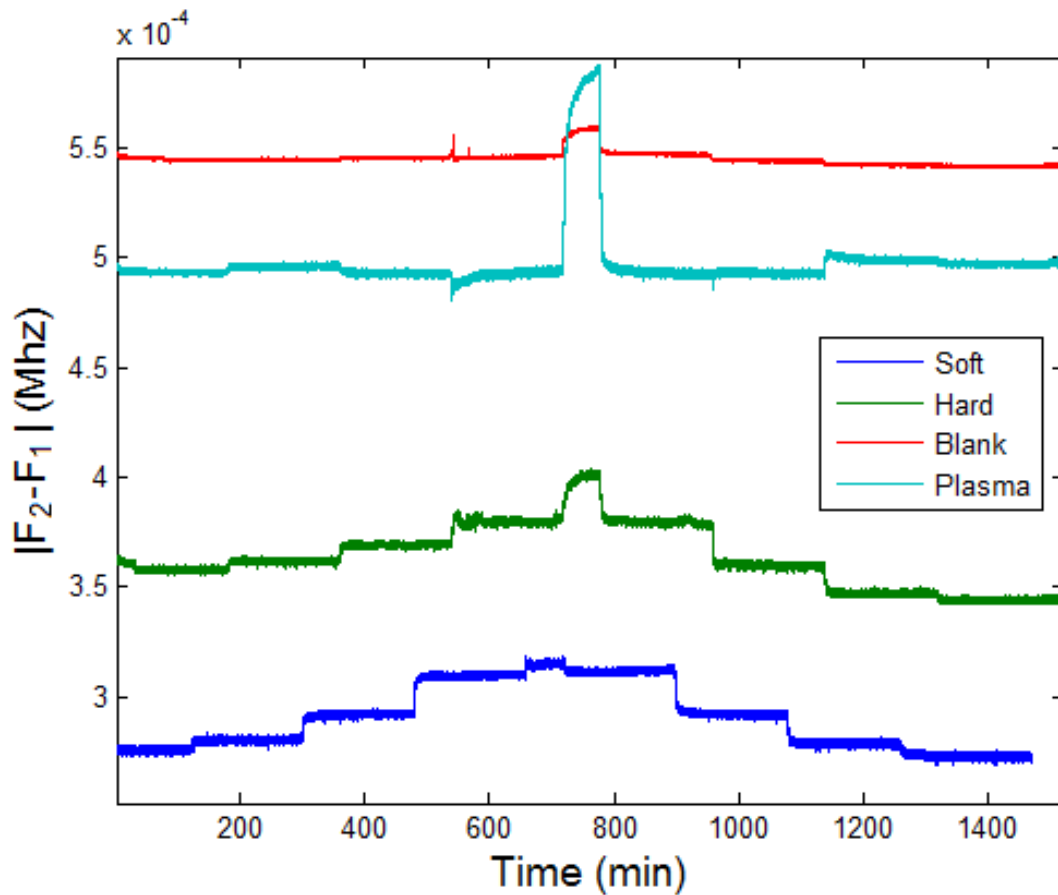


Figure 3.21:  $f_2 - f_1$  for the same crystal at different stages of processing presented in Figure 3.20. This shows the dissipative properties are a function of film treatment, which is more dominant than the humidity level.

In order to analyse the link between the dissipation properties and the absorption behaviour of the films  $\Delta(f_2 - f_1)$  is investigated as a function of humidity, shown in Figure 3.22(c). Across all crystals a curve emerges up to the 75%rh point followed by a sharp deviation, attributed to condensation which was also observed on the unloaded crystals, shown in Figure 3.22(b).

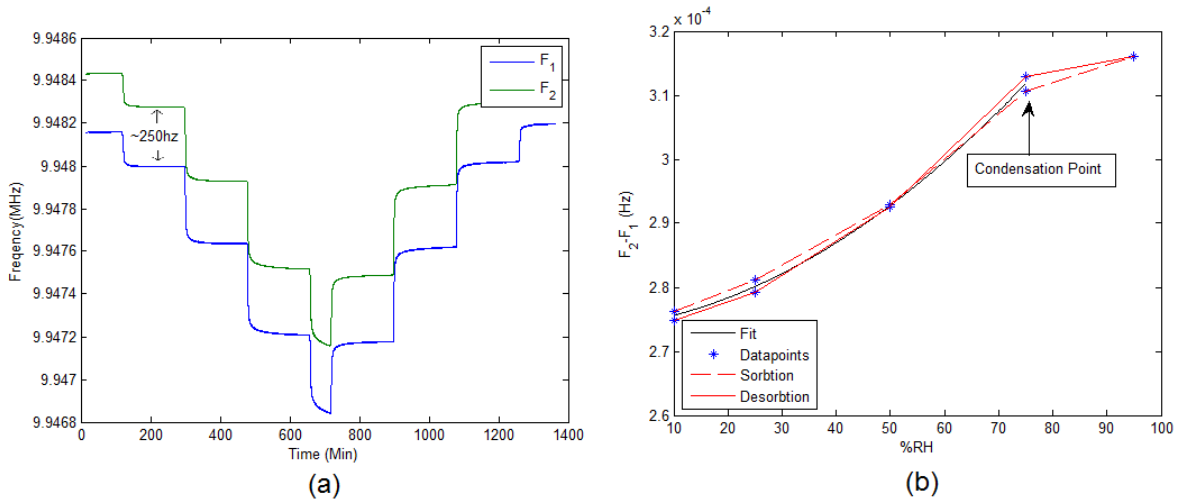


Figure 3.22: The viscoelastic properties of a thick film. (a) Shows the  $f_s$  and  $f_p$  plotted as a function of time in a calibration cycle in the thunder chamber. (b) shows the  $f_2 - f_1$  as a function of humidity.

Recent simulation work by Pandiyana et al., discussed in Chapter 1, outlined water absorption processes in epoxy polymer matrices[62]. It was suggested that at a certain humidity, an increase in the water content triggers the sharp formation of bigger water clusters leading to a difference in the mechanical properties of the polymer. This, rather than condensation, may be the cause of the change in dissipation that is observed.

The density and viscosity for hypothetical fluid surrounding all the films was calculated based on Equation 3.3. At a higher humidities this should reflect the properties of water due to the postulated condensation. However, the viscosity of water,  $\approx 9 * 10^{-3} gcm^{-1}s^{-1}$ , is much higher than is measured ( $\approx 8 * 10^{-5} gcm^{-1}s^{-1}$  at 95%rh). This is most likely as the water layer is not pseudo infinite, and may not even be continuous, as required by the model. Therefore, this model and measurement method cannot be considered quantitative, but only indicative of relative dissipation in the system.

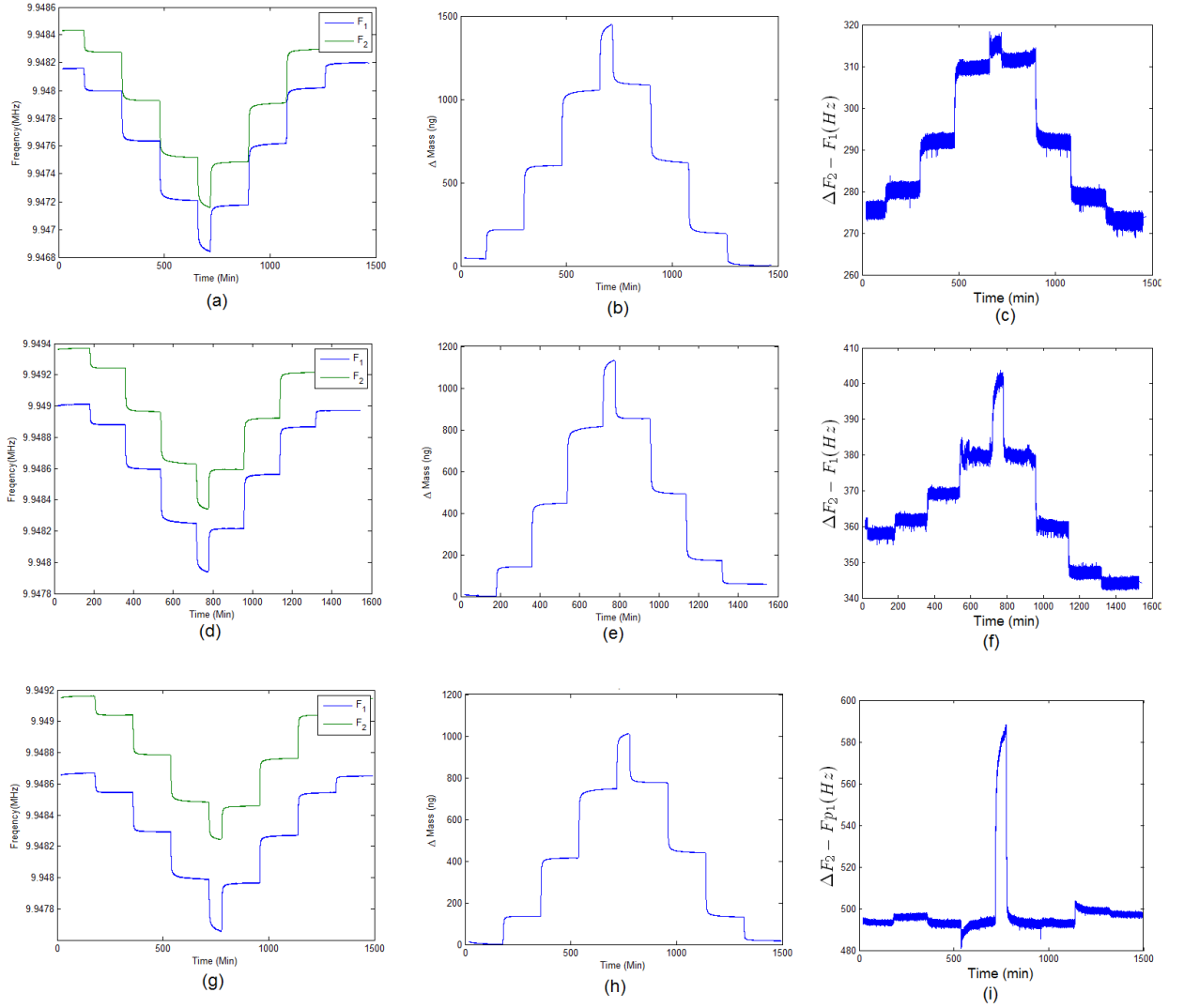


Figure 3.23: The QCM data from the same  $1\mu\text{m}$  polyimide thin film through a humidity cycle when the film is at different stages of processing. (a) Soft cured, frequency measurements. (b) Soft cured, mass measurements. (c) Soft cured,  $\Delta(f_2 - f_1)$ . (d) Hard cured, frequency measurements. (e) Hard cured, mass measurements. (f) Hard cured,  $\Delta(f_2 - f_1)$ . (g) Plasma etched, frequency measurements. (h) Plasma etched, Mass measurements. (i) Plasma etched,  $\Delta(f_2 - f_1)$ . (c), (f) and (i) show the change in the dissipative properties of the polyimide films through a humidity cycle. (i) is much flatter indicating that the dissipative properties of the film are less affected by humidity than the other two, (c), and (f). (i) also shows a peak at 95%rh, perhaps indicating condensation. The mean  $\Delta(f_2 - f_1)$  (comparing y axis scale bars for (c), (f) and (i)) has increased with each treatment implying that the treatment changes the dissipative properties of the film.

Figure 3.23 shows the QCM data from the same film at different stages of curing. Plasma etching, associated with a reduced hysteresis, shows a more consistent dissipation than the other two films despite showing similar amounts of water absorbed, ignoring condensation. An exhaustive study into the interpretation of the  $\Delta(f_2 - f_1)$  parameter has not been performed. However, two data sets were also acquired on a films which sorbed water vapour which would be expected to have varying dissipative

properties<sup>5</sup>. Polypyrrole (Figure A.9) which is known to swell in the presence of water vapour, had a mean  $\Delta(f_2 - f_1)$  of  $\sim 370Hz$  with a shift in  $\Delta(f_2 - f_1)$  though the humidity cycle of  $\sim 70Hz$  and a clear step change of  $\Delta(f_2 - f_1)$  with each humidity setpoint; making its dissipative characteristics similar to those of the hard cured film, as shown in Figure 3.23(f). The rigid film was a metal oxide,  $ZrO_x$  (Figure A.10) which had a mean  $\Delta(f_2 - f_1)$  of  $\sim 2300Hz$  with a shift in  $\Delta(f_2 - f_1)$  though the humidity cycle of  $\sim 40Hz$  with no obvious correlation with the humidity setpoints. The large  $\Delta(f_2 - f_1)$  of  $ZrO_x$  would be expected as the parameter, according to this model is proportional to  $(\rho\eta)^{\frac{1}{2}}$  of the hypothetical fluid surrounding the quartz resonator and the density of a metal oxide would be higher than that of polymer and quartz. Therefore, plasma etching makes the polyimide films dissipative properties behave more like a rigid film, without being quantitative.

In spite of the simplified model used, it is clear that the  $\Delta(f_2 - f_1)$  provides a qualitative manner with which to assess dissipative film properties by comparison to an ideal, in this case an unloaded resonator with only rigid gold electrodes, for which the results are shown. To expand this work further, the range of approaches to gain quantitative measurements[101, 116] on such films using QCM should be explored. This includes driving the crystal at its overtones, and rewriting the native Gamry software to read out the full data to enable post-processing.

While a more vigorous assessment of the viscoelastic properties of the material provides an intriguing sidetrack, the work presented in this section outlines a clear link between the dissipation of the polymer and the treatment of the film. Furthermore, the absorption is also linked to the dissipation, as shown in Figure 3.22(b) and (c). It unclear if this link is correlative, as both measurements are responding to water present in the film, or a more complex causative relationship exists.

## 3.6 Capacitance based Polymer Studies

Thus far the relationship between the mass of water vapour and the capacitance measured has not been explored. The commercial sensors considered here measure the capacitance, not the mass of the sensing element. While mass absorption within the polyimide is approximately linear with relative humidity, as shown in Figure 3.14, there is a non linear relationship between the capacitance and the mass of water vapour. This is explored here in this section. The capacitances of some test devices are considered and their behaviour in a range of humidities is compared to the equivalent QCM results.

### 3.6.1 The Fabrication and Use of Interdigitated Capacitor

#### Capacitance in polyimide and Water Vapour

<sup>5</sup>The details of these experiments are provided in the appendix, Section A.6.

Capacitance measures the ability of a dielectric material to store charge, as shown for a parallel plate capacitor in Equation 3.4 [117].

$$C = \frac{(1 + \chi_e)\epsilon_0 A}{D} \quad (3.4)$$

Where;  $\chi_e$  is the net electric susceptibility of the dielectric,  $C$  is the capacitance,  $\epsilon_0$  is a constant (the electric permittivity of free space),  $A$  is the area of the capacitor, and  $D$  is the distance between the electrodes.  $\epsilon_0\chi_e$  is the constant of proportionality between the electric field applied and the polarization vector of the molecules in the material, i.e. where;  $\vec{E}$  is the electric field vector and  $\vec{P}$  is the polarisation vector. The polarisation vector,  $\vec{P}$ , in a solid is defined by electronic displacement within the molecules.

For a gas of polar molecules, such as water vapour, the polarisability of the water vapour,  $P_{wv}$ , is defined by the ability of the permanent dipole moment,  $\vec{p}_0$ , to align within the applied field.

$$P_{wv} = \frac{N\vec{p}_0^2\vec{E}}{3kT} \quad (3.5)$$

The physical origins of the polarisation vector are well discussed elsewhere[117]. In a system such as this, in which there is a degree of chemical interaction between the film and the penetrant ( which is shown in Section 4.2.1) and the penetrant-penetrant in similar systems[65, 38, 62], the capacitance is not linear with respect to the mass uptake of an interacting diffusant. The chemical interactions act to minimise the energy of the system by bonding with the polar components of the polymer backbone and the water vapour itself, reducing the polarisability and hence the net electric susceptibility of the dielectric,  $\chi_e$ . The resulting net loss in polarisability results in a loss in capacitance.

### **Testing capacitance**

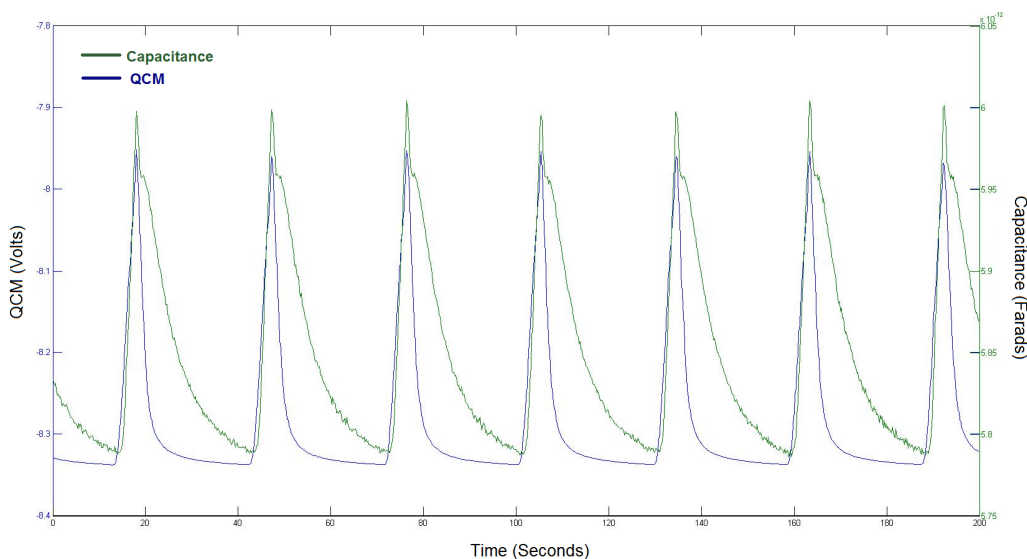


Figure 3.24: The response to a series of vapour pulses of both, a commercial sensor humidity sensor (capacitance) and QCM (mass). This is data acquired during the neutron scattering experiments, presented in chapter 5.

The response of a Honeywell 1820 capacitive humidity sensor<sup>6</sup> and QCM crystal with a  $1\mu\text{m}$  layer of polyimide, to a series of humidity pulses is shown in Figure 3.24.

Figure 3.24 shows a slower response to a sharp change in humidity for the capacitive based sensor when compared to the QCM. Commercially available sensors are designed to be robust with a range of additional layers to protect the sensing element, making a finished product unfit to assess material properties. Therefore, here a simple set of interdigitated, IDT, electrodes with contact pads were fabricated on resistive silicon using standard photo-lithography techniques to compare. A fabricated set of electrodes made up of a 5nm titanium adhesion layer and 95nm of gold with a range,  $5\mu\text{m}$  to  $30\mu\text{m}$ , of spacings between the teeth.

Following the fabrication of the electrodes, a 4:1 polyimide to solvent solution, with a reduced viscosity to ensure the polyimide would settle in between the electrodes, was spun over the electrodes at 1000RPM giving an estimated thickness of 100nm. The polyimide was then removed from the bonding pads by oxygen plasma etching, with the rest of the sensor masked with a glass slide. The device was then glued to a contact board and wire bonded to the contact board to form a sense dye. The sense dye was then soldered to a standard dual in-line package, DIL, plug shown in Figure 3.25(c).

<sup>6</sup>Capacitance measurements have been performed using either Aglient E480A or E481A measurement boxes, discussed in section 2.1.

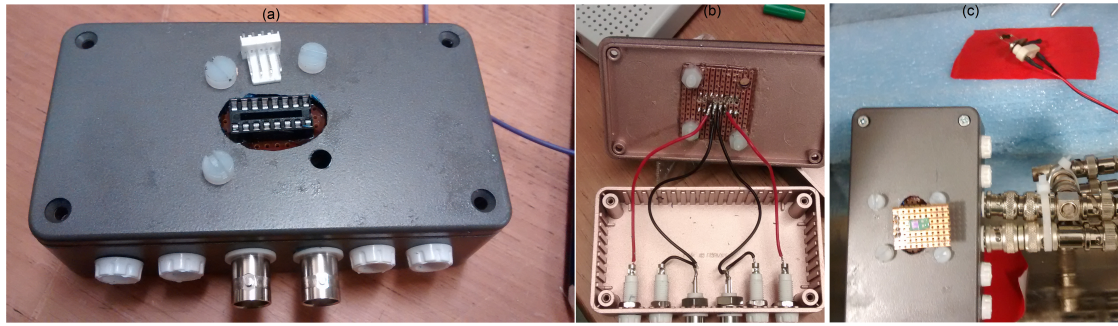


Figure 3.25: (a) The box with two BNC connections to connect to the capacitance meter and the DIL socket on top to plug devices in. (b) The wiring of the box with additional connections to run a voltage across a sensor. (c) The measurement box in the thunder chamber with the QCM in the back before a pseudo calibration cycle is performed.

Mechanical movements were limited by constructing a box with BNC plugs as shown in Figure 3.25. The DIL socket allowed devices to be plugged and unplugged as required. A series of pseudo humidity calibration cycles were then performed on fabricated devices.

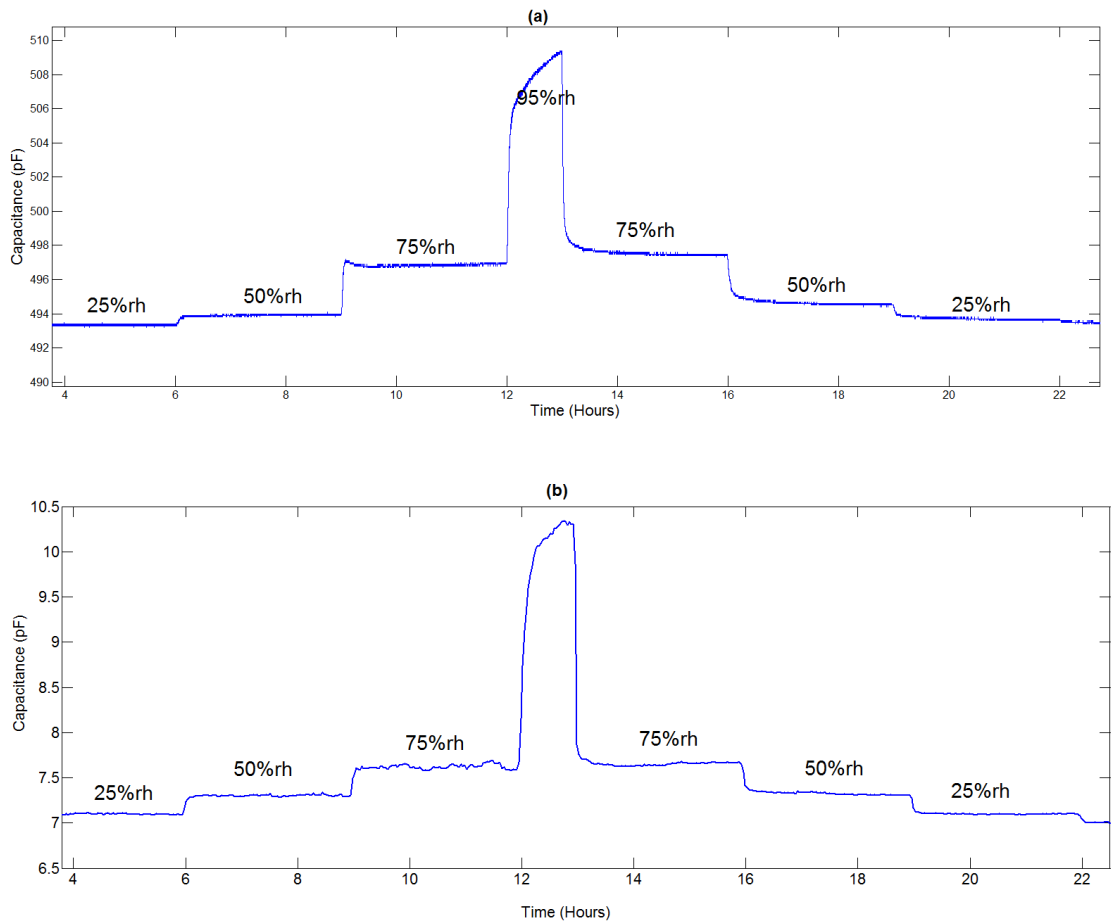


Figure 3.26: The capacitance from; (a) a nichrome IDT and (b) a 1820 Humidity sensor, in a thunder chamber on a humidity calibration run.

In addition to the titanium and gold electrodes, nickel-chromium alloy, nichrome electrodes were also fabricated. The results from a nichrome devices are shown in Figure 3.26 and 3.27. The material choice of nichrome for an electrode was intended to serve as a proof of concept for a more advanced sensor principle. Nichrome is well known for its use in a variety of devices where controlled electric heating is required. In nichrome the resistance is proportional to the temperature, allowing its use as a heating element. Therefore, monitoring the resistance of a nichrome electrode allows calorimetry tests on the polyimide. However, restrictions on both the time, and the availability of the thunder chamber, did not allow for the development of a sufficiently sensitive impedance measuring technique.

**IDT Device Results and Discussion** Figure 3.26 shows the capacitance of both (a) a nichrome device and (b) a commercial humidity sensor on a calibration humidity cycle. Both data sets show similar behaviour, with the capacitance change for a given %rh increase, increasing with relative humidity. For example, Figure 3.26 (a) shows a capacitance of approximately 0.5pF for difference between 25%rh and 50%rh, and approximately a 4pF for difference between 50%rh and 75%rh, a nonlinear increase.

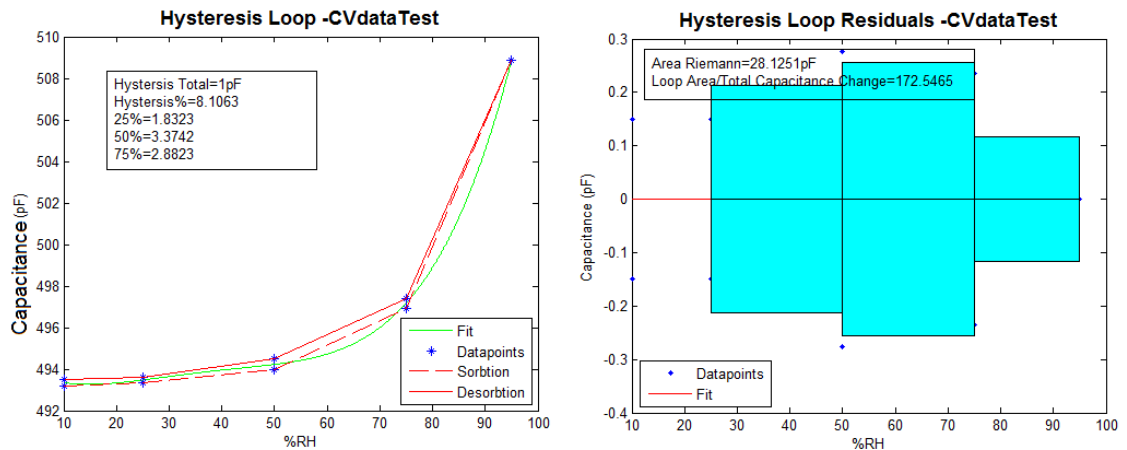


Figure 3.27: The hysteresis measurements on a nichrome IDT device. The data is shown in Figure 3.26.

The capacitance measurements shown in Figure 3.27(b) show a *hysteresis loop area/ total capacitance change* of 1.72, similar to mass based measurements of polyimide. However, the capacitance readings are not linear with respect to relative humidity, whereas the mass measurements from the QCM were reasonably fitted with a line. This is common across all capacitance measurements. This implies a

increased polarisability with an increase in water vapour content; which is surprising as it would be expected that increased amounts of water vapour would lead to the neutralisation of dipoles in the material.

It may be that the increase in humidity leads to a greater number of unbound water molecules in the polymer, and so to a greater measured capacitance. To investigate the mass-capacitance relationship further, measurements of both quantities simultaneously on the same film would be of great value. A device designed to perform such measurements is discussed next.

### **3.6.2 Capacitive QCM- Concept and Fabrication**

A device capable of measuring mass and capacitance on a given film is desirable. Such a device has been fabricated with a scheme, as shown in Figure 3.28(c). Here, the addition of a porous metal layer allowed capacitance measurements to be performed on top of an existing QCM. Figure 3.28 (a) shows data from a prototype Capacitive-QCM, CQCM, device with an additional metal layer sputtered on top of the polyimide. The additional metal layer, which was porous, was patterned with the use of a mask to avoid a short circuit with the other metallic layers, as shown in the photograph, Figure 3.28(b). The photograph also shows the third contact which was added to connect to the porous metal layer to the QCM holder. Both measurements are performed in alternation by switching the frequency at which the AC measurement is performed between the two contact legs. Figure 3.28(a) demonstrates that the QCM results are not disturbed by the additional porous metal layer and water is able to access the polymer. However; the quality of the contact, the degree to which the porous layer is continuous, and possible noise from the bottom contact, led to an inferior capacitance measurement. Regardless, such a device would allow the relationship between capacitance and mass uptake to be investigated on the same material in-situ. Additionally, the capacitance measurement is likely to have a different temperature response as it is not a function of the mechanical properties of the quartz.

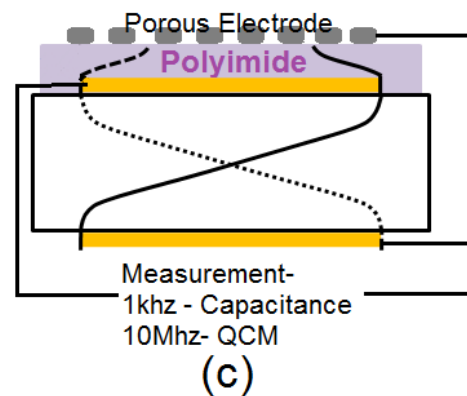
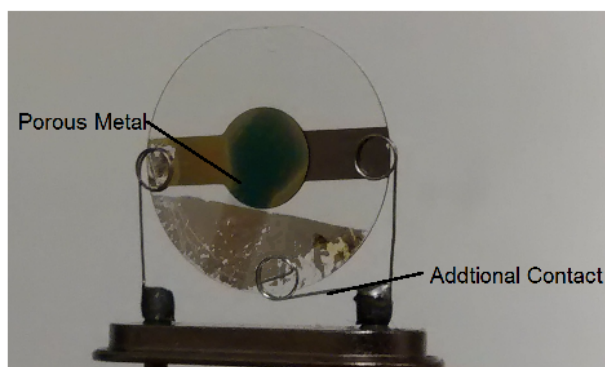
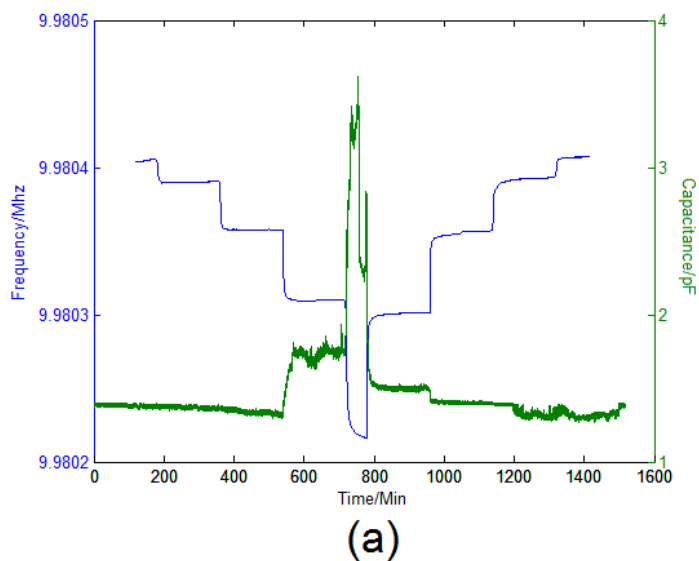


Figure 3.28: (a): The results of a CQCM device, both frequency output and capacitance. (b): A photograph of the CQCM device. (c) A illustration of the device.

A further possible application of interest is expansion of these sensing principles to measure other gases. Simultaneous measurements of both; the resistance and the mass of a sensing polymer have been performed in previous studies to produce an electronic nose, designed to detect the presence of a particular gas. In these studies separate devices to measure capacitance and mass were used [118, 119]. Here, we present a proof of a concept for a sensor capable of making both measurements on the same sensing element. These results will be discussed further in chapter 6.

## 3.7 Summary

QCM has been commonly utilised for a wide range of scientific purposes, and as a film thickness monitor. Yet it offers significant opportunities beyond its use as a simple film thickness monitor, and can act as a cost effective material probe. The goal of this chapter has been to explore its validity and limitations for such purposes.

In section 3.1 the use of a simple linear conversion from the central resonance frequency to mass were outlined along with alternative models of QCM behaviour. The section concluded by stating that best frequency to measure mass was the frequency at which the film's equivalent inductance and capacitance cancel. A model was introduced to relate the width of resonance peak,  $\Delta(f_2 - f_1)$ , to the dissipative properties of the film.

Section 3.2 presented the work performed as a proof of concept for the impedance sweep method of reading QCM frequencies. This resulted in a system to conduct impedance sweeps and obtain the necessary measurements. It was also shown that a linear conversion of frequency is a reasonable approximation for polyimide thin films at atmospheric humidities. The Gamry resonator box which performs the required measurements, and has the long term stability allowing the assessment of the polymer behaviour on a longer timescale, was introduced.

Methods of quantifying the hysteresis are shown in section 3.3, with the favoured method being a sum of the area between the absorption and desorption divided by the film mass.

Section 3.4 shows methods and results to measure the density, absorption by weight, and hysteresis on several films. The soft cured films are found to be both denser and have a greater amount of absorption attributed to some of the polyimide solvent, GBL, remaining in the film. There is some tentative indication that oxygen plasma etching reduces the hysteresis.

The work presented in section 3.5 outlines a clear link between the mechanical properties of the polymer and the treatment of the film. Furthermore, for polyimide, the quantity of water absorbed is correlated to the mechanical properties. It is unclear if the link between the absorption and the dissipation is correlative or causative.

The final section of this chapter began by outlining the need for a simple capacitance measurement device by comparing the response time of a commercial sensor, which has additional layers of material, and a polyimide coated QCM, in which the QCM was faster. The fabrication of a set of IDT electrodes on which the polyimide was deposited was discussed. The possibility of using such electrodes to perform calorimetry measurements was briefly mentioned, alongside the results from existing an IDT device. Capacitance measurements were shown not to vary linearly with mass uptake in the polyimide.

This led to the introduction of a proof of concept device, Capacitive CQCM, capable of measuring

both the capacitance and the mass of the same sensing element. The possibility of using such a device as a gas sensor via capacitance to mass ratio was mentioned.

## Chapter 4

# Transport Characterisation

Chapters 3 outlined techniques to measure the timescales for the transport of water vapour in polyimide thin films. In this chapter the results obtained are considered to form a coherent picture of the rate limiting factor in water transport through these polyimide thin films.

Firstly in section 4.1, Fick's model of diffusion is applied to the data acquired to understand the extent to which diffusion processes are responsible for the response of the sensor. It is concluded that the rate limiting factor is unlikely to be the transport of water vapour within the material as the analysis performed indicates a uniform diffusion coefficient across polyimide films of various thicknesses.

Section 4.2 then presents an investigation into the rate limiting factors in this system, and consequently, water transport models are discussed with the impact of chemical interaction and sticking probability considered.

Finally, the length scales of transport are considered by analysing the free volume within the polyimide. This is achieved through an analysis of spatial frequencies in TEM bright field images of the polyimide.

### 4.1 Interpreting Diffusion

In Chapter 1 Fick's diffusion laws were introduced, with diffusion defined as mass transport by random atomic motion. The diffusion coefficient, typically with units  $cm^2s^{-1}$ , appears in both of Fick's laws and is commonly used to compare different systems as it is a function of the material. Here, absorption processes are assumed to be the rate limiting step in the ingress of water vapour into the polyimide, an assumption discussed in the concluding parts of this section. The data acquired during the QCM studies is used to measure the diffusion coefficient across all the samples tested.

### 4.1.1 Ideal Sensor behaviour in a thunder chamber environment

Before proceeding to measure the diffusion coefficients, the response time is limited by the number of water molecules that will interact with the sensing element at a given temperature in the thunder chamber. This *best case* response time is calculated.

A simple calculation to relate the atmospheric conditions such as, humidity and temperature to the number and mass of water particles interacting with a given surface, in a given time frame are presented. These expressions are then applied to an area with the same dimensions as a QCM crystal in the thunder chamber environment for comparison with experiment. This is with a view to quantifying the extent to which the atmosphere is responsible for mass uptake timescales which have been measured. Equation 4.1 provides an estimate of the rate of the number of collisions,  $Z_w$ , between a given particle with mass,  $m$ , and an area,  $A$ , [45] as:

$$AZ_w = \frac{pA}{(2\pi mk_b T)^{1/2}} \quad (4.1)$$

Where;  $p$  is the partial pressure of the gas,  $T$  is the temperature and  $k_b$  is the Boltzmann constant.

Equation 4.1 shows the number of water particles hitting the sensor is a function of the partial pressure of the gas in the controlled environment of the thunder chamber. The partial pressure of water vapour is controlled by varying the absolute humidity,  $\varrho(\frac{g}{m^3})$ , which is read out from the thunder chamber's array of sensors.

The partial pressure of the water vapour can be calculated from the atmospheric absolute humidity by assuming the ideal gas law,  $P = \frac{n}{V}RT$ , as  $\frac{n}{V} = \varrho/m_{water}$ , where;  $m_{water}$  is the molecular weight of water ( $\approx 18 \frac{g}{mol}$ ),  $T$  is the temperature, and  $R$  is universal gas constant giving:

$$P_{water} = \frac{\varrho}{m_{water}}RT \quad (4.2)$$

Inserting Equation 4.2 into Equation 4.1 for the partial pressure, assuming a constant temperature, and recalling that  $R$ , the universal gas constant, is  $k_b * N_A$ , where;  $N_A$  is Avogadro's number, and  $k_b$  is the Boltzmann constant, gives:

$$AZ_w = \frac{\varrho}{m} N_A k_b T \frac{A}{(2\pi m k_b T)^{1/2}} = \frac{N_A A (k_b T)^{1/2}}{(2\pi m_{water}^3)^{1/2}} \varrho = k_{idealgas} \varrho \quad (4.3)$$

in which,  $k_{idealgas}$  is a constant allowing the number of particles striking a given area to be linked to the absolute humidity.

Inserting the values for the QCM-thunder chamber experiments<sup>1</sup> at  $T=297K(25^\circ C)$ ; gives the constant,  $k_{idealgas} = 1.57 \times 10^8 m^3 g^{-1} s^{-1}$ . The number of particles striking the QCM area can be used to calculate the mass of particles striking the area by multiplying through by the weight of the gas molecules. The mass of particles hitting the QCM surface is a given time is;  $\frac{dM_{in}}{dt} = \rho k_{massideal}$ , where,  $k_{MassIdeal} = 4692 m^3 g^{-1} s^{-1} ng$ , .

This gives a mass flux into the sensor,  $\frac{dM_{in}}{dt}$ , however, of course there is also a mass flux of the sensor  $\frac{dM_{out}}{dt}$ . The relationship to the measured mass,  $M_{QCM}(t)$ , is  $\frac{dM_{QCM}}{dt} = (\frac{dM_{in}}{dt} - \frac{dM_{out}}{dt})$ . For comparison,  $\frac{dM_{QCM}}{dt}$  was calculated for a given QCM by taking the numerical derivative of the measured mass  $M_{QCM}(t)$ , both of which will be shown later in Figure 4.7. These results are also used for comparison to the measure QCM mass in section 4.1.2.

### 4.1.2 Measuring the diffusion coefficient

Two approaches to measuring the diffusion coefficient were outlined in section 1.4. Firstly, neglecting the higher terms of Equation 1.11 yields  $\frac{M_t}{M_\infty} = \frac{4}{h} \left(\frac{Dt}{\pi}\right)^{0.5}$ . Therefore, plotting  $\frac{M_t}{M_\infty}$  against  $\sqrt{t}$  yields a gradient,  $m = \left(\frac{16D}{\pi l^2}\right)^{\frac{1}{2}}$ , giving  $D = \pi \left(\frac{lm}{4}\right)^2$ , where;  $l$  is the thickness of the material. A one term approximation of Equation 1.11 is reasonable on shorter time scales[51] but invalid on longer timescales, as shown in Figure 1.7. The second approach used here assumes a constant diffusion coefficient, the time taken for the mass to reach half its equilibrium position (a half life type measurement),  $t_{0.5}$ , can be used to calculate the diffusion coefficient as  $D_a = \frac{0.04914l^2}{t_{0.5}}$  where;  $D_a$  is the apparent diffusion coefficient which is derived from a two term approximation of Equation 1.10, a reasonable assumption on longer time scales[51]. Both of these methods have been utilised in this section as the underlying assumptions lead to one approach being more valid at longer timescales,  $D_a$ , and one approach being more valid at shorter time scales,  $D$ . It should also be noted that  $D_a$  only takes a single measurement of  $t$  at  $\frac{M_t}{M_\infty} = 0.5$  assuming that the atmosphere and diffusion are uniform. This will be discussed further later in this section.

Figures 4.1 and 4.2 show two data sets for different polyimide thicknesses,  $\approx 1\mu m$ , and a thinner  $\approx 120nm$  film, both of which had undergone a hard cure and an oxygen plasma etch. This raw data was

<sup>1</sup>  $m_{water} = 18 \frac{g}{mol}$ ,  $k_b = 1.38 \times 10^{-20} \frac{m^2 g}{s^2 K}$ , and  $A = 2.47 \times 10^{-5} m^2$  for this experiment.

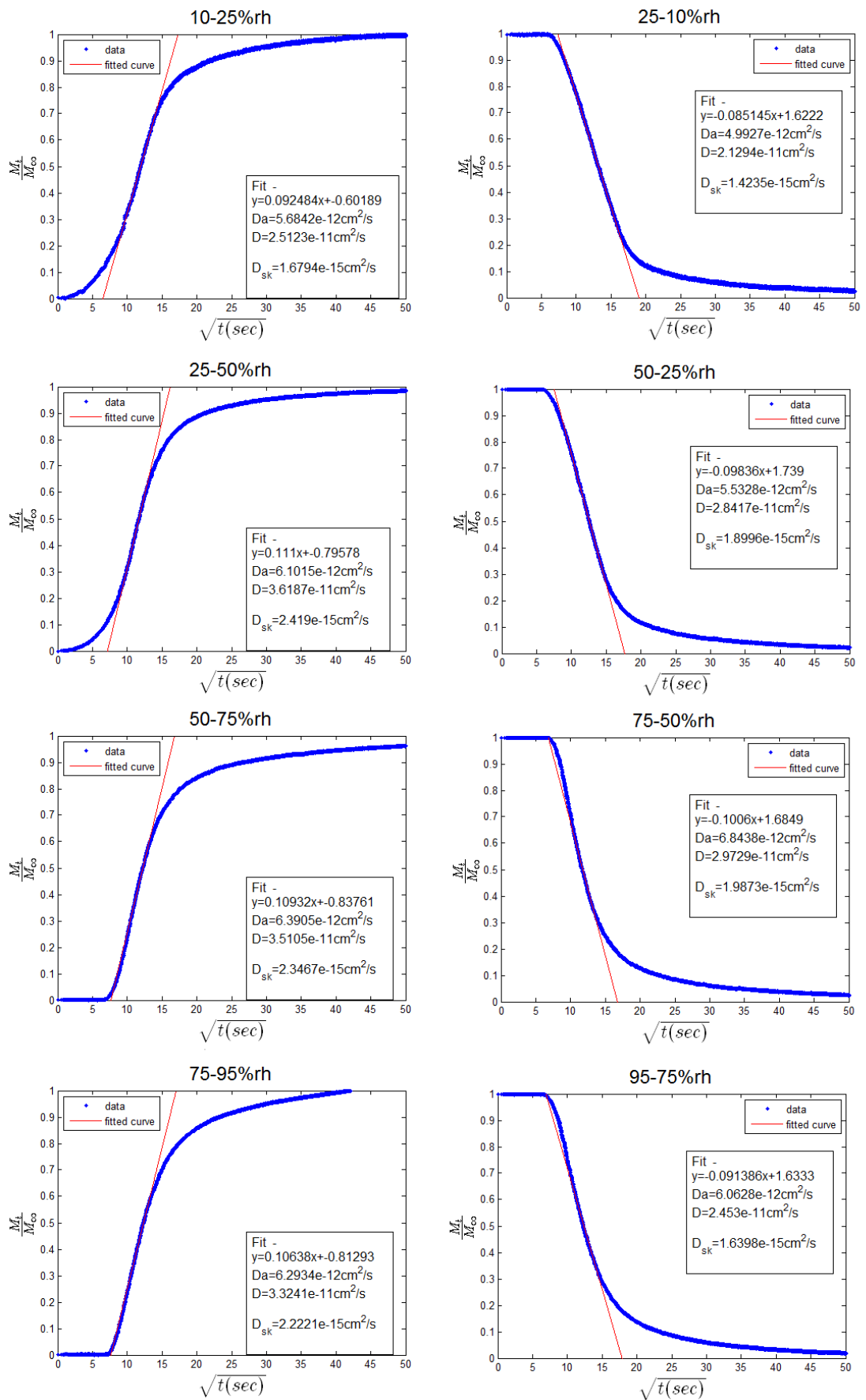


Figure 4.1: Measurements of the diffusion coefficient for a  $1\mu\text{m}$  thick film which has been hard cured and plasma etched.

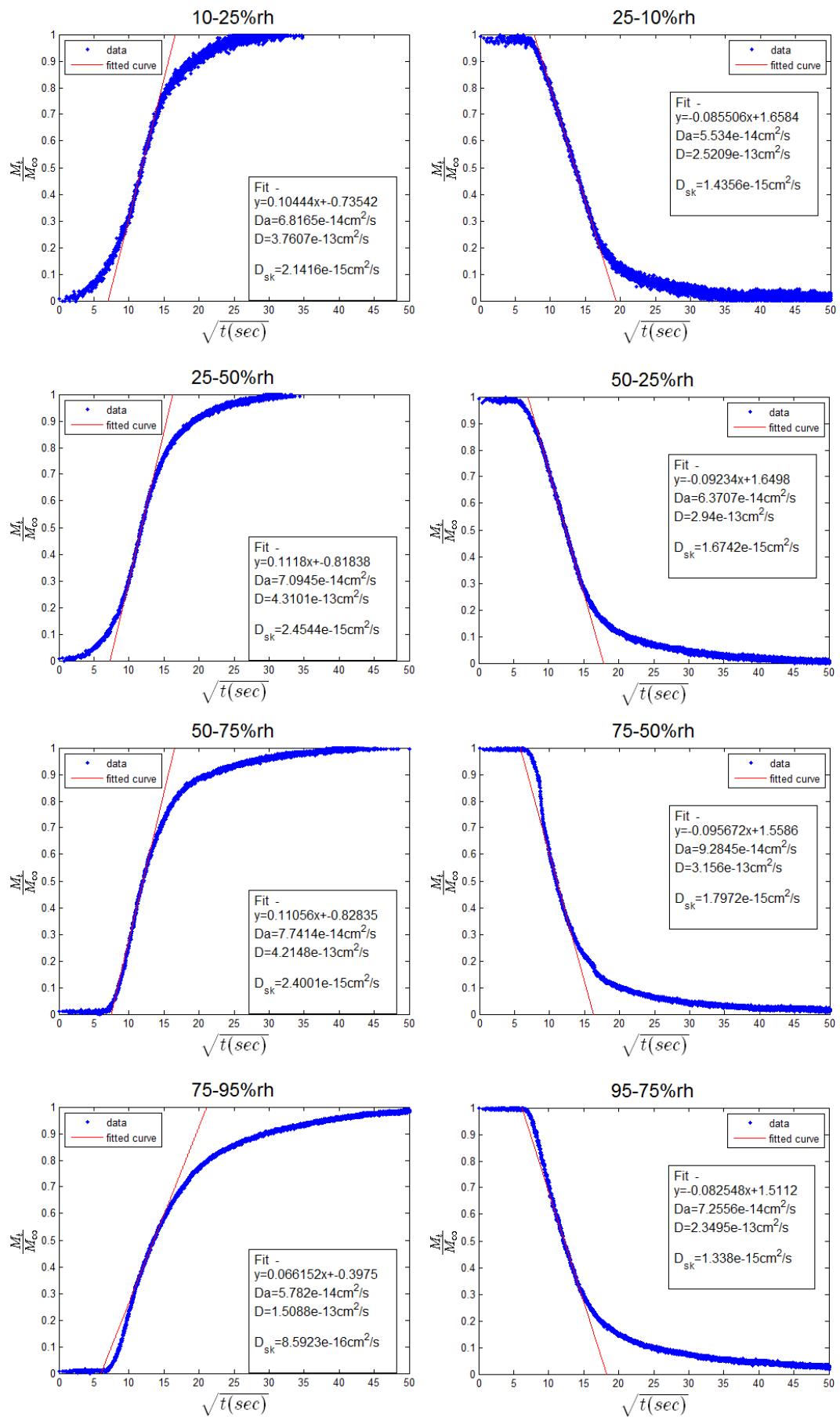


Figure 4.2: Measurements of the diffusion coefficient for a 120nm thick film which has been hard cured and plasma etched.

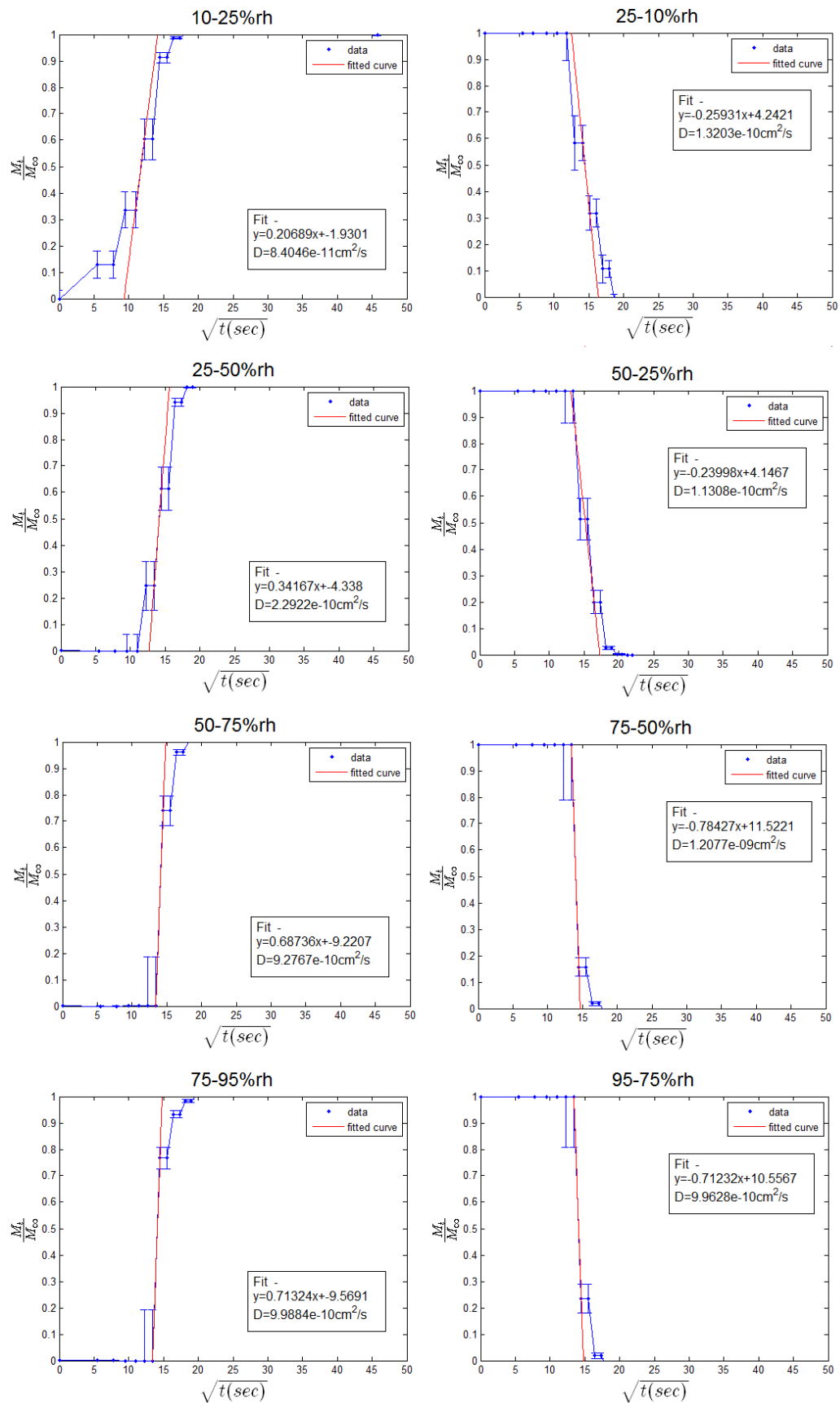


Figure 4.3: The maximum possible diffusion coefficients for a  $1\mu\text{m}$  thick film which absorbs all water which hits the surface based on thunder chamber partial pressure measurements. This is calculated from thunder chamber measurements as discussed in section 4.1.1.

collected during the QCM calibration cycles for each humidity set point and is presented here as a plot of  $\frac{M_t}{M_\infty}$  against  $\sqrt{t}$ . This allows the linear portion to be fitted to measure the diffusion coefficient  $M_\infty$ , for all set points except 75-95%rh, is approximated as the mass measurement after 150 minutes at same humidity set point. For the 75-95%rh set points the set point time was an hour (on other set points it is three hours), so  $M_\infty$  is assumed to be equal to the maximum mass of the film.  $D$  was measured by fitting a line to the graph from  $\frac{M_t}{M_\infty} = 0.3$  to  $\frac{M_t}{M_\infty} = 0.7$ , observed to be the linear portion of the graph.

$D_a$  was measured automatically, by finding the mass at  $\frac{M_t}{M_\infty} = 0.5$  and applying the method discussed. The resulting measurements of both  $D_a$  and  $D$  are displayed on the composite graph. The same analysis was performed on all the available data, some of which is available in the appendix (section A.4) for reference.

The relative humidity step changes 10-25%rh and 25-50%rh on Figures 4.1 and 4.2 appear to be sigmoidal, yet the behaviour for the remaining humidity step changes is well described as linear with  $\sqrt{t}$  (Fickian). Section 1.4 discussed the cause of sigmoidal diffusion, a slower initial uptake at the start of the diffusion process. Common potential causes are either, the changing characteristics of the polymer as the penetrant ingresses, or the timescale at which the ambient partial pressure exerted by the penetrant gas is similar to the response time of the sensor. The latter has been investigated using the work presented in the previous section, in which the mass of particles hitting an area the same size as the QCM electrodes under the same conditions was calculated, giving a mass against time plot. Inserting a thickness of  $1\mu m$ , and plotting this ideal data as  $\frac{M_t}{M_\infty}$  against  $\sqrt{t}$ , the fitting method used to find  $D$  is applied on this ideal data which was calculated to give the instantaneous response of an idealised sensor in the thunder chamber atmosphere. This is presented as the maximum possible diffusion coefficients,  $D_{Th}$ ; the fits are shown in Figure 4.3.

Comparing these fastest possible diffusion coefficients,  $D_{Th}$ , to the diffusion coefficients measured,  $D$ , reveals that  $D$  is much lower than the equivalent  $D_{Th}$  for the higher humidity steps of 50-75%rh, 75-95%rh, 95-75%rh, and 75-50%rh. However,  $D_{Th}$  for the 10-25%rh and 25-50%rh, shows a comparable response time, and the same sigmoidal characteristics as  $D$ , which is the same on all data sets. This is because the thunder chamber is slower to change its humidity at lower humidities.

Therefore, the sigmoidal diffusion on the 10-25%rh and 25-50%rh step changes (on Figures 4.1 and 4.2) are attributed to the ambient conditions. When considering the film alone the higher humidity steps better reflect the transport of water vapour in the polyimide. These steps are well described as Fickian.

Having established the diffusion is Fickian in nature, the best measurement method of the diffusion coefficient can now be discussed. There is a consistent discrepancy between  $D_a$  and  $D$ , which should

converge for single layer with Fickian diffusion characteristics.  $D_a$  shows a greater degree of consistency for a given data set when compared with  $D$ ; see Figures 4.1 and 4.2. However, in calculating  $D_a$ , a single diffusion coefficient from  $t = 0$  to  $t = 0.5$  with an atmosphere changing at a much faster rate than a diffusion timescale is assumed. This increases the likelihood of a systematic error in the measurements of  $D_a$  for two reasons; firstly,  $D_{Th}$  for some set points is same order of magnitude as both  $D_a$  and  $D$ .  $D$  neglects early diffusion effects as it is fitted from  $\frac{M_t}{M_\infty} = 0.35$  to  $\frac{M_t}{M_\infty} = 0.65$ , the linear portion of the diffusion, disregarding data that is affected by both the thunder chamber at early times, and the neglected higher terms of Equation 1.11 at longer times. Additionally the measurement of  $M_\infty$  is not measured but it is assumed that after 150min,  $\frac{M_t}{M_\infty} \simeq 1$ . Therefore, despite a greater variability of  $D$  when compared to  $D_a$  on a given data set,  $D$  can be considered a better measure of the true diffusion coefficient in this system.

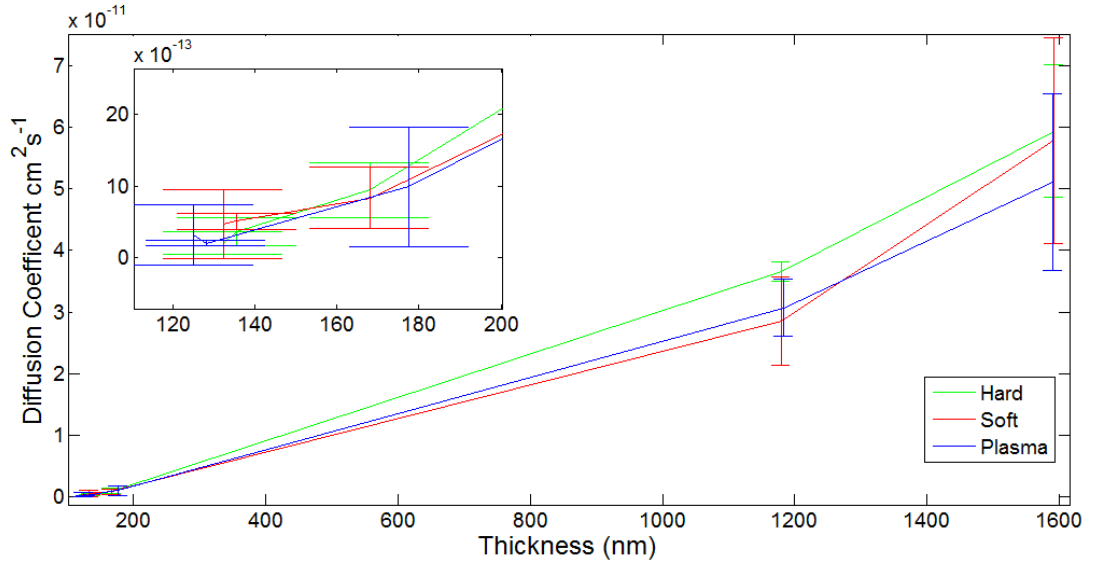


Figure 4.4: The diffusion coefficient as a function of thickness. The diffusion coefficient appears to vary in a non linear manner as a function of thickness which is surprising as it should only be a function of the material and not the material thickness.

Figure 4.4 shows the resulting averages of  $D$ , which varies as a function of the material thickness. Han et al. measured water diffusion in a range of polyimide membranes (thickness=10 – 15 $\mu m$ ) at room temperature. The diffusion coefficients found were in the range  $1.7 \times 10^{-10} - 10.5 \times 10^{-10} \frac{cm^2}{s}$  in one study[120] and in the range  $1 \times 10^{-9} - 3 \times 10^{-9} \frac{cm^2}{s}$  in another study[121]; all of which were Fickian. Seo et al. concluded that diffusion coefficients were “*quite different and strongly dependent upon the chemical structure of internal linkage and the morphological structure in films*”[121]. Elsewhere, a study of dense polyimide membranes (thickness=32 – 38 $\mu m$ ) has found diffusion coefficients in the

range  $1.5 \times 10^{-10} - 8.65 \times 10^{-10} \frac{cm^2}{s}$ [122]. Both of these studies used significantly thicker films than have been investigated here, and found a higher diffusion coefficient.

There is a clear upward trend in the diffusion coefficients with respect to thickness observed in Figure 4.4. Each of the three treatments, soft cured, hard cured, and plasma etched, exhibit a similar thickness dependent diffusion coefficient. Hwang et al. attributed similar behaviour to two diffusion coefficients in the given thin film, one arising from a denser skin layer, and another from the bulk[55]. Such an idea is corroborated by considering the skin layers observed which will be discussed in section 5.3. However, it would be expected that as  $l$ , the graph would level off as the influence of the fixed thickness skin layer diminished, which may explain why the diffusion coefficients measured here are lower than those reported in literature. This underscores the challenges in applying information from bulk film studies to thin films, in which surface effects play a greater role.

Furthermore, it is also observed that the timescale of the diffusion is the same irrespective of the film thickness. This is shown by imagining that all the samples consist of only a uniform layer of a thickness  $\approx 10nm$ . This is the equivalent of saying that the surface has much greater diffusion coefficient than the bulk, and this surface dominates the timescales of diffusion. Figures 4.1 and 4.2 display  $D_{sk}$  for each sub plot, this is a hypothetical diffusion coefficient (using the fitting method); the same data should the thickness of all the films be only  $10nm$ .  $D_{sk}$  is very consistent on all films and humidities; it returns relatively low diffusion coefficient of  $10^{-15}cm^2s^{-1}$ .

Clearly, the rate limiting factor is uniform on films of different thicknesses. There are two possible candidates for the limiting factor; either, a surface effect such as a skin layer, or some form of chemical bonding. The mass uptake is well described as Fickian, and yet has a uniform timescale with different thickness, this implies that diffusion through a layer common to all samples is the rate limiting factor of mass transport.

Interestingly,  $D_{sk}$  for water vapour ingress at a set point is generally slightly higher than for egress, indicating an asymmetric behaviour in the rate limiting factor making it harder for water to leave the film than to enter into it. The two afore mentioned candidates for the rate limiting factor are explored in section 4.2 (chemical bonding) and section 5.4(surface effects).

This section has shown the transport of water vapour in this polyimide as being well described as Fickian, proportional to  $\sqrt{t}$ , with any deviations well explained by the behaviour of the thunder chamber. Additionally, the rate of diffusion has been shown to be consistent across film thicknesses, indicating that diffusion in the bulk of the film is not the rate limiting factor. An asymmetric polyimide skin layer, or chemical bonding, are proposed as two potential causes for this effect. The next section explores the possible chemical bonding within these polymer thin films.

## 4.2 Applying Models of Mass Transport

Water diffusion in polyimides has been shown to be a ill understood process[121, 123, 65]. The total amount of water absorbed is a function of the specific chemistry of the polyimide chain (as demonstrated in sections A.6). The chemical interaction between water molecules and the sensing film is key. The outstanding issues for water transport in polyimide are well summarised by Mensitieri et al.[65] as, (i) the type of molecular interactions, and (ii) the number of polymer–penetrant interactions and/or penetrant self-interactions.

Few models yet describe the of sorption behaviour for systems in which hydrogen bonding is an important factor[65, 62]. This has been shown to be the case for imide groups for both polymer–penetrant and penetrant-penetrant interactions while performing spectroscopic studies and otherwise[65]. A degree of success has been obtained while using the simpler approach of BET (Brunauer, Emmett, and Teller) multilayer adsorption theory which accounts for distinct energetics for different penetrant layers[65], the Flory-Huggins and Vrentas Models[124, 125].

In this section the experimental results showing chemical bonding in this polymer are presented. These results are then compared to a simple model.

### 4.2.1 Chemical interactions between water vapour and polyimide

Measurements of the diffusion coefficients, which were presented in the previous section, show that the water transport timescales are not limited by diffusion through the bulk of film. The hysteresis occurs on a timescale of hours and so a study of bulk transport alone does not explain key behaviours of this system. Here an experimental result to show that chemical bonding is a factor in this system is presented. A model to account for such effects is then discussed.

#### **Attenuated Total Reflectance Spectroscopy to Probe Polyimide-Water Interactions**

Early results in this study had shown no shift in the Raman spectrum of of the polyimide peaks when a dry polyimide film was compared the same film in a high humidity atmosphere (results are shown in section A.7). However, using a more sensitive Attenuated Total Reflectance Spectroscopy, ATR, showed evidence of chemical bonding.

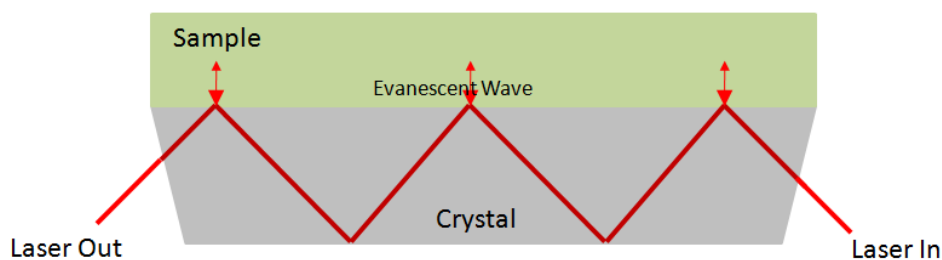


Figure 4.5: Attenuated total reflectance uses the evanescent wave of light to probe the sample.

Attenuated Total Reflectance Spectroscopy, ATR, uses the evanescent wave which permeates an interface at which total internal reflection occurs, at an interface as shown in Figure 4.5. A beam of infrared light is passed through the ATR crystal such that it totally internally reflects off the surface in contact with the sample. An evanescent wave penetrates into the sample probing the film properties. The penetration depth is a function of the wavelength of light, the angle of incidence, and the properties of the sample, but it's typically of the order  $1\mu\text{m}$  in this type of system.

ATR Fourier Transform Infrared, ATR-FTIR, has been used here as it allows the in-situ measurement of the spectra and has been used previously to investigate water absorption in polyimides by Alsten et al.[126]. That study of various polyimide chemistries concluded that *chain stiffness, crystallinity and density*; all of which are influenced by the curing regime, were key determinates in the diffusivity of a given polyimide.

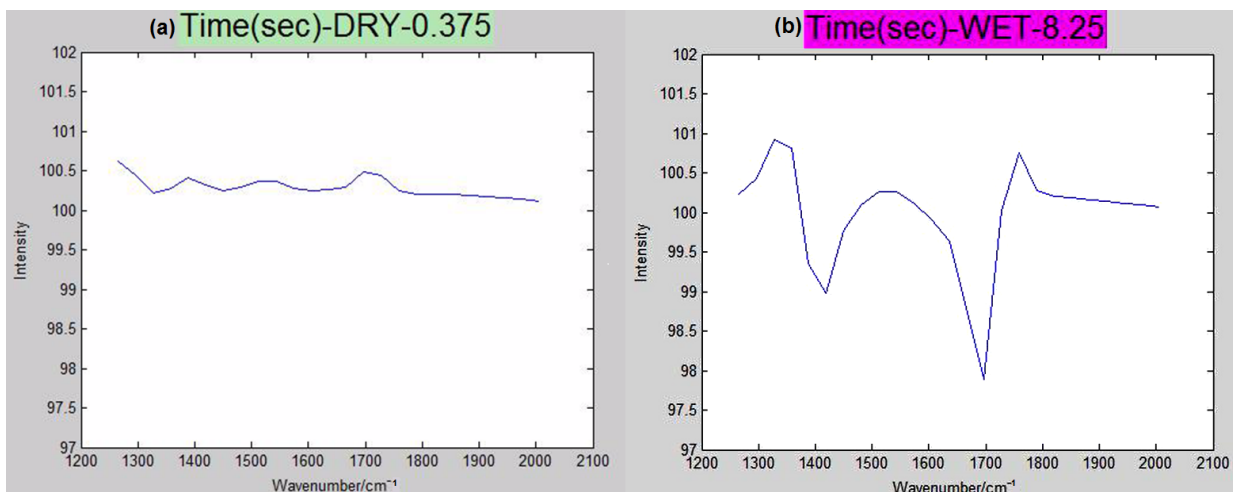


Figure 4.6: The ATR-FTIR measured spectrum was calibrated to read 100 units when the sample was in a dry state such that the peaks cannot be observed; as shown in (a). (b) shows the film in a humid atmosphere in which, a peak followed by a trough are observed at  $\lambda \approx 1380\text{cm}^{-1}$ , indicating a shift to a lower wavenumber for the C-N bond, and a trough followed by a peak at  $\lambda \approx 1750\text{cm}^{-1}$ , indicating a peak shifted to a higher wavenumber for the C=O bond[127]. Both bond are both Raman and Infrared active and are shown on Figure A.14, the Raman spectra of this polyimide.

Here, soft cured polyimide was prepared on top of a silicon ATR crystal, and spectra were obtained over a 5/5 second dry/wet cycle to confirm any chemical effects. Figure 4.6 shows the difference between the spectra in both states, with the dry spectra normalised and the wet spectra showing a marked difference. A water peak is expected to be observed in this range at  $\lambda \approx 1622\text{cm}^{-1}$ , the  $\delta(\text{HOH})$  vibration for H-bonding, but this is noted to be weak, and most water peaks are found at a higher wave number[38]. The rise and dip shown in the wet spectra indicate shifted peaks at  $\lambda \approx 1380\text{cm}^{-1}$  and  $\lambda \approx 1750\text{cm}^{-1}$  corresponding to the polyimide in IR.

Similar results have been observed Mensitieri et al.[38, 65] in which an investigation of a polyimide using IR in the wave number range  $1800 - 1680\text{cm}^{-1}$  allowed interaction sites on the polymer backbone to be identified. The shift toward lower wave numbers in the presence of absorbed water is attributed to the in-phase and out-of-phase carbonyl stretching modes. Furthermore, the shift has been observed to be linear with the amount of water absorbed in equilibrium, and it has been demonstrated that the effect is reversible, although the energetics are not discussed. Such shifts are attributed to the imide carbonyl group acting as proton acceptors in a polar-polar interaction with the electronegative water molecules. The results presented here are entirely consistent with the chemical bonding observed by Mensitieri et al. showing the same effect with this form of polyimide, although it is unknown if this shift is linear with water uptake.

This technique shows great promise, but the equipment to perform ATR-FTIR is available on a limited basis. Ideally, this technique can be used in future experiments within the thunder chamber to give the information on the chemical interaction involved in hysteresis phenomenon.

### **Modelling polyimide-water interactions and bond energetics**

The transport of water in the polymer has thus far been considered a diffusion phenomenon with all the material chemistry contained within the diffusion coefficient.

Here, the interaction of absorbed water molecules with the polyimide is considered with the rate limiting factor, assumed to be the rate at which water molecules find a site available in the polymer. The energy required to overcome any energy barrier of entry/exit for the water particles from this site is considered explicitly. Firstly, the Langmuir adsorption model is given in Equation 4.4.

$$\frac{d\theta}{dt} = k_a P N (1 - \theta) - k_d N \theta \quad (4.4)$$

Where;  $k_a$  is the rate constant for bonding, and  $k_d$  is the rate constant for breaking the bond;  $P$  is the

pressure,  $N$  is the number of sites, and  $\theta$  is the fraction of bonding sites occupied. At thermodynamic equilibrium  $\frac{d\theta}{dt} = 0$  and therefore,  $\theta = \frac{k_p}{1+k_p}$  where  $k = \frac{k_a}{k_d}$  gives the Langmuir isotherm. In this investigation, the scattering length density profiles, which will be presented chapter 5, indicate that this is not a surface effect, but rather an absorption situation. However, an analogy with the Langmuir isotherm is developed, allowing both the energetics, and the capacity to bond in this system to be probed. In Equation 4.5 it is assumed that transport of water particles is not the limiting factor when accessing bonding sites within the polymer.

$$\frac{dM}{dt} = k_a(AZ_w)M_{Full}(1 - \theta) - k_d(AZ_{Out})M_{Full}(\theta) \quad (4.5)$$

The mass flux is  $\frac{dM}{dt}$ , and the fraction of bonding sites available is  $M_{Full}(1 - \theta)$ , with  $M_{Full}$  being the maximum amount of water mass the polymer can hold. At thermodynamic equilibrium  $\frac{dM}{dt} = 0$ , and recalling that  $\theta = \frac{SitesOccupied}{SitesAvailable} = \frac{M_o}{M_{full}}$  Equation 4.5, gives  $\frac{k_a}{k_d} = \frac{M_o}{M_{full} - M_o}$ .

ATR results show evidence of bonding between the polymer and the water vapour molecules. Processes represented by  $k_a$  and  $k_d$  are assumed to be an Arrhenius like, being well described by  $k_a = S e^{\frac{E_A}{RT}}$  and  $k_d = D e^{\frac{E_D}{RT}}$  where;  $S$  and  $D$  are constants, and  $E_A$  and  $E_D$  are an activation energy per mole for the process required. The sticking probability,  $S$ , the probability that molecules are chemically bonded to the material, is unknown but may be inferred by comparing the number of molecules that hit the surface to the number in the film, both of which are known. By comparing the two sets of data in Figure 4.7(a),  $S$  is clearly of the order 0.01, as the measured mass changes are a fraction of the mass of particles hitting the surface.

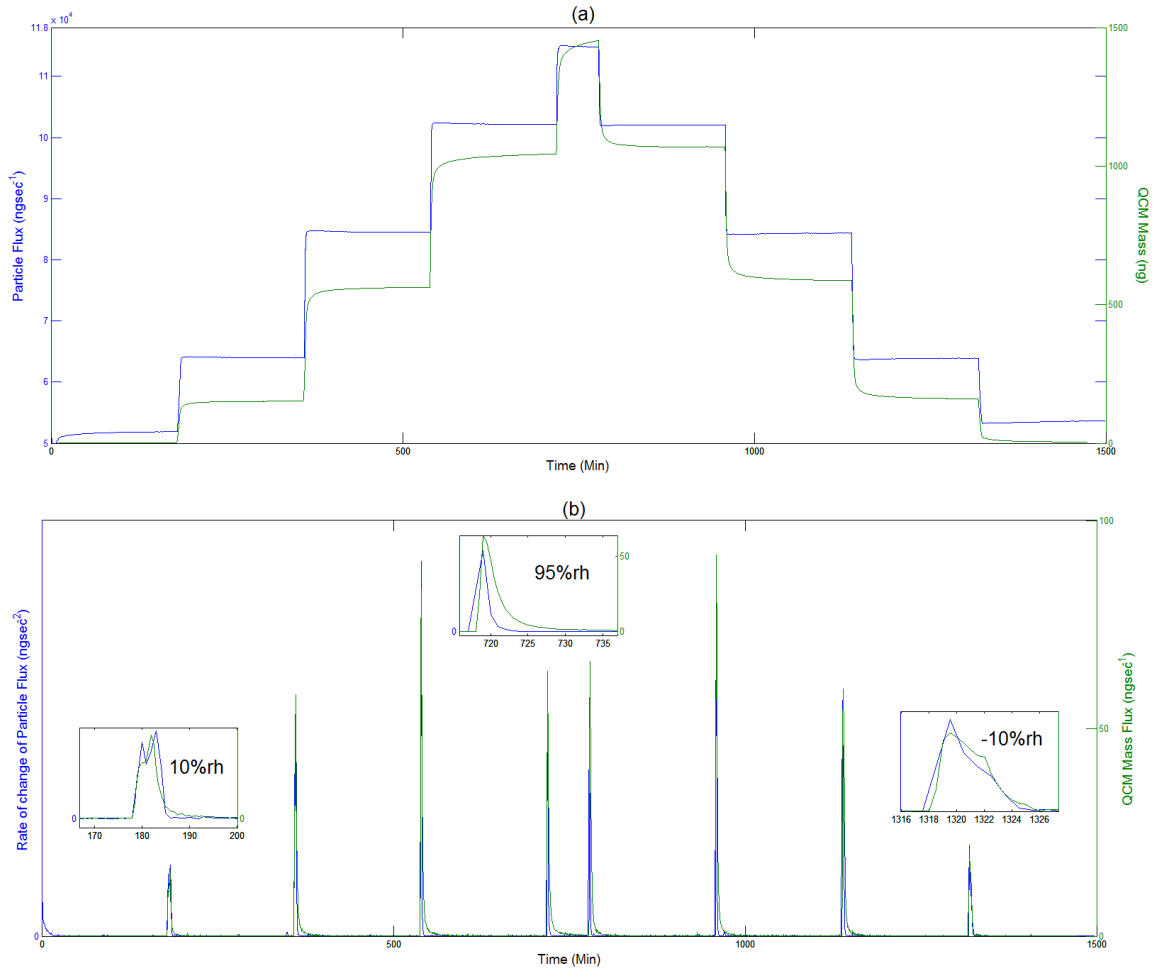


Figure 4.7: (a) The mass change for the thickest film measured is shown in Green, with the number of particles calculated to be hitting the surface (from Equation 4.3) shown in blue. (b) The absolute value of the numerical derivative of the above graph, showing the mass flux of the QCM,  $\frac{dM}{dt}$ , in green and  $\frac{dZ_w}{dt}$  in blue.

The model presented in Equation 4.5 assumes the only interaction taking place in this system is that of the individual water molecules bonding sites on the polymer backbone. This neglects water-water interactions which may result in clusters or multilayers of water. The ATR results indicate bonding sites at the C-N bond and the C=O bond of the polymer chains, as shown in Figure 4.6.

Figure 4.7(b) also shows that the measured mass flux,  $\frac{dM}{dt}$ , and the calculated number of particles hitting the surface, are well correlated. However at higher humidities, 75-95%rh, the mass influx response time is delayed due to a higher number of occupied sites, i.e. the polymer approaches saturation.

Furthermore, at low humidities, as  $\theta \rightarrow 0$  and at 0%rh, there is a reduced probability of penetrant-penetrant interaction. Additionally, as  $\theta \rightarrow 0$  Equation 4.5 reduces to  $\frac{dM}{dt} = Se^{\frac{E_A}{RT}}(AZ_w)M_{Full}$ .

Assuming an Arrhenius type bonding process, the type of bonding taking place can be inferred from the energetics as, for example, hydrogen bonding tends to have energies of the order of 5-30kJ/mol. A script has been developed to fit the decay of each peak to an exponential function to access the time constant, and hence the estimated activation energy. The output for the 10-25%rh and 25-10%rh steps changes of the 1500nm film is shown in Figure 4.8. The activation energy for ingress implied is of the order 1kJ/mol, indicating some weak van der Waals bonding between the polymer and the water molecules.

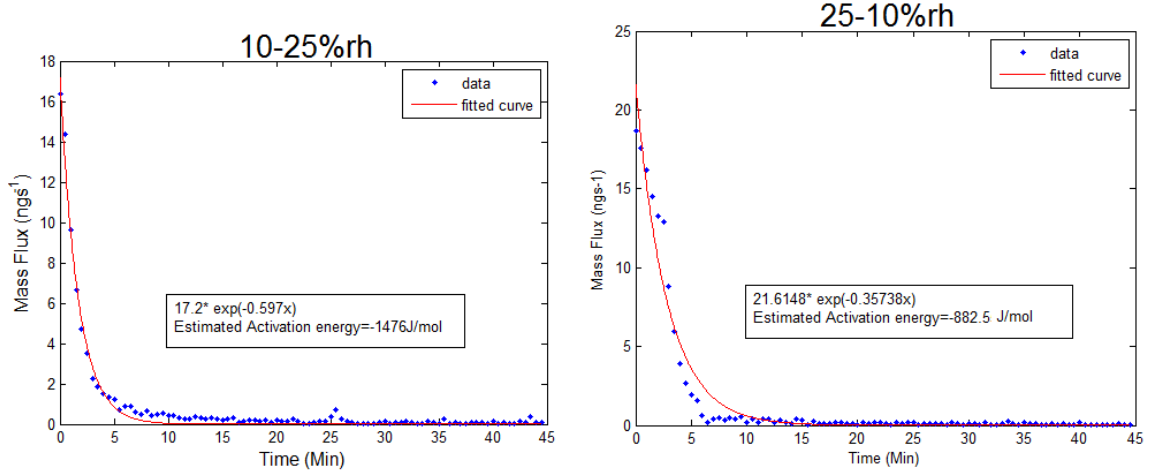


Figure 4.8: An exponential fit for the mass flux rate for the first two set points allowing an estimation of the activation energy.

Equation 4.6 has been compared to data. To do so the activation energies,  $E_A = 1000 J/mol$  (based on the fits shown in Figure 4.8) were fed into Equation 4.6.  $Z_{Out}$ , the number of water molecules leaving the film, was calculated from the absolute humidity in the film (which was calculated by dividing the QCM measured mass by the volume of the film). The remaining factors of Equation 4.6,  $S$ ,  $D$ ,  $\theta$  and  $M_{Full}$  are fitted to real data, with the range of allowed  $\theta$  being between 0 and 1.

$$\frac{dM}{dt} = AM_{Full} (k_a(Z_w)(1 - \theta) - k_d(Z_{Out}) * \theta) \quad (4.6)$$

A manual preliminary fit for data (1 $\mu$ msoft cured crystal) is shown in Figure 4.9. Figure 4.9 is a predicted mass flux from Equation 4.6 compared to mass flux data of the thin film in time. The fitted parameters were varied manually as automatic fitting algorithms tended to take the fit towards a flat line.

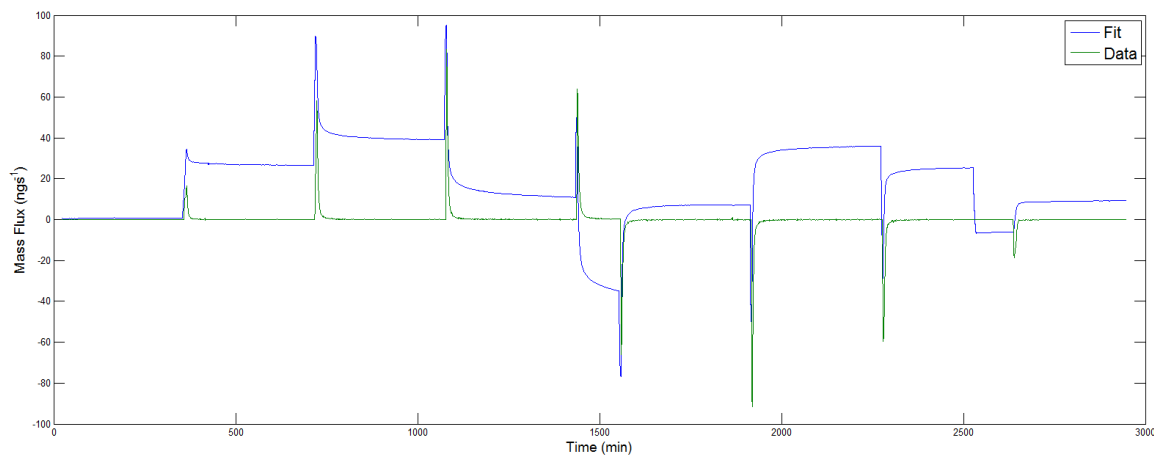


Figure 4.9: A fit using the preliminary model adapted from Langmuir adsorption model.

The model presented clearly lacks a further term, which is a function of the partial pressure of the gas, probably a diffusion term. This is a first attempt to model the behaviour of the water-polyimide system and it requires refinement by considering vapour clustering within the material and the diffusion of particles.

### 4.3 Transport Length Scales

Many studies of water-polyimide systems have noted the importance of density and morphology of the specific polyimide in understanding the water transport[121, 120, 126].

The term polyimide describes a class of materials with imide monomers, which are often customised for a specific purpose (discussed in section 1.3). Customisation may involve producing polyimide foamed membranes[128] with a range of pore sizes and micro fissures, enabling different modes of transport for a diffusant gas[30, 37, 129]. For this form of polyimide, both the time resolved neutron scattering profiles (Section 5.4), and QCM results (Section 3.4), indicate that any variations in transport mode from a variation of micro fissures were averaged out over the size of sample. Consequently, smooth diffusion curves, irrespective of any micro fissures (see Figure 3.12), are obtained. However, this information alone is not sufficient to discern between length scales of the diffusion i.e. from the molecular ( $\sim 10^{-10}$ m) to tens of nanometres ( $\sim 10^{-8}$ m) scale, are possible. Two possible extremes of mass transport envisaged are represented in Figure 4.10, (a) showing molecular diffusion, and (b) showing transport through fissures.

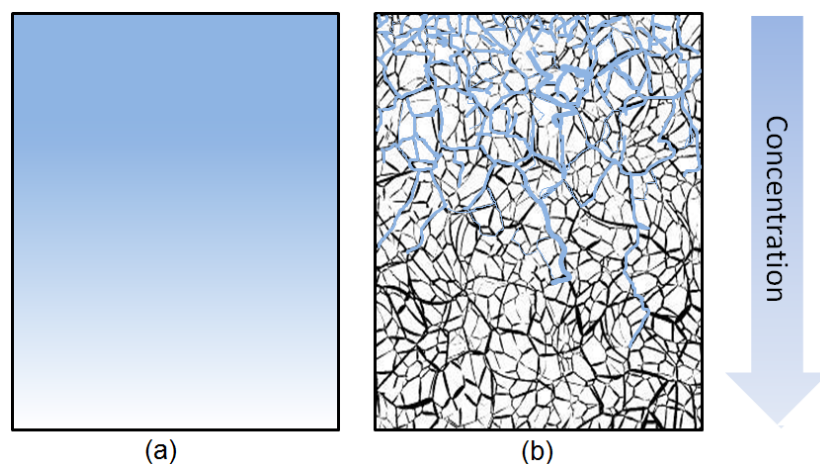


Figure 4.10: Two schemes of mass transport may give the same concentration profile. (a) Molecular diffusion scale throughout the polymer. (b) Diffusion via fissures and pore network.

In this section the structure of any free volume in this polyimide is investigated using permoporometry and TEM to establish the possible length scale of diffusion. The use of electron diffraction as a probe to gain information regarding the common spatial frequencies in the polymer is also explored.

### 4.3.1 Permporometry

Distinguishing between the two modes of mass transport shown in Figure 4.10 is possible by measuring the pore size distribution using permoporometry. The permoporometry measurements were carried out at The Fraunhofer Institute for Ceramic Technologies and Systems.

In this case, the polymer was spun onto ordered mesoporous ceramics, SiOC and SiCN, and soft cured. Here, non-condensable gases with different kinetic diameters, the two smallest being  $He$  (0.26 nm [130]) and  $H_2$  (0.29 nm [130]), have been passed over the sample and the permeation rate measured. The kinetic diameter of a water molecule is 0.265 nm [131], comparable to that of the  $He$  molecules used. In addition, the inert nature of  $He$  makes any adsorption or chemical reaction between the Polyimide and the  $He$  gas negligible. However, comparison with  $H_2$  gas is complicated by the possibility of chemical interaction. Permporometry and the use of the various gases and vapours to measure other systems are well discussed elsewhere [132, 133, 134].

Of the gases used, only Helium was able to permeate the polyimide. The next largest molecule  $H_2$  had no measurable permeation rate. Helium permeated at a rate of  $7 \times 10^{-3} \frac{ssc}{s}$ , cubic centimetres per second at 1 atm of pressure. Unfortunately, Permporometry cannot provide a pore size distribution or further elucidate on any of the transport mechanisms on such a small scale as it is conventionally used to measure micro porous structures [135].

Water molecules are similar in size to Helium molecules, consequently it is clear that this polyimide is well suited to selectively absorbing water molecules from the atmosphere, making it an ideal sensing element for robust humidity sensors.

### 4.3.2 TEM: Spatial Frequencies in amorphous materials

Permporometry may hint at some structure in the polyimide on a sub nanometer length scale. Characterising structure on such length scales is problematic as techniques commonly used to investigate pore sizes, such as positron annihilation spectroscopy[136, 137], SEM[138], and AFM, are not able to reliably map structures on length scales less than 1nm[139, 140]. Therefore, structure in this polyimide cannot be probed further using typical membrane characterisation techniques which are designed to probe microporous materials. Density in the polyimide may be correlated with spatial distribution of mass within the polymer, which in turn impacts on transport properties.

TEM offers high resolution and therefore polyimide samples have been probed for information about any common spatial frequencies or crystallinity. The use of the TEM with soft matter samples can be problematic as polyimide samples are prone to charging<sup>2</sup>. However, no beam damage<sup>3</sup>, which is common with polymers, was observed.

The lack of intrinsic (mass/thickness) contrast in the polymer means the dominant contrast arises from differences in the phase of the electron wave; phase contrast. Phase contrast is very sensitive to many factors, such as small changes in the thickness and orientation of the sample[89, 90], as it relates to the inner potential difference in samples, which was discussed in section 2.4[142].

To gain structural information about voids, other studies have introduced nano particles with a high atomic number into a polymer matrix to generate mass contrast, which is known as staining [140, 138]. Staining can sometimes lead to nano scale artefacts[143, 144]. In some studies the absorption of a solute consisting of metal salts into polyimide has been used to control the size and growth of nano particles that form within pores, and can be studied due to the high contrast generated in the TEM[145]. Very early on in this study, staining was attempted using two solutions of iron chloride and gold chloride in water. However, neither of the solutions permeated the surface of the polyimide. This section outlines the further steps taken to characterise the spatial frequencies in polyimide using TEM.

---

<sup>2</sup>Polyimide on a QCM crystal would charge to act like an electron mirror, see Figure A.4 in the appendix.

<sup>3</sup>Which generally degrades Polymer crystallinity [89, 141, 138]

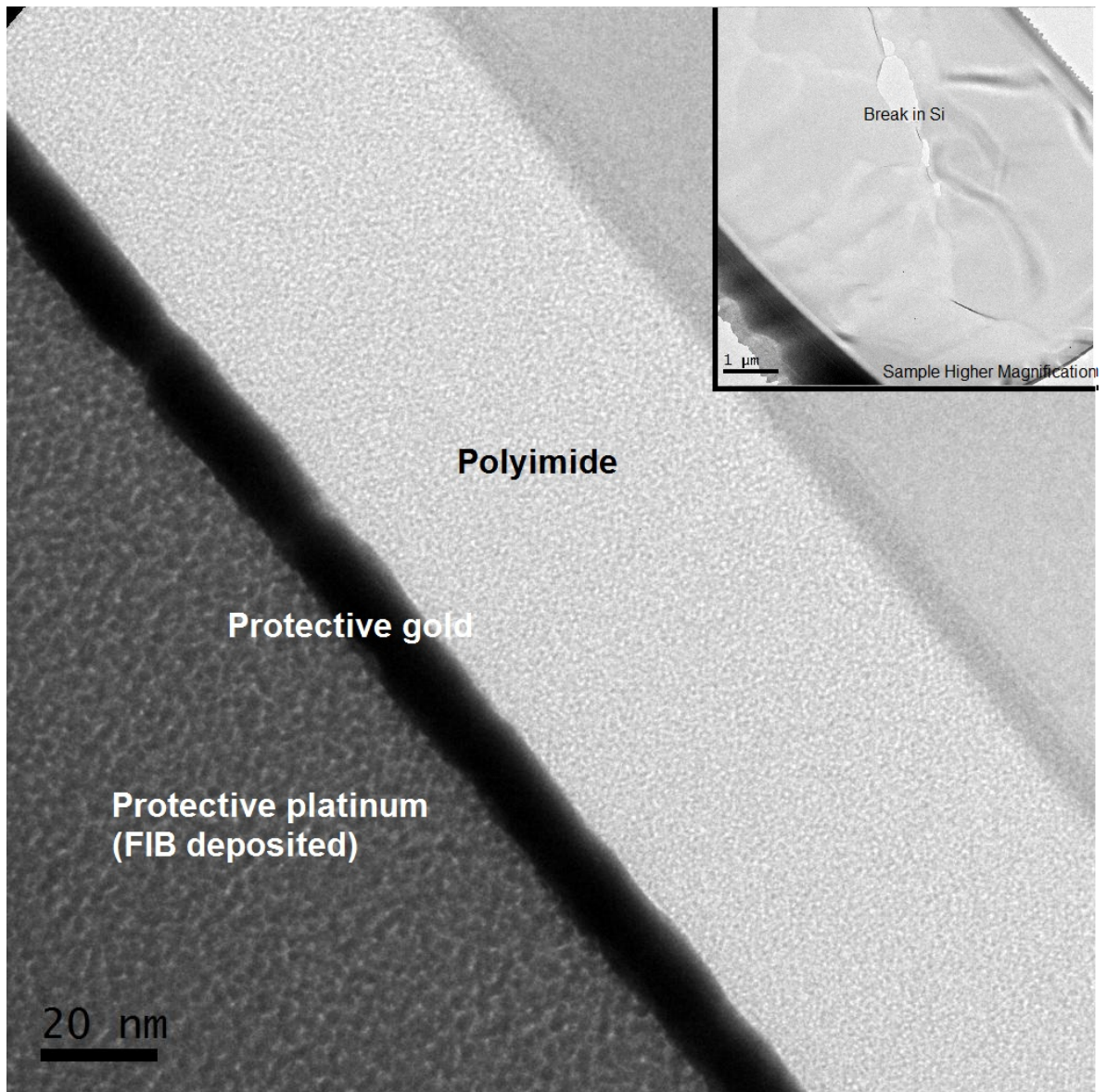
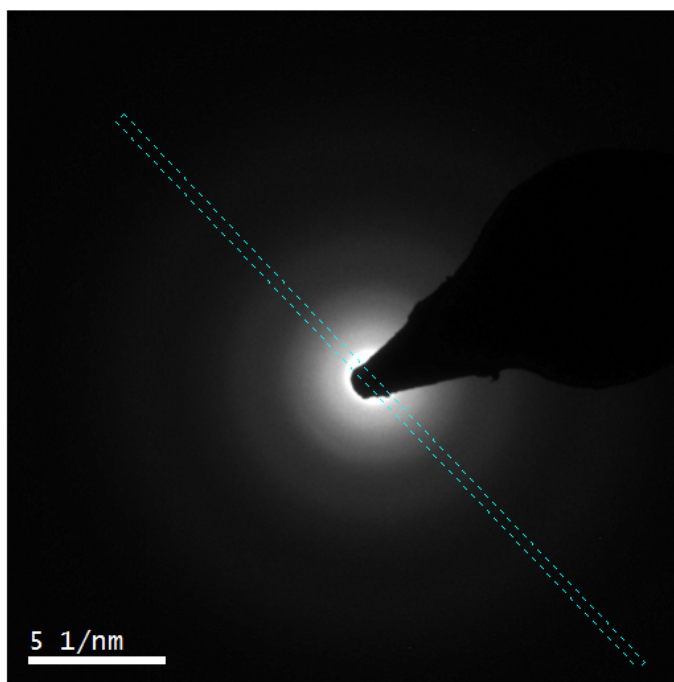


Figure 4.11: Polyimide on a silicon substrate with a with a gold protective layer. This is a bright field image acquired on a aberration corrected microscope with 80KeV beam (JEOL ARM200cF) by Dr Ian Maclaren. The sample was thinned using the FIB technique.

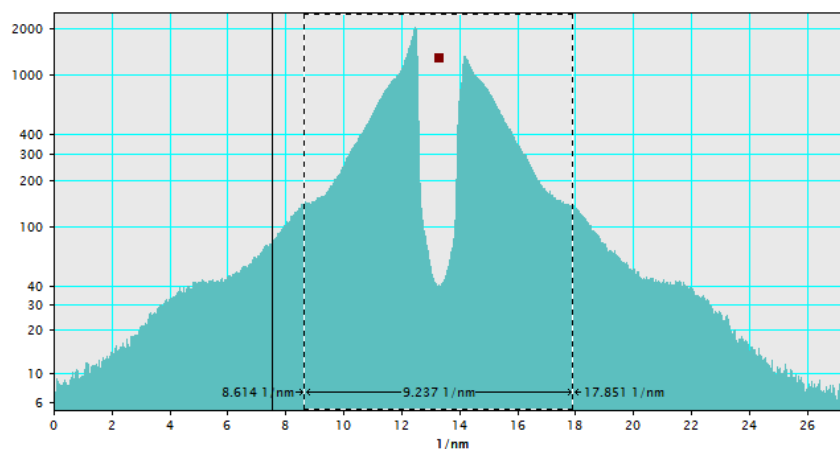
Phase contrast which is characteristic of this polyimide can be observed in Figure 4.11, a bright field image. The sample here was spun onto a silicon substrate and hard cured. A gold layer was then evaporated on top to prevent charging on the polyimide sample. Evaporation was chosen, as opposed to sputtering deposition, to minimise metal implantation that had occurred on previous images (Figure A.16, for example). The sample was prepared using a standard FIB procedure, and thinned with the ion beam as much as possible, until the supporting silicon began to crack. The image shows some phase contrast from features on a nanometer length scale. However, only a hard cured sample was

imaged and so no comparison to plasma etched or soft cured sample can be drawn.

The electron diffraction pattern for a given material maps various periodicities in the electrostatic potential distribution, which results in an ordered pattern for a crystal. For an amorphous material, randomly orientated but similarly spaced voids give rise to a circular halo around the un-scattered beam. Figure 4.12(b) shows a direct analysis of the diffraction pattern of soft cured polyimide. The halo rings shows a  $\frac{9.2}{2} 1/nm$  gap, corresponding to a spatial frequency of  $\approx 0.2nm$ . This agrees well with the permporometry measurements which indicated the maximum size of a diffusant in this polyimide is around  $0.27nm$ . This is not exhaustively quantitative but may be indicative of some structure on similar length scales. Larger periodicities in the electrostatic potential distribution in the sample result in less scattering and so are eclipsed by the brightness of the centre beam.



(a)



(b)

Figure 4.12: (a) A diffraction pattern of the polyimide (at a high magnification). (b) A line profile relating to (a). Any longer spatial frequencies are eclipsed by the central spot.

In the diffraction patterns acquired information about larger spatial frequencies are eclipsed by the unscattered beam. The Fourier transform of a real space image reveals the spatial frequencies in the that image. To visualise any systematic voids in the polyimide the beam can be deliberately defocused which enhances the phase contrast in polymer samples[141, 142, 144]. Under focusing results in additional interference of the scattered and unscattered waves to enhance the phase contrast visible in the BF image, although this does result in the degradation of the resolution[146, 92] and so

the use of defocusing observe such voids is briefly investigated here.

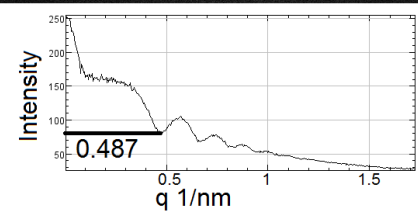
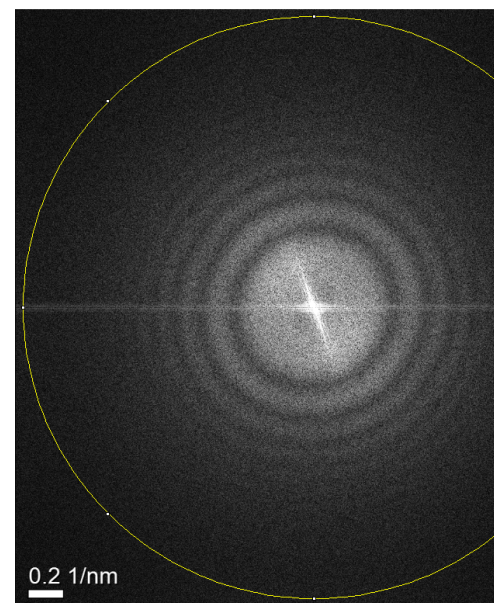
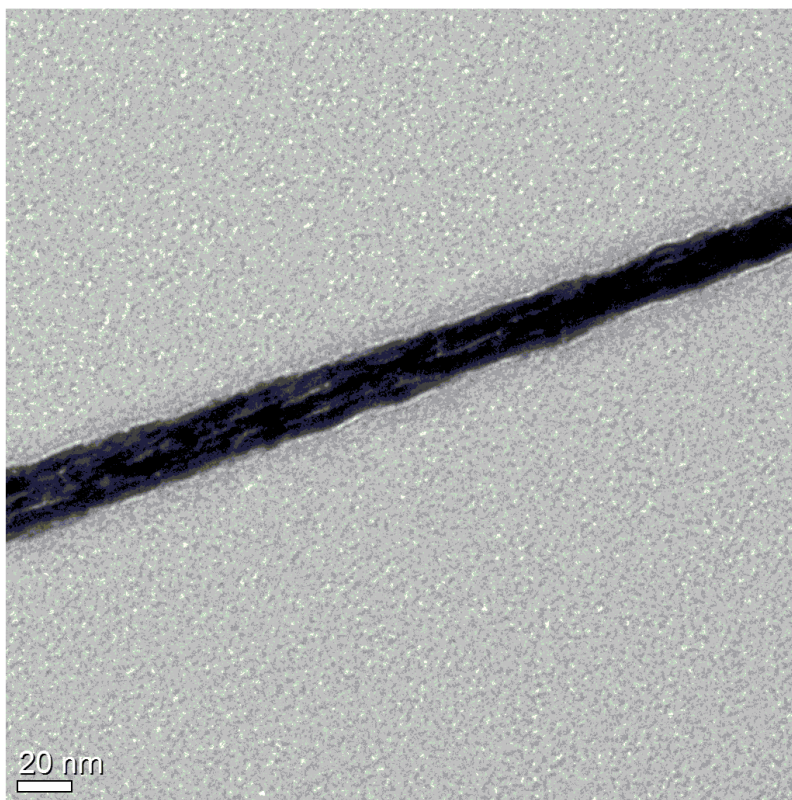
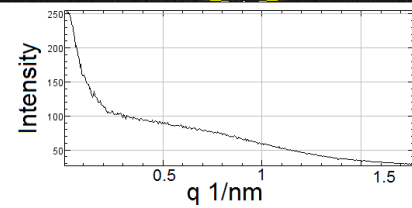
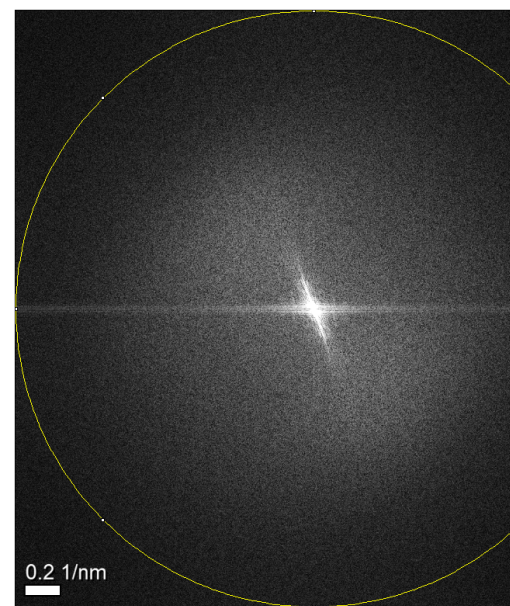
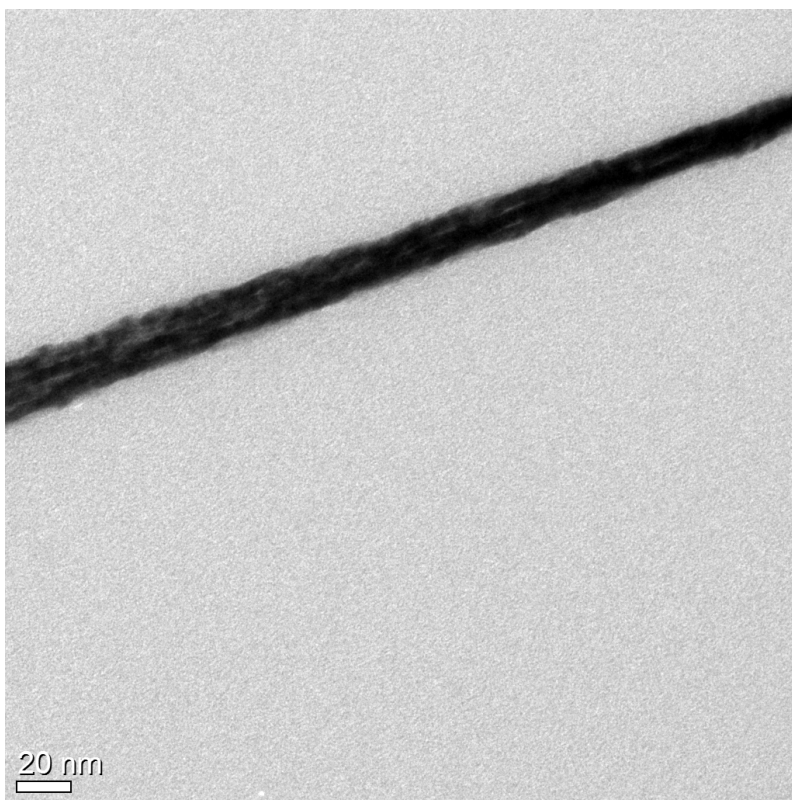


Figure 4.13: A focus series of the same part of the sample, which is polyimide, and the corresponding Fourier transforms, performed in digital micrograph. The samples are two polyimide layers separated by a platinum electrode.

Figure 4.13 shows two bright field images of a polyimide-platinum-polyimide sample, which has been cross sectioned using FIB techniques at both focus and underfocus. The obvious difference between the images is the increased grain like appearance as the image is moved out of focus showing Fresnel like diffraction on the edge of contrast generating features. Figure 4.13 also shows the Fourier transform of the corresponding images. As the images move further away from focus condition the Fourier transform displays the expected dark rings. The location of the first zeros in the angular sum of Fourier transform corresponds to real space distances of approximately 1.4nm and 2nm giving an estimate of the image resolution.

The defocus values shown in Figure 4.13 are calculated from setting a one term approximation of Equation 2.8<sup>4</sup>, equal to  $\pi$ , for destructive interference observed at the first dark ring. This yields the approximation  $\Delta f = \frac{1}{\lambda q^2}$ , where  $\lambda$  on the T20 microscope with a 200KeV beam was calculated as 0.00251nm, and  $q$  was measured from the Fourier transform as shown in Figure 4.13. This neglects the second term in Equation 2.8, which accounts for spherical aberration term as it contains a  $\lambda^3$  and  $q^4$  term, making it relatively small. At such resolutions no structure was observed and so this indicates that there is no nanometer length scale structure in the polymer, and the length scales of the variations in potential which create the observed phase contrast are on a smaller scale.

A future experiment may be to compare the pore size distribution applying permporometry to both the diffraction patterns and the Fourier transform of real space TEM images, across a range of samples. In this investigation, both bright field and diffraction TEM images suggest that the material is amorphous and dense in any structure on a small scale. This makes the material highly selective regarding the dimensions of molecules which can be absorbed into the polymer matrix, as water vapour, a small molecule, clearly does. The ability of polyimides to be tailored as gas separation membranes with a good selectivity has been discussed elsewhere[30].

## 4.4 Summary

This chapter began by interpreting the data obtained in Chapter 3 in light of Fick's model of diffusion. It began by considering the impact of the test chamber by calculating the number of particles hitting the surface of the active area of the QCM at 25°C over a range of humidities. Importantly, this was based on experimental data taken from the thunder chamber test environment in section 4.1.1. The mass of particles hitting the surface was found to be very large compared to the mass measured by the QCM technique, implying a low penetration for water molecules.

<sup>4</sup>Recall that Equation 2.8 is  $\chi(q) = \pi\Delta f\lambda q^2 + \frac{1}{2}\pi C_s\lambda^3 q^4$ . Symbols are defined in section 2.4.

This work directly informed section 4.1.2, in which the diffusion was characterised as Fickian, and the work allowed any anomalous sigmoidal behaviour to be explained by the behaviour of the test environment. There were two primary conclusions from the Fickian analysis of the QCM data; the first that the diffusion constants measured were a function the thickness of the material, implying that the film did not have a uniform diffusion coefficient, with surface effects playing a larger role in the thinner films. The second conclusion was that the rate limiting factor was thickness independent, as the timescale of the diffusion was the same across a  $170\text{nm}$  film and  $1\mu\text{m}$  film. It was suggested that such behaviour was a result of density, and hence free volume variations within the polymer, which is reinforced well by the data shown in Chapter 5.

Therefore, an investigation into the rate limiting factor is presented and chemical interactions are considered as a potential limiting factor in section 4.2. The results from ART-FTIR showed some form of polar-polar interaction between the polyimide backbone and the polar water vapour molecule. By fitting the time constant to the QCM data, and assuming an Arrhenius-like behaviour, an energy of the order of  $1\text{kJ/mol}$  is inferred for the rate limiting process.

This information was then considered, and a model of the water bonding within the polyimide based on Langmuir adsorption model was then presented. This model did not produce a good fit for the data, and it was speculated that an additional term for Fickian diffusion could be added to the model to better fit the data. A combination of the diffusion and chemical bonding are likely to limit the rate of water vapour ingresses into the polyimide.

The gas selectivity of the polyimide was then considered in section 4.3. Permporometry measurements implied that only particles of a similar or smaller volume as that of water vapour were able to enter into the polyimide. This explained the selectivity of capacitance based sensors as few molecules common in nature are both as small, and as polar, as water vapour. The common spatial frequencies were then investigated in the polyimide using electron diffraction. However, spatial frequencies larger than  $0.2\text{nm}$  were difficult to discern from the central spot. Defocusing the polyimide enhanced the contrast but, was found to have an insufficient resolution to be certain of the length scales. It was then suggested that future work may investigate ways in which length scales, in the range  $0.2\text{-}1\text{nm}$ , can be probed. The validity of electron diffraction based techniques to map spatial frequencies in amorphous materials may be ascertained by looking at samples of a known porosity.

## Chapter 5

# Acquiring concentration profiles - In-Situ Neutron Reflectivity

The results previously presented have raised several key issues regarding the influence of the surface of the polyimide, and a possible depth dependant diffusion coefficient (section 4.2). Additionally, the low permeation rate of non-condensable gases for this polyimide raises questions regarding the appropriate model of transport kinetics in this system; adsorption, absorption, or some combination such as adsorption followed by absorption. The free volume variations within the absorbent material, and the concentration profiles of the penetrant as it diffuses, can reveal such information. An in-situ probe capable of mapping density variations within the polyimide in the direction of the concentration gradient, i.e. normal to the interacting surface, is required.

Neutron reflectivity has been widely used to examine buried interfaces. The grazing incidence geometry of neutron reflection means it is sensitive to many types of layers which vary normal to the surface[74], and it has been used to probe dynamic changes in polymers[77] including the sorption of water vapour[147, 148]. Section 5.1, discusses the use and theory of neutron reflectivity, demonstrating that it is capable of acting as the required probe. The construction, operation and data processing of equipment and methods to make the measurements on this system are discussed in section 5.2. Results showing the density of the thin films as a function of depth, and equilibrium concentrations of penetrant vapour, are presented in section 5.3. The final results section outlines a novel method of acquiring time resolved density profiles of the absorbent material as the penetrant ingresses. The conclusions and limitations of this technique are discussed in section 5.5.

## 5.1 Neutron Reflectivity Theory

Neutron-matter interactions can be approached by considering the nuclear potential experienced by each neutron as it passes individual atoms. In this particle model<sup>1</sup>, matter was represented as series of point scatters, each point representing an atom. The field generated by a given atom is characterised by a cross section area,  $\sigma = \pi b^2$ , where  $b$  is known as the scattering length. In practice, matter of any practical size contains a large number of atoms and so many point scatterers. It is therefore more efficient to model such situations by considering the wave nature of the neutron beam.

This section is divided into two parts, the first, 5.1.1, discusses the wave model of neutron behaviour with a goal of giving simple equations with which to interpret the experimental results later presented. The second subsection, 5.1.2, shows how this model can applied to acquire concentration profiles of the polyimide and sample requirements.

### 5.1.1 Model of Neutron Reflectivity

The average scattering length, the scattering length density,  $SLD$ , is given by Equation 5.1 where;  $V$  is the given volume. For a given species of atom, the  $SLD$  consists of  $\rho_b$  and  $\rho_a$ , the real and imaginary components, respectively, of the  $SLD$ , known as the scattering coefficients.

$$SLD = \frac{\sum b}{V} \quad (5.1)$$

The refractive index for a neutron beam passing through a medium<sup>2</sup>, is shown as well approximated by Equation 5.2[72, 75, 81]. Equation 5.2 assumes the resulting neutron waves are the sum of scattering resulting from many point scatters acting on the incident wave; this formalism neglects local field effects and binding effects which are well discussed by Nowak et al.[149]. The neutron wavelengths,  $\lambda$ , are normally three orders of magnitude less than that of light, allowing much thinner films to be probed; additionally, the neutron beam also has a small attenuation relative to it's scattering strength when compared to EM radiation.

$$n = 1 - \lambda^2 \left( \frac{\rho_b}{2\pi} \right) + i\lambda \left( \frac{\rho_a}{4\pi} \right) \quad (5.2)$$

Importantly, in contrast to optical refractive indices, neutron refractive indices are directly related to composition of the material. It will later be discussed that the real component of the  $SLDs$ , for materials important in this investigation, are several orders of magnitude larger than the imaginary component

---

<sup>1</sup>Discussed at length in section 2.3

<sup>2</sup>This formalism of neutron behaviour was briefly discussed when considering neutron wave guides in section 2.3

which quantifies the attenuation of the wave (see Figure 5.2). Consequently,  $\rho_a$  is sufficiently small that the effects of attenuation can be neglected when calculating the refractive index, as is common in many reflectometer experiments, simplifying Equation 5.2 to two terms[75].

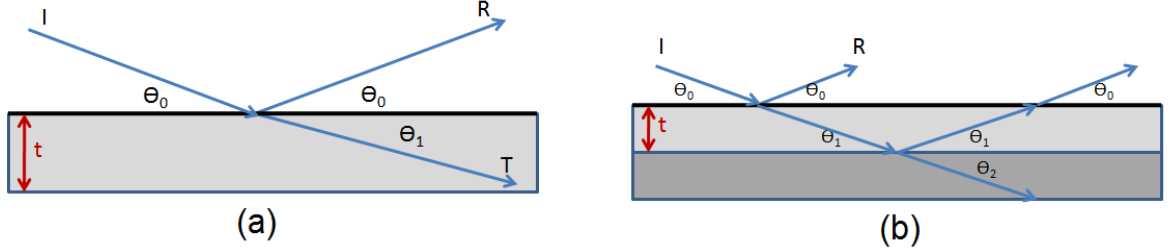


Figure 5.1: (a) A wave,  $I$ , passing from one medium to another, with a reflected wave  $R$  and transmitted wave,  $T$ . (b) A two layer system with reflection coming off the surface and second interface.

Figure 5.1(a), shows three waves; the incident beam,  $I$ , a reflected wave,  $R$ , and a transmitted wave,  $T$ , which is common for a reflection geometry. It can be shown by considering the wave functions of the reflected and transmitted neutron waves normal to the surface; the fraction of the incident beam energy reflected can be calculated by Equation 5.3[150].

$$R = \left| \frac{n_0 \sin \theta_0 - n_1 \sin \theta_1}{n_0 \sin \theta_0 + n_1 \sin \theta_1} \right|^2 \quad (5.3)$$

In Equation 5.3,  $R$  is the fraction of the incident beam which is reflected,  $\theta_0$  is the incident angle to the surface (referred to as  $\alpha$  for the first interface),  $\theta_1$  is the angle of the transmitted wave to the surface,  $n_0$  is the refractive index in the first medium and  $n_1$  is the refractive index in the second medium[150].

Equation 5.3 implies that at small angles the reflectivity is equal to unity, resulting in total external reflection or specular reflection. The largest glancing angle,  $\alpha$ , at which total external reflection occurs, is called the critical angle,  $\theta_c$ . The critical edge is the value of  $q$  at which the reflectivity reduces from unity. When  $\alpha > \theta_c$  energy is transmitted into the sample and so the reflectivity is reduced from unity. The refractive index is a function of the SLD and the neutron wavelength, so the reflectivity is also a function of the neutron wavelength. Consequently, plotting the reflectivity as a function of angle for non-monochromated beam does not allow the various scattering events to be discerned. The scattering vector,  $q = \frac{4\pi}{\lambda} \sin \theta$ , is the vectorial difference between the incident and reflected waves<sup>3</sup> and it is a function of both the wavelength/energy of the incident neutron, and the incident angle. The reflectivity profile is conventionally presented as a function of  $q$  rather than of  $\theta$ , as this allows the

<sup>3</sup>Discussed in section 2.3 extensively.

reflectivity to be presented as a function of the scattering strength for a non-monochromatic neutron beam.

Additionally, it has been shown that the reflectivity profile can be thought of as the Fourier transform of the spatial gradient of the SLD normal to the sample surface[150]. This is the result of the kinematic approximation which is only reasonable for weak scattering [150, 75, 73, 72]. Accordingly, this model is valid at  $q$  values where surface reflection is of lower significance, far away from  $q$  value for the critical edge where surface reflection effects are not dominant. Mapping the reflectivity at higher  $q$  provides an insight into a broader range of scattering events allowing the inferred density profile to be refined, which will be discussed in 5.1.2.

Approximating the reflectivity normal to the surface, in the direction normal to the surface,  $z$ , is possible by considering some simplifications to Equation 5.3. The  $z$  component of the wave is found when  $\theta_0 = 90^\circ$  which leads to  $\sin\theta_0 \simeq \sin\theta_1$  and as  $n_0 \approx 1$ (for a vacuum); this leads to Equation 5.4.

$$\sqrt{R} = \left| \frac{1 - n_1}{1 + n_1} \right| \approx \frac{1 - n_1}{2} \quad (5.4)$$

Equation 5.2 can be rewritten in terms of the wave number  $q$ , as from the definition of  $q$ ,  $q_z = 2k$  when  $\theta_0$  is close to  $90^\circ$  and so,  $\frac{q_z}{2} = k = \frac{2\pi}{\lambda}$ . So from Equation 5.2,  $n = 1 - \left(\frac{4\pi}{q_z}\right)^2 \left(\frac{\rho_b}{2\pi}\right) = 1 - \frac{8\pi\rho_b}{q_z^2}$ , neglecting the attenuation component giving Equation 5.5.

$$R \approx \frac{16\pi^2\rho_b^2}{q_z^4} \quad (5.5)$$

The validity of Equation 5.5 and the kinematic approximation to a reflectivity geometry is extensively discussed elsewhere[151, 74] and it is considered valid as when applied to polymers systems at a high  $q_z$  as discussed[75]. At smaller angles, say  $\theta = \theta_{critical}$ , the assumptions that;  $\sin\theta_0 \simeq \sin\theta_1$  and weak scattering, is not valid and therefore neither is Equation 5.5. This can be shown otherwise but ultimately is as the Born approximation does not hold for strong scattering[75]. However, at higher values of  $q$  with weaker scattering Equation 5.5 can provide a quick and useful way of analysing spectra at higher  $q$  ( $\sim q_z = 3q_{critical}$ ).

To gain an understanding of  $R(q)$ , Equation 5.5 can be applied to the ideal situation depicted in Figure 5.1(b). The SLD varies normal to the surface and the neutron wave is considered as it passes through three interfaces with SLDs;  $\rho_{b0}$ ,  $\rho_{b2}$  and  $\rho_{b2}$  respectively. This gives changes in SLD;  $\Delta\rho_1 = \rho_{b1} - \rho_{b0}$  and  $\Delta\rho_2 = \rho_{b2} - \rho_{b1}$ . If each surface is smooth the rate of these step changes in SLD normal to the

surface, can be modelled as delta functions giving Equation 5.6.

$$\frac{d\rho}{dz}(z) = \Delta\rho_1\delta(z) + \Delta\rho_2\delta(z+t) \quad (5.6)$$

In Equation 5.6;  $t$  is the thickness of the film, integrating for  $\rho_b(z)$ , substituting in and inserting into Equation 5.5, and considering the real component gives

$$R \approx \frac{16\pi^2}{q_z^4}(\Delta\rho_1 + \Delta\rho_2\exp\{-itq_z\})^2 = \frac{16\pi^2}{q_z^4}(\Delta\rho_1^2 + \Delta\rho_2^2 + 2\Delta\rho_1\rho_2\cos(q_z t)) \quad (5.7)$$

This approximation provides a quick and analytical first glance at the reflectivity profiles; here the striking feature is the interference (Kiessig) fringes. Equation 5.7 provides a tool to conduct a direct analysis of spectra. Considering a period of the Kiessig fringes; as  $\cos(q_z t) = \cos(2\pi) = 1$  an estimate of the film thickness can be obtained as  $t = \frac{2\pi}{\delta q_z}$ .

However, this does not deal with more complex systems and is inaccurate when dealing with fringes close to the critical edge. It is clear that the reflectivity profile contains a wealth of information about the scattering length density changes in samples therefore a more precise method of dealing with the data is desirable. Modern computation can easily deal with dividing up a given layer into many sub-layers each with a sharp interface between small SLD changes from the previous sub-layer. Essentially, taking a continuous medium and treating it as an SLD histogram, then calculating the superposition of the reflectivity from each boundary, giving a fitted reflectivity profile. Such an approach is summarised in Equation 5.8 [152, 153, 75, 74].

$$R_{total} = \left| \frac{r_{01} - r_{12}\exp\{2i\beta\}}{1 + r_{01}r_{12}n_1\exp\{2i\beta\}} \right|^2 \quad (5.8)$$

In Equation 5.8;  $\beta = \frac{2\pi}{\lambda}n_1t_1\sin\theta$  is the optical path length in the film and  $r_{ij} = \frac{n_i\sin\theta_i - n_j\sin\theta_j}{n_i\sin\theta_i + n_j\sin\theta_j}$  where  $i$  and  $j$  denote the layers of the system. This is a general expression for any layer in the film. The exponential term of Equation 5.8 deals with the attenuation of multiply reflected waves. A many layered model can be approximated by a series of different layers with each boundary adding another reflected wave, all the reflected waves are then summed while accounting for their relative phases. The calculated reflectivity is then the complex square of the reflected waves from each boundary. This relies of the wave of the neutron wave function being continuous across each boundary.

Often steps in  $\frac{d\rho}{dz}(z)$  are modelled not as delta functions as in Equation 5.6, but rather as a distribution function, normally a Gaussian with the roughness characterised by an error function associated with the given distribution function[152]. This can be computationally more efficient when working with rough surfaces as the roughness is summarised by the width of the distribution function rather than

many thin layers. This method is deployed in the MOTOFIT software which is used in this project to calculate theoretical reflectivity profiles and refine fits to data as detailed by Nelson[153].

### 5.1.2 Applying Neutron Reflectivity to polyimide

In this section it is shown with the aid of some simulation that neutron reflectivity can be applied to this system to map the density variations normal to the surface in the polyimide thin film, and hence the concentration levels of any penetrant.

Figure 5.2, shows the relative cross sections of important materials for these experiments and their SLDs, including Kapton, a well studied form of polyimide[154]. Considering these SLDs two points are clear: the contrast provided by  $D_2O$  is much higher than that of water vapour; and secondly, the attenuation, represented by the imaginary component of the SLD, is negligible.

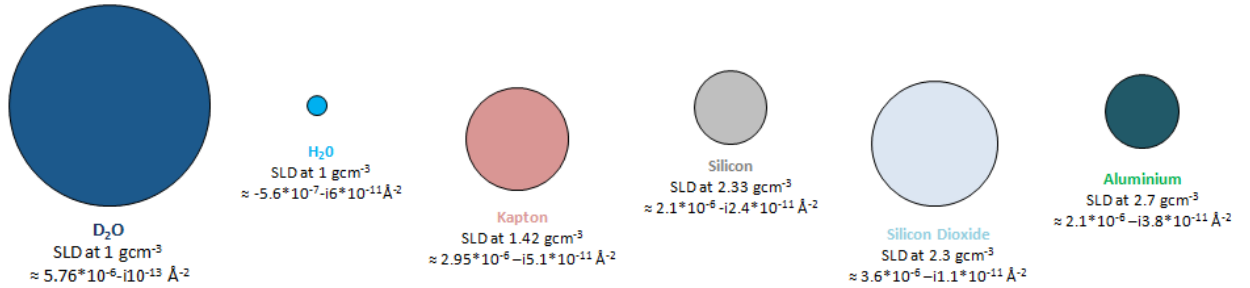


Figure 5.2: A pictorial representation of the relative SLDs of various materials at common densities at a neutron wavelength of 6 Å. The diameters of the circles are proportional to the real component of the SLD.

From Equation 5.2, gases such as air, with a low density when compared to solid materials, are reasonably approximated to have  $n_1 = 1$ . Typically, the scattering length densities for polymers are of the order  $10^{-6} \text{Å}^{-2}$ ; for example, for Kapton the SLD is  $\approx 2.95 \times 10^{-6} \text{Å}^{-2}$  for a typical neutron wavelength of 6 Å. This SLD results in a refractive index  $\sim 0.999968$ , which when inserted into Snell's law,  $\frac{n_1}{n_2} = \frac{V_1}{V_2} = \frac{\sin\theta_1}{\sin\theta_2}$ , where  $\theta$  is the angle to the normal, gives rise to total external reflection  $> 89^\circ$  and so a glancing angle for the neutron beam of  $\alpha \sim 1^\circ$  is required to observe total external reflection. Such conditions must be accommodated on the reflectometers used in this study to gain a full profile of the reflectivity[155].

An anticipated reflectivity profile can be calculated using the MOTOFIT software[153]. This is an important step as it will inform the types of samples about which useful information can be gained. Each layer in the modelling method used is represented by three numbers: a thickness, a roughness,

and an SLD as discussed. The properties of the substrate and the containment medium are fixed as they are well understood; silicon ( $SLD_{Silicon} \approx 2.07 * 10^{-6} \text{ \AA}^{-2}$ ) and air ( $SLD_{Air} \approx 0 \text{ \AA}^{-2}$ ). The fitting algorithms used are discussed in later sections. Here, this software is used to understand the expected reflectivity profile and understand the sample requirements.

Figures 5.3 and 5.4 depict a series of idealised situations of various samples. Firstly, Figure 5.3(a) simply shows a perfectly sharp interface between air and Kapton. As expected from Equation 5.3, Fresnel behaviour is observed with the reflectivity dropping exponentially with  $q$ . However, polymer samples tend to have a degree of roughness which affects the degree of sharpness of the drop in reflectivity. This is observed when comparing Figure 5.3(a), and Figure 5.3(b), which are the same except for the roughness of the interface. Interface roughness reduces the specular reflected intensity as some neutrons are scattered into non-specular directions. Specular reflectivity is only sensitive to changes in the SLD normal to the surface; the non-specular reflected intensity is sensitive to the in-plane features of the interface, since it has a non-zero component of the momentum in the x-y plane [76]. Therefore, a rougher surface leads to more diffuse reflection. Figure 5.3(c) has two perfectly sharp interfaces; a vacuum-Kapton interface and Kapton-silicon interface 60nm apart, the situation represented in Equation 5.7. Figure 5.3(c) shows the Kiessig fringes, and the period,  $\delta q_z$ , of the fringes, is slightly shorter close to the critical edge, 1 as marked on Figure 5.3(c), than on later fringes. This is the influence of the strong scattering from the critical edge for which Equation 5.7 is not accurate. This must be considered then making direct measurements from a reflectivity profile, which will be discussed further in section 5.2.3.

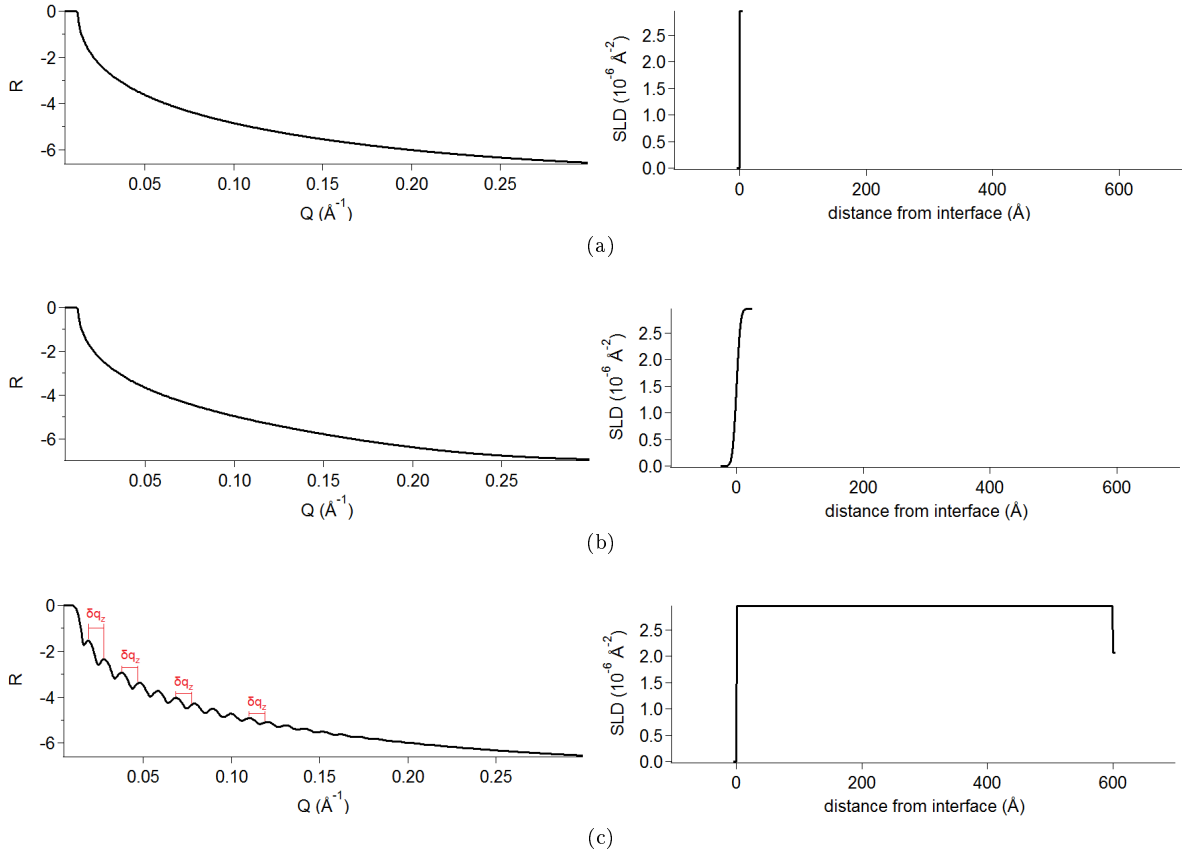


Figure 5.3: Each of these scenarios was simulated using the MOTOFIT scripts. The y-axis is the logarithm(base 10) of the reflectivity. (a) Fresnel like behaviour for a single sharp interface from a vacuum to Kapton of infinite thickness. (b) The same interference as in (a) with a surface roughness. Roughness is simulated as an error function with a width of 5nm. (c) Interference fringes arising from a Kapton layer of 60nm on an infinite Silicon substrate.

Figure 5.3(c) shows a 60nm thick Kapton layer on a silicon substrate; no fringes can be discerned after  $q \approx 0.15 \text{\AA}^{-1}$ . However, humidity sensors use layers of a much greater thickness,  $th$ , normally,  $th \approx 1 \mu\text{m}$ . From Equation 5.7 it is deduced that  $th = \frac{2\pi}{\delta q_z}$  so a greater thickness requires a better resolution in  $q_z$  to resolve the fringes and the fringe depth. This is observed by comparing Figure 5.4(a) and (b) which shows layers of 100nm and 300nm thickness respectively. This sets a resolution requirement (in  $q$ ) to probe a sample of a given thickness. Samples thicker can be probed, however the fringes will not be resolved, meaning that modelling the film accurately will be less likely.

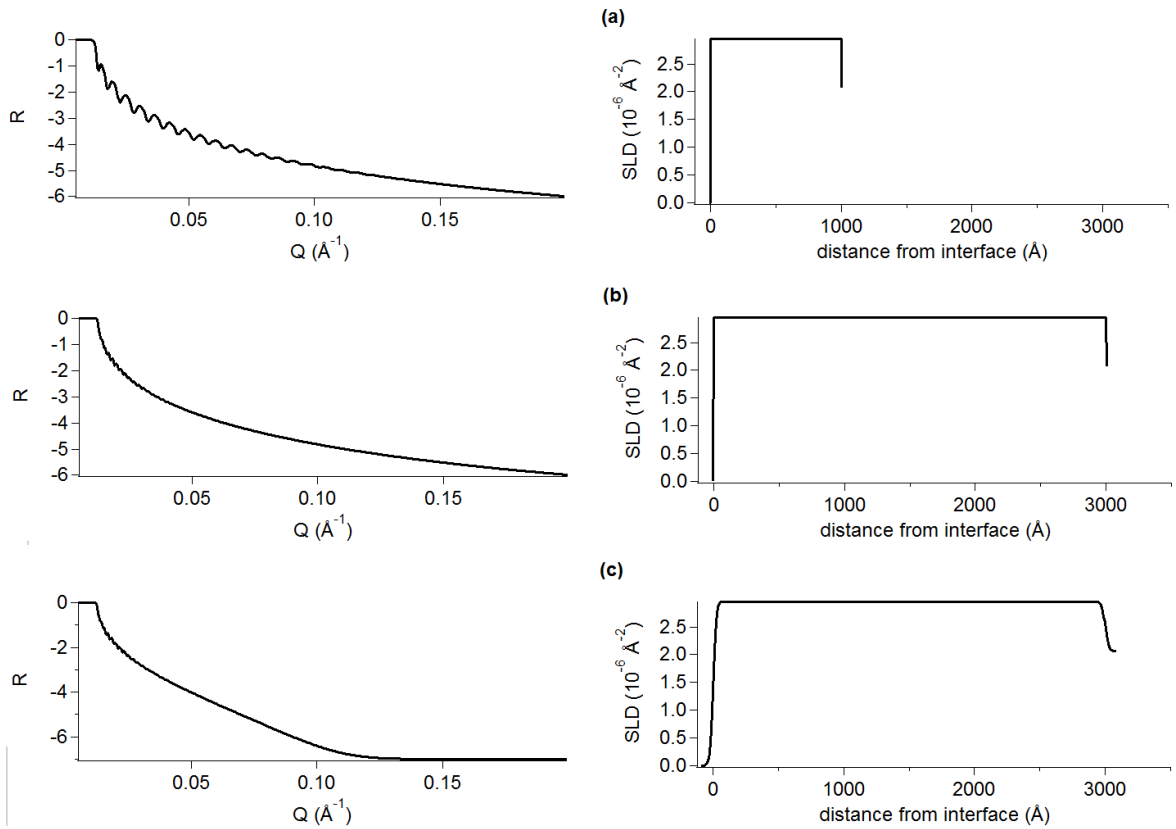


Figure 5.4: (a) A 100nm thick layer of polyimide on a silicon substrate with no interface roughness. (b) A 300nm thick layer of polyimide on a silicon substrate with no interface roughness. (c) A 300nm thick layer of polyimide on a silicon substrate with a 2nm interface roughness to show the effects of off-specular reflection on the reflectivity profile.

Figure 5.4(c) shows the type of reflectivity profile,  $R(q)$ , which can be anticipated. This is identical to Figure 5.4(c) but roughness has been added increasing the off-specular reflection. The range of  $q$  with features is approximately  $0-0.1\text{\AA}^{-1}$  when both the interfaces have a 2nm width for the distribution function describing the roughness. A final feature on all of the simulated spectra shown is the infinite silicon substrate. It is important to prevent features from a third interface being calculated in the modelled spectra as this only adds to complication in the model, and any fringes arising from the silicon block (thickness 1cm) will be beyond the resolution of the instrument. As a result, the calculation on any other interfaces is unnecessary and not of interest for this experiment.

It is clear from this section that with careful equipment selection and sample preparation, mapping  $R(q)$  is possible. Modelling the SLD from the  $R(q)$  map can then reveal any variation in the sample density.

## 5.2 Experimental Methods

This section is divided into three parts: the experimental planning, the data acquisition, and the data processing, of the experiments involving neutron reflectivity, respectively. The first section covers the sample preparation and use of an aluminium cell to create a  $D_2O$  vapour filled and  $N_2$  environment for the sample. The data acquisition then discusses the use of two neutron reflectometer at two facilities to collect a range of data. Finally, the data processing discusses extracting information from the acquired data sets.

### 5.2.1 Experimental Design

The neutron data in this project was acquired following the success of two applications for beam time, each to conduct four days of experiments. The two instruments are the D17 beam[82] at the Institut Laue-Langevin, ILL, and the Inter beam[83, 84] at Rutherford Appleton Laboratories, RAL as part of a collaboration<sup>4</sup>. Preparing for this experiment involved two tasks; the sample preparation, and the construction of equipment to control the humidity in the head space of the samples while NR profiles were acquired.

The size of the sample corresponds to the beam imprint available at the given instrument which depends on the reflectometer geometry. In principle, larger samples allow a larger beam footprint, leading to a higher number of neutrons and better Poisson statistics on the reflectivity count. The beam width is controlled by the slits, which are shown in Figure 5.5, leading to a typical imprint on the sample of a few square centimeters[156]. Sample uniformity parallel to the surface is imperative, as any variation can lead to errors in the  $R(q_z)$ . Polyimide thin films on top of 3" Si blocks of 1cm thickness have been used. Uniformity on wafers of this size is obtainable using standard spin casting techniques, as shown in section A.1. Polyimide layers with a range of thicknesses and processing steps had been prepared on silicon blocks. The samples were placed into an aluminium vapour cell that was constructed for a similar project[77, 157]. Aluminium was chosen as the cell material due to its relatively low NR scattering length when compared with other materials, as indicated in Figure 5.2. The cell was designed to hold such silicon blocks during NR measurement and has a gas inlet.

---

<sup>4</sup>Dr A. Glidle provided the sample chamber and guided its customisation to incorporate the QCM and Honeywell sensor.

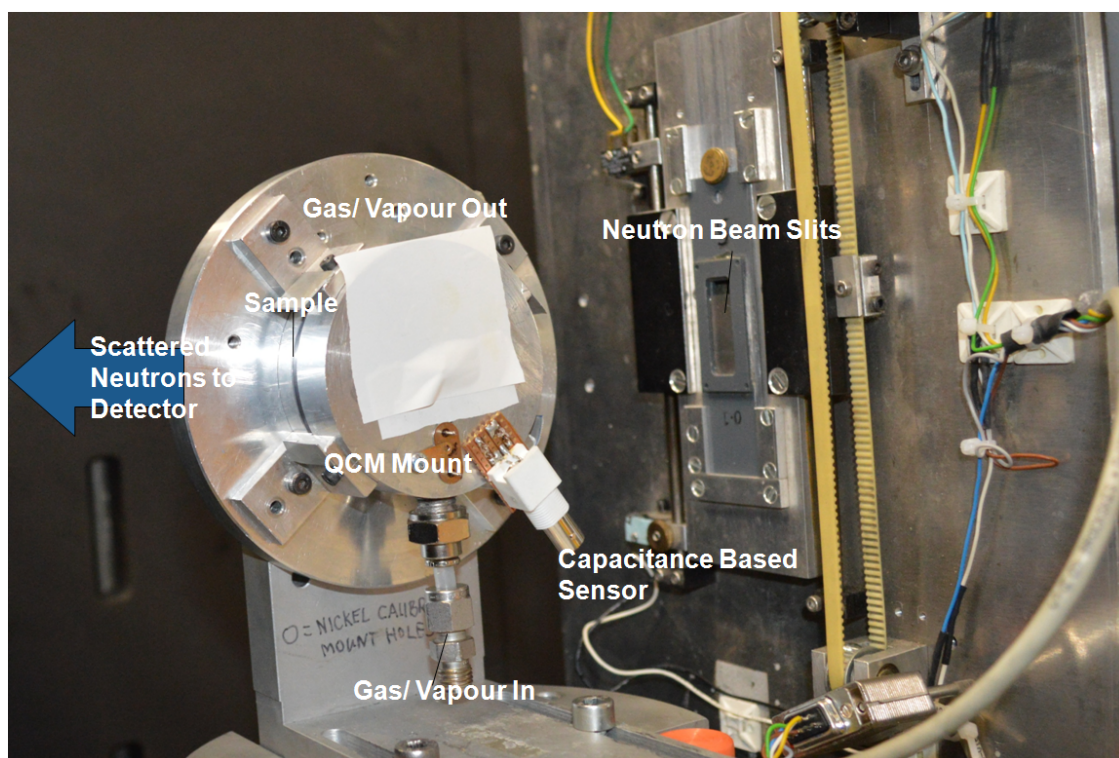


Figure 5.5: Shows the sample in the aluminium cell on the D17 neutron beam line. The slits which control the beam imprint on the sample can be seen. The cell itself has a space to insert a capacitance based humidity sensor with a BNC output, which is not plugged in. A QCM mount is also placed in the cell, which is again not plugged in. The gas inlet (bottom) is perpendicular to the direction of the neutron beam.

The sample cell was adjusted for this experiment by drilling a space to allow a DIL chip socket to be attached inside; this was connected to a BNC socket on the outside of the cell. During the experiments, a Honeywell 1820 commercial humidity sensor, which uses the same polyimide as a sensing element, was plugged in and capacitance readings of the sensor were measured using an Agilent E481A capacitance measurement box<sup>5</sup>.

Additionally, a Quartz Crystal Microbalance, QCM, crystal loaded with  $\sim 1\mu\text{m}$  thick polyimide film (Soft Cured), was included in the cell connected via another added opening. The QCM readout was performed using a comparator circuit Bruckenstein et al.[100]. This circuit is designed to output a voltage proportional to the resonance frequency difference between the loaded crystal in the cell, and the unloaded crystal in the circuit. This is common for QCM experiments requiring a fast readout[70]. Both the QCM voltage and capacitance of the 1820 sensor were logged as a function of time via a lab-view script, and output into a text file for later reference. This allowed the cell environment to be monitored, and also provided information regarding the typical time scales of absorption in commercial

<sup>5</sup>The measurement methods are discussed Section 2.1

sensors, and the weight of a polyimide film in the cell environment. Free volume in the aluminium cell was limited by packing the parts of the cell which were not in the beam path. The cell was allowed to equilibrate for several minutes at a set flow rate prior to the measurements of the reflectivity.

This experimental setup allowed a series of measurements of various polyimide films in a monitored ambient humidity which was controlled to be either water vapour or nitrogen rich.

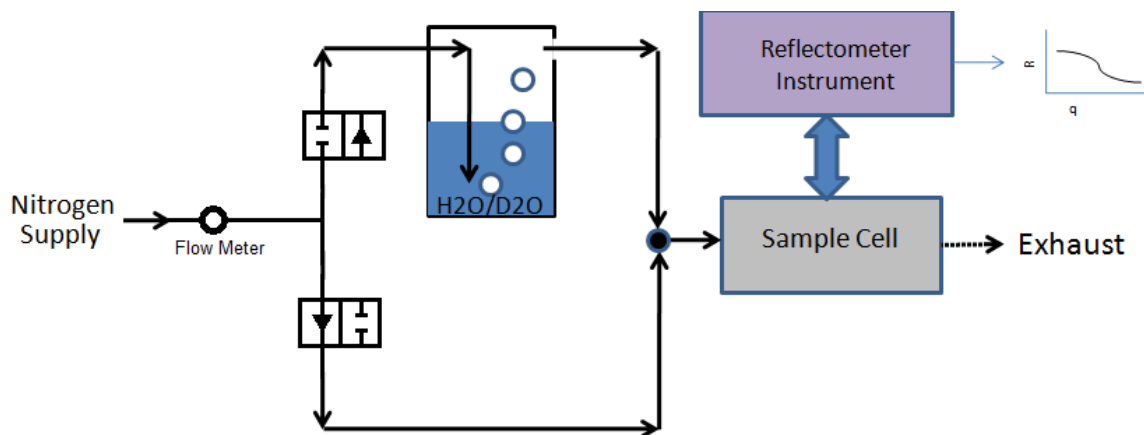


Figure 5.6: The scheme of the vapour pulsing system when acquiring static measurements. By default, dry nitrogen was passed in to cell.

The flow of gas into the cell was either, dry nitrogen or deuterated nitrogen gas as shown in Figure 5.6. By default, the dry nitrogen exits the tank supply directly into the cell, while flow rate was monitored. Alternatively, the nitrogen entered the cell via a gas bubbler. The flow line of the gas bubblers had a *closed by default* value, while an *open by default* value was placed in the flow line directly to the cell. Both valves were controlled by the same voltage supply and when the voltage was set above a set threshold the valves would switch. This allowed the manually set voltage to determine the flow path of the nitrogen supplied, and hence the vapour level in the cell could be manually switched between two extremes. As a result the cell, was under a constant positive pressure.

### 5.2.2 The Acquisition and Reduction of Data

The objective of the data collection was to obtain profiles of  $R(q_z)$  with sufficiently low error to then infer density variations in the polymer with good confidence. The features of particular interest are the critical edge, and the characteristic fringes.

To obtain data, the sample height and angle relative to the beamline was defined by adjusting the stage to which the aluminium cell was fastened. The angle depends on the  $q$  range desired, which is

a function of both the wavelength of the neutrons and the incidence angle. The measurand in NR experiments is the number of neutrons counts on a square pixel array. This produces an intensity map as shown in Figure 5.7. Several corrections; referred to as the data reduction, are needed to obtain a reflectivity profile,  $R(q_z)$ , this is discussed in this section.

The spectrometer is calibrated such that y-pixel position corresponds to a given change in wavelength for a set geometry. Conventionally, NR experiments are performed in order to gain information about density changes orthogonal to the plane of the sample, which is assumed to have a smooth surface. Therefore, summing the spectra in the x direction giving a spread in wavelength of the neutrons is common. The distribution of the neutrons in the x-pixel direction contains information about the surface roughness, as previously discussed. While it is becoming more common, the theoretical models of the off-specular reflectivity data is much more complex compared to the specular reflectivity; as a result x-pixel direction data is not conventionally analysed in a raw form[76].

Figure 5.7(a) and (b) are data acquired with an empty aluminium cell and so there are no Kiessig fringes. Such a run is conducted to profile the direct beam which will later be used to normalise the other reflectivity profiles. Figure 5.7 (c) and (d) shows the data collected at a glancing angle of  $0.8^\circ$  with a 95nm polyimide etched sample with dry nitrogen running across it. When (c) and (d) are compared to (a) and (b) the neutrons have undergone a wavelength shift and fringes are clearly visible. (e) and (f) show the same sample again but with an angle of incidence of  $3.0^\circ$  this illustrates the use of different angles to probe different scattering events in a sample. It should be noted that the number of counts is orders of magnitude different for each pair of graphs due to variations in the collection time.

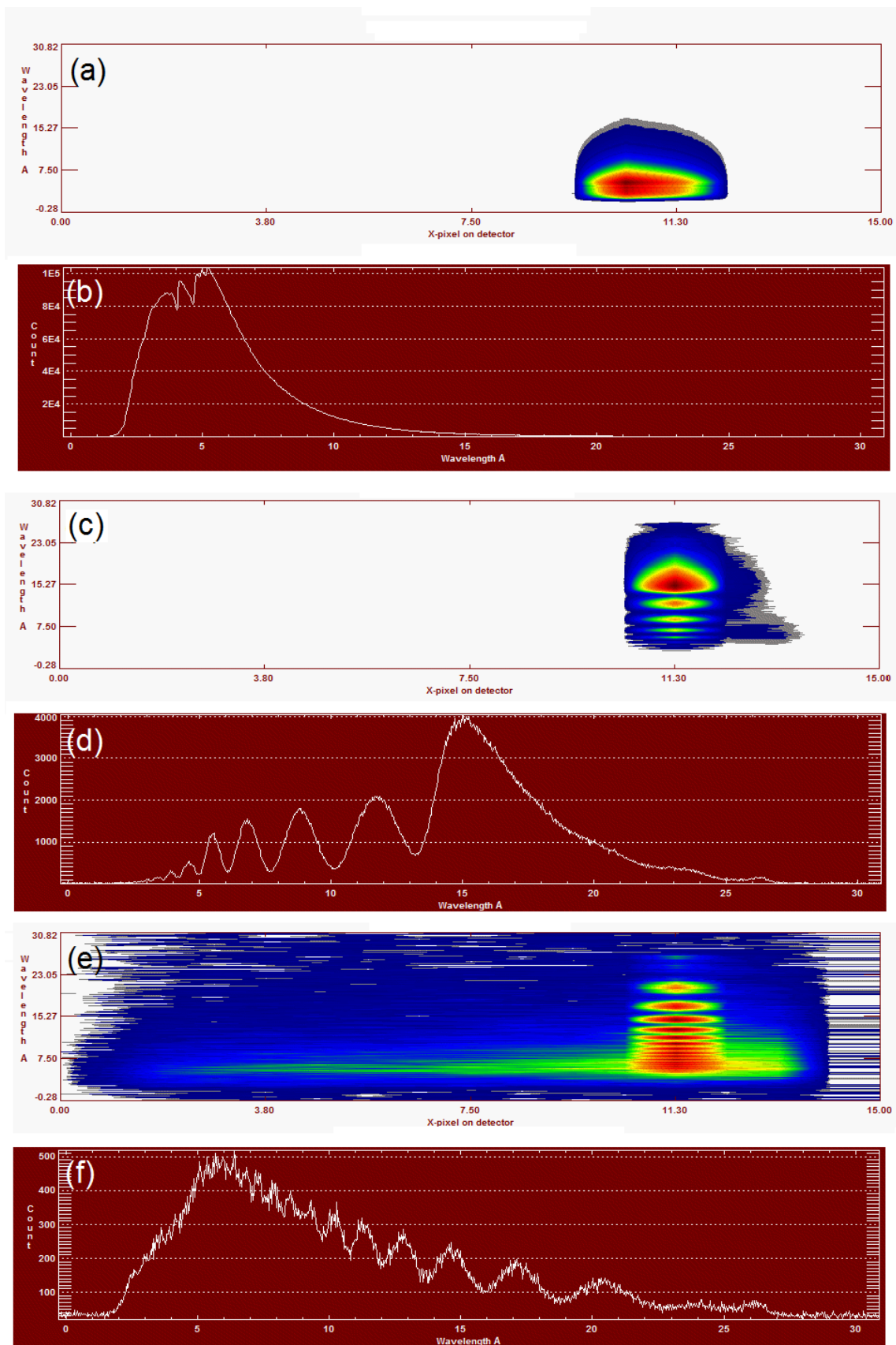


Figure 5.7: Neutron counts. (a), (c), and (f) are the raw neutron counts on the detector for the; (a) aluminium cell with no sample, (c) sample data taken at  $0.8^\circ$  angle of incidence, and (f) sample data taken at  $3^\circ$  angle of incidence. (b), (d), and (e) are the same data, respectively, summed along the x axis.

To obtain  $R(q)$ , instrument scientists have written scripts specific to each instrument with which to process the raw data. In this project *Mantid* software has been used to interpret the data from the Inter Reflectometer at RAL [158, 159, 83], shown in Figure 5.8, and Cosmos script based in IDL is used to process data from the D17 reflectometer at the ILL[155], shown in Figure 5.7.

Figure 5.8 shows two sets of data taken on the same sample at different angles re-binned into one spectrum. This is a common technique as it expands the range of  $q$  improving the Poisson statistics across the range.

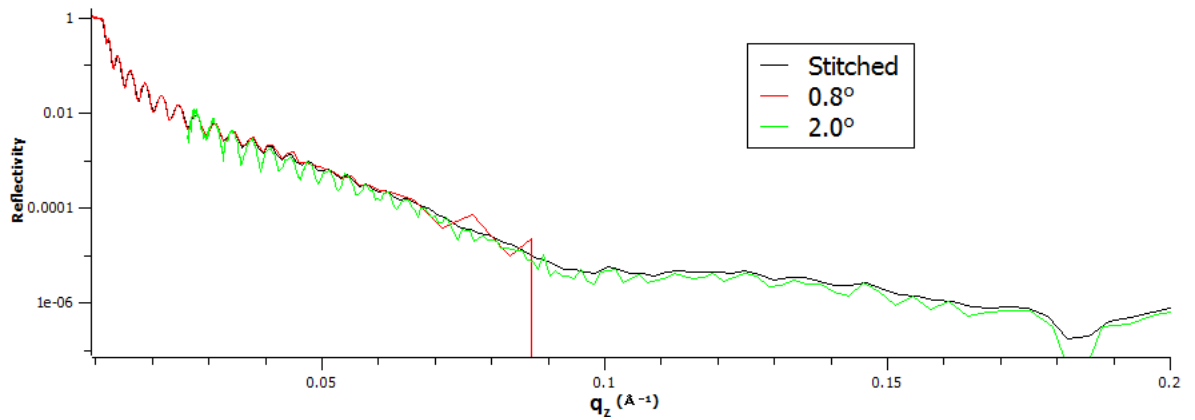


Figure 5.8: Sets of data from the same sample taken at red ( $0.8^\circ$ ) and green ( $2.0^\circ$ ). The black spectrum is the aggregate of the red and green reflectivity profile. Stitching or re-binning the data can also cause a reduction in the fringe amplitude and so it is also useful to look at the raw reflectivity profile from a given angle.

As the neutrons are counted on a pixel array, for a given angle each pixel represents a range of  $q_z$ , the bin width or resolution in  $q_z$ . The bin width is not uniform, but varies due to the spectrometer architecture. A sample piece of data showing the bin width as a function of  $q_z$  is shown in Figure 5.9. It shows an approximately linear relationship between the  $q_z$  values and resolution for data taken at  $0.8^\circ$  and  $3^\circ$ . This underscores the benefits of aggregating data across different angles to improve the statistics for a range of  $q_z$  in the reflectivity profile.

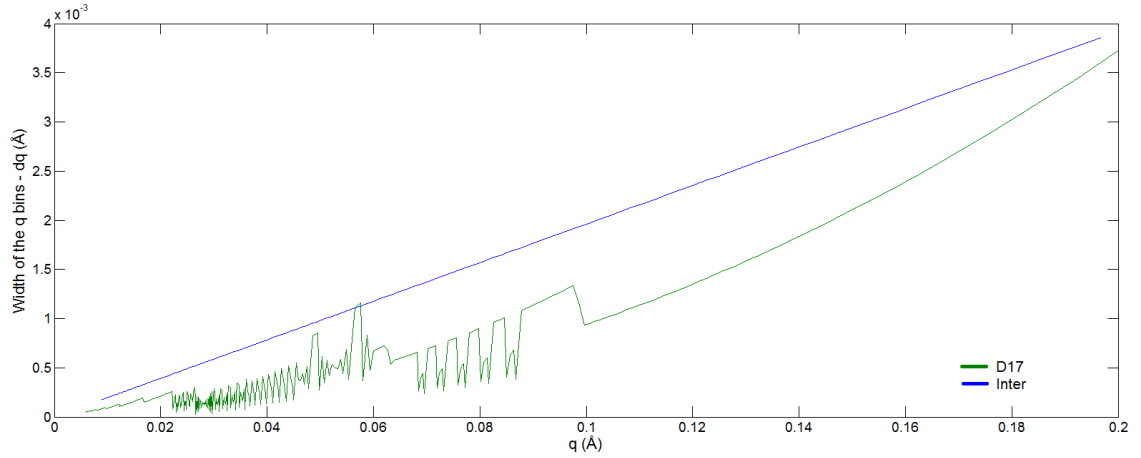


Figure 5.9:  $\frac{d}{dq}(q)$  plotted: Data is from the D17 reflectometer [82] at the ILL and Inter Reflectometer at RAL showing the bin width as a function of scattering vector. This shows a non-uniform bin width from both instruments linearly correlated with scattering vector for some stitched data. Consequently, features in the reflectivity profile at a higher  $q$  are sampled with a lower frequency.

The standard data reduction resulted in each spectrum in being represented by three columns;  $q_z$ , reflectivity, and error on reflectivity. Reduction was performed during the experiment to ensure that the profiles obtained had sufficient statistical significance: the aim being to reduce the Poisson noise on each reading to a few percent of the reading. This required a certain number of neutron counts, and would take a varying amount of time which depended on the beam flux, and the  $q_z$  range of interest. Generally, the data presented was aggregated over  $\approx 2$ hour period for each angle. The flow rate of the incoming gas was manually monitored to be  $\approx 5-6$  litres/min into the cell space which was  $\geq 0.1$ litres. Therefore, the stability of cell over the four hours required to collect data at two angles was close to constant, as monitored by the QCM and Capacitance sensors.

The anticipated width of reflectivity fringes for a layer of 180nm can be estimated as  $\sim 0.0034\text{\AA}$ . From the nyquist theorem the resolution of such fringes requires a minimum sampling rate of  $\sim 0.0017\text{\AA}$  and from Figure 5.9 the maximum  $q$  value at which such a bin width is obtained is  $\sim 0.01\text{\AA}$  for typical two angle data. This will be shown in later sections in which it appears that the fringes disappear at higher  $q$  values which is due to the wave length spread of the instruments used [84, 83]. Consequently, data at higher  $q$  values contains less useful information. In this project, the reflectivity profiles were truncated based on calculations of the required sampling rate.

### 5.2.3 Data Processing

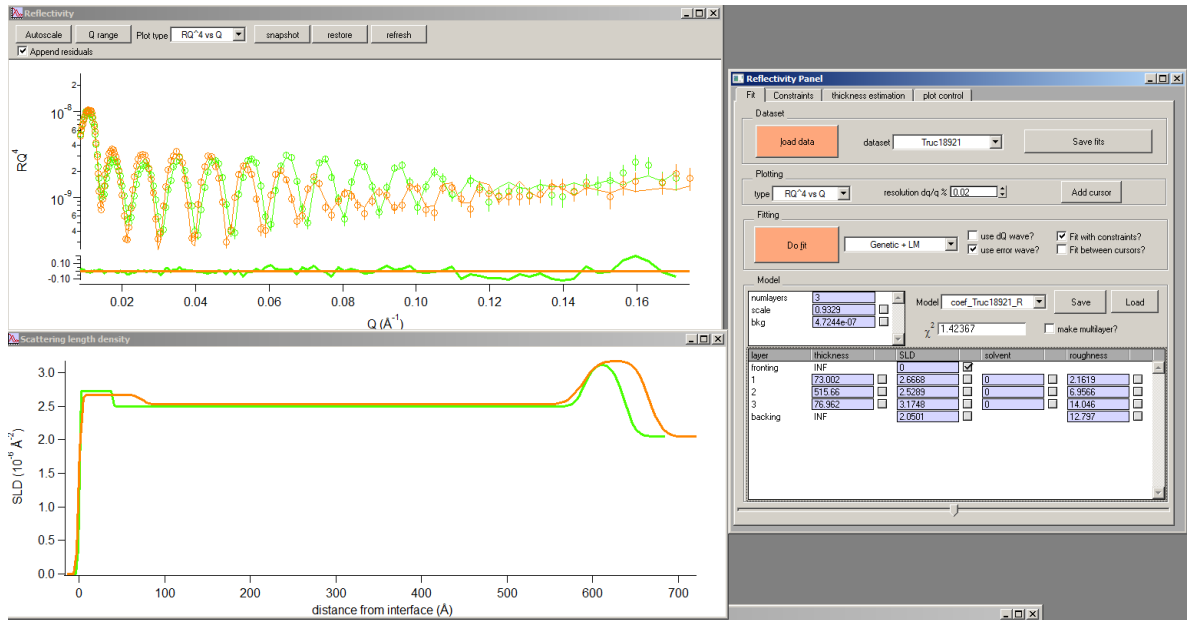


Figure 5.10: A screen shot from the Motofit script. In the top left hand corner two reflectivity profiles are shown with the data points and the fit. The fitted SLD profiles are shown underneath. On the right, the control panel of the model; this model shows three sample layers and their properties.

The reflectivity profiles  $R(q_z)$  were available to be plotted following the data reduction. A knowledge of the sample inferred from the preparation conditions and other means allowed a user defined initial estimate of the number of layers, and the approximate thickness & roughness of each layer. This allowed the calculation of an estimated SLD profile. Fitting the equivalent functions obtained from the estimated SLD profile to the measured  $R(q_z)$  allows a refined model of the SLD to be obtained.

Figure 5.10 shows a screen shot of the MOTOFIT package as  $R(q_z)$  is fitted. The goal of the fitting algorithm is to decrease the  $\chi^2$  goodness of fit parameter. The reflectivity drops exponentially with an increasing  $q_z$ , the profile is presented as  $RQ^4vQ$  (not as  $RvQ$ ) as this allows the fitting algorithm to give sufficient weight to the fringes higher  $q_z$ . Plotting  $RQ^4vQ$  allows weight to be given to any phase mismatch between the data and fit (shown later in Figure 5.11). The fitting algorithm was manually run iteratively, switching between plots of  $RvQ$  and  $RQ^4vQ$  to minimise the  $\chi^2$  on both the plots until the fitting routine returned the same models of SLD for both. Unless otherwise stated,  $\chi^2 < 1.5$  were obtained.

However, in complicated systems such as a multi-layered sample, it has been shown that there is often than one model of the sample that returns a modelled reflectivity profile with the same goodness of fit when compared to the data[72]. Therefore, in this study efforts have been undertaken to constrain

the parameter space for each variable to plausible values, using host of independent techniques to characterise sample roughness and thickness. These have included; TEM imaging, QCMs, and AFM imaging to inform the starting values and bounds for the coefficients.

## 5.3 Fitted Neutron Reflectivity Profiles

Following the data reduction fitting to refine the expected SLD profiles was undertaken. This section describes the process, the results and the verification of SLD profiles fitted to a range of samples in one of two extreme environments; with a high nitrogen gas content, or with a high vapour content. The implications of what is revealed from each fit are then discussed.

### 5.3.1 Polyimide Skin Layers

The purpose of this section is to present the SLD depth profile of the polyimide films in dry nitrogen. In order to achieve this, the reflectivity profiles from two 60nm films are fitted. The 60nm thickness has been chosen as these are the thinnest films examined and so the fringes will be much larger than the resolution in  $q_z$ . For comparison, two 60nm thin films which were prepared simultaneously are shown side by side; the sole difference between the films being the annealing regime (soft and hard cure), which is discussed in section 3.4. Surface sensitive techniques such as AFM showed no clear difference between the morphology of the two samples. However, section 3.4 showed that soft cured polyimide films absorb more water, and have an higher density, than the hard cured equivalent, yet a Fickian analysis showed no difference in the timescales of water vapour ingress. It was suggested that the difference in sorption properties resulted from the soft cured film containing a remnant amount of the polyimide solvent (GBL), which is hydrophilic.

An understanding of the depth profile may reveal any significant structural differences between the two films, about which very little is known. Therefore, the two profiles are presented in a dry nitrogen state.

#### The Fitting Procedure

Initially, attempts were made to fit the dry state profiles with a two layer + substrate model, a polymer layer, a  $SiO_x$  layer, and the silicon substrate, as shown in Figure 5.11.

Initial fit variables for the polymer layer were estimated based on the QCM results (thickness via a mass density calculation), AFM scans (roughness), and the manufacturers data sheets (SLD calculated from the chemical composition and density), for the given film. These estimations were fed

into the model as starting parameters, which could then be varied to obtain the minimum  $\chi^2$  goodness of fit test using a *Levenberg–Marquardt* [160], and *Optimization by Simulated Annealing*[161] fitting algorithms, which were native to MOTOFIT[61, 162]. When both fitting algorithms converged on the same solution, that solution was taken as the best fit.

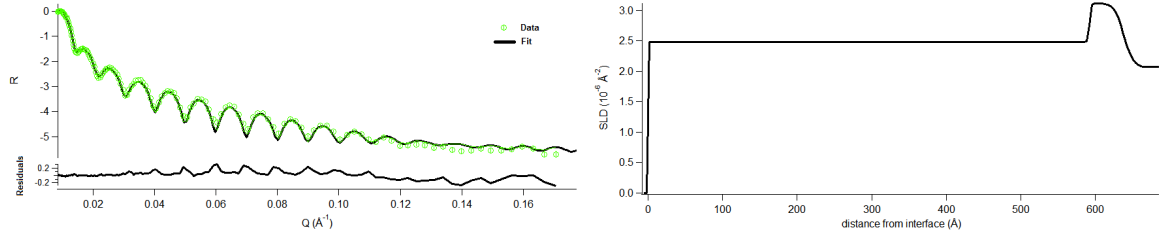


Figure 5.11: A two layer model fitted to  $R(q_z)$  of the soft cured sample. The reflectivity profiles (left) and the residuals (bottom) of the plot. The SLD profile (right) with  $\chi^2=3.72$ .

The best fits obtained assuming two layers are shown in Figure 5.11. The residual plot shows a periodic fluctuation, characteristic of a phase mismatch between the fitted model and the data, starting at a  $q_z$  value of around 0.04. The goodness of fit of the  $R(q_z)$  was higher than expected as  $\chi^2=3.72$ . This implies that the model is missing some features which may be present in the film.

The best fit SLD profiles were obtained using a three layer model, shown in Figure 5.12. These fits were obtained by splitting the polyimide layer into two equally sized layers with the same properties and allowing the fitting algorithm to vary the layer characteristics. The introduction of the additional layer eliminated the periodic variation in the residuals of the fitted line and improved the goodness of fit. It reveals a density variation in the polyimide, in the form of *skin*-like surface layer which has been found to be a feature on the best fit profiles of all the acquired reflectivity profiles. This as been observed in previous reflectivity studies of polyimide[128] and other materials[60, 163, 164]<sup>6</sup>.

The features of this fit were corroborated after the NR experiments using TEM. TEM samples were produced from three NR samples after the experiments conclusion by cross sectioning in the FIB. A sample structure of the polyimide-silicon oxide-silicon substrate has been verified with similar thickness and roughness values; one such image is presented in Figure A.16.

<sup>6</sup>Skin layers in absorbing materials was discussed in section 1.4.2.

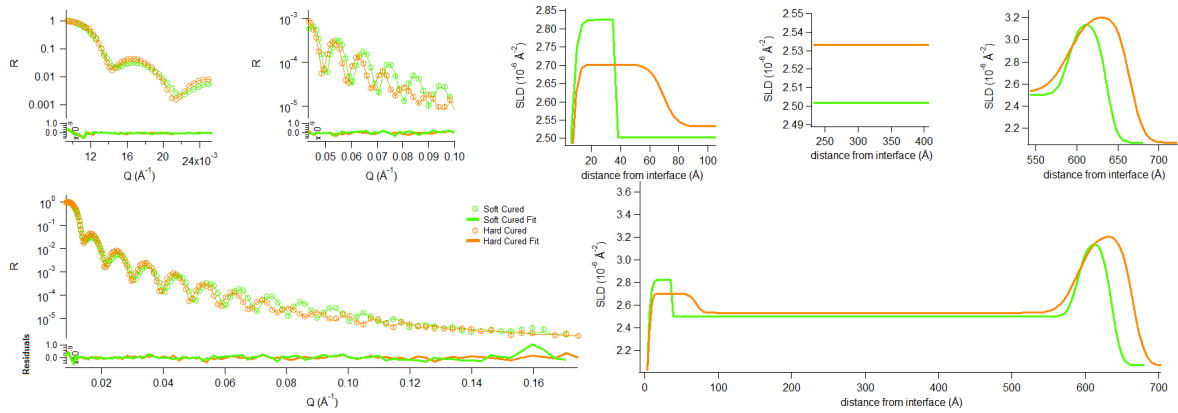


Figure 5.12: A three layer model fitted to  $R(q_z)$  with the SLD profiles (right) corresponding to the fit (left).  $\chi^2=1.14$  and  $\chi^2=1.34$  for soft cured and hard cured films respectively.

One troubling feature of the SLD profiles shown in Figure 5.12 is the thickness of the oxide layer. These silicon blocks were purchased from Crystran[165] and very little is known about their pre-treatment procedures. Conventionally, a native oxide layer on such a substrate would be expected to be a few nanometers[166]. Therefore, the chemical profile and composition of the TEM samples which were taken from the NR samples were investigated using EF-TEM. Figure 5.13 shows the oxygen profile of the 60nm hard cured sample, the NR fit for which was shown in Figure 5.12. Both techniques show a thicker than expected oxide layer with a thickness of approximately 10nm. When comparing the three samples examined, the EF-TEM images reveal a surprising variation (8-12nm) in the oxide layer thickness between samples, this variation must result from processing variability. The EF-TEM analysis confirmed a surprising result which originated from the fitted SLD profile.

It is unlikely that any processing steps undertaken during this investigation have caused such a growth in the oxide layer as typical thermal oxidation temperatures are of the order  $1000^\circ\text{C}$ [46].

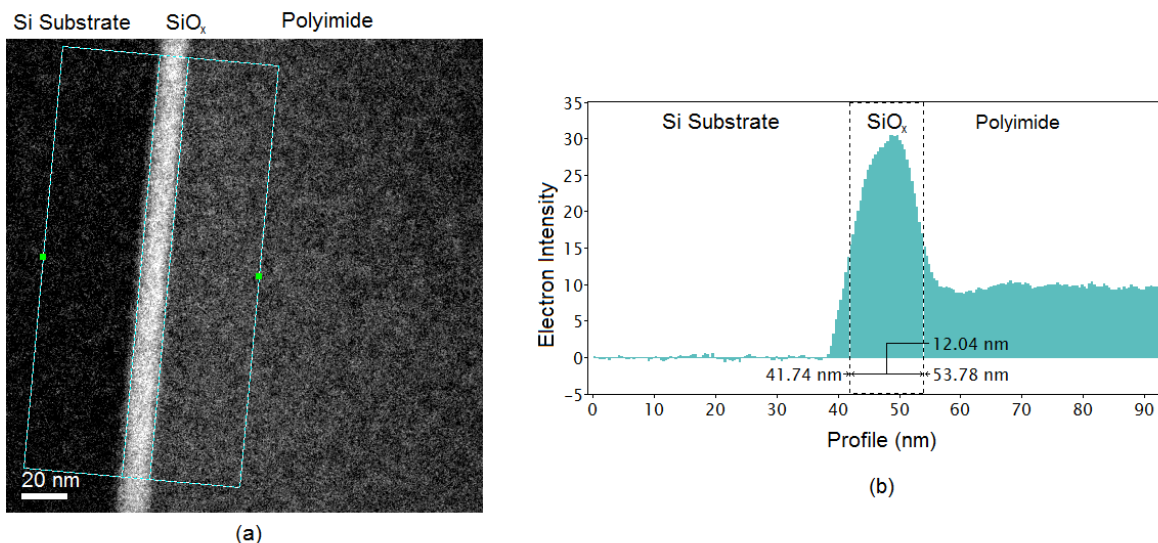


Figure 5.13: The oxygen profile (532eV energy) in the 60nm hard cured sample. (a) The EF-TEM image acquired using the three window technique. (b) The corresponding line profile showing the electron counts. Note: Longer frequency intensity variations in image (a) are due to sample thickness variations arising from FIB preparation.

The electron microscopy images did not show a skin layer, however the skin layer is  $\sim 7\text{nm}$  and from Figure 5.12 the SLD difference between the skin layer and bulk polymer is  $0.2 * 10^{-6} \text{\AA}^{-2}$  (for the hard cured sample) assuming that they are the same chemical composition, gives a density difference of  $\approx 0.12\text{gcm}^{-3}$  or 8%.

An attempt was made to investigate the skin layer using the HAADF scattering in a Scanning-TEM and the results were inconclusive. The intensity of the electrons scattered through a high angle in a sample of uniform chemical composition is proportional to the density of the sample. However, polyimide samples are prone to charging when exposed to an electron beam, as shown in Figure A.4, and a conducting layer is normally deposited on the surface of the sample. However, the deposition of a thin conducting layer affected the surface of the polymer, making surface related density variations difficult to discern. An example of metal implantation into the polyimide which would impact such a surface measurement is shown in Figure 5.29.

### Profile Discussion

The longer, hotter hard cure has had two consequences on the thin film; firstly, on the structure of the skin layer, and secondly, a slight change in the density of the polymer, as shown in Figure 5.12.

The bulk SLD measurement of the polyimide, measured to be  $\approx 2.5 * 10^{-6} \text{\AA}^{-2}$  according to Figure 5.12, returns a density of  $1.27\text{gcm}^{-3}$  according to Equation 5.1 and using the manufacturer provided chemical formula. This corroborates the measurements of density presented using the QCM/density

technique in Section 3.4, which gave densities of  $1.29gcm^{-3}$  for the soft cured films and  $1.25gcm^{-3}$  for the hard cured films.

A calculation of the density from an SLD profile requires a precise knowledge of the ratio of the elements present in the thin film. As noted in Section 3.4, on average the soft cured films tend to have a higher mass before undergoing a hard cure. A small quantity of the polymer solvent, gamma-Butyrolactone, GBL, which has a boiling point of  $204^{\circ}C$ , may remain in the thin film after a soft cure (maximum temperature of  $90^{\circ}C$ ). The slight variation in the SLD between the soft and hard cured films is  $\approx 3 * 10^{-8}\text{\AA}$  in the bulk; if GBL ( $C_4H_6O_2$ ) alone is responsible for this SLD difference the expect mass difference between the two films would be  $\simeq 0.03gcm^{-3}$ , where the QCM/AFM method showed a density difference of  $\simeq 0.04gcm^{-3}$  (Figure 3.15). This supports the theory that some GBL remains in the polymer after soft cure increasing its hydrophilicity.

Interestingly, the hard cure appears to cause the skin layer to grow thicker, from  $\sim 4nm$  to  $\sim 7nm$ , with a reduction in the peak SLD of  $0.12 * 10^{-6}\text{\AA}^{-2}$  for the skin layer. The two skin layers occupy a similar area on the SLD map in Figure 5.12; the soft cured layer has an SLD of  $0.32 * 10^{-6}\text{\AA}^{-2}$  greater than the bulk SLD and has a width of  $\sim 40\text{\AA}$ , while the hard layer has an SLD of  $0.2 * 10^{-6}\text{\AA}^{-2}$  greater than the bulk SLD and a width of  $\sim 70\text{\AA}$ ; approximating both to a rectangle gives areas on the graph of  $12.8\text{\AA}^{-1}$  and  $14\text{\AA}^{-1}$  for soft and hard film respectively. This implies that the skin layer density is spread out by the hard cure.

The observation of the skin layer is of significance as skin layers in general have been shown to impact on the transport properties of thin membranes[163, 52] and determine a membranes nanofiltration (NF) properties[139]. Abbott et al. showed a *highly orientated skin layer being resistant to solvent penetration* in another system using NMR[60]. Additionally, within membrane studies, mapping skins layers has been performed using SEM techniques[138]which would not work on such a thin skin layer. In polyimides skin layers have been discussed upon[163] and measured using low resolution NR for foamed polyimide[128].

Here, two types of very thin skin layer are reported with the nature of the skin layer affected by the curing type. The existence of a well defined skin layer would lead to two diffusion coefficients in the polyimide thin films, a skin diffusion coefficient and bulk diffusion coefficient. Consequently, the thickness dependant diffusion coefficient would have precisely the same features as were presented in Figure4.4; a diffusion coefficient which increases with thickness.

### 5.3.2 Deuterated polyimide Films

Having shown a credible model for the structure of the two 60nm thin films in a dry state, a SLD profile is now fitted for the same films in a vapour rich atmosphere. A full reflectivity profile will allow a better understanding of any clustering which may occur in the films, for example, if water vapour is adsorbed at an interface.

$D_2O$  rather than  $H_2O$  has been used to generate vapour. The use of the deuterated species of a given molecule is a common technique in neutron experiments to generate contrast[75, 156], and should not affect the scheme of mass transport significantly. The molecular dimensions of water and heavy water are similar, with masses being  $\approx 18g/mol$  and  $\approx 20g/mol$  respectively. Heavy water,  $D_2O$  has a significantly higher neutron cross section and a opposite sign to that of  $H_2O$  and so generates a higher contrast in the film.

#### The Fitting Procedure

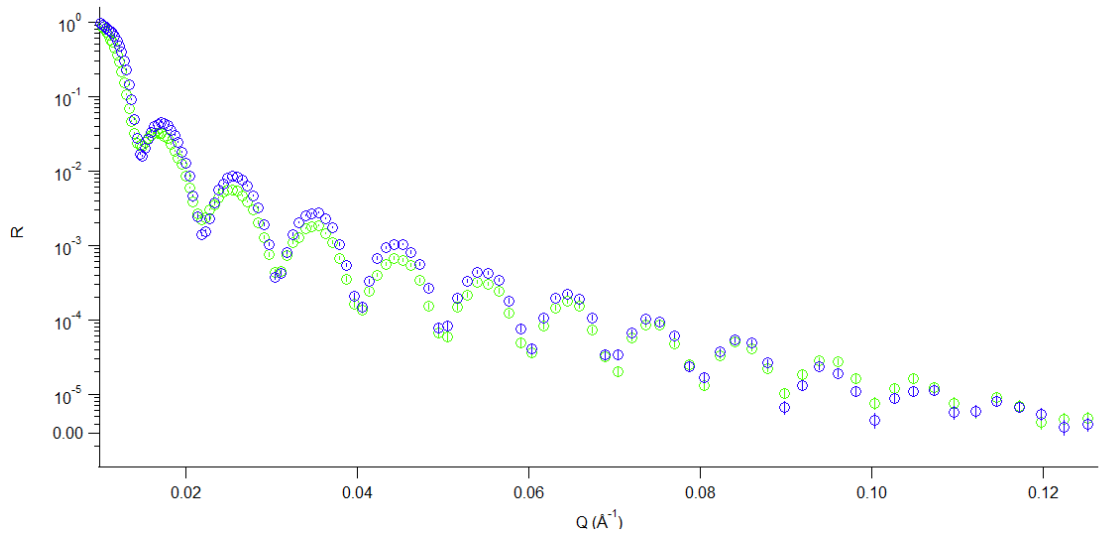


Figure 5.14: The raw data for the hard cured film in a dry and vapour rich atmosphere. There is a slight shift out in the critical edge of the wetted film and an increase in the fringe depth. However, surprisingly, the period of the fringes is the same on both films indicating that no swelling occurs upon absorption.

Before proceeding to fit the reflectivity profile, a preliminary qualitative analysis of the reflectivity profile data, which is shown in Figure 5.14, can be performed to help guide the fitting procedure. Section 5.1.2 discussed the relationship between the period of the Fresnel fringes and the sample thickness. Figure 5.14 shows no appreciable difference between period of the fringes in both the data sets; indicating that these polyimide films do not swell when water vapour is absorbed, which is

common in water absorbing systems[167]. This is not entirely surprising as studies of some polyimides have found very little swelling, such as that of Bhargava et al. who found 0.33% swelling in a HFPE-II-52 polyimide between 0%rh and 100%rh[168]. Figure 5.14 also shows a consistent increase in the fringe amplitude when vapour is present, indicating an increased contrast in the film, which is consistent with absorption.

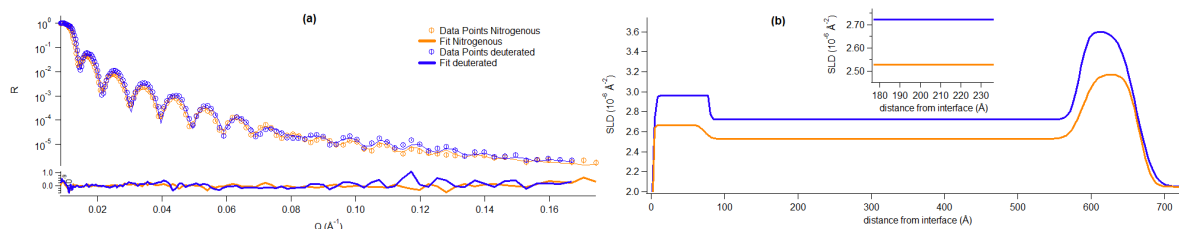


Figure 5.15: A badly fitted reflectivity profile using a three layer model. The reflectivity data points, (a) fitted reflectivity curve and (b) fitted SLD profiles for a hard cured film in a nitrogenous and vapour atmosphere. The  $\chi^2$  values for the fits are 1.41 for the dry film and 2.99 for the D<sub>2</sub>O.

Figure 5.15 shows the reflectivity profile and fit for a hard cured 60nm thin polyimide film in a nitrogenous and deuterated atmosphere. The fit shown in Figure 5.15(b) is the result of a fitted three layer model, for which the starting parameters were those of the equivalent dry fit. The fit shows a periodicity in the residuals and worse goodness of fit. In the previous section, the polyimide bulk layer had been split up to account for density variations in the polymer. The error level suggested that a three layer model did not provide sufficient mathematical tools to present an uneven distribution of  $D_2O$  in the polymer and so could only present a version of the dry profiles shifted to a higher SLD. Consequently, the bulk polyimide layers were split up repeatedly to gain the lowest goodness of fit parameters possible. To avoid over fitting, such that the model describes the noise in the measurement and not the underlying structure of sample, two indicators were used. Firstly; when additional layers caused no difference to the fit, which converged on the best solution, the additional layers served no purpose. Secondly, the residuals plot was indicative of systematic errors which were user identified and re-fitted as required.

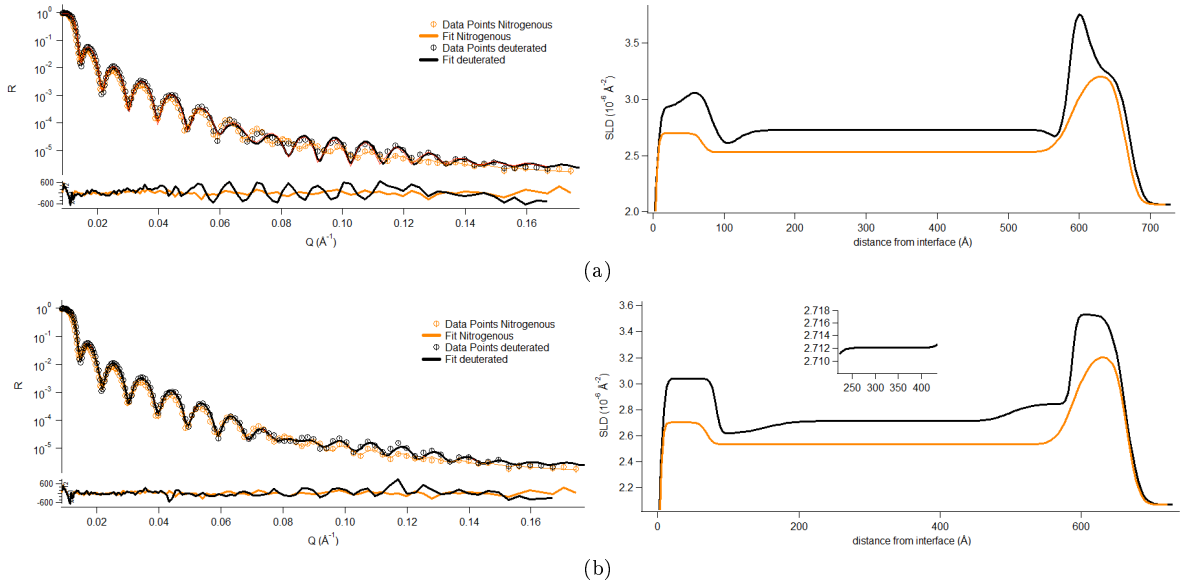


Figure 5.16: (a) A possible five layer fit for the soft cured 60nm film in which the oxide layer properties were frozen, i.e. assuming that vapour would not permeate the oxide layer. This resulted in a  $\chi^2 = 5.55$ . (b) A possible five layer fit for the soft cured 60nm with  $\chi^2 = 1.82$  in which the oxide layer characteristics were allowed to vary.

Surprisingly, the best fit profile across all data samples was obtained when the oxide layer was allowed to absorb water vapour. This is illustrated by comparing the fits shown in Figure 5.16 (a) and (b) which are the best fit solutions for an non-absorbing oxide layer and an absorbing oxide layer respectively. Although water vapour is conventionally thought of as adsorbing onto the surface of hydrophilic native silicon oxides[169], studies by Erlat et al. of polymer  $SiO_x$  interfaces[170], and Howkoo et al.[171], showed that water vapour permeation through  $SiO_x$  layer is a function of the defects, packing density, and morphology, of the layer. These factors are unknown in this oxide layer, the existence of which is surprising.

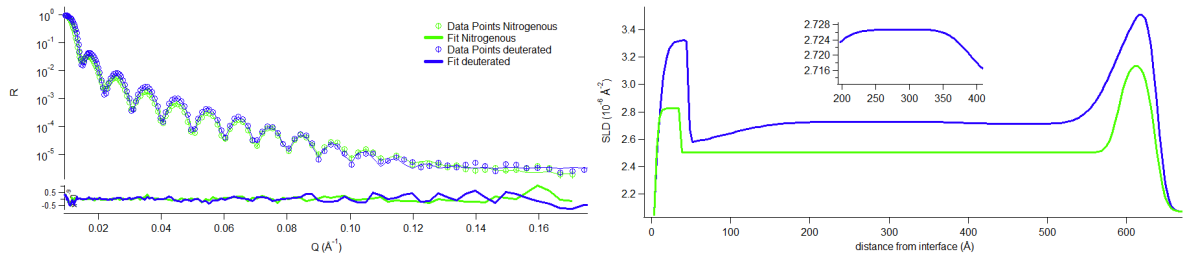


Figure 5.17: A five layer fit for the 60nm hard film when saturated with  $D_2O$ . The  $\chi^2$  is 1.54.

A five layer model gave the lowest best solution; this is presented in Figures 5.16(b) and 5.17 for the hard cured and soft cured films respectively. These models give an improved alternative fit for the  $D_2O$  sorption with a better goodness of fit. Although the residuals plot at higher  $q$  values shows a periodic oscillation effect implying a phase mismatch. However, the errors shown in the residual plots are several orders of magnitude lower than the readings.

### Profile Discussion

The existence of a skin layer corroborates the variable diffusion constant as a function of thickness of the films which was presented in Figure 4.4. Density variations have been shown to affect the transport and concentration properties of polymer materials, and a uniform thickness skin layer would play a larger role in the transport properties of a thinner film[52, 163]. The profiles shown in Figure 5.12 imply little change in the properties after the initial surface. This is reinforced by studies performed in the TEM, such as is presented in Figures A.16, in which the contrast is uniform in the polymer.

The profile of water vapour shows that for the bulk polyimide layer the soft cured films absorb more water vapour than those films which had undergone a hard cure, which was corroborated by QCM results<sup>7</sup> The concentration of  $D_2O$  increases around the silicon oxide layer, which is likely to have hydrophilic properties[172, 173].

The 60nm thickness allows an increased confidence in the fitted SLD profile as the Kiessig fringes have a larger period in  $q_z$  on smaller films (See Equation 5.8). Therefore the Kiessig fringes are sampled at much higher frequency than their oscillation frequency, with greater than 10 samples per period up to  $q_z = 0.01\text{\AA}^{-2}$  on a this film, see Figures 5.15(a).

Comparing the dry profiles and wetted profiles shows distribution of the  $D_2O$  is higher at the surface and the substrate than the bulk. This is surprising as the surface is shown to be denser than the bulk, with less free volume. However, immediately after the surface the concentration is lower than the bulk, therefore the higher concentration at the surface may be because  $D_2O$  that hasn't yet fully penetrated into the polymer.

In short, a vapour distribution scheme of: high concentration on the surface of the polymer, followed by a lower concentration in the skin layer, then the bulk layer, and finally a hydrophilic substrate, is evident when analysing Figures 5.16 and 5.17. This explains why extra layers are required to model

---

7

Relevant QCM results are presented section 3.4.

the deuterated reflectivity profile as, in addition to the three layers shown in the dry state profiles (skin-bulk-oxide), two transition layers are also required in between the three layers to model the  $D_2O$  distribution.

A Fickian analysis of the QCM results reveals that the timescales of diffusion are uniform across different thicknesses of the polyimide (compare Figure 4.1 to Figure 4.2). Therefore it is proposed that this is set by the surface layer properties. However, the absolute amount of water ingress into the film is set by the capacity of the film to hold water vapour, which is a function of the size, morphology and chemistry of the film.

### **5.3.3 The Impact of Oxygen Plasma Etching on polyimide**

Oxygen plasma etching is used by Honeywell as part of the standard process to bring the dimensions of spun cast polymer films within the tolerance levels required. The process involves the use of a high frequency electric field to produce an oxygen plasma. Placing the samples in the plasma atmosphere results in the bombardment of high energy ions onto the sample surface. This in turn attacks the surface resulting in a reduction in the dimensions of the polymer. The impact of etching on both the surface, and the overall vapour density of the thin film, are of interest. Additionally, the previous section discussed the importance of the skin layer in the transport properties of the polyimide. However, the Fickian analysis presented in this section showed no difference in the timescales of diffusion between plasma etched samples and others; which is surprising as the surface treatment would be expected to influence transport timescales and certainly impacts the interface properties, as shown in Figure 5.18.

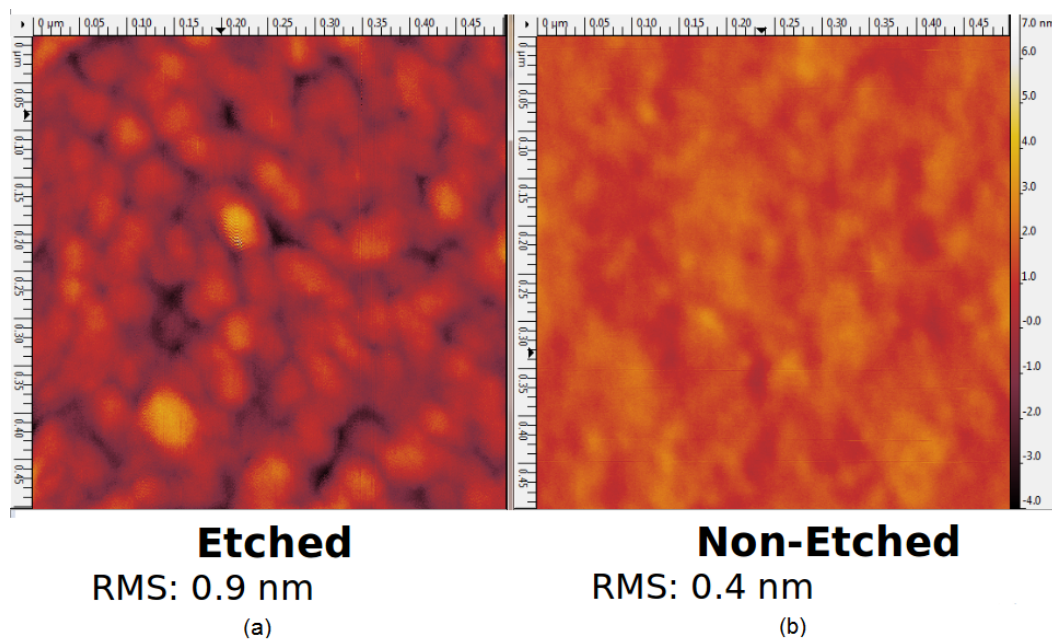


Figure 5.18: An AFM scan of two polyimide surfaces. (a) Shows the etched polyimide with a higher surface roughness and (b) Shows a smoother surface.

In this investigation  $O_2$  plasma etching has been performed on two polyimide films, these reflectivity profiles were acquired on the D17 instrument. The process used to etch the films was calibrated by masking off a section of the thin film and placing it inside the plasma environment, which created a step height that was then measured using standard AFM techniques. Figure 5.18 shows the morphology of an etched and non-etched hard cured film. Etching increases the surface roughness as the Oxygen atoms attack the surface. This is of particular interest as the rougher surface equates to an increase in the surface area of the polymer film.

### The Fitting Procedure

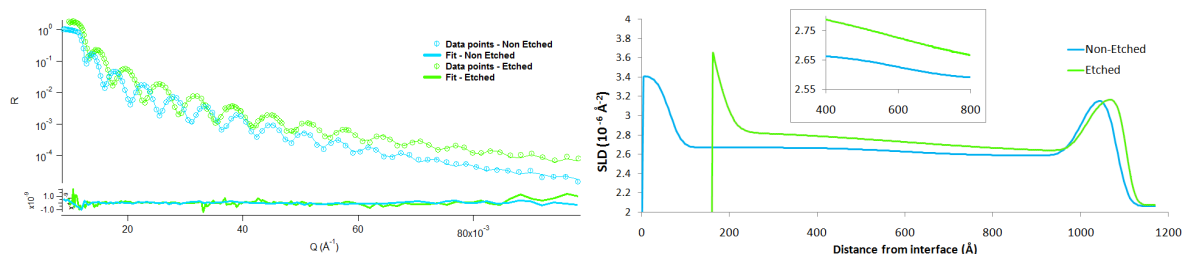


Figure 5.19: The reflectivity of the Etched ( $\chi^2=1.57$ ) and Non-etched ( $\chi^2=1.99$ ) films in a Nitrogenous atmosphere, the films were spun with a target thickness of 90nm and one of the films was then etched. These reflectivity profiles were acquired on the D17 instrument

Figure 5.19 shows the neutron reflectivity profiles of two samples prepared using the same solution and spinning conditions, after which both samples had undergone a hard cure. The two samples were then separated and one was etched. The data shown in Figure 5.19 were collected at two different facilities; D17 at ILL [82] for the etched film (*thickness*  $\approx 80\text{nm}$ ), and Inter at RAL [84, 83] for the non etched films(*thickness*  $\approx 95\text{nm}$ ). The SLD and roughness values shown in the previous section were used as the starting SLD parameters for these fits before the refinement through fitting.

In Figure 5.19 the bulk SLDs of the films is  $2.65 * 10^{-6} \text{\AA}^{-2}$  (non-etched) to  $2.75 * 10^{-6} \text{\AA}^{-2}$  (etched) implies a density increase following the etching procedure from  $1.33\text{gcm}^{-3}$  to  $1.38\text{gcm}^{-3}$ , assuming no chemical changes in the polyimide. This increased surface density is observed directly in the reflectivity profile in which the critical edge of the etched films are shifted to a higher  $q_z$ . Both of these values are higher than those obtained in the QCM analysis of  $1.25\text{gcm}^{-3}$  and  $1.29\text{gcm}^{-3}$ , but the increase in density is similar and the densities are not constant in the films as a function of depth. The density measured for these 90nm films is also higher than the equivalent (60nm) films measured at the Inter instrument, perhaps indicating some small systematic error.

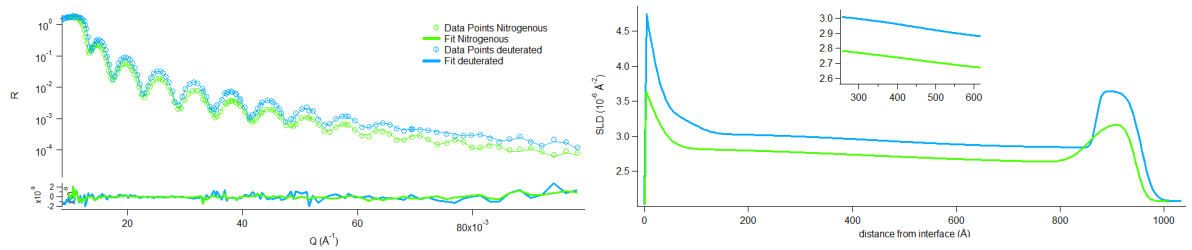


Figure 5.20: The 80nm Etched film with dry nitrogen( $\chi^2 = 1.64$ ) and  $D_2O$  ( $\chi^2 = 3.4$ ) in the atmosphere.

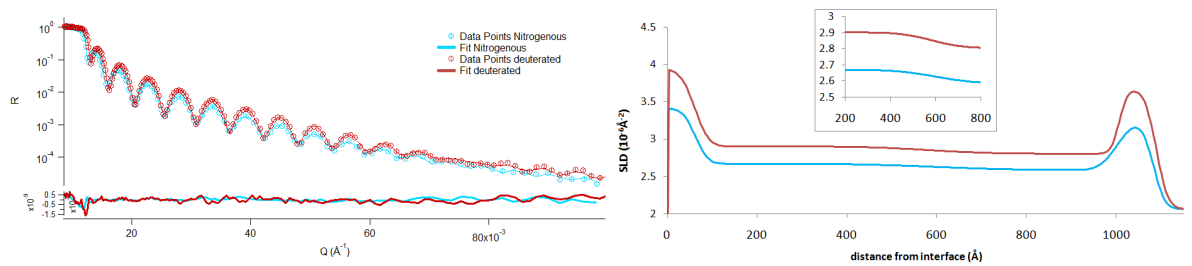


Figure 5.21: The 95nm non-etched film with dry nitrogen( $\chi^2 = 2.4$ ) and  $D_2O$  ( $\chi^2 = 2.0$ ) in the atmosphere.

The films shown in Figure 5.19 are shown again in a  $D_2O$  vapour atmosphere in Figures 5.20(etched) and 5.21(non-etched). The five layer fits show an even distribution of  $D_2O$  however the best fit obtained

still has a relatively large  $\chi^2$  when compared to the thinner films. This may be as expected as the film thickness is increased, however each period included in the fit is sampled a minimum of six times per oscillation. Various strategies to improve the fit were attempted, including adding more layers, however the best fits are presented. Any conclusion to be drawn from the fitted SLD profiles must take account of this.

### Profile Discussion

The major result from this section is the increased SLD of the etched films when compared to the non-etched films. Such a density increase would be expected to impact on the transport properties of polyimide and inhibit the water absorbed. This agrees well with QCM results, which show etched films absorb less water vapour (see Figure 3.16). This may explain the lower sorption in etched film as measured by the QCM. However, while the vapour uptake in the films appears similar, as indicated by the SLD shift in the bulk of both films of  $\sim 0.2 \times 10^{-6} \text{ \AA}^{-2}$ , the uptake varies through the film. As a result, the QCM measurements, which were taken in a much better controlled environment, are more likely to provide a better reading.

The etching procedure appears to have shifted the skin layer deeper into the film. The model indicates an increase in the roughness (the definition of which was discussed in section 5.1 and is detailed as described by Nelson et al.[162],) as a result of etching, from 0.2nm to 1.1nm, and the AFM measurement also showed an increase in the roughness of the etched film. However, while the two measurements of roughness are of the same order of magnitude, they cannot be compared as the AFM measurements do not account for longer frequencies of roughness<sup>8</sup>.

### 5.3.4 $H_2O$ and $D_2O$ Contrasting

$D_2O$  has been used as a proxy for  $H_2O$  during the course of this study. For completeness, an SLD profile with  $H_2O$  vapour in the atmosphere is presented in this section. The reflectivity from the 80nm etched film, shown in Figure 5.20, has been measured in a  $H_2O$  atmosphere.

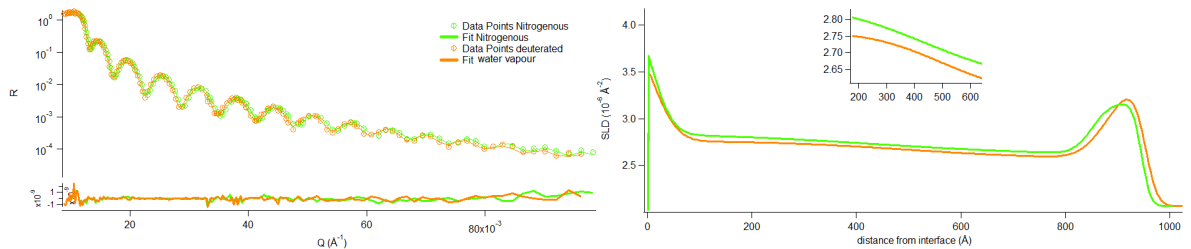


Figure 5.22: Water saturated (orange) and dry (green) etched polyimide film. The  $\chi^2$  values for the fits are 1.64 for the dry film 1.6 for the  $H_2O$ .

<sup>8</sup>This is illustrated in a larger AFM scan shown in Figure A.3

As previously noted, the neutron cross sections of water and heavy water have opposite signs which is observed when contrasting Figure 5.22 and 5.20. It was previously noted that ingress of  $D_2O$  in the film is even and results in a bulk uptake of  $0.034gcm^{-3}$ . Figure 5.22 distribution is even, ingress of  $H_2O$  returns an SLD difference of  $-4.5 * 10^{-8} \text{ \AA}^{-2}$  which implies a water ingress of  $0.08gcm^{-3}$ . This is an interesting difference as it implies that a greater mass of  $H_2O$  enters the film when compared to  $D_2O$  at the same flow rate of nitrogen. or some variation in the nitrogen flow. Lapham et al. indicated that the diffusion coefficient for  $D_2O$  is lower than that of  $H_2O$ . Additionally, a variation in the nitrogen flow into the cell may have caused a difference of  $\sim 20\%$  in the reading. The distribution pattern in both SLD profiles is approximately even, and consequently,  $D_2O$  can still be used as a good indicator of the movement of water vapour in the polyimide.

## 5.4 Time Resolved Neutron Reflectivity

Readings of the density profile of the thin films in a static atmosphere are capable of providing limited information about the transport mechanisms at work. However, a time resolved density profile series with a time resolution less than the diffusion time can provide an insight into how the vapour moves through the polymer. This section presents a novel method capable of making such measurements.

Generally, the time taken to acquire a neutron reflectivity profile with sufficient statistics ( $\sim 2hrs$ ) is much longer than the time constants of the diffusion in the thin film. The time taken to acquire profiles has limited the capabilities of NR experiments to probe dynamic systems in the past. However, relatively recently techniques have been developed to allow reversible events to be probed giving time resolved NR profiles. This allows time resolution on the order of seconds[77, 174] and most recently using other neutron based techniques has tracked water ingress in polymer films without giving an SLD profile[78].

In this study the neutron collection and the atmospheric changes in the duty cycle are synchronized to allow time resolution. Although a similar technique has been used to obtain small angle neutron scattering data with time resolutions of the order of microseconds[175, 176], the time resolution of neutron reflectometer has been limited. The collection of full reflectivity profiles is more often performed on the order of seconds, as demonstrated in studies performed by Glidle et al. in 2009[77]. More recent instrumentation improvements have allowed dynamic changes in vapour levels within the polymer to be probed with 200ms time resolution[177].

Thus far, the samples which have been probed have focused on transport within the polyimide. How-

ever, Honeywell sensors require the transport of vapour through the metal overlayer, which acts as a top electrode in the capacitance sensors, and which may affect water vapour penetration into the film. As a result time resolved data has been collected for systems with a metal overlayer.

### 5.4.1 Experimental Methods

The neutron reflectivity measurements presented here were performed using the Inter reflectometer operating in time-of-flight mode. For static measurements, two paths for  $N_2$  flow are available; directly into the cell or via the gas bubblers to produce vapour, generating a dry and humidified cell atmosphere respectively. The path taken was determined by a DC voltage fed into two valves; a *normally closed* (by default) value and an *normally open* (by default) value; both valves were supplied by the same power supply. Here, the voltage was supplied by a wave pulse generator. This determined the duty cycle, leading the cyclical vapour loading/unloading of the film associated with the changes in the ambient vapour concentration.

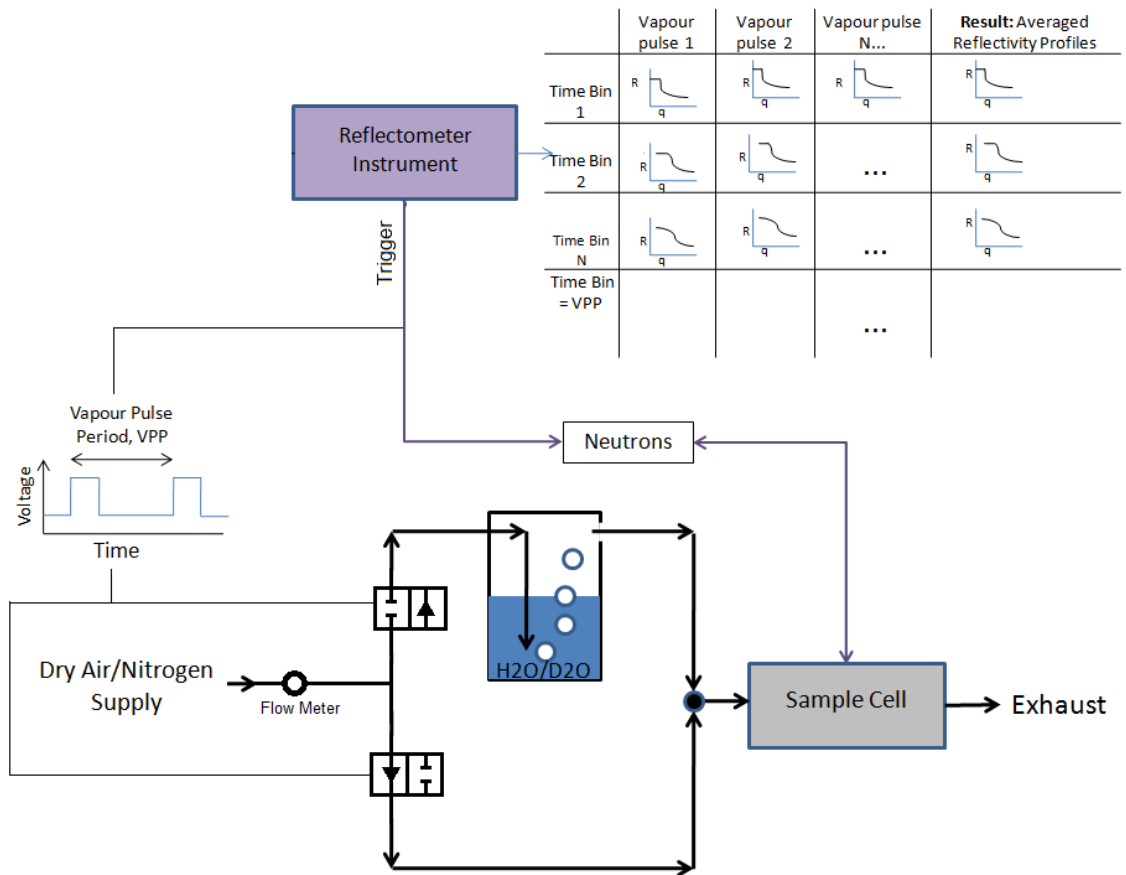


Figure 5.23: The scheme for taking dynamic measurements. A wave generator was able to control the duty cycle.

The rising edge signified the start of the duty cycle, triggering; the start of the binning into the first *time bin* and a change in flow path of the nitrogen. This led to neutrons from the equivalent point in several duty cycles to be allocated into the same time bin, with each time bin containing a reflectivity profile. Figure 5.23 shows a scheme for dynamic measurements in which the pulsing of the neutron beam is synchronised with a pulse of water vapour in the sample.

The repeated cycles resulted in a *box car* averaged reflectivity profile, for which the Poisson statistics of profiles would continue to improve until the cessation of the experiment. The eventual result being an array of reflectivity profiles with each profile corresponding to a given time in the duty cycle.

The size of the time bin is manually set, but limited to being a multiple of the neutron chopper wheel rotation speed, .i.e. the maximum period at which neutrons could arrive at the sample.

The capacitive based humidity sensor's response time was reported by Honeywell to be on the order of one minute (to obtain steady state readings). Therefore, 200ms time resolution was considered sufficient to capture the kinetics of the mass transport in this system. The use of the same pulse generator to control the duty cycle of both, the vapour and the reflectometer binning, ensured time synchronisation. The cell was under constant positive pressure, and so the exit piping was open to the atmosphere, as shown in Figure 5.5.

To gain a spectrum with good statistics  $\sim 2hrs$  per angle is desirable. Here, with each time bin producing a reflectivity profile, there was a collection time of  $2hrs \times \text{the number of time bins}$ . For example; a dynamic data set with a vapour pulse period lasting 40s, and with a time resolution of 0.2s, results 200 reflectivity profiles. However, collection of such reflectivity profiles generally took place overnight for 10 hours; each resulting reflectivity profile would have 15min worth of counts. Therefore the confidence level of the data acquired using this method is significantly lower than the static reflectivity profile.

Static measurements presented in the previous section have enabled an understanding of the films in a dry and wet state. This information then informed the fitting procedure for the time resolved reflectivity profile during fitting.

## 5.4.2 Data Processing

The acquisition and reduction of the reflectivity profile was performed using the software provided by the instrument scientists. The time resolved data was then summarised in a three dimensional matrix with the three columns;  $q_z$ ,  $R(q_z)$ , and  $dq_z$ , repeated n-times where n is the number of time bins. This section outlines some post processing steps performed on the reduced data which were developed for this project.

### Direct analysis of $R(q_z)$

A MatLab script was coded for this project to filter data with a low statistical significance to obtain direct measurements of the behaviour of key features of the reflectivity profile. This script utilised Equation 5.5 to allow a fast read out of the critical edge,  $\Delta q_{critical}$ , and the period of the Kiessig fringes, without the need to fit a complete model. When processing time resolved data such an analysis proved especially useful, as it allows the analysis to be focused on the reflectivity profiles which capture a largest mass flux. Figure 5.26 shows a typical output of the script which presents information from all the detection mechanisms; QCM, capacitance, and neutron fitting in a single graphic.

Firstly, to filter the data, any data point with  $\frac{dq}{q} > 0.3$ , i.e. the error is greater than 30% of the reading, was disregarded as this was deemed to have insufficient statistical significance. The reflectivity profile was also truncated at high  $q$ -values due to lower counts and poor resolution (see Figure 5.9).

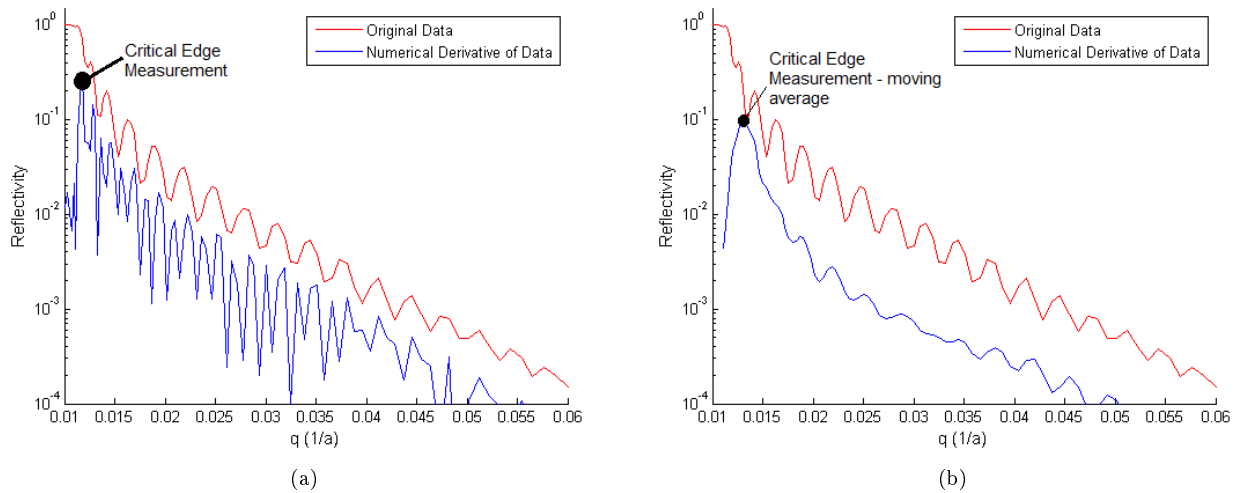


Figure 5.24: A reflectivity profile of a 180nm polyimide oxygen plasma etched thin film with 5nm of gold sputtered on the surface shown with, (a) its numerical derivate, as the peak in the derivative shows the critical edge, and (b) the ten point moving average of its derivative. Averaging skews the absolute measurement of the critical edge.

Monitoring the critical edge allows the surface state of the sample to be understood. The variation in the shape of the reflectivity profile around the critical edge,  $q_{crit}$ , is a function of the surface roughness, which was described in section 5.1. A robust automated method of identifying  $q_{crit}$  is desirable to estimate the timescales involved in vapour reaching the sample surface. Here, the peak of the absolute value of the numerical derivative, the peak in  $\frac{dR}{dq}$ , as shown in Figure 5.24, is used to find the critical edge. This was successful on the static data, due to a good signal to noise ratio, as in

Figure 5.24 (a). However, time resolved data sets with a lower signal to noise ratio leads to a noisy numerical derivative,  $\frac{dR}{dq}$ , which results in inaccuracies in the determination of the critical edge using this method.

A moving average on the data as shown in Figure 5.24(b) acts to smooth the plot of  $\frac{dR}{dq}$ . The moving average also results in a skewed measurement of  $q_{crit}$  due to the significantly lower values of reflectivity as  $q$  increases. This can be observed by comparing the reading of the critical edge on Figure 5.24(a) and (b), the same data set. Therefore, only the shift in the critical edge,  $\Delta q_{critical}$ , can be measured after the derivate graph has been averaged.

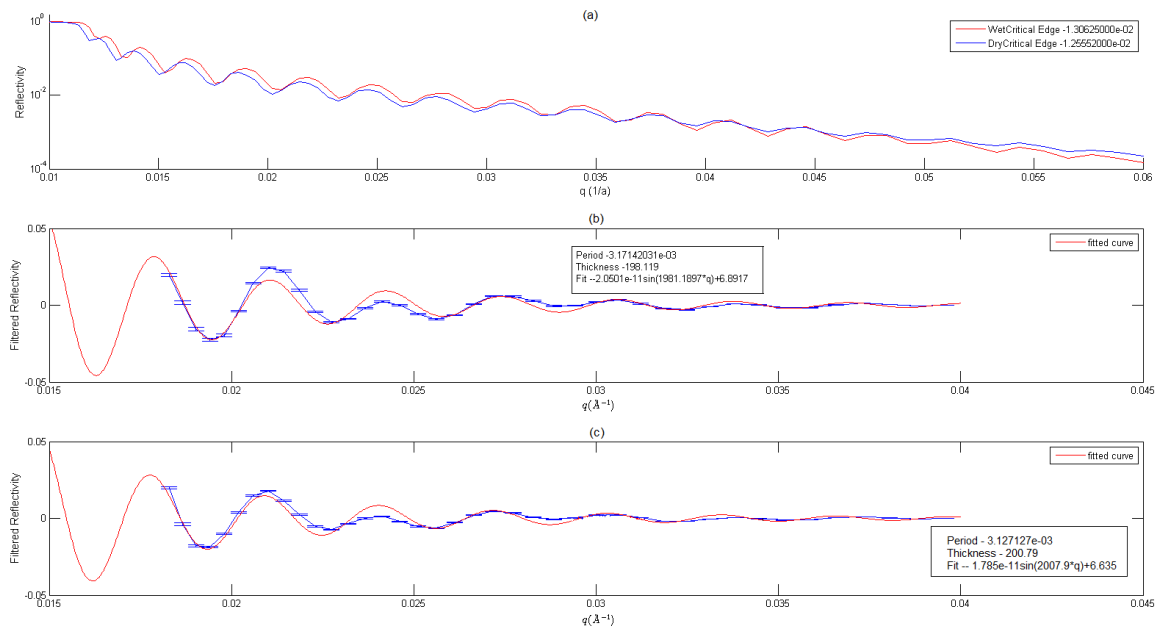


Figure 5.25: An example of the output from the scripts developed to perform a direct analysis of the reflectivity data. (a) shows two sets of data, in a vapour and dry atmosphere, of the 180nm polyimide film. (b) shows the vapour atmosphere data fourier filtered for longer spatial frequencies and fitted with a sinsoidal wave. (c) shows the dry atmosphere data fourier filtered for longer spatial frequencies and fitted with a sinsoidal wave.

Other features of interest in a given spectrum are the period and the change in the amplitude of the fringes as described by Equation 5.7. The validity of Equation 5.5 was discussed in section 5.1 and it was noted that the underlying kinematic assumption was not valid close to the critical edge. The impact of the kinematic assumption can be directly observed by studying the variation in the periods of the two reflectivity profiles shown in Figure 5.25(a), the Fresnel fringes of the two data sets begin with a phase mismatch at the critical edge, coming in phase at around  $q=0.03$ . Therefore, it is desirable to remove the effects of the critical edge when analysing fringes. As such, a low frequency Fourier filter

has been applied to the data. The frequency beneath which to filter is estimated as a 0.1\*expected fringe frequency. The expected fringe frequency can be estimated from the target film thickness of the films, via part of Equation 5.7,  $t = \frac{2\Pi}{\Delta q_z}$ .

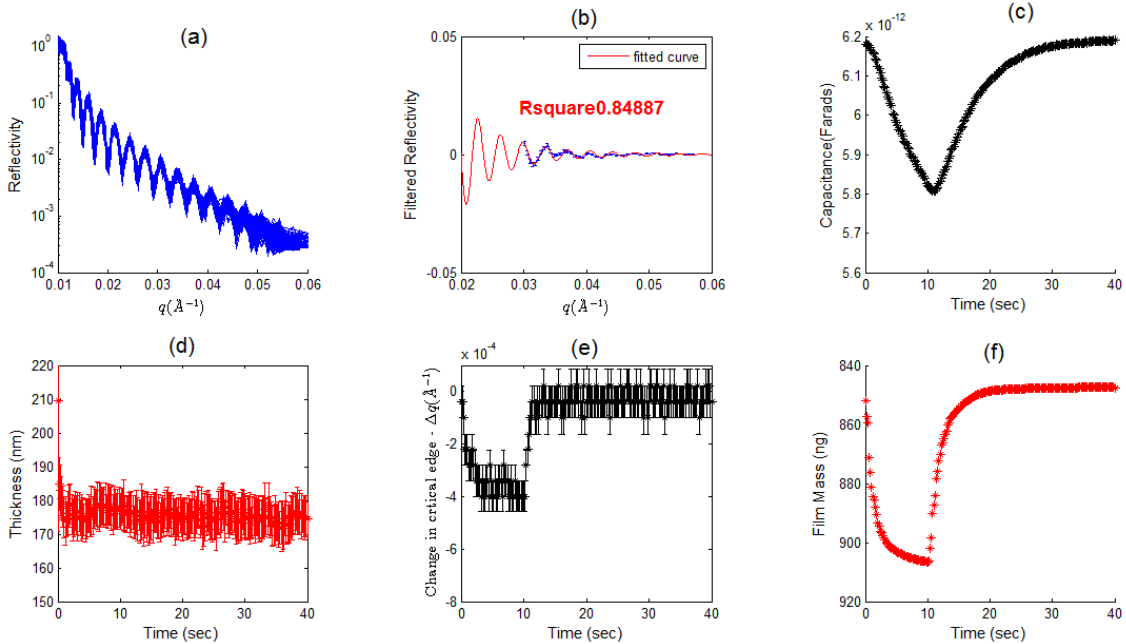


Figure 5.26: The output of a script designed to fit each reflectivity profile in a given data set and compare it with the data from the QCM/Capacitive sensors. This data set shows the characteristics of two hundred reflectivity profiles acquired on an etched 180nm polyimide thin film with gold sputtered on the surface as it is exposed to nitrogen gas (for 10s) and vapour (for 30s) on a 40s duty cycle. (a) All of the reflectivity profiles,  $R(q)$ , plotted. Each profile corresponds to a 0.2s time bin within the 40sec duty cycle. (b) An example of a Fourier filtered reflectivity profile and the fit used to measure the thickness of the film. The fitted reflectivity profiles shown correspond to the last 0.2s time bin in the duty cycle. (c) The capacitive humidity sensor readout as a function of time though one duty cycle. (d) The thickness deduced from each fit to the profiles shown in (a), plotted as a function of time though the duty cycle. (e) The critical edge shift plotted as a function of time, measured from the reflectivity profiles shown in (a). (f) The QCM readout plotted as a function of time though a duty cycle.

The resulting wave is then fitted with a function of the form of Equation 5.7 which assumes a single layer on a substrate. The form used is  $(A \frac{16\pi^2}{q^4} \sin(th * q + \phi))$  where;  $A$  is an amplitude constant,  $th$  is a thickness estimate in  $\text{\AA}$  and  $\phi$  is the phase. This type of analysis of the reflectivity wave coupled with measurements from the capacitive sensor and the QCM mass read out is shown in Figure 5.26. To insure the fitting quality, an r-squared goodness of fit test was applied to each fit and could later be plotted along with the other coefficients of the fit.

**Fitting SLD profiles to time resolved data** Following the direct analysis and truncation of the

reflectivity profiles, the time resolved data sets have been processed using a variety of methods in order to extract the most pertinent information.

A standard SLD fitting script in the MOTOFIT package[153] enabled each reflectivity profiles in a data set to be fitted in turn using the values obtained in the previous fit as the starting parameters. This process led to a large table of fitted coefficients (thickness, SLD and roughness for each layer,) which could then be interpreted as an SLD profile for each of the reflectivity profiles. However, as previously noted, the statistical significance of the dynamic data are significantly worse than for the static reflectivity profiles, and automated fitting scripts do not distinguish between random and systematic errors, as is possible for a user performing a manual fit. Furthermore, fit parameters sometimes stray, skewing the fit away from the correct solution. Fitting each reflectivity profile individually would have been time inefficient.

However, few reflectivity profiles show a significant dynamic shift. This is shown in Figure 5.26(e), in which the greatest shift in the critical edge occurs in short spaces of time when compared to the full duty cycle. It would therefore be prudent to place additional emphasis on investigating the reflectivity profiles corresponding to a greater degree of change.

In order to identify the reflectivity profiles at key points in the duty cycle, a MatLab script was written to select reflectivity profiles from the time resolved data sets which corresponded to a large critical edge shift. The time resolved data was divided into four sub-data sets for each duty cycle, reflectivity profiles which represent a film in a; dry, wet, drying, and wetting state. The example shown in Figure 5.26 is processed again as shown in Figure 5.27; the reflectivity profiles have been split up into the four categories by the shift in the critical edge. The wet and dry reflectivity profiles were identified by binning each data point in Figure 5.27 according to the critical edge value into a four bin histogram. The first and last bin signified the reflectivity profiles corresponding to dry and wet, respectively.

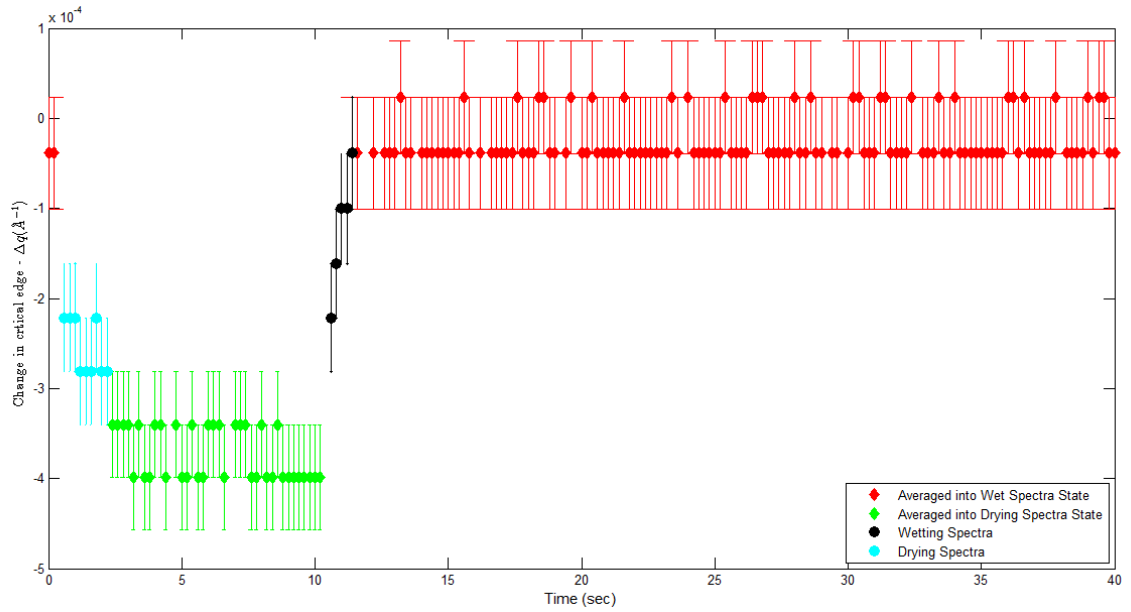


Figure 5.27: The critical edge shift as a function of time for a 180nm polyimide thin film which is etched and coated in 5nm of metal. 10 seconds dry - 30seconds of D2O vapour. The errors are the bin width in  $q$ .

After the reflectivity profiles had been identified as wet and dry, marked on Figure 5.27, the corresponding reflectivity profiles were aggregated to form two averaged reflectivity profiles. Each reflectivity profile was assumed to have an equal statistical significance. This is reasonable as the flux at the beam line was assumed to be close to constant.

To find the reflectivity profiles that corresponded to dynamic changes, a numerical differentiation was then performed on the data shown in Figure 5.27. All the reflectivity profiles showing a shift in the critical edge were fitted with two Gaussians are marked in Figure 5.27 as the drying and the wetting reflectivity profiles from Figure 5.26. These reflectivity profiles were then modelled, as detailed in the next section.

### 5.4.3 Polyimide with metalised layer

Honeywell sputter deposit a metal layer of  $\sim 5nm$  on top of the etched polyimide, which forms a porous top electrode for their humidity sensors through which water permeates. Data acquired on a sample prepared in a similar fashion to reflect the architecture of the sensors is studied in this section. Time resolved neutron reflectivity profiles were collected to probe the dynamics of this system, alongside static state NR profiles to understand the film profile at the extremes.

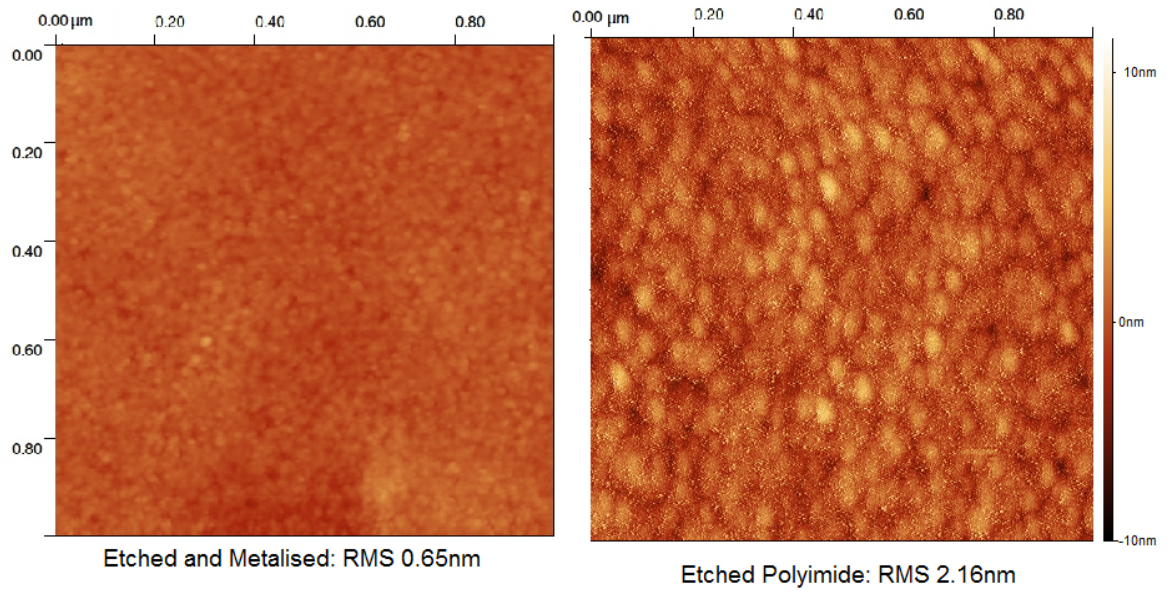


Figure 5.28: An AFM scan of the polyimide with sputtered metal layer on top and the etched polyimide on the same length scale.

Firstly, it should be noted that the metal coated polyimide is smoother than the etched polyimide layer, which implies that the metal settles into the voids created by the etching; see the roughness difference indicated in Figure 5.28. This is corroborated in Figure 5.29, which is a cross section (produced using a FIB) of the  $\approx 180nm$  sample, which is discussed in this section. The image shows signs of metal implantation into the polymer layer. Again, TEM images have been used to inform the fitting procedure.

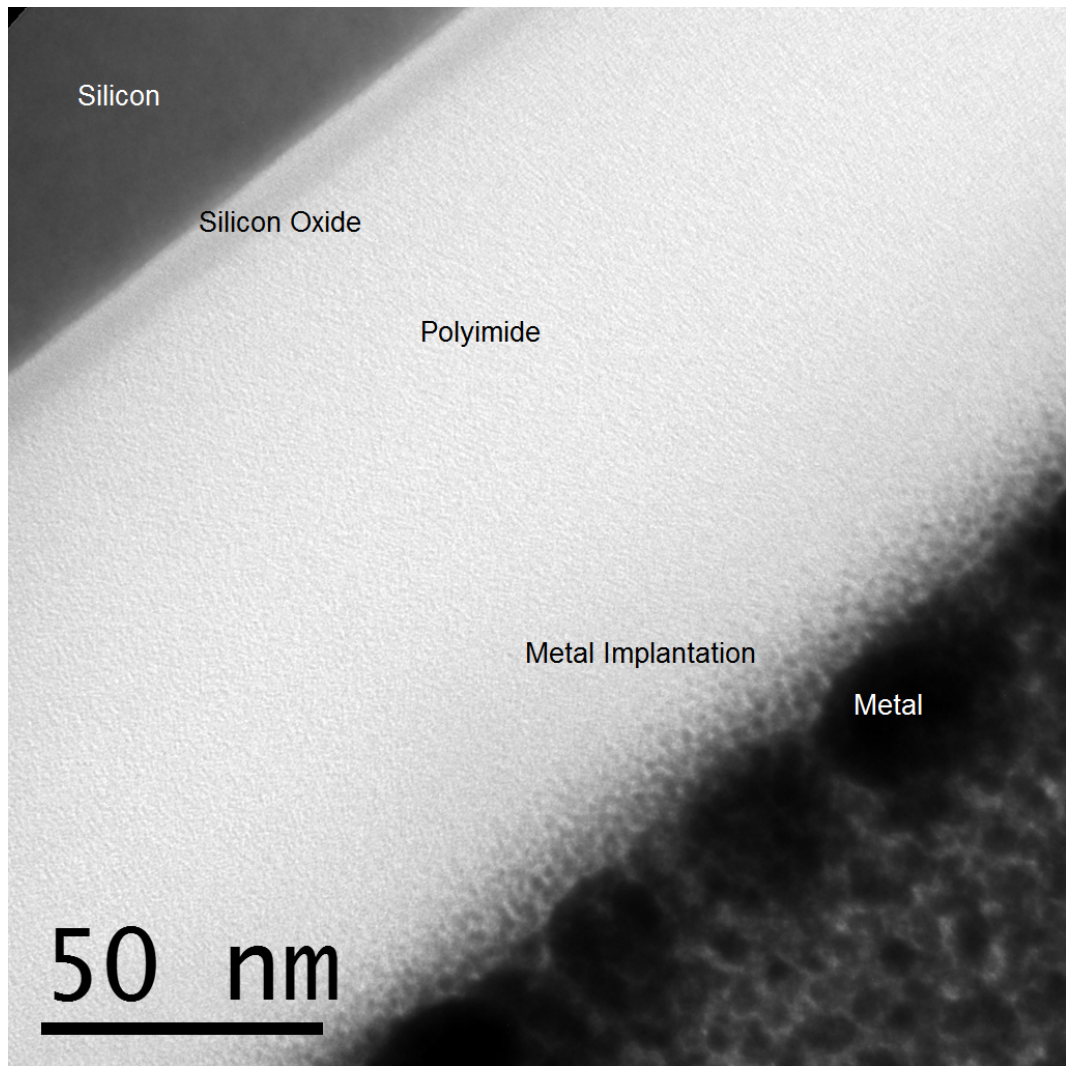


Figure 5.29: A bright field TEM image of the sample used in this section. The bulk polyimide is in the middle with the silicon substrate in the top left hand corner.

**Data Processing and Fitting** The dynamic reflectivity profiles were prepared for fitting as discussed in section 5.2.3. The data set shown in Figures 5.26 and 5.27 is discussed here. The anticipated width of reflectivity fringes for a layer of 180nm is  $0.0034 \text{ \AA}$ . In order to resolve these fringes a width of the  $q$  bins of at least half this size were required. The highest value at which the fringes of  $0.0034 \text{ \AA}$  are resolvable is  $q \approx 0.1 \text{ \AA}^{-1}$  according to Figure 5.9. Therefore, the reflectivity profiles were truncated at high values of  $q$  as features are non-resolvable. The truncated spectra were then modelled.

To allow for changes in the SLD profile within the bulk layer, the fitted model was split into four giving a total of six layers. This allowed the fitting algorithm to be given sufficient mathematical possibilities to allow for any non-intuitive absorption mechanisms. All the models presented in Figure 5.30 have

$\chi^2 < 1.2$ . The fitted SLD models reveal a gentle gradient in the polymer density in a dry atmosphere, shown in Figure 5.30.

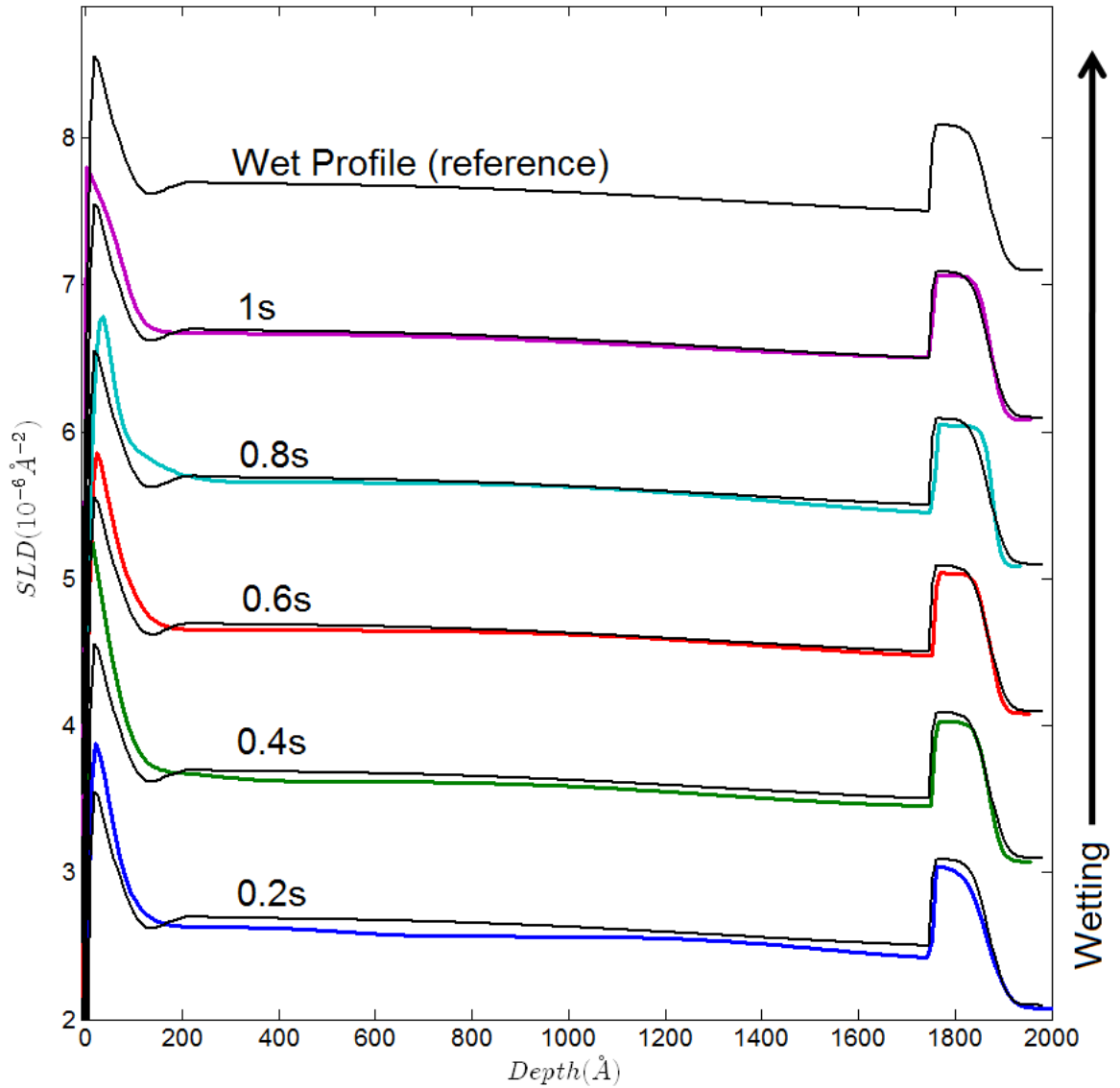


Figure 5.30: Diagrams showing the density profile of the polyimide and gold films in a vapour atmosphere. The profiles are vertically displaced by  $1 \text{ \AA}^{-2}$ , with the vapour saturated reflectivity profile overlaid next to each reflectivity profile for reference. This data had been identified as *wetting* in Figure 5.27. The corresponding fits to the reflectivity profile are in the appendix; Figure A.17.

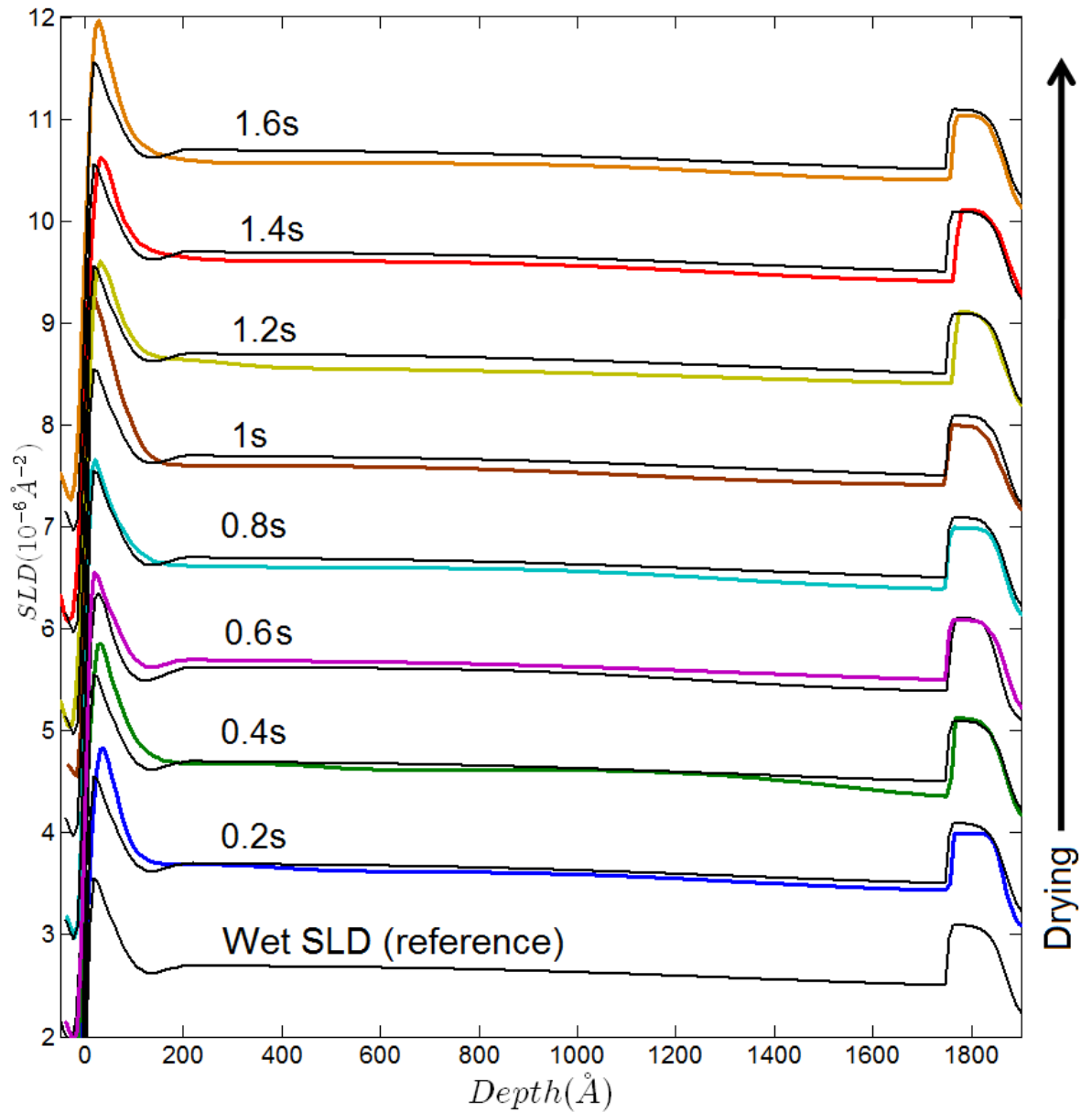


Figure 5.31: A diagram showing the density profile in the polyimide films, as the film dries out. The profiles are vertically displaced by  $10^{-2}$ . This data was identified as *drying* in Figure 5.27. The corresponding fits and reflectivity profiles are in the appendix; Figures A.18 and A.19.

### Discussion

The 10s-30s dry-wet duty cycle, the results of which are shown in Figures 5.30 and 5.31, was designed to allow the film to wet and monitor the timescale and concentration profiles of the drying process. It can be observed that the surface of the film, which can be directly monitored by observing the critical edge, appears to reach equilibrium state while wetting in about 1s, while the drying process takes

longer. During the wetting process, Figure 5.30, the metal/skin surface appears to wet first at 0.4s, the bulk polymer layer then absorbs the vapour very fast having an approximately even distribution thereafter. For the drying process, shown in Figure 5.31, the oxide retains vapour for an extended period compared to the bulk

It is possible that asymmetry in the profile, the metal/skin layer, is leading to different wetting and drying characteristics. To compare the drying and wetting on this time scale a complimentary set of data was recorded. This data set consisted of a 10-30 seconds wet-dry cycle, although the statistics on this data set are worse. The critical edge shift is shown in Figure 5.32. Comparing, Figures 5.27 and 5.32, the time scales of the shift in the critical edge look slower in Figure 5.32, however both data sets present a  $\Delta q_z = 0.004$ .

It is very difficult to draw conclusions from the data as Figure 5.32 is very noisy. Additionally, the box car averaging doesn't account for the cumulative effect of repeated duty vapour cycles.

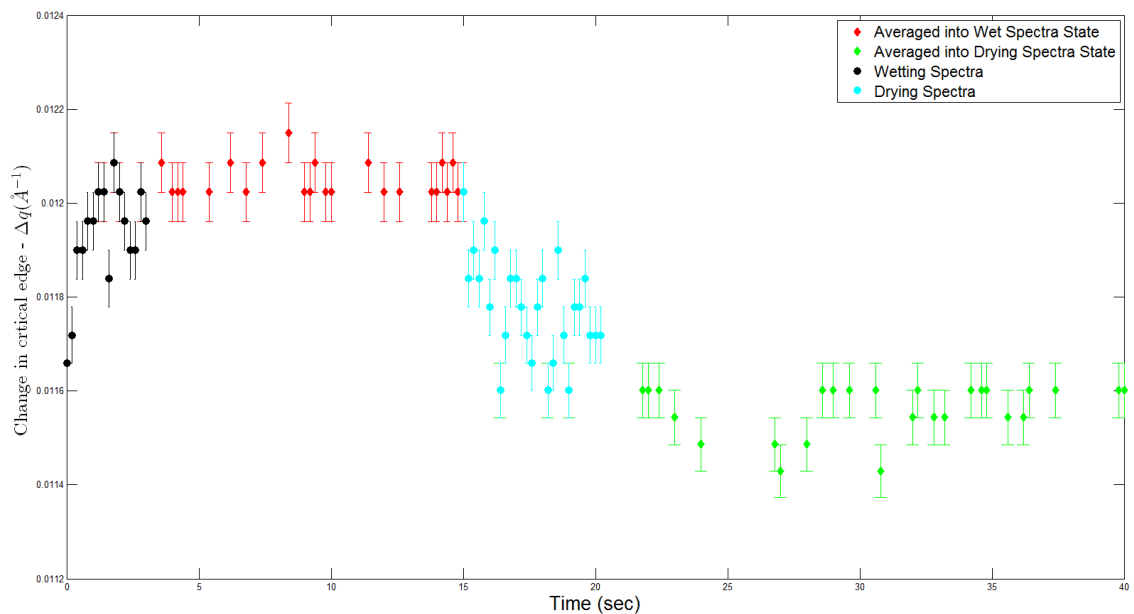


Figure 5.32: The shift in the critical edge of the 10s wet 30s dry dynamic spectra to compliment the data presented in Figure 5.27. The statistics on the data set are very low and show a systematic analysis is not possible.

**Box Car averaging and Longer Time scales** The critical edge reaches a steady state in the dynamic profiles. However, the amplitude of the Fresnel fringes in the dynamic spectra do not reach the extreme values shown in the equivalent static measurements. This is reflected in the modelled SLDs.

For the time resolved measurement the modelled profiles return a  $\Delta SLD = 0.15 * 10^{-6} \text{\AA}^{-2}$ , was the difference between the wet and dry profiles. This is a lower SLD difference than was observed between the wet and dry static state reflectivity profiles for which  $\Delta SLD \approx 0.2 * 10^{-6} \text{\AA}^{-2}$ . This is not likely to be a result of the cell atmosphere as the flow rate of the inlet gas was monitored and controlled to be 6 to 7 litres of Nitrogen per minute into a volume  $\sim 10 \text{cm}^3$ . The cell turn over time would therefore be of the order of 100ms, faster than the time resolution between each spectra.

Figure 5.33 shows a comparison between two spectra; the box car averaged dry spectrum (marked dry in figure 5.27), and the dry spectrum measured using the static measurement technique. The critical edge is the same in both reflectivity profiles, however the reflectivity profiles show a varying amplitude of the Fresnel fringes. Figure 5.33 implies that the film does not fully reach a steady state in the dynamic runs despite the critical edge shift reaching a steady state. As discussed in section 5.1, the critical edge shift represents surface properties, while the Fresnel fringe amplitude is indicative of contrast within the polymer.

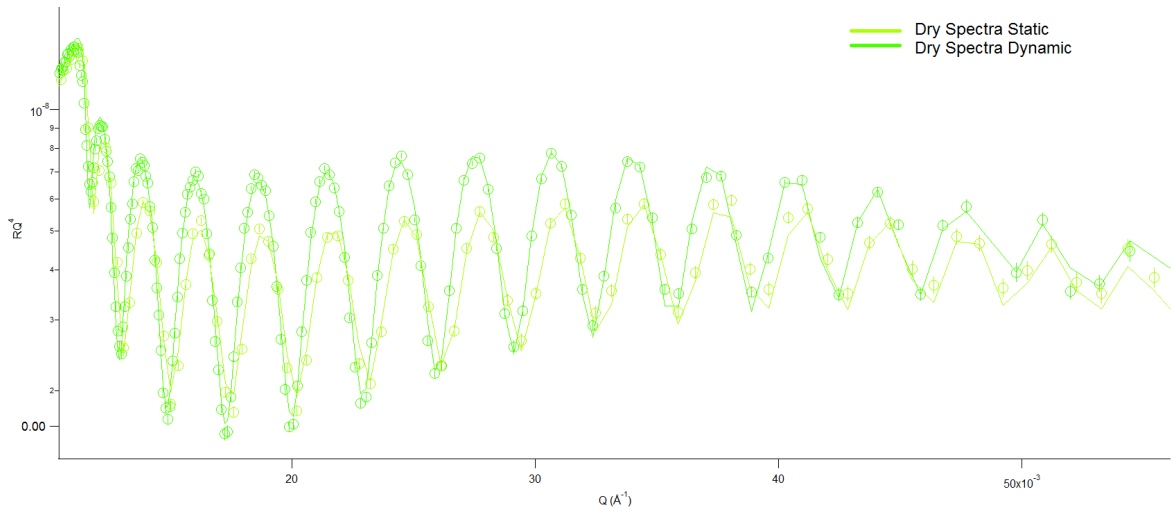


Figure 5.33: A contrast between the dry static spectra measurement and the aggregate dry 10 dry -30 wet profiles shown in Figure 5.27 at similar flow rates. Interestingly the critical edge is similar, yet the amplitude of the fringes remains greater in the dynamic spectra, implying the film is not fully dry in the ten second time frame despite similar surface properties.

Figure 5.33 shows significant differences in fringe amplitude at every  $R(q_z)$  value implying that there is some larger source of contrast in the polymer in the static state profiles, i.e. the bulk of polymer retains some vapour. Therefore, it seems very credible that the polymer has not fully dried or wetted in the cycles performed, despite the stable surface properties. Clearly, there are longer term effects

in the polymer which are not reflected in the extreme positions of the time resolved cycle as this is averaged out using the box car technique.

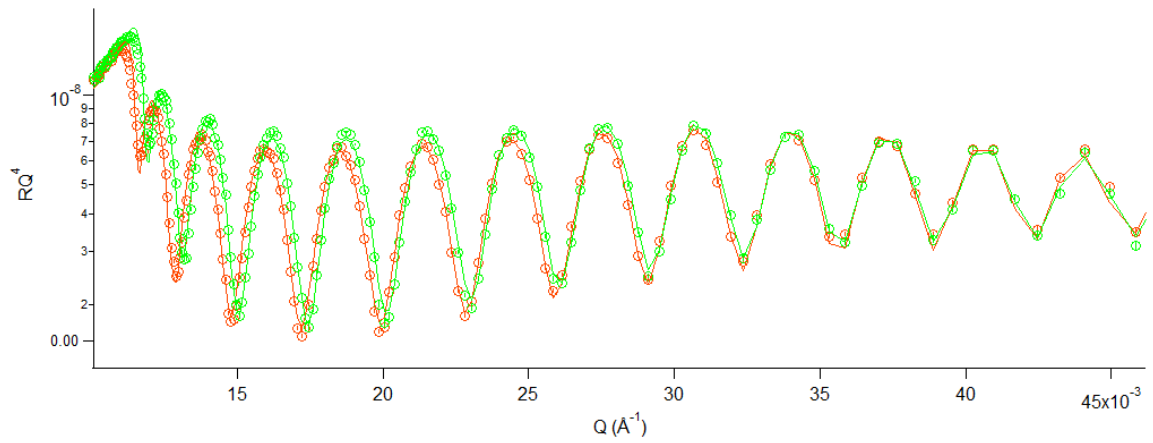


Figure 5.34: Extreme points for the 10wet-30Dry cycle. The critical edges are shifted with respect to each other but the fringes are the same indicating measurements deeper in the film converge.

This is expected as the timescales of transport in this polymer, as characterised in Section 4.1, are much longer than the duty cycles probed in this experiment. Therefore, the cumulative effects of cyclically wetting the polyimide as required by the box car averaging technique results in a skewed reflectivity profile in which extremes of behaviour are averaged out. The mean polymer vapour content would continue to vary with each duty cycle.

#### 5.4.4 Concentration Profiles in a fast changing atmosphere

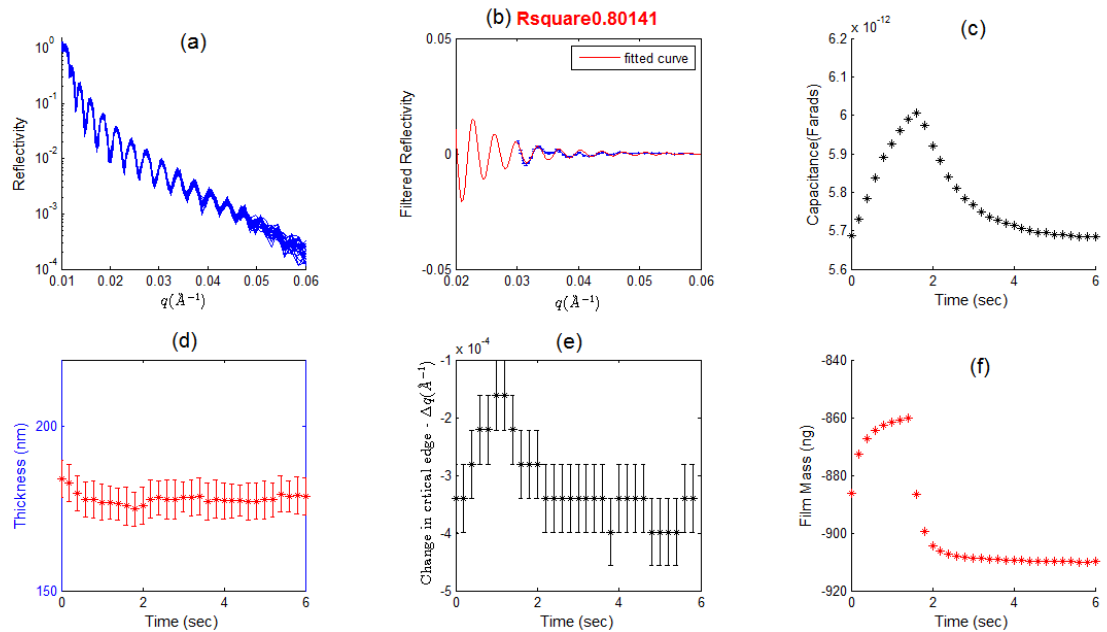


Figure 5.35: The summarised output of the 1sec wet/5sec dry dynamic reading in the cell. (a) All of the reflectivity profiles,  $R(q)$ , plotted. Each profile corresponds to a 0.2s time bin within the 6sec duty cycle. (b) An example of a Fourier filtered reflectivity profile and the fit used to measure the thickness of the film. The fitted reflectivity profiles shown correspond to the last 0.2s time bin in the duty cycle. (c) The capacitive humidity sensor readout as a function of time though one duty cycle. (d) The thickness deduced from each fit to the profiles shown in (a) and fitted in (b), plotted as a function of time though the duty cycle. (e) The critical edge shift plotted as a function of time, measured from the reflectivity profiles shown in (a). (f) The QCM readout plotted as a function of time though a duty cycle.

The previous section demonstrated that time resolved NR profiles were not able to reliably elucidate reflectivity profiles which involved a shift in contrast deep in the polyimide. In order to further investigate the characteristics of the shorter time scales a dynamic profile was acquired of 1sec wet -5sec dry on the same sample discussed in the previous section. The critical edge shift for this profile is shown in Figure 5.36 along with the composite fitted SLD profiles shown in Figure 5.37 and the QCM measurements shown in Figure 5.35.

The short timescale and minimal amount to wetting in this duty cycle; 1second wet and 5 seconds dry, should mean that despite the effect of the averaging, which was discussed in the previous section, this data set may some value in understanding water transport though a polymer/metal interface. This would be achieved by carefully modelling both the shape and position of the critical edge while being aware that each added duty cycle, while increasing the statistical significance of the reflectivity profile,

also averages out the extremes of the film behaviour.

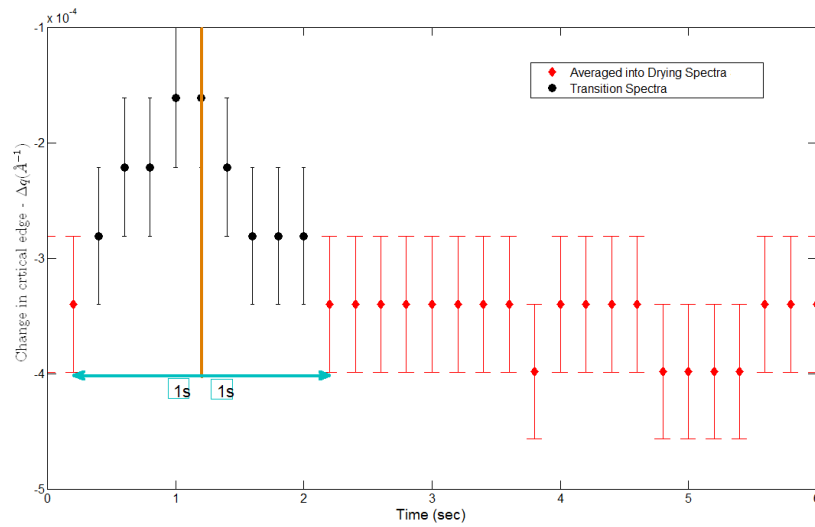


Figure 5.36: Showing the shift in the critical edge from the run of 1-5, wet-dry, performed on the 180nm etched + 5nm Au sample. This can be compared to Figure 5.27 to show that the same critical edge shift is achieved but the film is not allowed to equilibrate in a wetted state. The black vertical line does not have symmetry for the marked transition spectra.

Interestingly, the critical edge shift shown in Figure 5.36 appears to be approximately symmetric about a centre point in time. Therefore, the MatLab script used to process the data was re-written in order to divide the spectra into two; the aggregate of the dry spectra, and the transition spectra, as indicated in Figure 5.36. The results of the fitting procedure are shown in Figure 5.37.

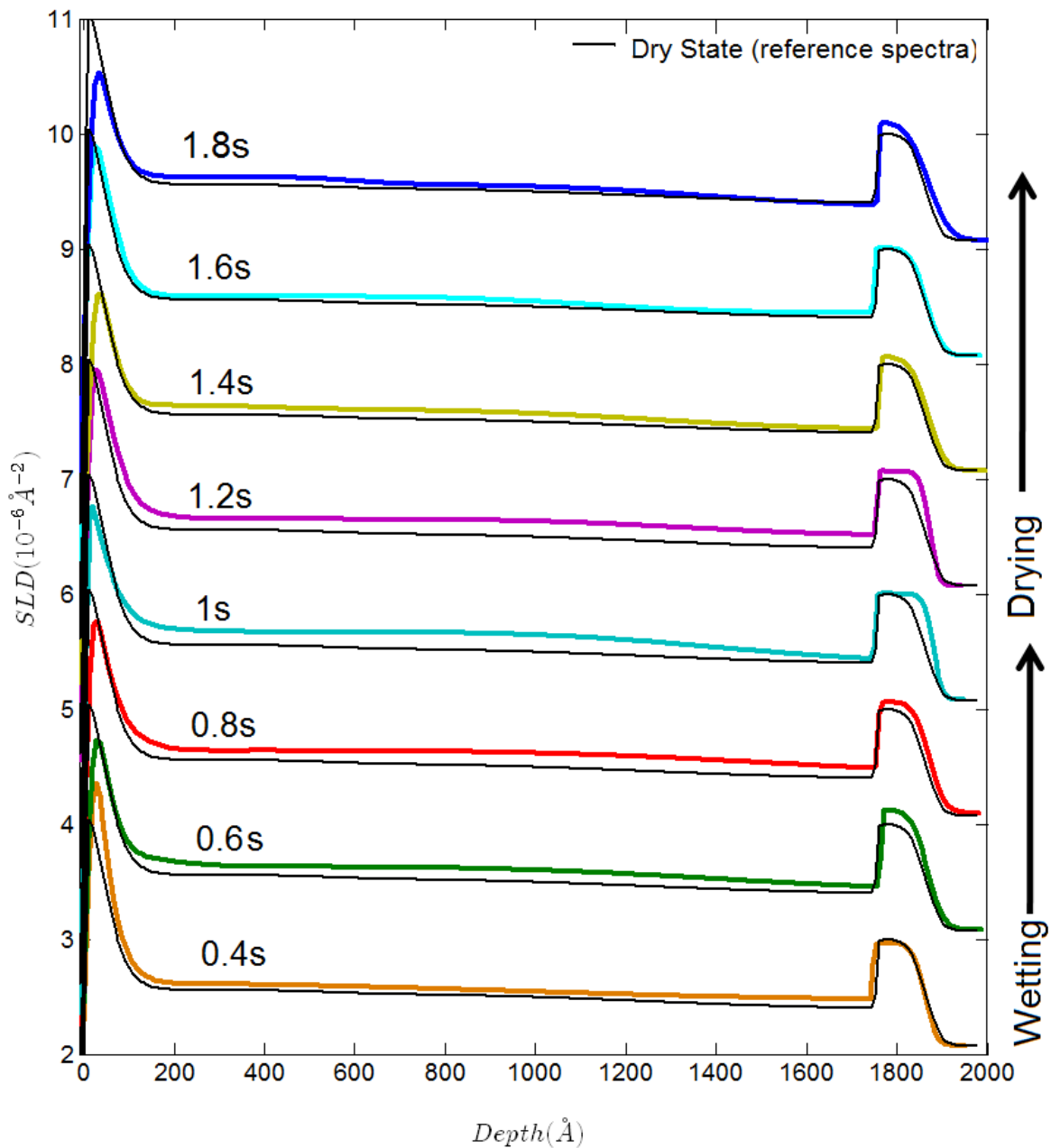


Figure 5.37: The concentration profiles shown for the data point marked in Figure 5.36 as *transition*. Fits are shown in the appendix, Figures A.20 and A.21.

The best fit SLD profiles of the first transition spectra, taken at 0.4sec into the cycle, show a sharp peak on the surface and a gradient in the bulk polymer layer, with little or no change from the dry SLD profile on the oxide layer deep into the film. This concentration gradient is reduced in the next spectra at 0.6sec, which shows a more even distribution in the bulk layer and the ingress of water into the hydrophilic oxide layer.

Over the following spectra, taken 0.8-1.2sec into the cycle, the film reaches an approximate stasis with

the head space until the drying begins. The oxide layer is last to dry fully. Although the dynamic spectra have a lower degree of certainty, due to the lower number of counts, a trend is clearly noticeable for the response of the film on fast time scales. Remarkably, within the bulk layer the SLD is close uniform throughout a given duty cycle, showing that the transport in this layer is faster than can be captured with 0.2s resolution.

## 5.5 Summary

This chapter outlined the use of neutron reflectivity to probe the transport properties in polyimide thin films. The rationale for pursuing neutron reflectivity was discussed for this investigation in sections 5.1. The application of neutron reflectivity for this system was shown with the aid of some simulated reflectivity profiles. This outlined the requirements to develop equipment capable of pulsing vapour into a neutron transparent, but vapour containing cell, in section 5.1.2. The construction of the required equipment and samples for this project was recorded in section 5.2.

A series of measurements of the polyimide films in a static atmosphere were then presented which included key results about the structure of the polyimide films. Firstly, the existence of a dense polyimide skin layer, showing an asymmetry in the film density. This was an important result as such characteristics were indicated in Figure 4.4 and confirmed in this section.

Next the impact of process steps on the film SLD was discussed. The oxygen plasma etched films were shown to be denser than the other two films, confirming an earlier result and explaining the lower mass uptake of plasma etched film. SLD profiles acquired in a Deuterated atmosphere enabled the mass and distribution of the vapour to be measured, with variations shown between different films; for example plasma films absorbed less vapour. This was maybe caused by either an increase in the density of the film or a change in the chemistry of plasma etched films.

While these results were important, the oxide layer in the samples, which was shown to be thicker than previously thought, may have impacted on the concentration profile of the vapour and added to the complexity of the modelling. In future experiments such a layer should be removed.

The behaviour of a film prepared to reflect the properties of the commercial humidity sensor was then studied as the environment oscillation between these two extremes was also explored as a function of time. The reflectivity profile stabilised with a time period on the order of seconds. However, there is some indication, from the results presented in Chapter 5, that the mass flux in this system varies on longer timescales.

In the final section of this chapter, the reflectometer in time of flight mode to gain time resolved concentration profiles of the film. To achieve this, a degree of both standard and non-standard data

post processing was required. The time resolution achieved was 200ms, much better than has been achieved in previous studies [77], enabled by improvements in reflectometer technology. The dynamic profiles showed that the mass transport of vapour in the bulk of the polymer was faster than the time scales probed, with the metal skin layer delaying transport slightly. However, the use of box car averaging was shown to obscure longer term changes in the polyimide.

## Chapter 6

# Conclusions and Future Work

This chapter is divided into three parts, a very brief summary of the key findings from each chapter & a discussion of the key conclusions, areas of future work, and an evaluation to place the results presented into context.

### 6.1 Summary of Results

Chapter 3 showed the application of a common QCM based technique[70], which had previously been applied to monitor sorbtion in other studies[97, 23], to be suitable as a test-bed to investigate polymer behaviour without having to fabricate full devices (Figure 3.7). The correct model to interpret this data was explored and the validity of the Sauerbrey equation[69] for this system was tested. Additionally, it was shown that the dissipative properties of the polyimide films can be probed by analysing the impedance spectrum(as a function of frequency) of a coupled QCM close to resonance (Section 3.5), which has also been shown by Parlak et al.[71]. The QCM showed that the dissipative properties of the films were a function of the annealing regime and the environmental humidity.

The density and mass uptake of vapour of these polyimide films was measured as the environmental humidity was cycled from low, to high, and back again to low humidities (Section 3.4). The hysteresis effect has been characterised as a material property, rather than a property of a particular device architecture. Film annealing and etching procedures was shown to affect the density and mass uptake of the polyimide films. Oxygen plasma etching was found to reduce the hysteresis & dissipation, and increase the film density in this polyimide. This density increase was confirmed using neutron reflectivity (Figure 5.19).

Capacitance measurements of polyimide thin films spun onto interdigitated electrodes were performed on fabricated devices (Section 3.6). The capacitance of such films was shown to vary in a non-

linear manner with mass uptake in the polyimide, which was expected from theory. This led to the introduction of a proof of concept device, Capacitive QCM, capable of measuring both the capacitance, and the mass of the same sensing element. Such a device may be useful to evaluate materials in the future and to distinguish penetrant gases based on a capacitance to mass ratio.

Chapter 4 then discussed the time and length scales of the diffusion process. A Fickian analysis of the data acquired in the previous chapter showed a thickness and treatment independent timescale of diffusion (Section A.4). As a result, measurements of the diffusion coefficient, which are normally thickness independent, were shown to be a function of the film thickness 4.4. Therefore it was concluded that the rate limiting factor was not linked to diffusion through the bulk of the polymer, but may be a function of surface layer which is a uniform feature on all samples.

Chemical processes which may contribute to mass transport timescales were also explored. ATR-IR spectroscopy revealed a weak bonding interaction between the water vapour and the polyimide, estimated to be of the order of 1KJ/mol. A model to represent this diffusion behaviour was explored, but this requires further work to account for the diffusion of the material.

The length scales of mass transport were then explored using Permporometry and TEM to characterise the common spatial frequencies in the polyimide (Section 4.3). It was inferred that particles of a similar or smaller volume to water vapour were able to enter into the polyimide. This explained the selectivity of the commercial humidity sensors, as water molecules are particularly small and polar when compared to other molecules common in the atmosphere. No pore network was found and the diffusion occurs on a molecular length scale.

Finally, Chapter 5 used neutron reflectivity to be an effective method for mapping vapour concentrations in polyimide thin films. Equipment, experimental setup, and data analysis to show the SLD profiles of thin films were discussed.

A dense polyimide skin layer was shown to be ubiquitous on all polyimide samples and no polymer swelling was detected during the absorption process (Section 5.3). It is postulated that this dense surface polyimide layer is the layer responsibly for setting the diffusion time scales as the vapour moves faster through the bulk polymer than the surface layer.

Modelled SLD profiles were obtained by comparing the measured reflectivity curves to a hypothetical sample to produce a modelled reflectivity curve and modelled SLD depth profiles. Therefore, the veracity of the SLD depth profiles was dependent on the quality of the modelled reflectivity curve. The Poisson noise on the reflectivity curves obtained was relatively low as the count time was, by design, long enough to reduce the random noise to an acceptable level. The machine corrections were performed using a well tested routine and so the reflectivity curves are of a high quality. The fitting

parameters were constrained by measurements using a host of other techniques such as TEM imaging of samples. However, each fit required many layers to model the reflectivity and so over-fitting was a concern, particularly on the thicker samples with a lower resolution for the equivalent feature size, and due to the unusually thick oxide layer (Figure 5.13). Consequently, common features on all the SLD fitting profiles across a range of sample thicknesses are emphasised, with the notable common feature being the highly dense skin layer on the surface of the polyimide.

The modelled reflectivity profiles allowed the impact of process steps on the density (SLD) profile of the thin films. This allowed density variations between sample films which had undergone different treatments were compared. The distribution of vapour in each of these films was mapped in a high vapour atmosphere. The SLD profiles obtained in a vapour rich environment showed an approximately even distribution of vapour in the thin film, with the surface having a higher and then an immediately lower concentration when compared to the bulk.

Additionally, a reflectometer in time of flight mode was used to gain time resolved density profiles as the vapour atmosphere was switched between two extreme conditions, a very high and very low humidity environment (Section 5.4). The time resolution achieved was 200ms, much better than has been achieved in previous studies carried out by Glidel et al.[77]. To this author's knowledge, no diffusion study has been carried out since improvements in reflectometer technology enabled such time resolution[83]. Transport in the bulk of the polymer was found to occur on a time scale less than 200ms. However, the averaging necessary to gain sufficient numbers of neutron counts to form a profile was found to obscure any long term effects in the polyimide rendering; much of the time resolved data which was acquired was of limited use.

## Discussion

A variety of studies have investigated the transport of water vapour through polyimides, characterising diffusion[168, 122, 120] and chemical properties[65, 127] of films of various structures. However, these studies have focused on thicker polyimide films and little is known about how the received wisdom applies to thin films ( $< 1\mu m$ ), which are of increasing importance as the spatial dimension of devices shrink.

The structure of thin polyimide films as characterised using the SLD profiles (in Figure 5.12) provides a good explanation for apparent variations of the diffusion coefficient with sample thickness (Figure 4.4), which would otherwise be troubling. The SLD profiles imply two layers within a given polyimide thin film; a bulk layer and skin layer of thickness  $\sim 5nm$  which is on the surface of all samples. As the timescales of the diffusion are similar across a range of film thicknesses (Figures 4.2 and 4.1), the

rate limiting factor is thickness independent. This is evident from the consistency of the hypothetical diffusion coefficient of the skin layer  $D_{sk}$  which was similar on almost all measurements. Such a scheme has been proposed previously in other works concerning diffusion within Polymers[52, 60] and has been suggested as an explanation for the diffusion behaviour of various polyimides[30], but it has not been demonstrated experimentally prior to this study. Additionally, it was shown that time resolved neutron reflectivity profiles can be used to probe diffusion properties in polymer thin films on with a 0.2s time resolution; however such experiments are of limited use when the timescales of diffusion are much longer than the duty cycle used. A further attempt to use time resolved neutron reflectivity to investigate water transport across the metal/polymer interface, similar to that of Honeywell's devices was presented. However, again the *box car* averaging made it difficult to draw any firm conclusions.

Surprisingly, **oxygen plasma etching** appeared to increase the density of the polyimide thin film (SLD profile Figure 5.19), and the skin layer appears to shift into the film. This density increase in turn appears to have lowered the water uptake in the etched polyimide films (Figure 3.16) and apparently reduced the hysteresis as shown in Figure 3.18. The QCM measurements show a lower dissipation in etched films, corroborating measurements that showed an increased density in etched thin films. There are two possible explanations for the lower hysteresis; firstly, the increased density leads to less free volume and less water uptake, so there are lower numbers of chemical bonds between water-polyimide, or water-water molecules, in the sample. Alternatively, the electronegative oxygen molecules from the plasma during etching partially compensate for the polar elements on the polymer backbone; again resulting in a fewer bonding sites. Both of these explanations are not mutually exclusive and assume that the hysteresis is a consequence of a difference in the activation energy of chemical interactions taking place during the wetting and drying processes. The chemical bonding between the (water-polyimide) was implied experimentally (by ATR FTIR - in Figure 4.6).

The diffusion was shown to be well **characterised as Fickian**, implying that the Deborah number of the polyimide is either  $\gg 1$  or  $\ll 1$ . Measurements of the dissipative properties of polyimide thin films(Figure 3.21) imply the film is rigid and so the Deborah number would then seem to be  $\gg 1$  i.e. much more rigid than a fluid (Figure 3.22) .

The raw mass readings of the polymer were hysteretic, implying that it is residual water in the polymer, not a mechanical or electronic artefact causes the commercial sensors to present hysteresis. The ATR FTIR experiments should be carried out in the thunder chamber to check if there is any correlation between the hysteresis and the bonds which are active in such a case.

It is proposed that water ingresses into the polyimide with the timescale of this ingress set by the diffusion properties of the skin layer. This is as Fick's law describes the mass transport into the polymer well. However, after entering into the polymer water vapour undergoes a form of bonding,

and the difference in energetics causes a slight hysteresis. The length scale of free volume in the polyimide is implied to be  $\sim 0.25$  nm, implying that no large clusters of water can form. Hence, the important bonds are most probably either, two water molecules bonding into a dimer, or water-polymer backbone interactions. The plasma etched film, with increased density and possible saturation of such polar components of the backbone, exhibits a lower hysteresis.

## 6.2 Future Works

Several sections have discussed potential expansions of the work performed. Beyond what has already been discussed, this section focuses on three investigations the nature of which is beyond repetition or expansion of experiments which have already been discussed.

### **Time resolved Neutron Reflectivity and an in-situ ATR-FTIR as a hysteresis probe.**

Neutron reflectivity has been used alongside in-situ ATR-FTIR measurements to gain simultaneous chemical and density information on polymer samples[178, 179]. Combining the two measurements would give complete indication of the interactions of the vapour and the relationship between the chemical interactions and the mechanical transport.

The Neutron Reflectivity investigation presented was focused on the short time scale behaviour of the polyimide. This was for two reasons; firstly, the importance of the longer term polymer behaviour was not well understood at the time of the experiment and, consequently, single experiments lasting several days did not seem like a good use of the limited reflectometer time. Secondly, the equipment to produce a sufficiently stable atmosphere to perform such measurements with confidence was lacking. Having understood the importance of the hysteresis effect and having noted that the time of flight techniques obscure longer timescales, it would be desirable to perform the longer term humidity cycles while data of the chemical and density (as a function of depth) of the polyimide-water system are monitored.

A stable environment is possible as some commercial companies that produce cells designed for in-situ optical microscopy with humidity and temperature controls have been capable of achieving the stability required in a transportable cell [180]. Further investigation of the available systems is needed to understand the suitability of such cells for neutron reflectivity. Alternatively, such a cell can be developed.

The motivation for performing longer term experiments, such as the calibration profiles used during the QCM investigations, on thin films, while monitoring the reflectivity profiles, is to see the source

of the Hysteresis. Neutron reflectivity profiles would be acquired as static profiles, without box car averaging or repetitive cycles of the film, as it is taken through a pseudo calibration profile. This may take some time as the films would be required to be close to equilibrium before the NR measurement could begin. It may be possible to run two experiments simultaneously.

The first stage would be to perform ATR-FTIR measurements in the thunder chamber. Then to develop or purchase a transportable cell which produces the same hysteresis results with QCM and ATR-IR monitors. Neutron Reflectivity measurements can then be added to further enhance the work. Dalglish et al.[78] has also discussed the possibility of mapping the diffusion in systems in three dimensions which may be another interesting possibility, although not necessary for monitoring the hysteresis.

### **Modelling and Computation.**

Polyimide films have been shown to be dense, and porous only to small gas molecules such as *He* and *H<sub>2</sub>O* with no pore network. Transport occurs on a molecular level through the matrix in this system. Simulations on other systems have had a degree of success when modelling water transport and chemical interactions of the water with an absorbent polymer[62]. For polyimide, Flory–Huggins based models, which are well discussed by Hancock et al.[124] has shown promise[125, 167]. None of these models have yet described the hysteresis which may result from modelling of the longer term behaviour of the system.

Any such description would need to arise from molecular level considerations, as bonding is likely to play a role. It may be possible to simulate such interactions with software packages (such as comsol) as a time efficient way of achieving such results. Such modelling may lead to an enhanced understanding of the cause of the hysteresis when modelled behaviour is compared to experimental results.

### **A MEMs resonator to monitor the Dew Point.**

The ability to detect condensation or dew point with a QCM by studying the shape of the impedance profile was noted during this investigation (see section 3.5).

The dew point is very well defined as it is based on the triple point of water. Consequently, dew point hygrometers are often used as the standard by which to calibrate humidity sensors. However, traditionally, dew point hygrometers have been expensive due to the required laser and photodiodes[5]. The setup of a conventional dew point hygrometer has been miniaturised into a MEMs device for medical applications[13].

Elsewhere, a peltier cooled QCM has been used to monitor the dew point using a Sauerbrey type mass detection[23]. Here, a dew point hygrometer based on monitoring the impedance spectrum of a MEMs piezoelectric resonator is proposed. Such a device would not require a full impedance sweep; the impedance at a set frequency in the linear portion of the impedance spectrum (between  $f_1$  and  $f_2$ ) of a well characterised resonator can be monitored. A polyimide layer placed between the environment and the resonator can act as a gas filtration membrane due to its good gas selectivity, as has been shown during Permporometry experiments.

However, two (rather broad) patents from a start-up company Femtoscale Inc. covering the use of a MEMs resonator to monitor dew points has been published in the middle of 2014[181, 14]. The design shown implies a temperature closed loop feedback system, which alters the temperature to maintain a constant thin film of water vapour on a resonating element.

It may be possible to tailor a surface of a resonator to have an increased hydrophilicity (or other affinity to other vapours of interest), and then to heat up the sensing element to maintain a constant vapour thin film calibrating the devices in a range of humidities. This would eradicate the need to use a Peltier based technique to cool the surface. A piezoelectric dew point measure would maintain the measurement accuracy while decreasing the cost of devices significantly; no such device is available in the market place yet.

### 6.3 Evaluation

With the increased use of smart gadgets the demand for cost effective accurate Humidity sensing has increased significantly[10]. Device engineers have successfully increased the accuracy and efficiency of devices. Improvements of devices now stem from material level understanding of the sensing element. Understanding the materials level behaviours in order to define the cause of phenomena such as hysteresis is a challenge with high levels of commercial opportunities. Therefore, one of the goals of this study was to evaluate the interaction of water vapour in polyimide, the existing sensing material used by Honeywell. This has been performed with the aid of two methods to evaluate materials; Neutron Reflectivity and QCM. In both cases the limits of the techniques were pressed and developed to characterise the transport properties of polyimide. These techniques have shown that the shorter term behaviour of the sensors is not limited by the sensing material, in contrast to the longer term behaviour. The QCM procedures outlined have provided Honeywell with a cost effective method of understanding the mass uptake properties of a range of materials and the possibility of expanding measurements to probe a given material's mechanical properties. This fulfils one of the key goals of this project; a cost effective materials test bed. Additionally, the use of such techniques acts as a road

map for such studies in which vapour transport in a given material is important.

Incremental improvements resulting from this study in the process and function of the humidity sensor can lead to a significant impact due to the size and scale of Honeywell's operation. Additionally, this study can serve as a good example of a successful mutually beneficial collaboration between industry and academia.

# Appendix A

## Appendix

Here, some supplementary information is provided which is referred to in the main body of the text. Although, this information is not required to understand the main conclusions, it is recorded for anyone wishing to repeat the experiments and posterity.

### A.1 Spin Coating polyimide Calibrations

Polyimide thin films have been prepared throughout this study with standard spin casting techniques. A range of thicknesses are required in this investigation, particularly in reflectivity experiments. Therefore, at the beginning of this study spin conditions were calibrated to develop the knowledge required to consistently produce of the desired polyimide films.

This section is divided into two parts; firstly the factors which can influence both the thickness and other characteristics of polymer films arising as a result of spin casting are discussed, and finally calibration data is presented.

#### A.1.1 Spin coating Forces and factors

Spinning casting is a commonly used technique to prepare polymer thin films. The polymer precursor is the solution containing the polymer molecules in a solvent. This is prepared by the manufacturer to produce a given thickness under a given set of conditions. Manufacturers can alter the thicknesses produced by varying the viscosity of the precursor, and normally provide a spin calibration curve as part of the specifications sheets.

In this study polyimide precursor was developed to produce a thickness of just over 1 $\mu$ m at spin speed of 5000RPM on standard 4" Si wafers meeting industry requirements.

Firstly it is worth considering the forces relevant to spin casting. The centripetal force which drives the solution to spread across the substrate. For a given particle of the solution on the substrate the centripetal force is proportional to the distance away from the centre,  $r$ , described by  $F = m\omega^2r$  where  $F$  is the centripetal force,  $m$  is the mass of the particle, and  $\omega$  is the angular velocity. The rate at which the precursor is spread over the surface is determined by both the spin speed and viscosity of the precursor. It is therefore important to place the solution in the middle of the substrate such that an even coating is obtained. The boiling point of the solvent is of the order  $80^\circ C$  and therefore the solvent will begin to evaporate at room temperature, altering the viscosity, and therefore the spinning characteristics.

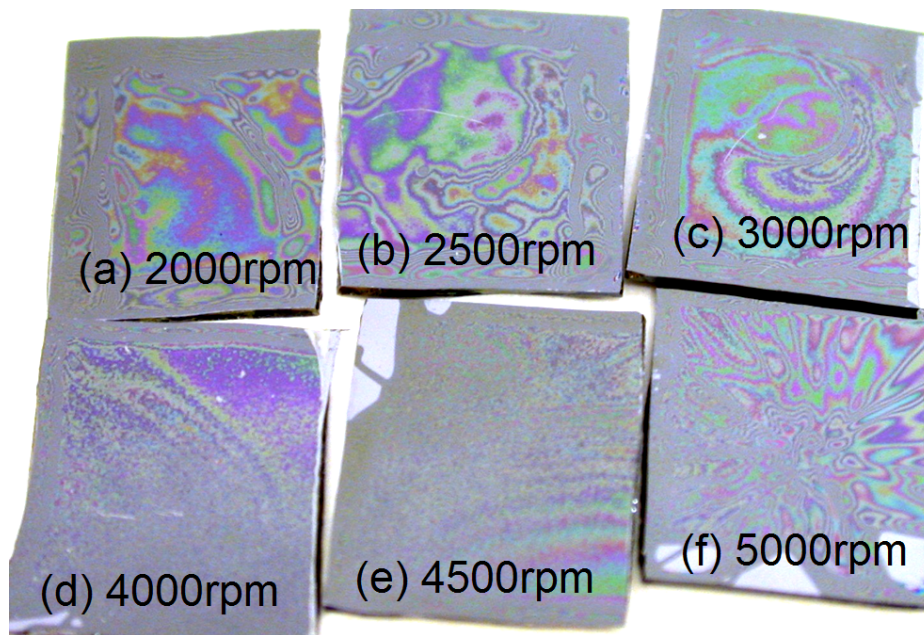


Figure A.1: A high resolution photograph of the polyimide solution spun onto small Silicon substrates to illustrate the effects of spinning to slowly leading to a film with a variable thickness (a-c) and to fast lead to a film with artefacts of acceleration(f).

Figure A.1 shows photographs of the polyimide precursor obtained for use in this experiment spun at different speeds. Of the six images (a), (b) and (c) both show an uneven coating, while (f) shows an off center dispersion with too high an acceleration rate. In order to stop the acceleration being a determining factor, a pre-spinning step of 5sec at 500RPM has been introduced into all subsequent results.

### A.1.2 Calibration Curves

A series of dilute precursors have been produced with various ratios of precursor to solvent which was observed to decrease the viscosity of the precursor. These solutions have then been spun onto a silicon substrate. Measurements of the thickness of the layer have been performed with the following procedure;

- The solvent and precursor were measured out in beakers to the relevant ratio. Both were added to a glass bottle and sonicated for 10 minutes to ensure an even mix.
- The substrate was placed inside a beaker filled with Acetone and associated for 5 minutes. This was repeated for isopropyl alcohol, IPA.
- The substrate was then dried using a Nitrogen gun, taking care to move from one side of the substrate to the other.
- The solution was placed into a pipette. The substrate was then placed in the center of the spin coater and given one final gust of Nitrogen. The contents of the pipette were then emptied onto the substrate in the centre.
- The film was spun using the relevant solution at 500RPM for 5 seconds, followed by a 60second spin at the final spin speed.
- The films were then transferred to an oven held at  $80^{\circ}C$ , the solvent boiling point, and cured for 2hrs to drive off the majority of the solvent. This would be referred to as the soft cure.
- A razor blade was then used to scratch down to the substrate, using a height measurement taken using a Veeco DekTak 6M Height Profile.
- The films could then be cured closer the glass transition temperature for the polyimide in what is referred to as the hard cure. This was performed in Nitrogen environment using an 16 hour heating cycle, ramp peaking at  $400^{\circ}C$ . The Nitrogen environment was necessary to lower oxidation effects. A thickness measurement was then performed once again.

The results of such hard cured measurements are presented in Figure A.2 that shows a reduction in the thickness with an increase in the solvent and spin speed. A range of dilute precursor, produced by mixing the polyimide precursor with the additional solvent, was obtained separately. This allowed a decrease in the viscosity of the polyimide thin films to produce thinner films. Effort was taken to ensure that the DekTak measurements were valid on the thinnest films where they had been shown to correlate.

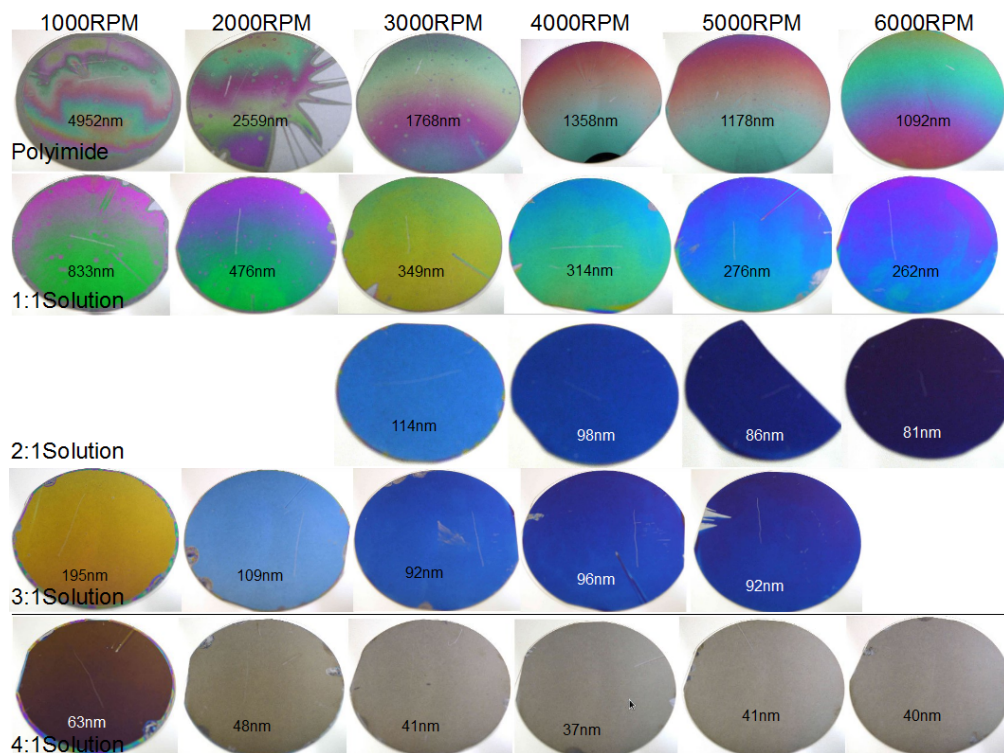


Figure A.2: Various photographs of 4" silicon wafers with different polyimide solutions spun. From top to bottom the concentration of the polyimide precursor to the solvent by volume is decreased, shown on the left hand side as a ratio. From left to right the spin speed is increased shown at the top in rotations per minute.

It should be noted that when illuminated by white light the colour of the film on silicon corresponds to a thickness difference due to interference effects. This is a useful method of evaluating thickness and consistency of films when a quick estimation of of a given sample is required.

Furthermore, no there is no obvious change in the thickness for films having undergone a hard cure. This will be explored further in investigations concerning the effect that curing has on polyimide films.

## A.2 Roughness probed with AFM

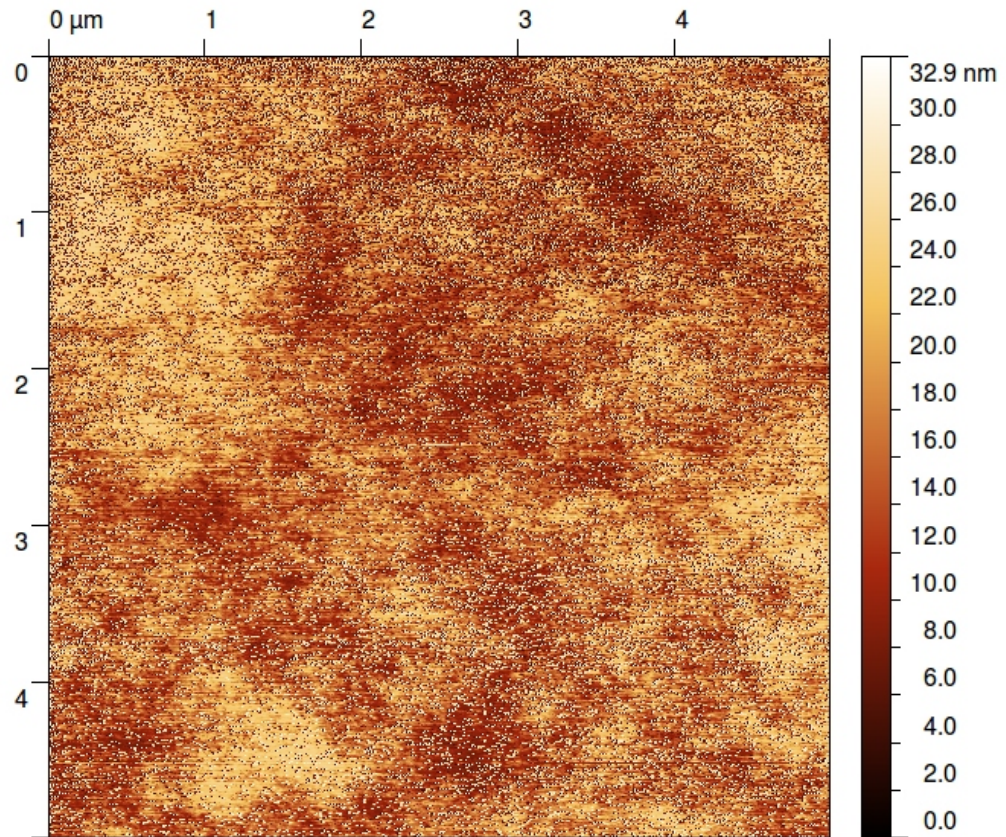


Figure A.3: AFM scan showing witness sample showing two spatial frequencies of roughness of the soft cured polyimide. This illustrates that the NR thickness measurement cannot be compared to local AFM thickness measurements.

## A.3 Evidence of polyimide Charging

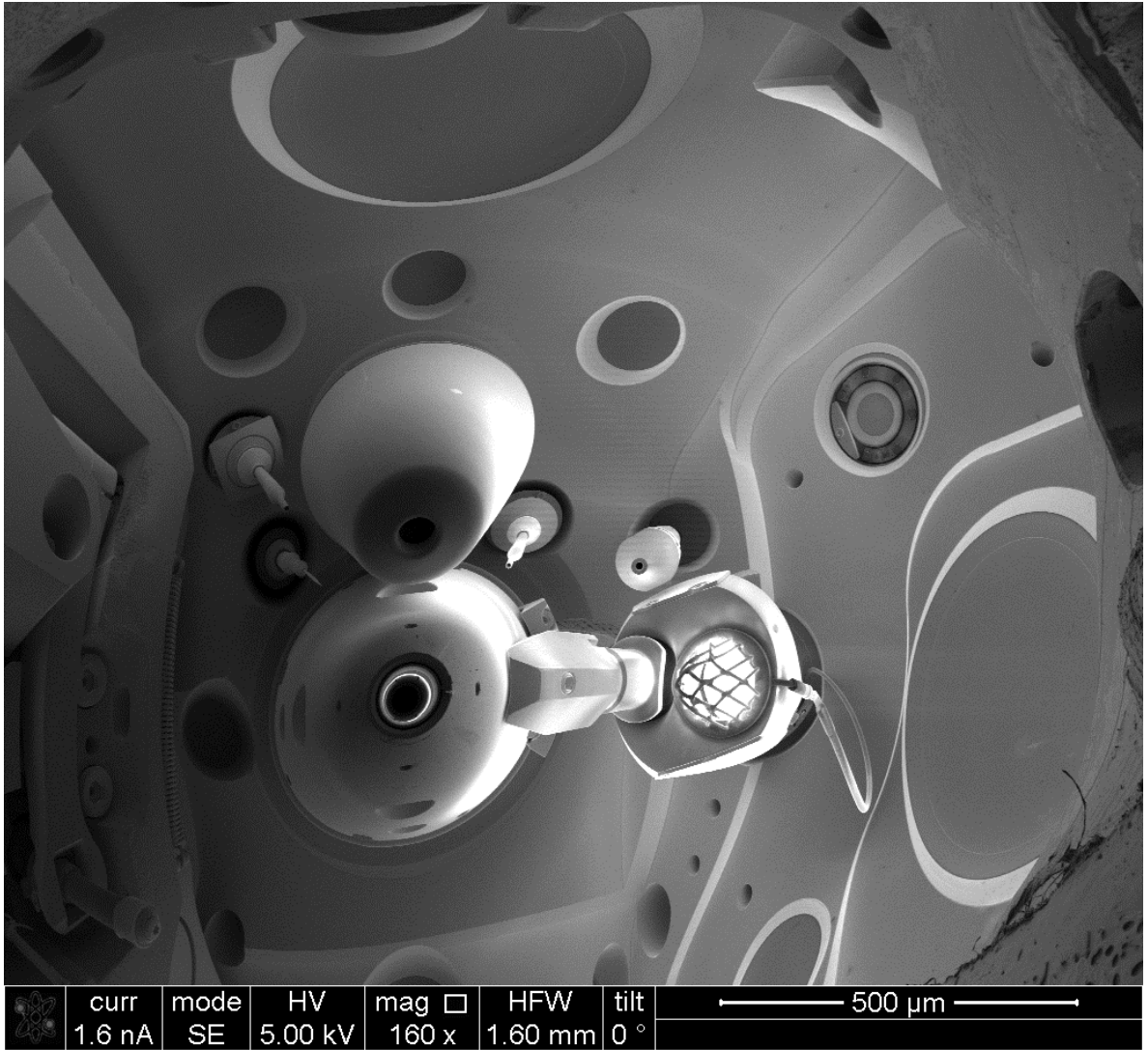


Figure A.4: Polyimide on the Quartz Crystals charges acts like an electron mirror to show the SEM from the point of view of a sample.

#### A.4 Diffusion coefficient Measurements

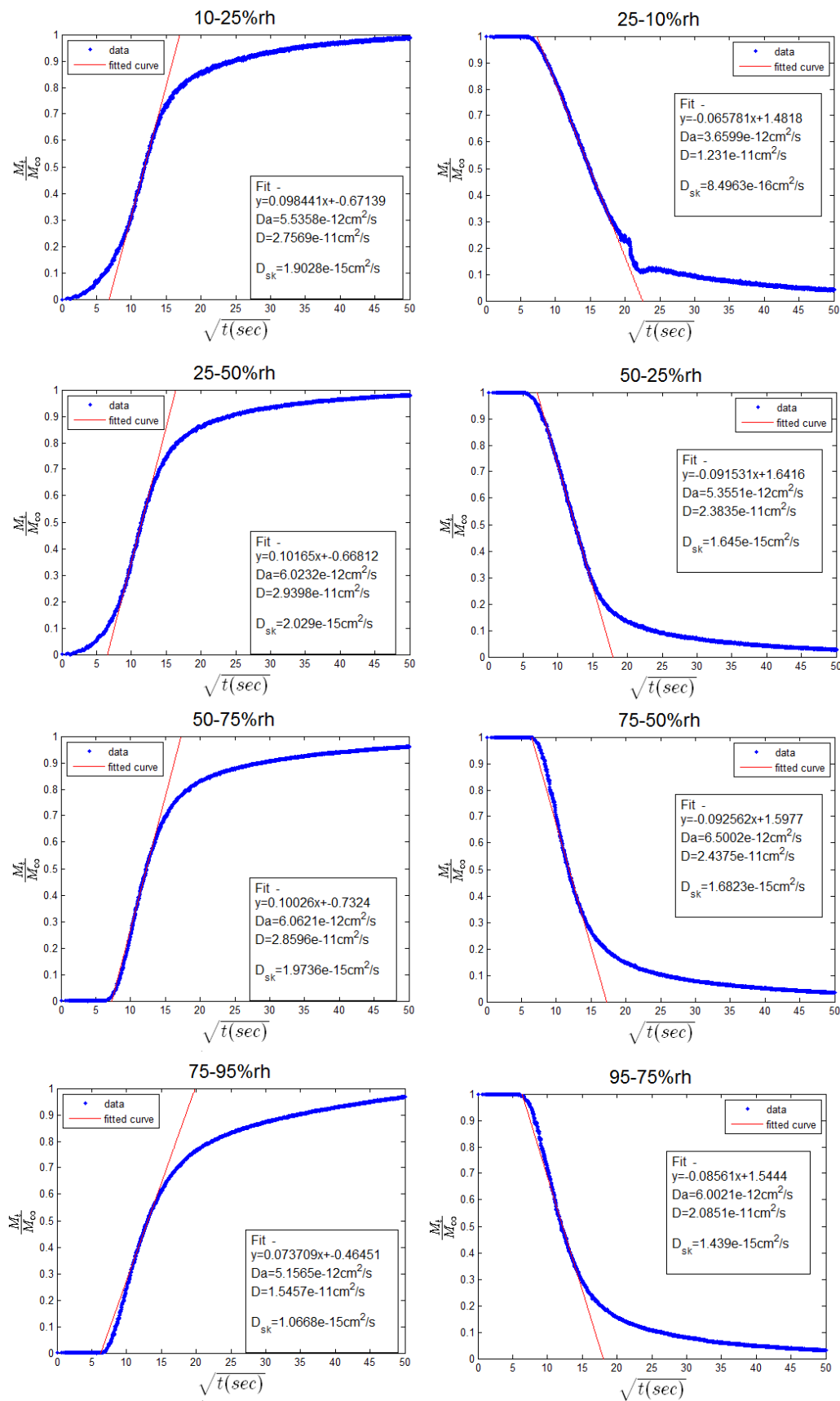


Figure A.5: Measurements of the diffusion coefficient for a  $\approx 1\mu\text{m}$  thick film which has been soft cured. The hypothetical skin diffusion coefficient is constant.

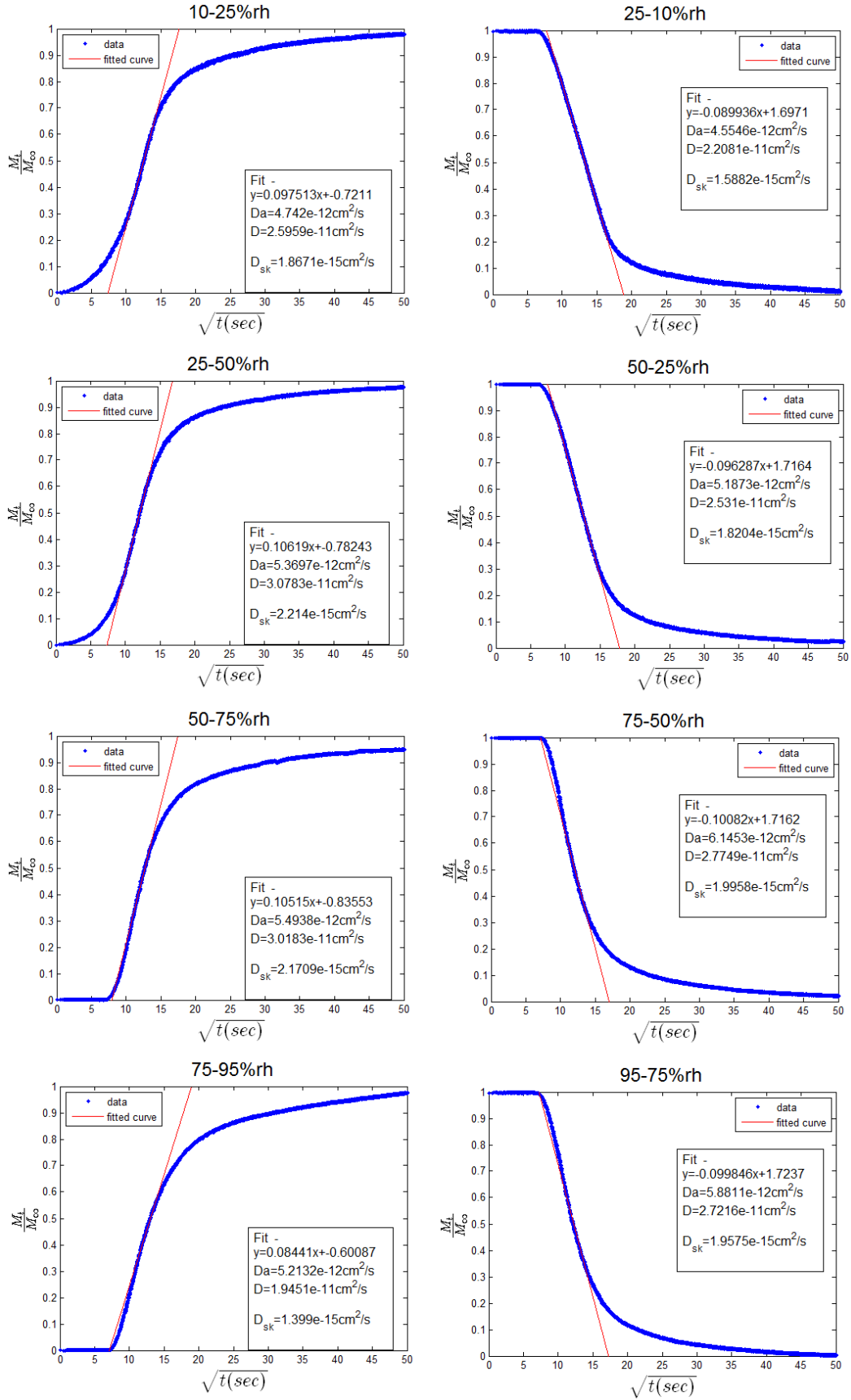


Figure A.6: Measurements of the diffusion coefficient for a  $\approx 1\mu\text{m}$  thick film which has been Hard cured. The 75-95%rh point had less time to reach equilibrium and so  $M_{\infty}$  used for this plot is not accurate. The hypothetical skin diffusion coefficient is constant.

## A.5 QCM sweep measurements

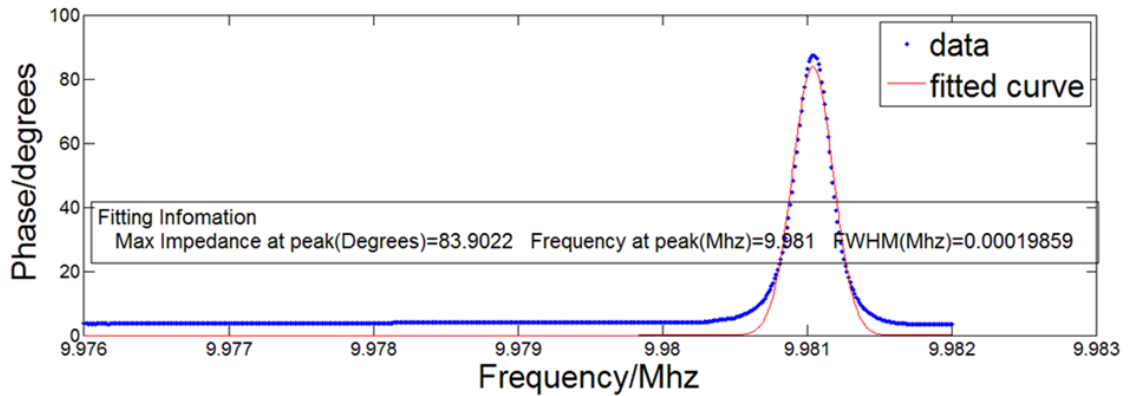


Figure A.7: Showing the fitted phase shift for a crystal. The fitting algorithm was sufficiently robust to find the resonance peak at the extremes of the frequency range.

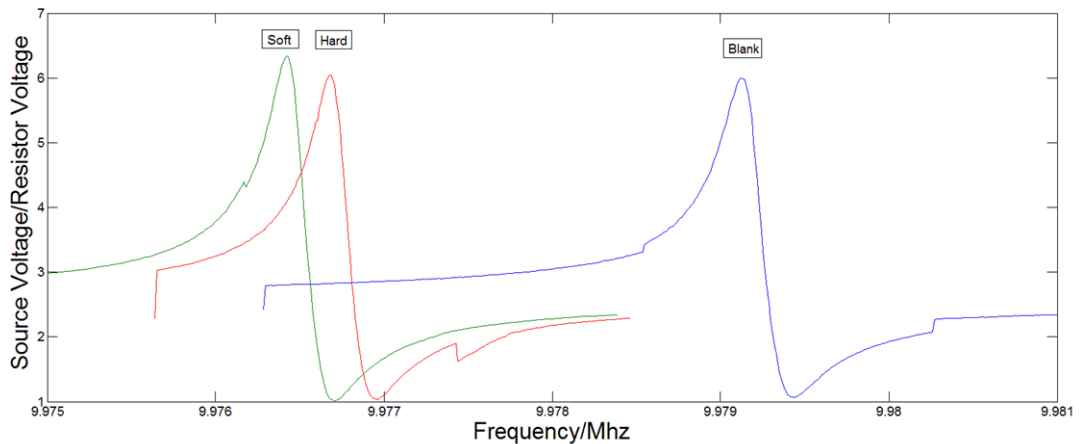


Figure A.8: Impedance sweeps using the Picoscope and the MatLab script. A single crystal is was measured when unloaded, after spinning and curing of the polyimide film.

## A.6 QCM: A test bed for materials

QCM has been used to probe various materials for their sorption and dissipative properties. This was for a variety of reasons such as providing contrast with the polyimide QCM measurements, and to demonstrate QCM as a viable material test bed for industrial purposes. Therefore, in this section measurements from a selection of materials are presented for posterity.

## Polypyrrole

Polypyrrole is a conducting polymer[182] which is easily integrated into CMOS methods[183]. It has been previously utilised as the sensing element in resistive gas sensors[118, 119, 183] and so has the ability to absorb ambient gases. However, its hysteresis and absorption characteristics for water vapour have not been characterised to a high degree of accuracy. Polypyrrole, purchased from Sigma Aldrich in a water solution, was deposited on a QCM using standard spin casting methods and placed into an oven at  $90^{\circ}C$  for 60 minutes to drive off the aqueous solvent. A film mass of 43960ng at 12%rh was measured. A standard calibration profile was acquired on the resulting crystal with an assessment of the dissipative properties over a range of humidities.

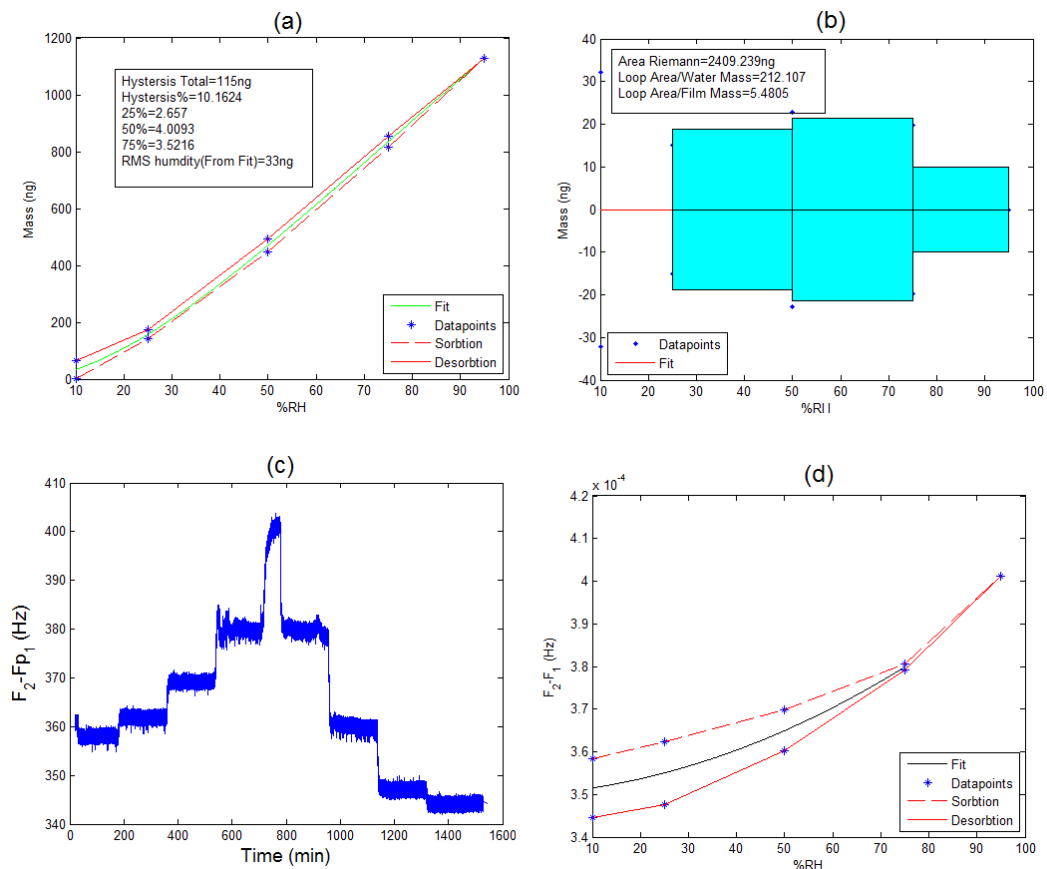


Figure A.9: The analysis of Polypyrrole assuming a density 1.48[182]. The top line shows the mass analysis, (a) hysteresis loop and (b) the hysteresis residuals. The bottom line is to investigate the dissipative properties; (c) as a function of time, and (d) as function of humidity.

The mass of water absorbed by the polypyrrole sample is approximately 1100ng over a calibration cycle, shown in Figure A.9. This is comparable to that of the hard cured polyimide sample with a film mass 37962ng which absorbed 1135ng. However, the hysteresis is much higher with, *the loop area/mass of*

water absorbed at 2.12, when compared to the polyimide films of a similar thickness which gave 0.5-1. This is reflected in the two graphs which show the dissipation of the polypyrrole thin film in Figure A.9(c) and (d), which exhibit a great deal of hysteresis.

The induced volume changes of polypyrrole have been well studied elsewhere[184, 183] and it can be assumed that the observed effect is a consequence of such a phenomenon, a hysteretic dissipation. This indicates that the material properties play a significant role in the hysteresis beyond the simple model of more water resulting in more hysteresis. In this case, the known mechanical swelling of Polypyrrole when absorbing a solvent correlates with a high hysteresis.

## Zirconium Oxide

Both industry and academia have used a variety of materials as a sensing element in capacitive humidity sensors. Metal oxides [185], including zirconium oxide,  $ZrO_x$ , are commonly deployed as a sensing layer[186, 187].

Therefore, a  $ZrO_x$  layer was deposited at room temperature with 30mTor of oxygen by Pulsed Laser Deposition, PLD, over the centre electrode of the QCM with the edges masked. The interest in this project is due to the vastly different mechanical properties of a thin  $ZrO_x$  layer when compared to a polymer layer. It is anticipated that, as a rigid layer, the dissipation in zirconium oxide will contrast with the polypyrrole presented in the last section.

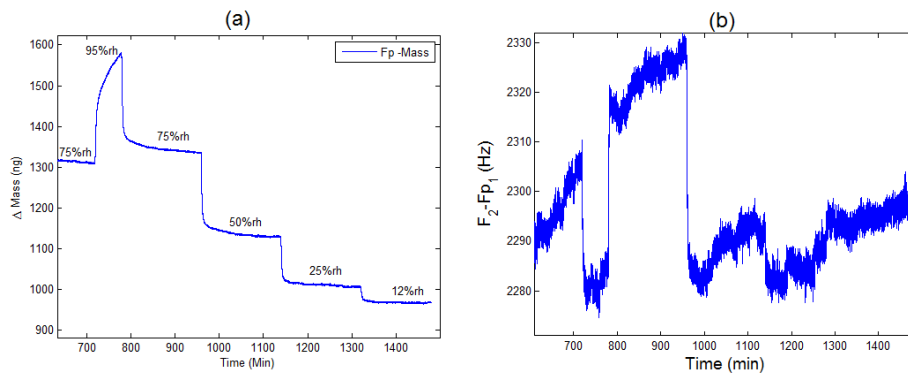


Figure A.10: The latter half of a calibration cycle of Zirconium Oxide; (a) mass and (b)  $\Delta(f_2 - f_1)$  showing the dissipative characteristics.

Due to an electronic issue with the QCM box, the first half of this calibration cycle is not available for presentation. However, the latter half is shown in Figure A.10. A thickness estimate based on the assumed density of  $ZnO_2$  as  $5.68 \text{ g/cm}^3$ , gives a film of 138nm.

The total mass of water absorbed between 12%rh and 95%rh is approximately 600ng, much greater than a polyimide film of similar thickness in the same cycle which absorbed approximately 130ng. The dissipation measure,  $\Delta(f_2 - f_1) = 50\text{hz}$ , about twice that of a polyimide film of a similar thickness as shown in Figure 3.20. This is as expected due to the increased density, and hence the mass ( $M_{ZnO} = 18812ng$ ), of this layer when compared to polyimide is ( $M_{PI} = 4113ng$ ). The coupling of the viscosity and density parameters make it hard to quantitatively compare the two films. Qualitatively however, Figure A.10(b) shows no systematic change at lower humidities and appears noisy, which contrasts with readings on the polyimide where the dissipation parameter scales with humidity. At higher humidities Figure A.10 (b) does show some dependence of the dissipation properties on humidity, this is attributed to condensation. This demonstrates the use of the QCM to probe the stability of materials in various environments, although further readings of the higher harmonics of the crystal are required to be quantitative.

## Polyimides

As discussed in section 1.3, polyimide refers to a broad group of materials with a common imide monomer to make up the backbone. To investigate the influence of the specific chemistry, two polyimides were purchased from HD micro systems, PI 2555 and PI 2610. Crystals were produced with a target thickness of  $\approx 1\mu\text{m}$  by diluting the original precursor, and both crystals were soft cured.

The calibration profile shows a water uptake by weight from 12%rh to 95%rh of 2.8%, and 1.3% for the PI 2555 and PI 2610 respectively, as shown in Figures A.11 and A.12. This is less than the soft cured polyimide at 4%, which has been used in this investigation. Both crystals exhibited hysteresis characteristics and appeared to show a hysteric humidity dependent dissipation.

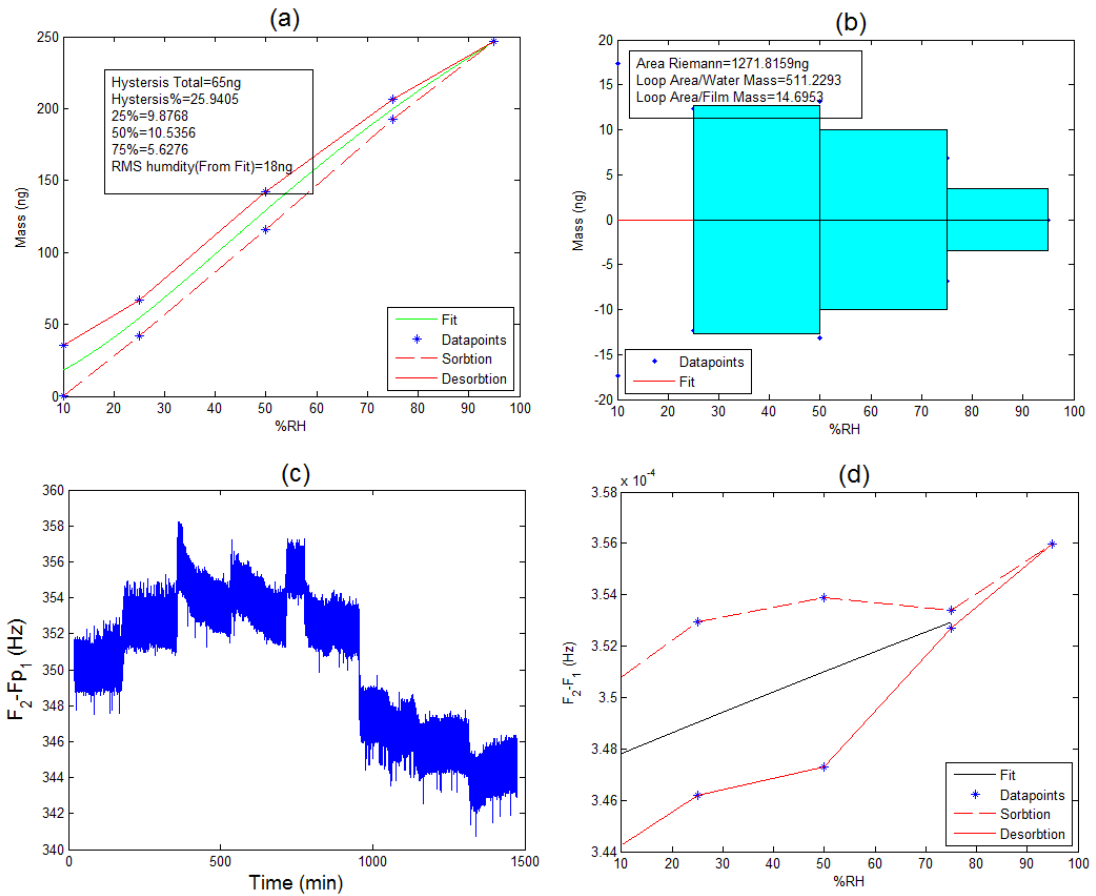


Figure A.11: The analysis of polyimide 2555, assuming a density 1.42. The top line shows (a) the mass hysteresis loop and (b) hysteresis residuals. The bottom line is to investigate the viscoelastic properties; (c) as a function of time, and (d) as function of humidity.

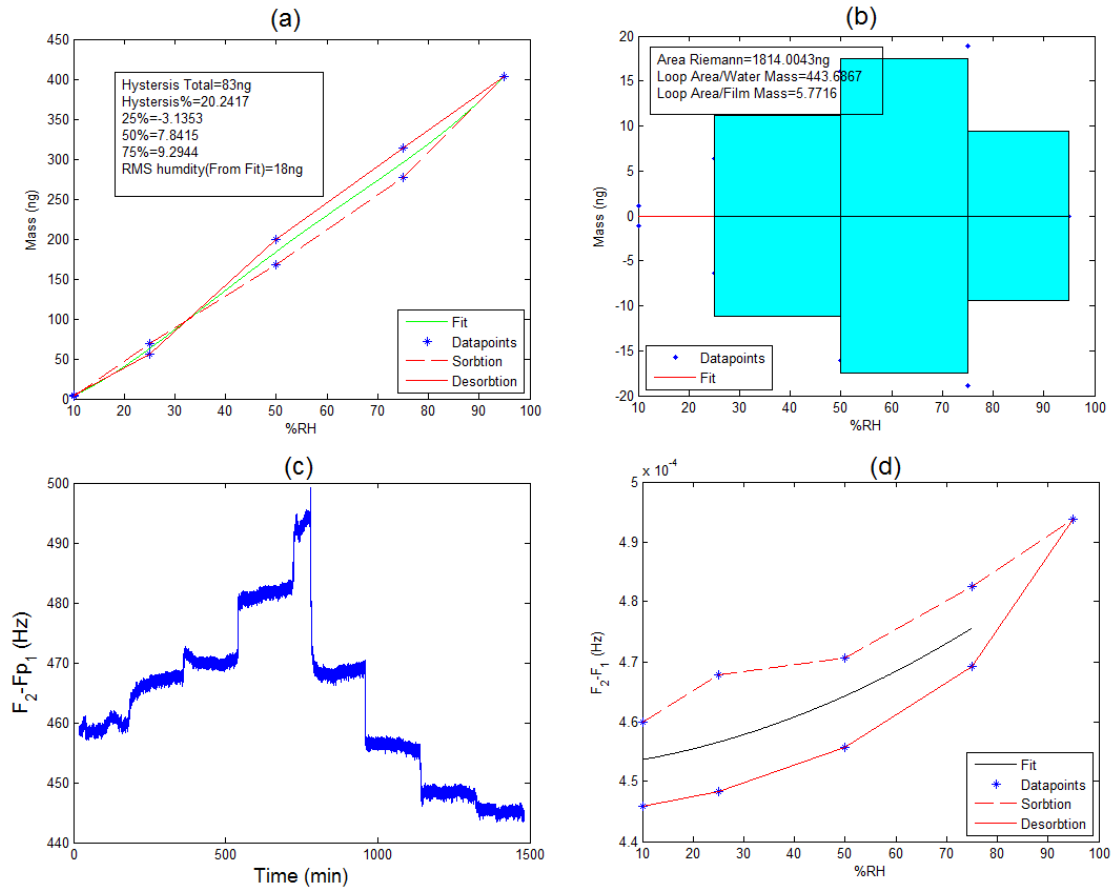


Figure A.12: The analysis of polyimide 2610 assuming a density 1.42. (a) The mass hysteresis loop (b) residuals of the fitted line on the right. The bottom line is to investigate the viscoelastic properties; (c) as a function of time, and (d) as function of humidity (right).

Table A.1 summarises the findings of the QCM investigation into various materials. The hysteresis loop area/film mass ratio is shown to present hysteresis varied in both materials. .

Material	Film Mass (ng)	Water Uptake (%)	hysteresis/Film Mass (%)	Mean $\Delta(f_2 - f_1)$
Polypyrrole	43960	2.6	5.5	371
Zirconium Oxide	10921	5.9	n/a	2050
PI 2555	8654	2.8	15	464
PI 2610	31430	1.3	5.8	351
Polyimide (Soft)	39162	3.7	3.7	293
Polyimide (Hard)	37862	3	6.4	364
Polyimide (Plasma)	37968	2.7	3.5	498

Table A.1: A table to compare the QCM reading from various materials. Water uptake is shown by weight and the hysteresis loop/film mass is also given.

Preliminary readings show the hysteresis to be very high in PI 2555 (Figure A.11(a)). Alongside a higher hysteresis, PI 2555 also shows a more constant dissipation level when compared to the other polyimides (Figure A.11(c)). This confirms that the hysteresis is a function of the specific material chemistry and that the water transport properties of different polyimides can vary. It would be of interest to measure the dielectric properties of these polyimides along the mass uptake, to understand how the materials dielectric properties and mass hysteresis relate, as both are influenced by the polarity of the molecules in the material.

## Summary

The mean  $\Delta(f_2 - f_1)$  has registered the significantly different material properties of the  $ZnO_x$  as compared to the other materials. Additionally, the neutron SLD profiles indicated that bulk soft cured polyimide was of lower density than the hard cured polyimide with the plasma etched being the most dense,  $\Delta(f_2 - f_1)$ , which is linked to the mechanical properties which follows the same pattern.

The water transport properties of each of these materials have been successfully measured using the QCM technique and the dissipation indicated. More work is required to link the  $\Delta(f_2 - f_1)$  measurements to the mechanical properties of the film quantitatively. QCM has shown itself to be a good technique to evaluate two of the most important factors in choosing a sense element material; the mechanical properties, qualitatively, and absorption characteristics, quantitatively.

## A.7 Raman Spectroscopy to Probe Polyimide-Water Interactions

Permporometry and TEM revealed likely molecular length scales of the water transport within the polyimide. Previous chapters discussed the measurement of timescales of transport. However, factors determining those timescales include the degree of chemical interaction between the penetrant and the thin film. Therefore, a technique to probe extent to which water vapour impacts on the molecular vibrational modes of the polymer may contribute to how freely the water vapour can move within the polymer, and hence the diffusion rate.

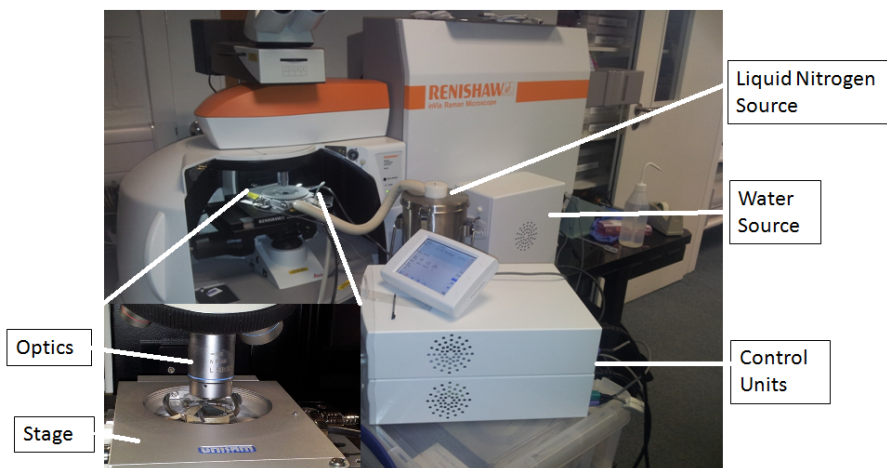


Figure A.13: The experimental setup for the Raman microscope showing the chamber and the water control equipment.

Raman spectroscopy utilises the inelastic scattering of monochromatic light[42]. The laser light interacts with excitations in the system, such as molecular vibrations, which results in the energy shift of the laser photons. The shift in energy corresponds to activated vibrational modes in the samples. Here the polyimide on silicon samples were illuminated with a green (514nm) laser beam in a Renishaw InVia Raman microscope. Light from the illuminated spot was collected and elastic scattered radiation was filtered out, leaving the rest of the collected light dispersed onto a detector.

The resulting spectra gives a map of the various molecular vibrations in the system. By performing this experiment in a nitrogen atmosphere, and in the presence of water vapour, any chemical bonding between the water vapour and the polyimide should act to change the energetics of the molecular vibration mode, leading to a shift in the Raman spectra. Here a humidity and temperature stage with an optically transparent window from LiNKAM Scientific Instruments was used in the Raman microscope to provide the atmospheric control required as shown in Figure A.13.

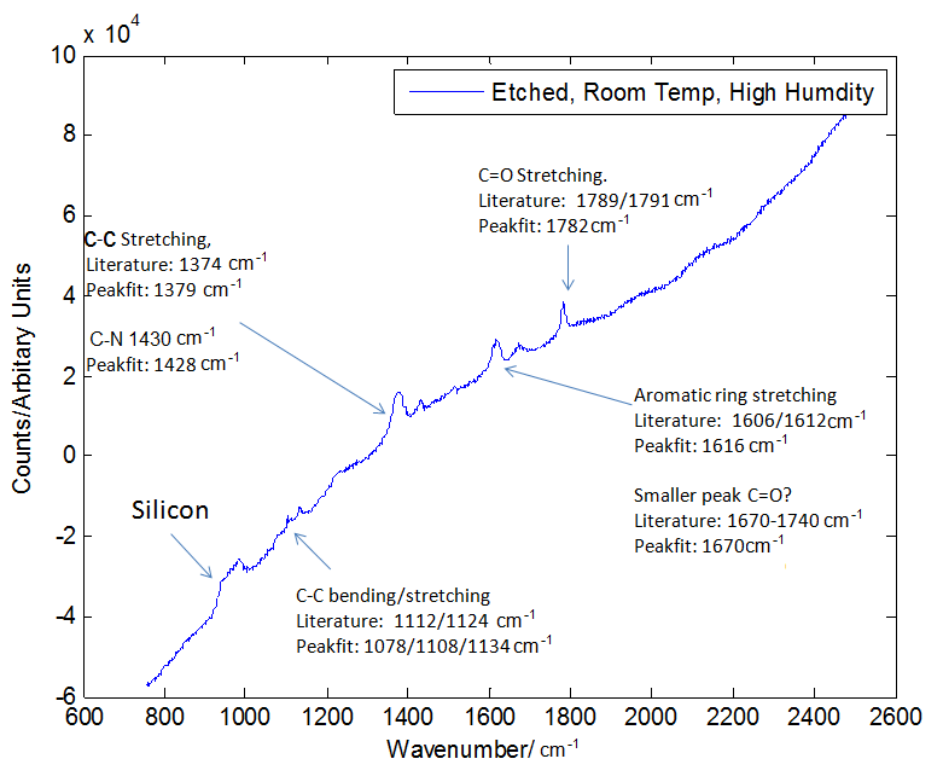


Figure A.14: The Raman spectra of soft cured polyimide in a dry state. Peaks we assigned by comparison with the work of Gu et al.[188]

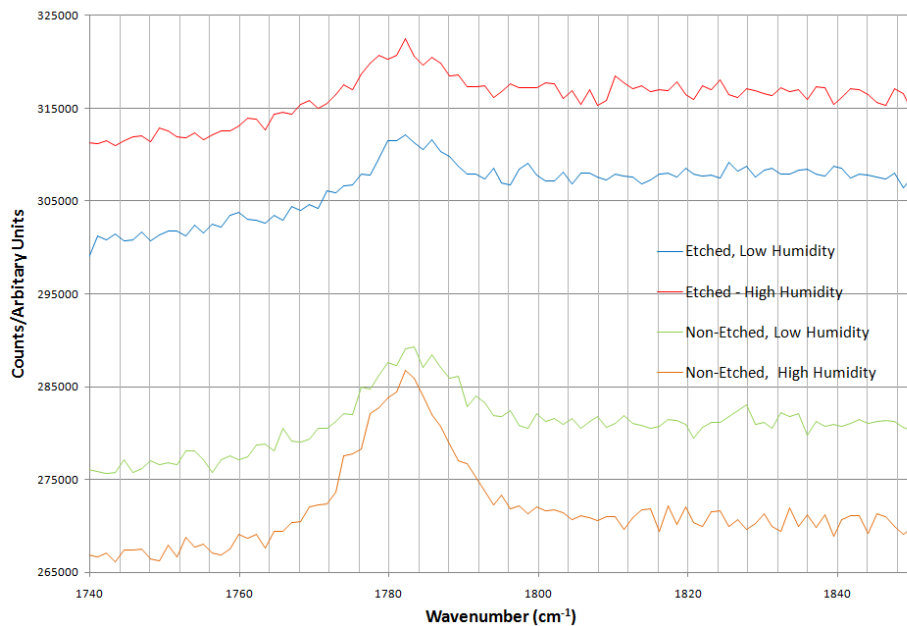


Figure A.15: The C=O peak shown from film in both a dry and humid state for etched and non-etched films.

The *finger print region*, so called as it allows the material to be identified from the vibrational spectra of the polyimide is shown in Figure A.14. The common vibrational modes for polyimide are marked, with a particular interest in the polar carbonyl, C=O, peak as IR spectroscopy studies have shown it to interact with the polar water molecule[38].

The carbonyl peak shown in Figure A.15, shows no appreciable shift in the features of the spectra when observed between the wet and dry state. This shows little or no change in the vibrational modes of the polyimide in the presence of water vapour on the scale of tens  $cm^{-1}$ . However, if the interaction is very weak the number of counts may be too low to notice a subtle change in the spectra, and therefore difference spectroscopy in which a difference spectra is displayed, may be better to observe this interaction. This is presented in the next subsection.

## A.8 Bright Field image of Neutron 150nm Hard Cured Neutron Sample

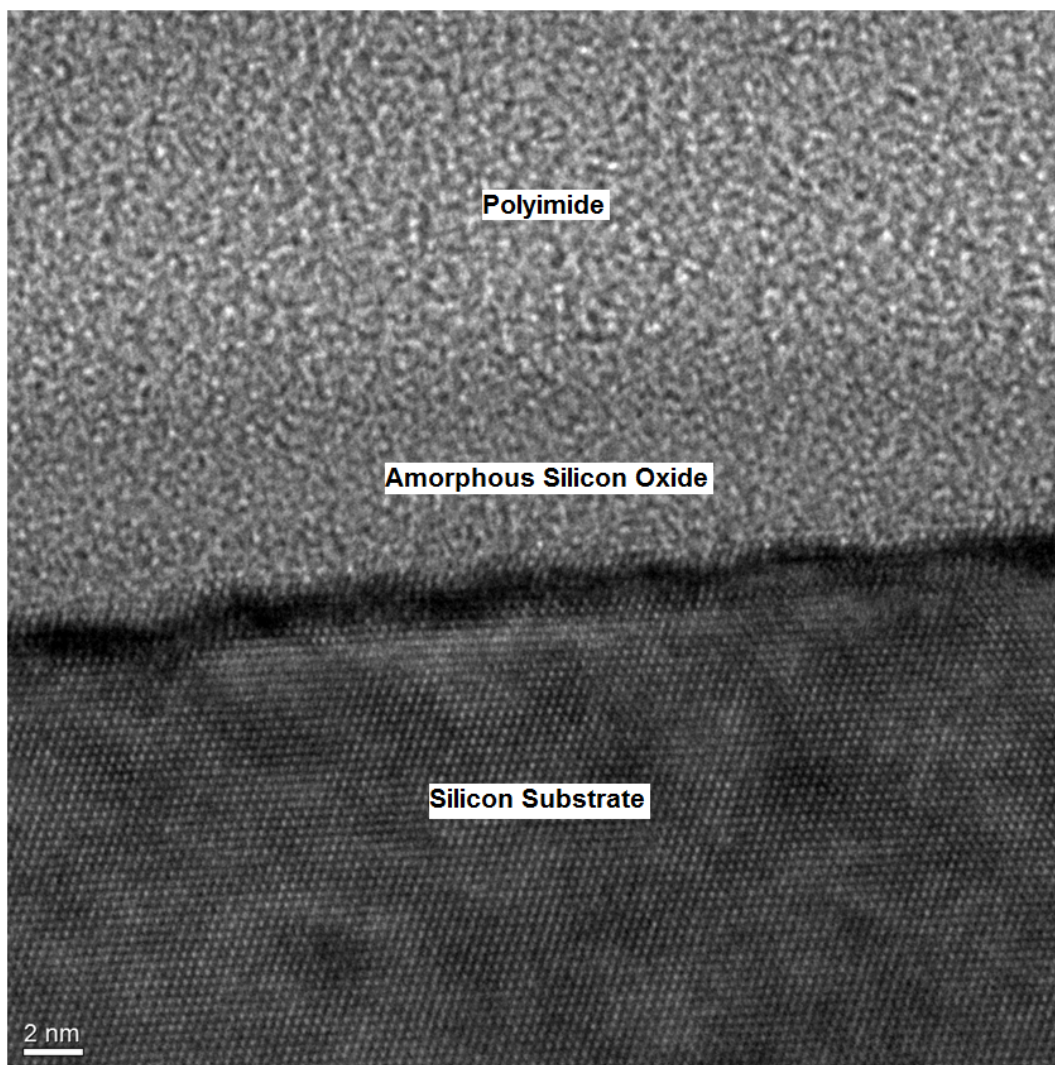


Figure A.16: Bright field TEM image of the 150nm neutron sample. Shows an ordered silicon substrate with two amorphous materials on top which can be distinguished by the marked change in spatial frequency.

## A.9 Time Resolved SLD Profile fit

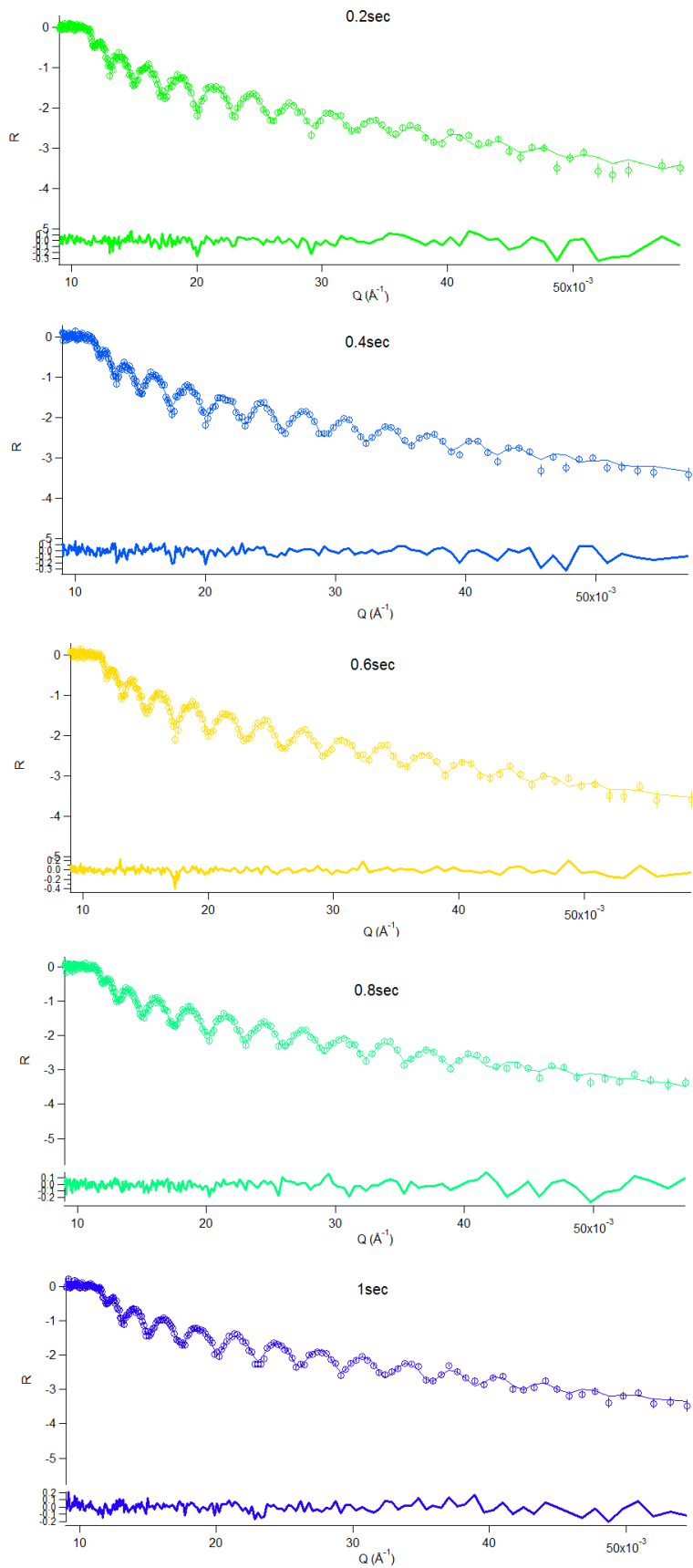


Figure A.17: Corresponding to Figure 5.30.

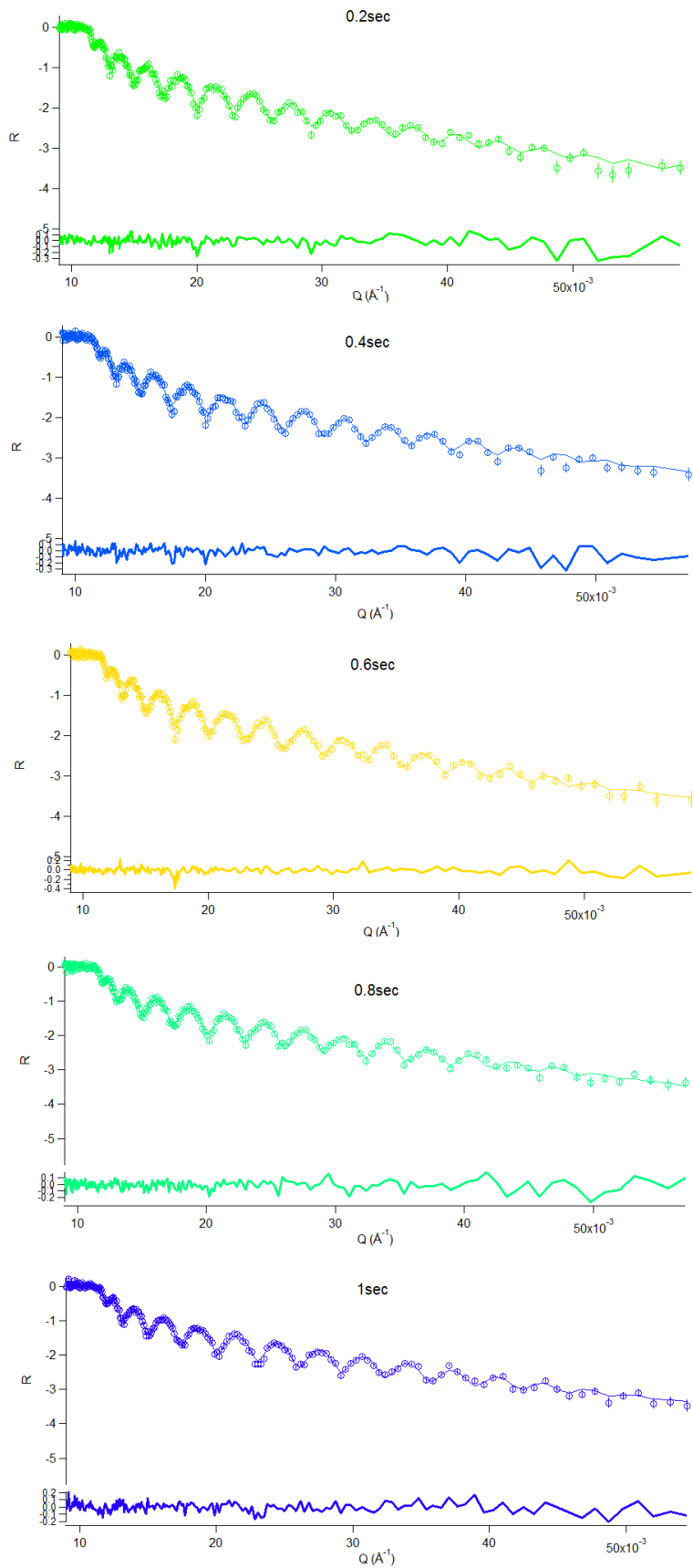


Figure A.18: Corresponding to Figure 5.31.

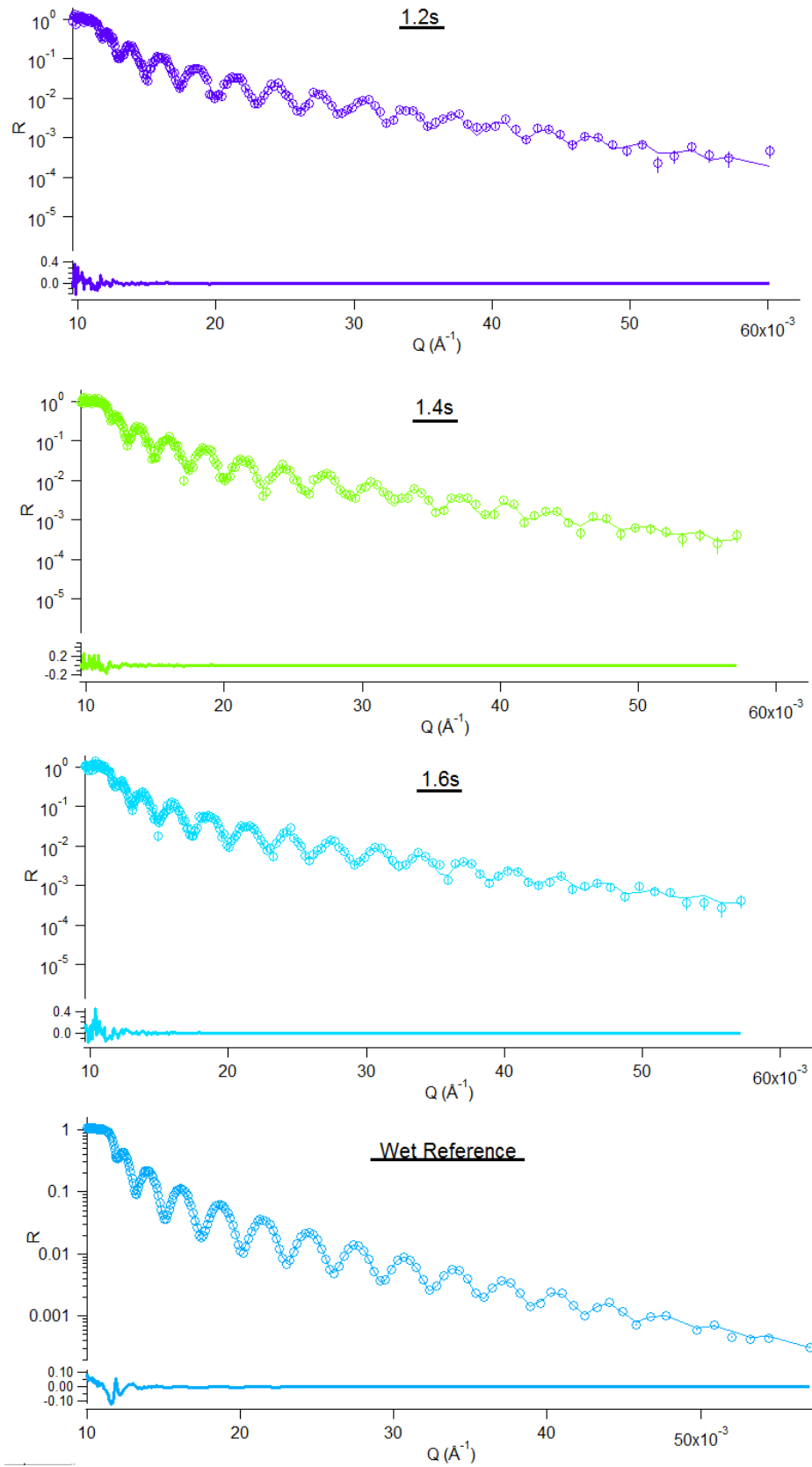


Figure A.19: Corresponding to Figure 5.31.

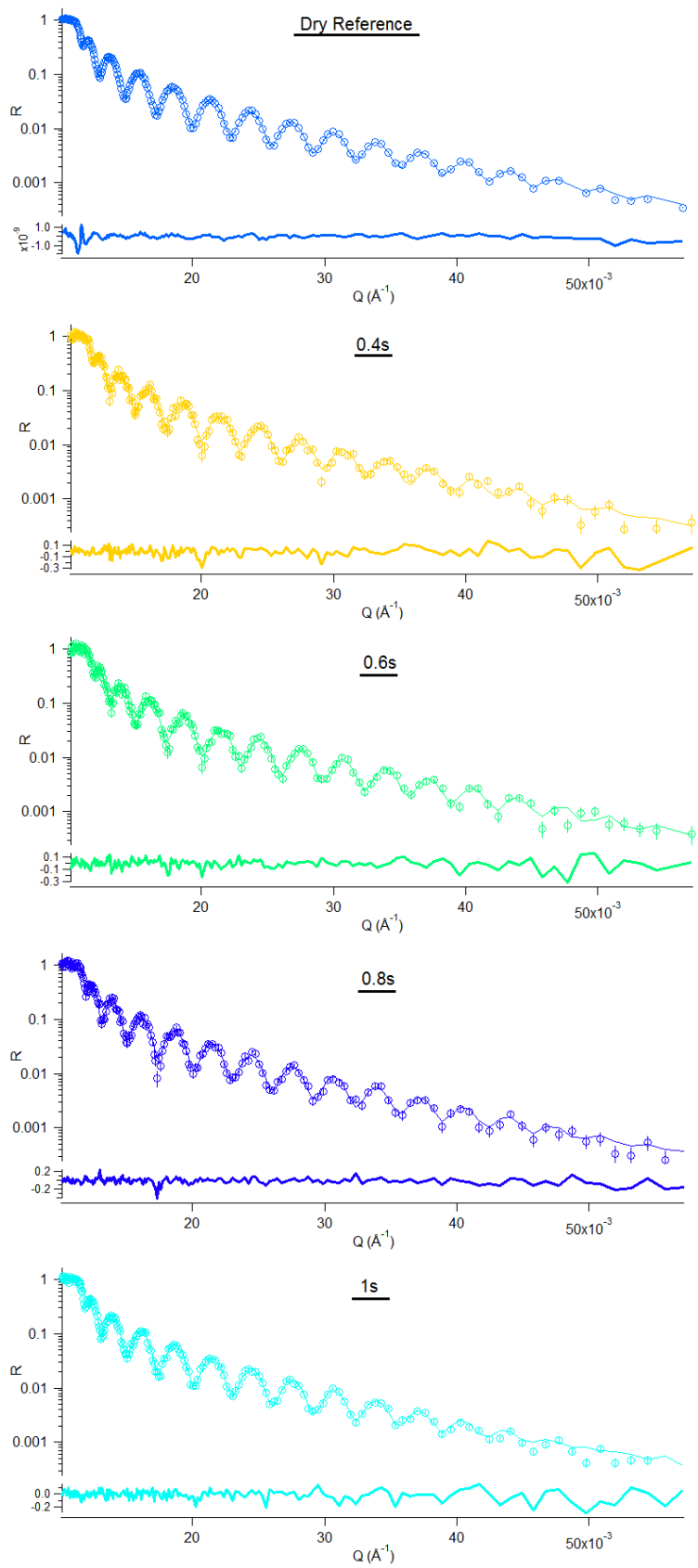


Figure A.20: Corresponding to Figure 5.37.

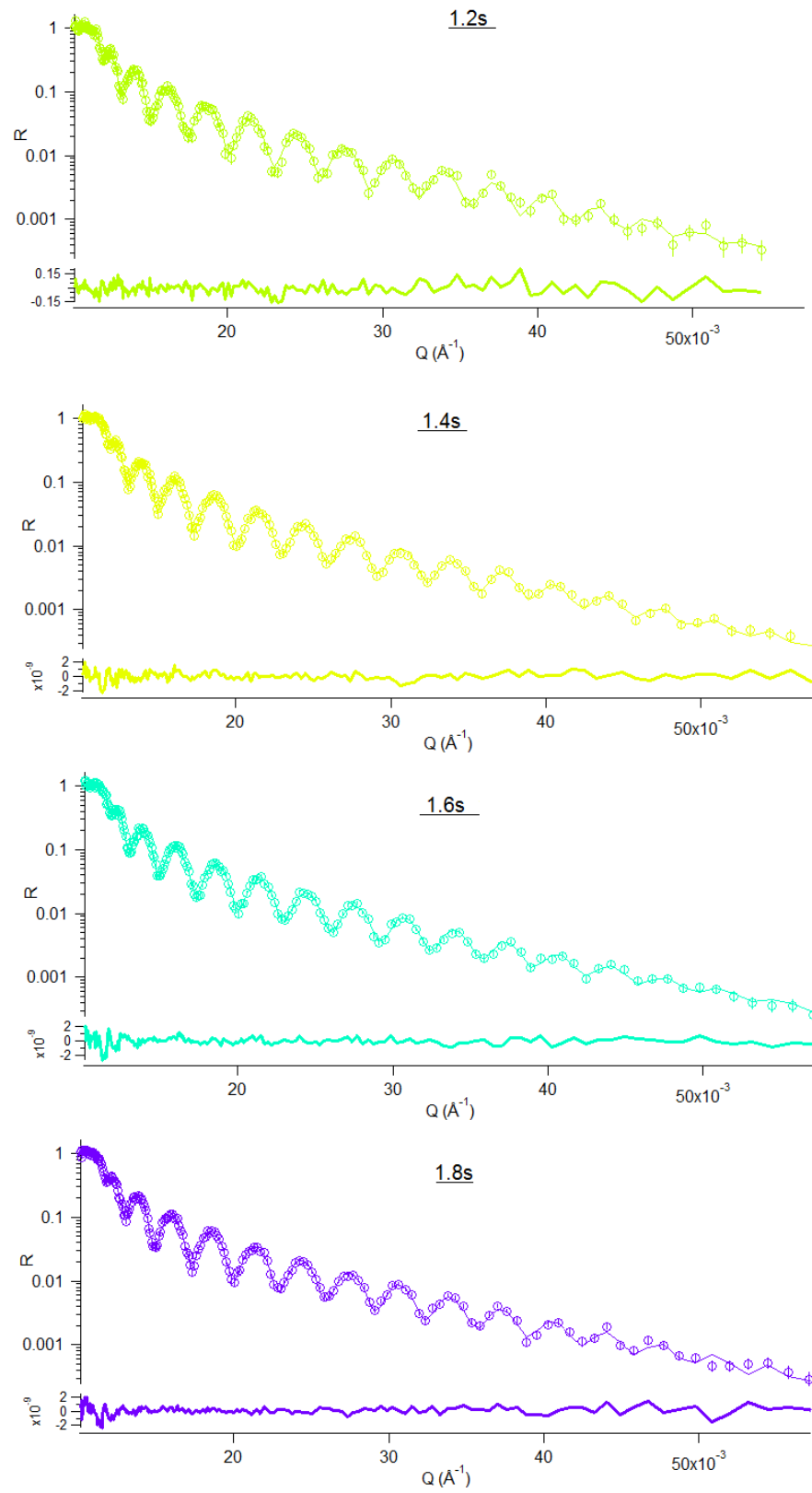


Figure A.21: Corresponding to Figure 5.37.

# List of Figures

- 1.1 (a) An illustration of the structure of a sandwich type humidity sensor (b) A schematic of the water molecule showing the origins of the intrinsic polarity. . . . . 8
- 1.2 A graph provided by Honeywell of the output from a humidity sensor. The sensor exhibits the hysteresis effect. An illustration is added in the bottom right hand corner to depict the sensors hysteretic behaviour. . . . . 9
- 1.3 A illustration of the phase diagram for water showing the dew point or 100%RH boundary, which is highlighted. The triple point and critical points of water are marked. . . . 11
- 1.4 A comparison between the relative humidity(linear) and dew point temperature as a function of absolute humidity at 1atm and 20°C. Data is taken from Noor et al. [18]. . . 13
- 1.5 (a) The functional group of polyimide. R, R and R refer to any kind of side chain attached to the functional group. (b)The chemical structure of Kapton (*DuPont<sup>TM</sup>* [33]), a common form of polyimide. . . . . 15
- 1.6 A diagram to show the non-fickian diffusion conditions in which  $(DEB)_D \sim 1$ . Diffusion is non-Fickian when the material acts like a fluid  $(DEB)_D \ll 1$  or an elastic solid  $(DEB)_D \gg 1$ . . . . . 20
- 1.7 Plots of three term approximations for Equations 1.8 and 1.9 for a  $1\mu m$  film with a diffusion constant of  $10^{-12}cm^2s^{-1}$ . For the three term approximation shown, the impact of losing the higher terms means that Equation 1.8 never reaches zero and Equation 1.9 reduces. . . . . 21
- 2.1 Two methods for the measurement of impedance (a) The simplest form, an alternating potential is placed across the device and the resulting current wave is measured. (b) A known resistor is placed in series with the device under test (DUT) and the ratio of the voltages across the DUT and the device allows the characteristics to be inferred. . . . . 27
- 2.2 Quartz under mechanical stress. It is shown that under tension and compression a potential is generated in the quartz. . . . . 29

2.3	The sheer mode oscillation in (a) an uncoated QCM (b) a rigid film. . . . .	29
2.4	The scattering of a neutron wave by a single nucleus. The scattered wave will have amplitude $\frac{b}{r}$ . The plane wave fronts from the left denote the neutrons which are scatter radially from the nucleus as shown. Adapted from Pynn et al.[72]. . . . .	31
2.5	(a) Elastic scattering ( $k = k'$ ): Shows an elastic scattering process where there is no transfer of energy between the neutron and the sample. (b) Inelastic scattering ( $k \neq k'$ ): Shows the possibilities for inelastic scattering where energy is transferred between the neutron and the sample. Adapted from Pynn et al.[72]. . . . .	33
2.6	The chain reaction causing the production of neutrons. Firstly, an incident particle causes the Uranium 235 to become an unstable isotope Uranium 236. Uranium 236 then break down into krypton (36) and Barium(56) releasing neutrons. . . . .	34
2.7	A photo showing the various instruments in the main hall of the second target station at the ISIS neutron facility. There is capacity for a total of 18 instruments, and building is ongoing with the three operational instruments labelled. Additionally, the Larmor instrument, on the right hand side, is commissioning. As a result, spatial restrictions are significant. . . . .	35
2.8	The layout of D17 in monochromator mode. Adapted from Cubitt et al.[82]. . . . .	36
2.9	The layout of the Inter beam line adapted from Webster et al. [84]. . . . .	38
2.10	The various signals emitted from a thin sample when illuminated by an electron beam, each signal can provide different information about the sample. . . . .	40
2.11	Layout of a typical TEM column in bright field mode. This shows the electromagnetic lenses and apertures used to generate an image. The diffraction lens and selected area aperture are not shown. Adapted from Williams and Carter[89]. . . . .	41
2.12	The Electron Gun. The cross over point can be considered the source, and the angular divergence is determined by both of the characteristics of the Wehnelt. . . . .	42
2.13	2D depiction of magnetic flux lines (dashed) from a short coil in cross section. . . . .	43
2.14	Various detectors are required to pick up signals scattered though different scattering vectors. The bright field detector. BF, has a high electron count and is therefore required to be more robust. The high angle dark field detector is designed to pick up fewer electrons and is therefore more sensitive. . . . .	45
2.15	The optics results in each point on the sample, $f(x,y)$ , being respresented by an extended disk, $g(x,y)$ . . . . .	47

2.16	Showing the Pre, Post, and final images in producing an oxygen Map. The sample is polyimide spun onto a silicon wafer, here the oxide layer is mapped. . . . .	48
2.17	illustration diagram showing beam path of Bragg scattered beam and the path difference generated. . . . .	49
2.18	Two diffraction patterns. (a) A gold cross grating with well defined common spatial frequencies, and (b), for amorphous polyimide with more diffuse rings corresponding to less well defined spatial frequencies. . . . .	51
2.19	Showing the working principles of the NT-MDT Solver NEXT AFM. Deflections in the laser are detected to map the surface properties. . . . .	52
2.20	A photograph of the thunder scientific thunder chamber Model 2500 Benchtop/Mobile "Two-Pressure" Humidity Generator setup before a calibration run. . . . .	54
2.21	The flow diagram showing the movement of heating fluid in the Thunder chamber. . . .	54
2.22	The flow of dry air in the Thunder-chamber. $P_{Saturated}$ is the pressure of saturated water vapour at the set temperature. $P_{Chamber}$ is controlled by the expansion valve. . . .	55
3.1	(a) A Butterworth Van Dyke circuit representing a blank QCM [70]. (b) A possible circuit representing a QCM loaded with a viscoelastic film presented by Parlak et al.[71].	58
3.2	Admittance sweep of a blank QCM showing the various admittance at frequencies close to resonance. . . . .	59
3.3	A photograph of a 10Mhz AT cut crystal in the holder which was used for this project. These crystals were ordered with deposited electrodes on either side of the crystal (10nm/100nm, Ti/Au), mounted inside the holder and unbonded to the holders from International Crystal Manufacturing Inc. (Product# 151218-10) [108]. The diameter of the electrode is 0.51cm, the total crystal diameter being 1.36cm. On this crystal, a polyimide has been spun later (as detailed in section A.1) over the centre electrode and the crystal has then been attached to the holder using conductive silver paint (which can be seen on the left hand side). . . . .	60
3.4	A circuit diagram showing the method of measuring the impedance of the QCM which was discussed by Shirazi[109]. The QCM is represented here by its equivalent BvD circuit.	61
3.5	The phase shift from the starting positions for the 70nm crystal when it is unloaded, after the deposition of a polyimide film (soft cured), and after a longer anneal (hard cure).	62
3.6	Shows the Impedance of crystals of various thicknesses of soft cured polyimide. The raw frequency, not the shift in frequency, is shown. . . . .	63

3.7	Frequency shift as a function of thickness for polyimide thin films on QCM. The thickness measurements are taken from the AFM scans performed on witness samples, and the frequency readings are read from the fitted Gaussian function to the relative phase shift of the voltage and current waves as discussed. . . . .	64
3.8	A screen shot of the Gamry resonator software. Two increases in humidity were generated to check the response of the system. The top graph shows the data and fit of the current reading. The bottom graph shows the measured frequencies as a function of time. . . . .	65
3.9	The frequency readout for the same film on a QCM at three different temperatures as the humidity is varied. . . . .	66
3.10	(a): The Temperature (green), and frequency (blue), readout of a blank crystal as a function of time. (b): Frequency as function of temperature showing a cubic fit. . . . .	67
3.11	(a) Output from the thunder chamber sensors on a test cycle (pseudo calibration) run. The temperature is held at $25^{\circ}C$ and the humidity is well controlled. (b) Shows no hysteresis in the chamber. . . . .	68
3.12	The change in mass as a function of time for a soft cured polyimide film. The 50%rh point is zoomed in on for both wetting and drying showing a small mass flux on a nanogram scale after 3 hours. . . . .	68
3.13	The data shown in Figure 3.12 flipped and plotted to show the existence of hysteresis as measured by a MatLab script. . . . .	69
3.14	Shown are the methods of measuring the hysteresis. (a) The mass of the film as a function of %rh. (b) Residuals of the fit with the fitted line in the middle. (c) Showing the measurement of the area of the hysteresis loop. . . . .	70
3.15	Density measurements of the polyimide thin films at different process stages, across a range of thicknesses. . . . .	72
3.16	The mass of water absorbed as a function of film weight for five polyimide thin films of different thicknesses deposited on a QCM. Three data sets are shown for the same set of crystals after a soft cure, after a hard cure, and a oxygen plasma etched. . . . .	72
3.17	(a) The hysteresis loop area as a function of film mass. (b) The hysteresis loop area/Film mass as a function of film mass. (c) The hysteresis loop area as a function of water uptake in each film. . . . .	73
3.18	The Hysteresis loop area for each film deposited on a QCM is shown in a different colour. The x-axis is divided to show the three processing stages sequentially. . . . .	74

3.19	A screen shot of Gamry software showing the measurement of $f_s$ and $f_p$ using a fitting function. The data is shown in red and the fit is shown in blue. This is not a good fit and so can lead to an error in frequency measurement of $f_p$ of tens of hertz. . . . .	75
3.20	The viscoelastic properties of a 130nm plasma treated film through a humidity cycle. (a) The $f_1$ and $f_2$ of a QCM with a polyimide film on the surface. (b) The mass calculated from $\Delta f_2$ using the Sauerbrey equation. (c) $f_2 - f_1$ reflecting the viscoelastic properties of the film and surrounding medium as discussed. . . . .	76
3.21	$f_2 - f_1$ for the same crystal at different stages of processing presented in Figure 3.20. This shows the dissipative properties are a function of film treatment, which is more dominant than the humidity level. . . . .	78
3.22	The viscoelastic properties of a thick film. (a) Shows the $f_s$ and $f_p$ plotted as a function of time in a calibration cycle in the thunder chamber. (b) shows the $f_2 - f_1$ as a function of humidity. . . . .	79
3.23	The QCM data from the same $1\mu\text{m}$ polyimide thin film though a humidity cycle when the film is at different stages of processing. (a)Soft cured, frequency measurements. (b)Soft cured, mass measurements. (c) Soft cured, $\Delta(f_2 - f_1)$ .(d) Hard cured, frequency measurements. (e)Hard cured, mass measurements. (f) Hard cured, $\Delta(f_2 - f_1)$ . (g)Plasma etched, frequency measurements. (h)Plasma etched, Mass measurements. (i)Plasma etched, $\Delta(f_2 - f_1)$ . (c), (f) and (i) show the change in the dissipative properties of the polyimide films through a humidity cycle. (i) is much flatter indicating that the dissipative properties of the film are less affected by humidity than the other two, (c), and (f). (i) also shows a peak at 95%rh, perhaps indicating condensation. The mean $\Delta(f_2 - f_1)$ (comparing y axis scale bars for (c),(f) and (i)) has increased with each treatment implying that the treatment changes the dissipative properties of the film. . . . .	80
3.24	The response to a series of vapour pulses of both, a commercial sensor humidity sensor (capacitance) and QCM (mass). This is data acquired during the neutron scattering experiments, presented in chapter 5. . . . .	83
3.25	(a) The box with two BNC connections to connect to the capacitance meter and the DIL socket on top to plug devices in. (b) The wiring of the box with additional connections to run a voltage across a sensor. (c) The measurement box in the thunder chamber with the QCM in the back before a pseudo calibration cycle is performed. . . . .	84
3.26	The capacitance from; (a) a nichrome IDT and (b) a 1820 Humidity sensor, in a thunder chamber on a humidity calibration run. . . . .	84

3.27	The hysteresis measurements on a nichrome IDT device. The data is shown in Figure 3.26. . . . .	85
3.28	(a): The results of a CQCM device, both frequency output and capacitance. (b): A photograph of the CQCM device. (c) A illustration of the device. . . . .	87
4.1	Measurements of the diffusion coefficient for a $1\mu m$ thick film which has been hard cured and plasma etched. . . . .	93
4.2	Measurements of the diffusion coefficient for a $120nm$ thick film which has been hard cured and plasma etched. . . . .	94
4.3	The maximum possible diffusion coefficients for a $1\mu m$ thick film which absorbs all water which hits the surface based on thunder chamber partial pressure measurements. This is calculated from thunder chamber measurements as discussed in section 4.1.1. . . . .	95
4.4	The diffusion coefficient as a function of thickness. The diffusion coefficient appears to vary in a non linear manner as a function of thickness which is surprising as it should only be a function of the material and not the material thickness. . . . .	97
4.5	Attenuated total reflectance uses the evanescent wave of light to probe the sample. . . . .	100
4.6	The ATR-FTIR measured spectrum was calibrated to read 100 units when the sample was in a dry state such that the peaks cannot be observed; as shown in (a). (b) shows the film in a humid atmosphere in which, a peak followed by a trough are observed at $\lambda \approx 1380cm^{-1}$ , indicating a shift to a lower wavenumber for the C-N bond, and a trough followed by a peak at $\lambda \approx 1750cm^{-1}$ , indicating a peak shifted to a higher wavenumber for the C=O bond[127]. Both bond are both Raman and Infrared active and are shown on Figure A.14, the Raman spectra of this polyimide. . . . .	100
4.7	(a) The mass change for the thickest film measured is shown in Green, with the number of particles calculated to be hitting the surface (from Equation 4.3) shown in blue. (b) The absolute value of the numerical derivative of the above graph. showing the mass flux of the QCM, $\frac{dM}{dt}$ , in green and $\frac{dZ_w}{dt}$ in blue. . . . .	103
4.8	An exponential fit for the mass flux rate for the first two set points allowing an estimation of the activation energy. . . . .	104
4.9	A fit using the preliminary model adapted from Langmuir adsorption model. . . . .	105
4.10	Two schemes of mass transport may give the same concentration profile. (a) Molecular diffusion scale throughout the polymer. (b) Diffusion via fissures and pore network. . . . .	106

4.11	Polyimide on a silicon substrate with a with a gold protective layer. This is a bright field image acquired on a aberration corrected microscope with 80KeV beam (JEOL ARM200cF) by Dr Ian Maclaren. The sample was thinned using the FIB technique. . . . .	108
4.12	(a) A diffraction pattern of the polyimide (at a high magnification). (b) A line profile relating to (a). Any longer spatial frequencies are eclipsed by the central spot. . . . .	110
4.13	A focus series of the same part of the sample, which is polyimide, and the corresponding Fourier transforms, performed in digital micrograph. The samples are two polyimide layers seperated by a platinum electrode. . . . .	112
5.1	(a) A wave, I, passing from one medium to another, with a reflected wave R and transmitted wave, T. (b) A two layer system with reflection coming off the surface and second interface. . . . .	117
5.2	A pictorial representation of the relative SLDs of various materials at common densities at a neutron wavelength of 6 Å. The diameters of the circles are proportional to the real component of the SLD. . . . .	120
5.3	Each of these scenarios was simulated using the MOTOFIT scripts. The y-axis is the logarithm(base 10) of the reflectivity. (a) Fresnel like behaviour for a single sharp interface from a vacuum to Kapton of infinite thickness. (b) The same interference as in (a) with a surface roughness. Roughness is simulated as an error function with a width of 5nm. (c) Interference fringes arising from a Kapton layer of 60nm on an infinite Silicon substrate. . . . .	122
5.4	(a) A 100nm thick layer of polyimide on a sillicon substrate with no interface roughness. (b) A 300nm thick layer of polyimide on a sillicon substrate with no interface roughness. (c) A 300nm thick layer of polyimide on a sillicon substrate with a 2nm interface roughness to show the effects of off-specular reflection on the reflectivity profile. . . . .	123
5.5	Shows the sample in the aluminium cell on the D17 neutron beam line. The slits which control the beam imprint on the sample can seen. The cell itself has a space to insert a capacitance based humidity sensor with a BNC output, which is not plugged in. A QCM mount is also placed in the cell, which is again not plugged in. The gas inlet (bottom) is perpendicular to the direction of the neutron beam. . . . .	125
5.6	The scheme of the vapour pulsing system when acquiring static measurements. By default, dry nitrogen was passed in to cell. . . . .	126

5.7	Neutron counts. (a), (c), and (f) are the raw neutron counts on the detector for the; (a) aluminium cell with no sample, (c) sample data taken at $0.8^\circ$ angle of incidence, and (f) sample data taken at $3^\circ$ angle of incidence. (b), (d), and (e) are the same data, respectively, summed along the x axis. . . . .	128
5.8	Sets of data from the same sample taken at red ( $0.8^\circ$ ) and green ( $2.0^\circ$ ). The black spectrum is the aggregate of the red and green reflectivity profile . Stitching or re-binning the data can also cause a reduction in the fringe amplitude and so it is also useful to look at the raw reflectivity profile from a given angle. . . . .	129
5.9	$\frac{d}{dq}(q)$ plotted: Data is from the D17 reflectometer [82] at the ILL and Inter Reflectometer at RAL showing the bin width as a function of scattering vector. This shows a non-uniform bin width from both instruments linearly correlated with scattering vector for some stitched data. Consequently, features in the reflectivity profile at a higher q are sampled with a lower frequency. . . . .	130
5.10	A screen shot from the Motofit script. In the top left hand corner two reflectivity profiles are shown with the data points and the fit. The fitted SLD profiles are shown underneath. On the right, the control panel of the model; this model shows three sample layers and their properties. . . . .	131
5.11	A two layer model fitted to $R(q_z)$ of the soft cured sample. The reflectivity profiles (left) and the residuals (bottom) of the plot. The SLD profile (right) with $\chi^2 = 3.72$ . . .	133
5.12	A three layer model fitted to $R(q_z)$ with the SLD profiles (right) corresponding the to fit (left). $\chi^2 = 1.14$ and $\chi^2 = 1.34$ for soft cured and hard cured films respectively. . . . .	134
5.13	The oxygen profile (532eV energy) in the 60nm hard cured sample. (a) The EF-TEM image acquired using the three window technique. (b) The corresponding line profile showing the electron counts. Note: Longer frequency intensity variations in image (a) are due to sample thickness variations arising from FIB preparation. . . . .	135
5.14	The raw data for the hard cured film in a dry and vapour rich atmosphere. There is a slight shift out in the critical edge of the wetted film and an increase in the fringe depth. However, surprisingly, the period of the fringes is the same on both films indicating that no swelling occurs upon absorption. . . . .	137
5.15	A badly fitted reflectivity profile using a three layer model. The reflectivity data points, (a) fitted reflectivity curve and (b) fitted SLD profiles for a hard cured film in a nitrogenous and vapour atmosphere. The $\chi^2$ values for the fits are 1.41 for the dry film and 2.99 for the D2O. . . . .	138

5.16 (a) A possible five layer fit for the soft cured 60nm film in which the oxide layer properties were frozen, i.e. assuming that vapour would not permeate the oxide layer. This resulted in a $\chi^2 = 5.55$ . (b) A possible five layer fit for the soft cured 60nm with $\chi^2 = 1.82$ in which the oxide layer characteristics were allowed to vary. . . . .	139
5.17 A five layer fit for the 60nm hard film when saturated with $D_2O$ . The $\chi^2$ is 1.54. . . . .	139
5.18 An AFM scan of two polyimide surfaces. (a) Shows the etched polyimide with a higher surface roughness and (b) Shows a smoother surface. . . . .	142
5.19 The reflectivity of the Etched( $\chi^2=1.57$ ) and Non-etched ( $\chi^2=1.99$ ) films in a Nitrogenous atmosphere, the films were spun with a target thickness of 90nm and one of the films was then etched. These reflectivity profiles were acquired on the D17 instrument .	142
5.20 The 80nm Etched film with dry nitrogen( $\chi^2= 1.64$ ) and $D_2O$ ( $\chi^2= 3.4$ ) in the atmosphere. . . . .	143
5.21 The 95nm non-etched film with dry nitrogen( $\chi^2= 2.4$ ) and $D_2O$ ( $\chi^2= 2.0$ ) in the atmosphere. . . . .	143
5.22 Water saturated (orange) and dry (green) etched polyimide film. The $\chi^2$ values for the fits are 1.64 for the dry film 1.6 for the $H_2O$ . . . . .	144
5.23 The scheme for taking dynamic measurements. A wave generator was able to control the duty cycle. . . . .	146
5.24 A reflectivity profile of a 180nm polyimide oxygen plasma etched thin film with 5nm of gold sputtered on the surface shown with, (a) it's numerical derivative, as the peak in the derivative shows the critical edge, and (b) the ten point moving average of its derivative. Averaging skews the absolute measurement of the critical edge. . . . .	148
5.25 An example of the output from the scripts developed to perform a direct analysis of the reflectivity data. (a) shows two sets of data, in a vapour and dry atmosphere, of the 180nm polyimide film. (b) shows the vapour atmosphere data fourier filtered for longer spatial frequencies and fitted with a sinusoidal wave. (c) shows the dry atmosphere data fourier filtered for longer spatial frequencies and fitted with a sinusoidal wave. . . . .	149

5.26	The output of a script designed to fit each reflectivity profile in a given data set and compare it with the data from the QCM/Capacitive sensors. This data set shows the characteristics of two hundred reflectivity profiles acquired on an etched 180nm polyimide thin film with gold sputtered on the surface as it is exposed to nitrogen gas (for 10s) and vapour (for 30s) on a 40s duty cycle. (a) All of the reflectivity profiles, $R(q)$ , plotted. Each profile corresponds to a 0.2s time bin within the 40sec duty cycle. (b) An example of a Fourier filtered reflectivity profile and the fit used to measure the thickness of the film. The fitted reflectivity profiles shown correspond to the last 0.2s time bin in the duty cycle. (c) The capacitive humidity sensor readout as a function of time though one duty cycle. (d) The thickness deduced from each fit to the profiles shown in (a), plotted as a function of time though the duty cycle. (e) The critical edge shift plotted as a function of time, measured from the reflectivity profiles shown in (a). (f) The QCM readout plotted as a function of time though a duty cycle. . . . .	150
5.27	The critical edge shift as a function of time for a 180nm polyimide thin film which is etched and coated in 5nm of metal. 10 seconds dry - 30seconds of D2O vapour. The errors are the bin width in $q$ . . . . .	152
5.28	An AFM scan of the polyimide with sputtered metal layer on top and the etched polyimide on the same length scale. . . . .	153
5.29	A bright field TEM image of the sample used in this section. The bulk polyimide is in the middle with the silicon substrate in the top left hand corner. . . . .	154
5.30	Diagrams showing the density profile of the polyimide and gold films in a vapour atmosphere. The profiles are vertically displaced by $1\text{\AA}^{-2}$ , with the vapour saturated reflectivity profile overlayed next to each reflectivity profile for reference. This data had been identified as <i>wetting</i> in Figure 5.27. The corresponding fits to the reflectivity profile are in the appendix; Figure A.17. . . . .	155
5.31	A diagram showing the density profile in the polyimide films, as the film dries out. The profiles are vertically displaced by $1^{-2}$ . This data was identified as <i>drying</i> in Figure 5.27. The corresponding fits and reflectivity profiles are in the appendix; Figures A.18 and A.19. . . . .	156
5.32	The shift in the critical edge of the 10s wet 30s dry dynamic spectra to compliment the data presented in Figure 5.27. The statistics on the data set are very low and show a systematic analysis is not possible. . . . .	157

5.33	A contrast between the dry static spectra measurement and the aggregate dry 10 dry -30 wet profiles shown in Figure 5.27 at similar flow rates. Interestingly the critical edge is similar, yet the amplitude of the fringes remains greater in the dynamic spectra, implying the film is not fully dry in the ten second time frame despite similar surface properties. . . . .	158
5.34	Extreme points for the 10wet-30Dry cycle. The critical edges are shifted with respect to each other but the fringes are the same indicating measurements deeper in the film converge. . . . .	159
5.35	The summarised output of the 1sec wet/5sec dry dynamic reading in the cell. (a) All of the reflectivity profiles, $R(q)$ , plotted. Each profile corresponds to a 0.2s time bin within the 6sec duty cycle. (b) An example of a Fourier filtered reflectivity profile and the fit used to measure the thickness of the film. The fitted reflectivity profiles shown correspond to the last 0.2s time bin in the duty cycle. (c) The capacitive humidity sensor readout as a function of time though one duty cycle. (d) The thickness deduced from each fit to the profiles shown in (a) and fitted in (b), plotted as a function of time though the duty cycle. (e) The critical edge shift plotted as a function of time, measured from the reflectivity profiles shown in (a). (f) The QCM readout plotted as a function of time though a duty cycle. . . . .	160
5.36	Showing the shift in the critical edge from the run of 1-5, wet-dry, performed on the 180nm etched + 5nm Au sample. This can be compared to Figure 5.27 to show that the same critical edge shift is achieved but the film is not allowed to equilibrate in a wetted state. The black vertical line does not have symmetry for the marked transition spectra. . . . .	161
5.37	The concentration profiles shown for the data point marked in Figure 5.36 as <i>transition</i> . Fits are shown in the appendix, Figures A.20 and A.21. . . . .	162
A.1	A high resolution photograph of the polyimide solution spun onto small Silicon substrates to illustrate the effects of spinning to slowly leading to a film with a variable thickness (a-c) and to fast lead to a film with artefacts of acceleration(f). . . . .	174
A.2	Various photographs of 4" silicon wafers with different polyimide solutions spun. From top to bottom the concentration of the polyimide precursor to the solvent by volume is decreased, shown on the left hand side as a ratio. From left to right the spin speed is increased shown at the top in rotations per minute. . . . .	176

A.3	AFM scan showing witness sample showing two spatial frequencies of roughness of the soft cured polyimide. This illustrates that the NR thickness measurement cannot be compared to local AFM thickness measurements. . . . .	177
A.4	Polyimide on the Quartz Crystals charges acts like an electron mirror to show the SEM from the point of view of a sample. . . . .	178
A.5	Measurements of the diffusion coefficient for a $\approx 1\mu m$ thick film which has been soft cured. The hypothetical skin diffusion coefficient is constant. . . . .	179
A.6	Measurements of the diffusion coefficient for a $\approx 1\mu m$ thick film which has been Hard cured. The 75-95%rh pont had less time to reach equilibrium and so $M_\infty$ used for this plot is not accurate. The hypothetical skin diffusion coefficient is constant. . . . .	180
A.7	Showing the fitted phase shift for a crystal. The fitting algorithm was sufficiently robust to find the resonance peak at the extremes of the frequency range. . . . .	181
A.8	Impedance sweeps using the Picoscope and the MatLab script. A single crystal is was measured when unloaded, after spinning and curing of the polyimide film. . . . .	181
A.9	The analysis of Polypyrrole assuming a density 1.48[182]. The top line shows the mass analysis, (a) hysteresis loop and (b) the hysteresis residuals. The bottom line is to investigate the dissipative properties; (c) as a function of time, and (d) as function of humidity. . . . .	182
A.10	The latter half of a calibration cycle of Zirconium Oxide; (a) mass and (b) $\Delta(f_2 - f_1)$ showing the dissipative characteristics. . . . .	183
A.11	The analysis of polyimide 2555, assuming a density 1.42. The top line shows (a) the mass hysteresis loop and (b) hysteresis residuals. The bottom line is to investigate the viscoelastic properties; (c) as a function of time, and (d) as function of humidity. . . . .	185
A.12	The analysis of polyimide 2610 assuming a density 1.42. (a) The mass hysteresis loop (b) residuals of the fitted line on the right. The bottom line is to investigate the viscoelastic properties; (c) as a function of time, and (d) as function of humidity (right). . . . .	186
A.13	The experimental setup for the Raman microscope showing the chamber and the water control equipment. . . . .	188
A.14	The Raman spectra of soft cured polyimide in a dry state. Peaks we assigned by comparison with the work of Gu et al.[188] . . . . .	189
A.15	The C=O peak shown from film in both a dry and humid state for etched and non-etched films. . . . .	189

A.16 Bright field TEM image of the 150nm neutron sample. Shows an ordered silicon substrate with two amorphous materials on top which can be distinguished by the marked change in spatial frequency. . . . .	191
A.17 Corresponding to Figure 5.30. . . . .	192
A.18 Corresponding to Figure 5.31. . . . .	193
A.19 Corresponding to Figure 5.31. . . . .	194
A.20 Corresponding to Figure 5.37. . . . .	195
A.21 Corresponding to Figure 5.37. . . . .	196

# Bibliography

- [1] D.J. Wales, J. Grand, V.P. Ting, R.D. Burke, K.J. Edler, C.R. Bowen, S. Mintova, and A.D. Burrows. Gas sensing using porous materials for automotive applications. *Chem. Soc. Rev.*, 44:4290–4321, 2015.
- [2] A. R. Mohd Syaifudin, S. C. Mukhopadhyay, and P. L. Yu. Modelling and fabrication of optimum structure of novel interdigital sensors for food inspection. *International Journal of Numerical Modelling: Electronic Networks, Devices and Fields*, 25(1):64–81, 2012.
- [3] G. Hanreich, J. Nicolics, M. Mündlein, H. Hauser, and R. Chabicovsky. A new bonding technique for human skin humidity sensors. *Sensors and Actuators A: Physical*, 92(13):364 – 369, 2001. Selected Papers for Eurosensors XIV.
- [4] J.M. Lopez-Higuera, L. Rodriguez Cobo, A. Quintela Incera, and A. Cobo. Fiber optic sensors in structural health monitoring. *Lightwave Technology, Journal of*, 29(4):587–608, Feb 2011.
- [5] H. Farahani, R. Wagiran, and M.N. Hamidon. Humidity sensors principle, mechanism, and fabrication technologies: A comprehensive review. *Sensors*, 14(5):7881, 2014.
- [6] Basudam Adhikari and Sarmishtha Majumdar. Polymers in sensor applications. *Progress in Polymer Science*, 29(7):699 – 766, 2004.
- [7] R.J. Maughan, H. Otani, and P. Watson. Influence of relative humidity on prolonged exercise capacity in a warm environment. *European Journal of Applied Physiology*, 112(6):2313–2321, 2012.
- [8] R.N. Dean, A.K. Rane, M.E. Baginski, J. Richard, Z. Hartzog, and D.J. Elton. A capacitive fringing field sensor design for moisture measurement based on printed circuit board technology. *Instrumentation and Measurement, IEEE Transactions on*, 61(4):1105–1112, April 2012.
- [9] P.G. Su, C.J. Ho, Y.L. Sun, and I.C. Chen. A micromachined resistive-type humidity sensor with a composite material as sensitive film. *Sensors and Actuators B: Chemical*, 113(2):837 – 842, 2006.

- [10] Intechno. Sensors markets 2016: Development of sensors markets for the non-military, open world market until 2016. Technical report, 2016. [http : //www.intechnoconsulting.com/ic/press/details/e – press – se2016 – us.pdf](http://www.intechnoconsulting.com/ic/press/details/e-press-se2016-us.pdf).
- [11] CENSIS: Innovation Centre for Sensor & Imaging Systems. <http://censis.org.uk/about/>.
- [12] Y. Feng, L. Xie, Q. Chen, and L-R. Zheng. Low-cost printed chipless rfid humidity sensor tag for intelligent packaging. *Sensors Journal*, pages 3201 – 3208, 2015. 10.1109/JSEN.2014.2385154.
- [13] R.S. Jachowicz, J. Weremczuk, D. Paczesny, and G. Tarapata. A mems-based super fast dew point hygrometer construction and medical applications. *Measurement Science and Technology*, 20(12):124008, 2009.
- [14] FemtoScale Inc. Resonant dew point measuring device, us patent application ser no. 61 735 333, 2013.
- [15] S.V. Silverthorne, C.W. Watson, and R.D. Baxter. Characterization of a humidity sensor that incorporates a cmos capacitance measuring circuit. *Sensors and Actuators*, 19(4):371 – 383, 1989.
- [16] C.B.P. Finn. *Thermal Physics, Second Edition (Physics & Its Applications)*, volume 2. CRC Press, 1993. ISBN-13: 978-0748743797 ISBN-10: 0748743790.
- [17] J.W. Gibbs. A method of geometrical representation of the thermodynamic properties of substances by means of surfaces. *Transactions of the Connecticut Academy of Arts and Sciences*, page 400, 1873.
- [18] M.Y. Mohd Noor, G-D. Peng, and G. Rajan. *Optical Fiber Sensors: Advanced Techniques and Applications*. Taylor and Francis Group, 2015. Chapter 15.
- [19] P.R. Story, D.W. Galipeau, and R.D. Mileham. A study of low-cost sensors for measuring low relative humidity. *Sensors and Actuators B: Chemical*, 25(13):681 – 685, 1995.
- [20] J.G. Gallegos, R. Benyon, S. Avila, A. Benito, R.M. Gavioso, H. Mitter, S. Bell, M. Stevens, N. Base, V. Ebert, M. Heinonen, H. Sairanen, A. Peruzzi, R. Bosma, and M. Val’kovaj. An investigation of the comparative performance of diverse humidity sensing techniques in natural gas. *Journal of Natural Gas Science and Engineering*, 23:407 – 416, 2015.
- [21] Q.Y. Tang, Y.C. Chan, and K.L. Zhang. Fast response resistive humidity sensitivity of polyimide/multiwall carbon nanotube composite films. *Sensors and Actuators B: Chemical*, 152(1):99 – 106, 2011.

- [22] T. Kuroiwa, T. Hayashi, A. Ito, M. Matsuguchi, Y. Sadaoka, and Y. Sakai. A thin film polyimide based capacitive type relative humidity sensor. *Sensors and Actuators B: Chemical*, 13(13):89 – 91, 1993.
- [23] S.Y. Kwon, J.C. Kim, and B.I. Choi. Accurate dew-point measurement over a wide temperature range using a quartz crystal microbalance dew-point sensor. *Measurement Science and Technology*, 19(11):115206, 2008.
- [24] T.L. Yeo, T. Sun, and K.T.V. Grattan. Fibre-optic sensor technologies for humidity and moisture measurement. *Sensors and Actuators A: Physical*, 144(2):280 – 295, 2008.
- [25] S.I. Ohira, P.K. Dasgupta, and K.A. Schug. Fiber optic sensor for simultaneous determination of atmospheric nitrogen dioxide, ozone, and relative humidity. *Analytical Chemistry*, 81(11):4183–4191, 2009.
- [26] S.I. Ohira, P.K. Dasgupta, and K.A. Schug. Fiber optic sensor for simultaneous determination of atmospheric nitrogen dioxide, ozone, and relative humidity. *Analytical Chemistry*, 81(11):4183–4191, 2009. PMID: 19402646.
- [27] D.J. Liaw, K.L. Wang, Y.C. Huang, K.R. Lee, J.Y. Lai, and C.S. Ha. Advanced polyimide materials: Syntheses, physical properties and applications. *Progress in Polymer Science*, 37(7):907 – 974, 2012. Topical Issue on Polymer Synthesis.
- [28] V. Ayala, E.M. Maya, J.M. García, J.G. De La Campa, A.E. Lozano, and J. De Abajo. Synthesis, characterization, and water sorption properties of new aromatic polyamides containing benzimidazole and ethylene oxide moieties. *Journal of Polymer Science Part A: Polymer Chemistry*, 43(1):112–121, 2005.
- [29] M. Ding. Isomeric polyimides. *Progress in Polymer Science*, 32(6):623 – 668, 2007.
- [30] K. Vanherck, G. Koeckelberghs, and I.F.J. Vankelecom. Crosslinking polyimides for membrane applications: A review. *Progress in Polymer Science*, 38(6):874 – 896, 2013.
- [31] M. Hasegawa and K. Horie. Photophysics, photochemistry, and optical properties of polyimides. *Progress in Polymer Science*, 26(2):259 – 335, 2001.
- [32] A.J. Kirby. *Polyimides: Materials, Processing and Applications*, volume vol. 5. p. 158. of *Rapra Review Reports*. Rapra Technology Ltd, 1992. ISBN-10: 0080419666 ISBN-13: 978-0080419664.
- [33] DuPont Website. <http://www.dupont.com/products-and-services/membranes-films/polyimide-films/brands/kapton-polyimide-film.html>.

- [34] David F. Cadogan and Christopher J. Howick. *Ullmann's Encyclopedia of Industrial Chemistry: Plasticizers*. Wiley-VCH Verlag GmbH & Co. KGaA, 2000.
- [35] J.J. Krol, M. Boerrigter, and G.H. Koops. Polyimide hollow fiber gas separation membranes: preparation and the suppression of plasticization in propane/propylene environments. *Journal of Membrane Science*, 184(2):275 – 286, 2001.
- [36] C. Fuhrman, M. Nutt, K. Vichtovonga, and M. R. Coleman. Effect of thermal hysteresis on the gas permeation properties of 6fda-based polyimides. *Journal of Applied Polymer Science*, 91(2):1174–1182, 2004.
- [37] X. Qiao and T-S. Chung. Diamine modification of p84 polyimide membranes for pervaporation dehydration of isopropanol. *AIChE Journal*, 52(10):3462–3472, 2006.
- [38] P. Musto, G. Mensitieri, M. Lavorgna, G. Scarinzi, and G. Scherillo. Combining gravimetric and vibrational spectroscopy measurements to quantify first- and second-shell hydration layers in polyimides with different molecular architectures. *The Journal of Physical Chemistry B*, 116(4):1209–1220, 2012. PMID: 22204392.
- [39] D. Cangialosi, V.M. Boucher, A. Alegria, and J. Colmenero. Physical aging in polymers and polymer nanocomposites: recent results and open questions. *Soft Matter*, 9:8619–8630, 2013.
- [40] M.H. Klopffer and B. Flaconnèche. Transport properties of gases in polymers: Bibliographic review. *Oil & Gas Science and Technology*, 56(3):223–244, 2001. DOI : 10.2516/ogst : 2001021.
- [41] M.S. Arayne and N. Sultana. Porous nanoparticles in drug delivery systems. *Pakistan journal of pharmaceutical sciences*, 19(2):158–69, April 2006.
- [42] D.I. Bower. *An Introduction to Polymer Physics*. Cambridge University Press, 2002. Section 2.6 Infrared and Raman spectroscopy, ISBN-10: 052163721X.
- [43] A. Fick. On liquid diffusion. *Annalen der Physik und Chemie*, 1855. Reprinted:Journal of Membrane Science 100 (1995) 33-38.
- [44] M. Hulden and C.M. Hansen. Water permeation in coatings. *Progress in Organic Coatings*, 13(3):171 – 194, 1985.
- [45] P.W. Atkins. *Physical Chemistry*. Oxford, 4th edition, 1990. ISBN-10: 019855284X ISBN-13: 978-0198552840 Pg 770-771.
- [46] B. E. Deal and A. S. Grove. General relationship for the thermal oxidation of silicon. *Journal of Applied Physics*, 1965.

- [47] J. Crank. A theoretical investigation of the influence of molecular relaxation and internal stress on diffusion in polymers. *Journal of Polymer Science*, 11(2):151–168, 1953.
- [48] J. S. Vrentas, C. M. Jarzebski, and J. L. Duda. A Deborah number for diffusion in polymer-solvent systems. *AIChE Journal*, 21(5):894–901, 1975.
- [49] G.K. van der Wel and O.C.G. Adan. Moisture in organic coatings: a review. *Progress in Organic Coatings*, 37(12):1 – 14, 1999.
- [50] J. Crank. *The Mathematics of Diffusion*. Oxford University Press, 1975. ISBN–10 : 0198534116.
- [51] C. M. Balik. On the extraction of diffusion coefficients from gravimetric data for sorption of small molecules by polymer thin films. *Macromolecules*, 29(8):3025–3029, 1996.
- [52] C.M. Hansen. The significance of the surface condition in solutions to the diffusion equation: explaining anomalous sigmoidal, case ii, and super case ii absorption behavior. *European Polymer Journal*, 46(4):651 – 662, 2010.
- [53] C.M. Hansen. Aspects of solubility, surfaces and diffusion in polymers. *Progress in Organic Coatings*, 51(1):55 – 66, 2004.
- [54] S.N. Kim and K. Kammermeyer. Actual concentration profiles in membrane permeation. *Separation Science*, 5(6):679–697, 1970. 10.1080/00372367008055530.
- [55] S.T. Hwang and K. Kammermeyer. Effect of thickness on permeability. *Permeability of plastic films and coatings*, pages 83–83, 1974.
- [56] M.A. Grayson, P.S. Pao, and C.J. Wolf. Transport of methylene chloride in poly(aryl-ether-ether-ketone) (peek). *Journal of Polymer Science Part B: Polymer Physics*, 25(4):935–945, 1987.
- [57] J. S. Vrentas and J. L. Duda. Diffusion of large penetrant molecules in amorphous polymers. *Journal of Polymer Science: Polymer Physics Edition*, 17(6):1085–1096, 1979.
- [58] G. S. Park. An experimental study of the influence of various factors on the time dependent nature of diffusion in polymers. *Journal of Polymer Science*, 11(2):97–115, 1953.
- [59] R.J. Kokes and F.A. Long. Diffusion of organic vapors into polyvinyl acetate1. *Journal of the American Chemical Society*, 75(24):6142–6146, 1953.
- [60] R.J. Abbott, J.A. Chudek, G. Hunter, and L. Squires. Skin layer effects on the diffusion of carbon tetrachloride into injection moulded polypropylene studied by 1h nmr microimaging. *Journal of Materials Science Letters*, 15(13):1108–1110, 1996.

- [61] T.B. Nielsen, , and C.M. Hansen. Significance of surface resistance in absorption by polymers. *Industrial & Engineering Chemistry Research*, 44(11):3959–3965, 2005.
- [62] S. Pandiyan, J. Krajniak, G. Samaey, D. Roose, and E. Nies. A molecular dynamics study of water transport inside an epoxy polymer matrix. *Computational Materials Science*, 106:29 – 37, 2015.
- [63] B. Wunderle, E. Dermitzaki, O. Hölck, J. Bauer, H. Walter, Q. Shaik, K. Rätzke, F. Faupel, B. Michel, and H. Reichl. Molecular dynamics approach to structure property correlation in epoxy resins for thermomechanical lifetime modeling. *Microelectronics Reliability*, 50(7):900 – 909, 2010.
- [64] J. Mijovic and H. Zhang. Local dynamics and molecular origin of polymer network water interactions as studied by broadband dielectric relaxation spectroscopy, ftir, and molecular simulations. *Macromolecules*, 36(4):1279–1288, 2003.
- [65] G. Mensitieri, M. Lavorgna, D. Larobina, G. Scherillo, G. Ragosta, and P. Musto. Molecular mechanism of h<sub>2</sub>o diffusion into polyimides: A model based on dual mobility with instantaneous local nonlinear equilibrium. *Macromolecules*, 41(13):4850–4855, 2008.
- [66] Agilent Technologies. Agilent impedance measurement handbook, 2010-2013.
- [67] J. Curie and P. Curie. Développement par compression de l’électricité polaire dans les cristaux hémihédres à faces inclinées (development, via compression, of electric polarization in hemihedral crystals with inclined faces). *Bulletin de la Société minérologique de France*, 1880.
- [68] J.F. Alder and J.J. McCallum. Piezoelectric crystals for mass and chemical measurements. a review. *Analyst*, 108:1169–1189, 1983.
- [69] G. Z. Sauerbrey. Verwendung von schwingquarzen zur wägung dünner schichten und zur mikrowägung. *Phys. Verhandl.*, page 193, 1959.
- [70] A.R. Hillman. The eqcm: electrogravimetry with a light touch. *Journal of Solid State Electrochemistry*, 15(7-8):1647–1660, 2011.
- [71] Z. Parlak, C. Biet, and S. Zauscher. Decoupling mass adsorption from fluid viscosity and density in quartz crystal microbalance measurements using normalized conductance modeling. *Measurement Science and Technology*, 24(8):085301, 2013.
- [72] R. Pynn. *Neutron Imaging and Applications: A Reference for the Imaging Community (Neutron Scattering Applications and Techniques)*. Springer US, 1 edition, 2009. 10.1007/978-0-387-78693-3 Softcover ISBN: 978-1-4419-4619-5.

- [73] R.K. Thomas. Neutron reflection from liquid interfaces. *Annual Review of Physical Chemistry*, 55(1):391–426, 2004.
- [74] J. Penfold and R.K. Thomas. The application of the specular reflection of neutrons to the study of surfaces and interfaces. *Journal of Physics: Condensed Matter*, 2(6):1369, 1990.
- [75] J.S. Higgins and H.C. Benoit. *Polymers and Neutron Scattering*. (Oxford Series on Neutron Scattering in Condensed Matter), 1997. ISBN – 13 : 978 – 0198500636 ISBN – 10 : 0198500637.
- [76] R.M. Dalgliesh. Application of off-specular scattering of x-rays and neutrons to the study of soft matter. *Current Opinion in Colloid & Interface Science*, 7(34):244 – 248, 2002.
- [77] A. Glidle, A.R. Hillman, K.S. Ryder, E.L. Smith, J. Cooper, N. Gadegaard, J.R.P. Webster, R. Dalgliesh, and R. Cubitt. Use of neutron reflectivity to measure the dynamics of solvation and structural changes in polyvinylferrocene films during electrochemically controlled redox cycling. *Langmuir*, 25(7):4093–4103, 2009.
- [78] L. Topozini, V. Garcia-Sakai, R. Bewley, R.M. Dalgliesh, T. Perring, and M.C. Rheinstadter. Diffusion in membranes: Toward a two-dimensional diffusion map. *EPJ Web of Conferences*, 83:02019, 2015.
- [79] K.T. Tan, B.D. Vogt, C.C. White, K.L. Steffens, J. Goldman, S.K. Satija, C.C., , and D.L. Hunston. On the origins of sudden adhesion loss at a critical relative humidity: Examination of bulk and interfacial contributions. *Langmuir*, 24(17):9189–9193, 2008. PMID: 18683955.
- [80] B. D. Vogt, H. J. Lee, V. M. Prabhu, D. M. DeLongchamp, E. K. Lin, W. Wu, and S. K. Satija. X-ray and neutron reflectivity measurements of moisture transport through model multilayered barrier films for flexible displays. *Journal of Applied Physics*, 97(11):–, 2005.
- [81] J. Penfold. Neutron reflectivity and soft condensed matter. *Current Opinion in Colloid & Interface Science*, 7(12):139 – 147, 2002.
- [82] R. Cubitt and G. Fragneto. D17: the new reflectometer at the ill. *Applied Physics A*, 74(1):s329–s331, 2002.
- [83] J.R.P. Webster, S. Langridge, R.M. Dalgliesh, and T.R. Charlton. Reflectometry techniques on the second target station at isis: Methods and science. *The European Physical Journal Plus*, 126(11), 2011.
- [84] J.R.P. Webster, S. Holt, and R.M. Dalgliesh. Inter: the chemical interfaces reflectometer on target station 2 at isis. *Physica B: Condensed Matter*, 385-386, Part 2:1164 – 1166, 2006. Proceedings of the Eighth International Conference on Neutron Scattering.

- [85] A. Gabriel. Position sensitive x-ray detector. *Review of Scientific Instruments*, 48(10):1303–1305, 1977.
- [86] S. Zhao, X. Xie, G.D. Smith, and S.J. Patel. Microstructural stability and mechanical properties of a new nickel-based superalloy. *Materials Science and Engineering: A*, 355(12):96 – 105, 2003.
- [87] G.Y. Zsigmond, L. Bata, and E. Kisdi-Kosza. Slow neutron chopper-monochromator with curved slits. *Nuclear Instruments and Methods*, 45(2):255 – 260, 1966.
- [88] E. Ruska. The development of the electron and of electron microscopy. *Nobel Lecture*, 1986. [http://www.nobelprize.org/nobel\\_prizes/physics/laureates/1986/ruska-lecture.html](http://www.nobelprize.org/nobel_prizes/physics/laureates/1986/ruska-lecture.html).
- [89] D.B. Williams and C.C. Barry. *Transmission Electron Microscopy: A Textbook for Materials Science 2nd Edition*. Springer, 2009. ISBN9780387765013 - 9780387765006.
- [90] R. F. Egerton. *Physical Principles of Electron Microscopy: An Introduction to TEM, SEM, and AEM*. Springer, 2005. ISBN – 10 : 0387258000.
- [91] Ludwig Reimer and Helmut Kohl. *Transmission Electron Microscopy: Physics of Image Formation*. Springer; 5th edition, 2008.
- [92] E.J. Roche and E.L. Thomas. Defocus electron microscopy of multiphase polymers: use and misuse. *Polymer*, 22(3):333 – 341, 1981.
- [93] B. Gralla and H. Kohl. Optimisation of the positions and the width of the energy windows for the recording of efem elemental maps. In M. Luysberg, K. Tillmann, and T. Weirich, editors, *EMC 2008 14th European Microscopy Congress 15 September 2008, Aachen, Germany*, pages 379–380. Springer Berlin Heidelberg, 2008.
- [94] V.L. Mironov. Fundamentals of scanning probe microscopy the textbook for students of the senior courses of higher educational institutions. *The Russian Academy of Sciences*, 2004. [www.ntmdt.com/.../fundamentals\\_of\\_scanning\\_probe\\_microscopy.pdf](http://www.ntmdt.com/.../fundamentals_of_scanning_probe_microscopy.pdf).
- [95] P. Klapetek, D. Necas, and C. Anderson. Gwyddion: A user guide. <http://gwyddion.net/>, 2004–2009.
- [96] Thunder Scientific. Series 2500 benchtop two-pressure humidity generator. *Operating Manual*, 2014.
- [97] L. Grasjo and M. Seo. Measurement of absorption of hydrogen and deuterium into palladium during electrolysis by a quartz crystal microbalance. *Journal of Electroanalytical Chemistry and Interfacial Electrochemistry*, 296(1):233 – 239, 1990.

- [98] M.R. Deakin and D.A. Buttry. Electrochemical applications of the quartz crystal microbalance. *Analytical Chemistry*, 61(20):1147A–1154A, 1989.
- [99] S.M. Notley, M. Eriksson, and L. Wågberg. Visco-elastic and adhesive properties of adsorbed polyelectrolyte multilayers determined in situ with qcm-d and {AFM} measurements. *Journal of Colloid and Interface Science*, 292(1):29 – 37, 2005.
- [100] S. Bruckenstein and M. Shay. Experimental aspects of use of the quartz crystal microbalance in solution. *Electrochimica Acta*, 30(10):1295 – 1300, 1985.
- [101] D. Johannsmann. Viscoelastic analysis of organic thin films on quartz resonators. *Macromolecular Chemistry and Physics*, 200(3):501–516, 1999.
- [102] K. Kanazawa and J.G. Gordon II. Frequency of a quartz microbalance in contact with liquid. *Analytical Chemistry*, 57(8):1770–1771, 1985.
- [103] H.L. Bandey, S.J. Martin, , R.W. Cernosek, and A.R.Hillman. Modeling the responses of thickness-shear mode resonators under various loading conditions. *Analytical Chemistry*, 71(11):2205–2214, 1999.
- [104] W.P. Mason and H. Baerwald. *Piezoelectric Crystals and Their Applications to Ultrasonics*. American Institute of Physics, 1951. Bell laboratories series. ASIN: B0007DOFF6.
- [105] S.J. Martin, V.E. Granstaff, and G.C.Frye. Characterization of a quartz crystal microbalance with simultaneous mass and liquid loading. *Analytical Chemistry*, 63(20):2272–2281, 1991.
- [106] A. Itoh and M. Ichihashi. A frequency of the quartz crystal microbalance (qcm) that is not affected by the viscosity of a liquid. *Measurement Science and Technology*, 19(7):075205, 2008.
- [107] M.S.R. Gomes. Application of piezoelectric quartz crystals to the analysis of trace metals in solution: a review. *Sensors Journal, IEEE*, 1(2):109, Aug 2001.
- [108] International Crystal Manufacturing Inc. <https://www.icmfg.com/technicaldata.html>. Product Number 151218-10.
- [109] H.M. Shirazi. *Quartz Crystal Microbalance/ Heat Conduction Calorimetry (QCM/HCC), a new technology capable of isothermal, high sensitivity, mass and heat flow measurements at a solid/gas interface*. PhD thesis, Drexel University, 2000. PhD Thesis.
- [110] Department of Electrical Engineering at the University of Nebraska Lincoln. Phase measurement. <http://eeshop.unl.edu/pdf/OscilloscopeTutorial-PhaseMeasurement.pdf>.

- [111] Gamry Instruments Inc. eqcm 10m: Electrochemical quartz crystal microbalance manual. <http://www.gamry.com/assets/Uploads/eQCM10M-Product-Brochure.pdf>.
- [112] F.L. Walls and J-J Gagnepain. Environmental sensitivities of quartz oscillators. *Ultrasonics, Ferroelectrics, and Frequency Control, IEEE Transactions on*, 39(2):241–249, 1992.
- [113] Measurement Standard Laboratory of New Zealand. Humidity sensor calibration. <https://www.msl.irl.cri.nz/research/temperature-and-humidity/humidity-sensor-calibration>.
- [114] Sensirion Inc. Sensor specification statement: How to understand specification of relative humidity sensors. [http://www.sensirion.co.jp/fileadmin/user\\_upload/customers/sensirion/Dokumente/Humidity/Sensirion\\_HU](http://www.sensirion.co.jp/fileadmin/user_upload/customers/sensirion/Dokumente/Humidity/Sensirion_HU)
- [115] A. Bolotov, I. Cibulka, and L. Hnedkovsky. Partial molar volumes and partial molar isentropic compressions of gamma-butyrolactone and gamma-caprolactone at infinite dilution in water at temperatures (278.15 to 318.15) k and at atmospheric pressure. *Journal of Solution Chemistry*, 40(5):751–763, 2011.
- [116] G. Dunera, E. Thormanna, and A. Dedinaitea. Quartz crystal microbalance with dissipation (qcm-d) studies of the viscoelastic response from a continuously growing grafted polyelectrolyte layer. *Journal of Colloid and Interface Science*, 408:229 – 234, 2013.
- [117] R. P. Feynman, R. B. Leighton, and M Sands. Feynman lectures on physics. vol. 2, chap: 10 (dielectrics), sec: 3, 1989. ISBN 0-201-50064-7.
- [118] M. J. Swann, A. Glidle, L. Cui, J. R. Barker, and J. M. Cooper. The determination of gaseous molecular density using a hybrid vapour sensor. *Chem. Commun.*, pages 2753–2754, 1998.
- [119] M.J Swann, A Glidle, N Gadegaard, L Cui, J.R Barker, and J.M Cooper. Distribution of adsorbed molecules in electronic nose sensors. *Physica B: Condensed Matter*, 276-78:357 – 358, 2000.
- [120] H. Han, C.C. Gryte, and M. Ree. Water diffusion and sorption in films of high-performance poly(4,4'-oxydiphenylene pyromellitimide): effects of humidity, imidization history and film thickness. *Polymer*, 36(8):1663 – 1672, 1995.
- [121] J.Seo and H. Han. Water sorption behaviour of polyimide thin films with various internal linkages in the dianhydride component. *Polymer Degradation and Stability*, 77(3):477 – 482, 2002.
- [122] C. Zeng, J. Li, T. Chen, J. Chen, and C. Chen. Dynamic sorption and transport of water vapor in dense polyimide membranes. *Journal of Applied Polymer Science*, 102(3):2189–2198, 2006.

- [123] B.S. Lim, A.S. Nowick, K-W. Lee, and A. Viehbeck. Sorption of water and organic solutes in polyimide films and its effects on dielectric properties. *Journal of Polymer Science Part B: Polymer Physics*, 31(5):545–555, 1993.
- [124] B.C. Hancock and G. Zografi. The use of solution theories for predicting water vapor absorption by amorphous pharmaceutical solids: A test of the flory-huggins and vrentas models. *Pharmaceutical Research*, 10(9):1262–1267, 1993.
- [125] Y. Liu and B. Shi. Determination of flory interaction parameters between polyimide and organic solvents by hsp theory and igc. *Polymer Bulletin*, 61(4):501–509, 2008.
- [126] J.G. Van Alsten and J.C. Coburn. Structural effects on the transport of water in polyimides. *Macromolecules*, 27(14):3746–3752, 1994.
- [127] M.L. Maurer, A.C. Tooker, and S.H. Felix. Characterization of polyimide via ftir analysis. *Lawrence Livermore National Laboratory Report*, 2014. <https://e-reports-ext.llnl.gov/pdf/780487.pdf>.
- [128] H.R. Kricheldorf, K.R. Carte, and Hendrick. *Progress in Polyimide Chemistry: II*. 1999. Section 5.2: Nano foamed Polyimides, ISBN: 978-3-540-64963-2.
- [129] V. Stannett. The transport of gases in synthetic polymeric membranes: an historic perspective. *Journal of Membrane Science*, 3(2):97 – 115, 1978.
- [130] G. Shen, Q. Mei, V.B. Prakapenka, P. A. Lazor, S. Sinogeikin, Y. Meng, and C. Parka. Effect of helium on structure and compression behavior of *sio*<sub>2</sub> glass. *Proceedings of the National Academy of Sciences of the United States of America.*, 2011.
- [131] A.F. Ismail, K. Khulbe, and T. Matsuura. *Gas Separation Membranes: Polymeric and Inorganic*. Number Pg 14. Springer, 2015. ISBN 978-3-319-01095-3.
- [132] T. Tsuru, T. Hino, T. Yoshioka, and M. Asaeda. Permporometry characterization of microporous ceramic membranes. *Journal of Membrane Science*, 186(2):257 – 265, 2001.
- [133] T. Tsuru, S. Wada, S. Izumi, and M. Asaeda. Silica zirconia membranes for nanofiltration. *Journal of Membrane Science*, 149(1):127 – 135, 1998.
- [134] G.Z. Cao, J. Meijerink, H.W. Brinkman, and A.J. Burggraaf. Permporometry study on the size distribution of active pores in porous ceramic membranes. *Journal of Membrane Science*, 83(2):221–235, 1993.

- [135] D. Korelskiy, M. Grahn, J. Mouzon, and J. Hedlund. Characterization of flow-through micropores in membranes by permoporometry. *Journal of Membrane Science*, pages 183 – 192, 2012.
- [136] A. CanoOdena, P. Vandezande, K. Hendrix, R. Zaman, K. Mostafa, W. Egger, P. Sperr, J. De Baerdemaeker, and I.F.J. Vankelecom. Probing the molecular level of polyimide-based solvent resistant nanofiltration membranes with positron annihilation spectroscopy. *Journal of Physical Chemistry B*, 2009.
- [137] Z. Chen, K. Ito, H. Yanagishita, N. Oshima, R. Suzuki, and Y. Kobayashi. Correlation study between free-volume holes and molecular separations of composite membranes for reverse osmosis processes by means of variable-energy positron annihilation techniques. *The Journal of Physical Chemistry C*, 115(37):18055–18060, 2011.
- [138] D.A. Patterson, A. Havill, S. Costello, Y.H. See-Toh, A.G. Livingston, and A. Turner. Membrane characterisation by sem, tem and esem: The implications of dry and wetted microstructure on mass transfer through integrally skinned polyimide nanofiltration membranes. *Separation and Purification Technology*, 66(1):90 – 97, 2009.
- [139] J. Stawikowska and A.G. Livingston. Nanoprobe imaging molecular scale pores in polymeric membranes. *Journal of Membrane Science*, pages 1 – 16, 2012.
- [140] J. Stawikowska, J. F. Kim, and A.G. Livingston. Pore-flow calculations based on pore size distributions in polyimide membranes determined by a nanoprobe imaging technique. *Chemical Engineering Science*, 97:81 – 95, 2013.
- [141] L.C. Sawyer, D.T. Grubb, and G.F. Meyers. *Polymer Microscopy*. Springer, 2008. ISBN-10: 0387726276 ISBN-13: 978-0387726274.
- [142] D.L. Handlin Jr and E.L. Thomas. Phase contrast imaging of styrene-isoprene and styrene-butadiene block copolymers. *Macromolecules*, 16(9):1514–1525, 1983. 10.1021/ma00243a019.
- [143] T.M. Chou, P. Prayoonthong, A. Aitouchen, and M.Libera. Nanoscale artifacts in ruo<sub>4</sub> stained poly(styrene). *Polymer*, 43(7):2085–2088, 2001.
- [144] M. J. Miles and J. Petermann. Application of defocus transmission electron microscopy to polymers. *Journal of Macromolecular Science, Part B*, 16(2):243–258, 1979.
- [145] J.S. Maeng, D.J. Choi, K. Ahn, and Y-H. Kim. Synthesis of dual nanoparticles embedded in polyimide and their optical properties. *Electronic Materials Letters*, 10(6):1019–1025, 2014.

- [146] M.A. Dyson, A.M. Sanchez, J.P. Patterson, R.K. O'Reilly, J. Sloan, and N.R. Wilson. A new approach to high resolution, high contrast electron microscopy of macromolecular block copolymer assemblies. *Soft Matter*, 9:3741–3749, 2013.
- [147] J. R. Lu and R. K. Thomas. Neutron reflection from wet interfaces. *J. Chem. Soc., Faraday Trans.*, 94:995–1018, 1998.
- [148] R.J.L. Welbourn, S.Y. Lee, P. Gutfreund, A. Hughes, A. Zarbakhsh, and S.M. Clarke. Neutron reflection study of the adsorption of the phosphate surfactant nadehp onto alumina from water. *Langmuir*, 31(11):3377–3384, 2015.
- [149] E. Nowak. On the refractive index for neutrons. *Zeitschrift fur Physik B Condensed Matter*, 49(1):1–8, 1982.
- [150] L. Van Hove. Correlations in space and time and born approximation scattering in systems of interacting particles. *Phys. Rev.*, 95:249–262, Jul 1954.
- [151] D. S. Sivia. On the kinematic approximation to specular reflectivity data. *Philosophical Magazine*, 87(10):1575–1580, 2007.
- [152] L. Nevot and P. Croce. Caracterisation des surfaces par reflexion rasante de rayons x. application a l etude du polissage de quelques verres silicates. *Revue de physique appliquee*, pages pp.761–779, 1980.
- [153] A. Nelson. Co-refinement of multiple contrast neutron / x-ray reflectivity data using motofit. *Journal of Applied Crystallography*, 39(2):273–276, Apr 2006.
- [154] R. Li, C. Li, S.H., M. Di, and D. Yang. Damage effect of kev proton irradiation on aluminized kapton film. *Radiation Physics and Chemistry*, 77(4):482 – 489, 2008.
- [155] Institut Laue-Langevin: Neutrons for Science. <http://www.ill.eu/instruments-support/instruments-groups/instruments/d17/description/instrument-layout/>.
- [156] NIST Center for Neutron Research. Summer school on neutron scattering and reflectometry from submicron structures, June 2004. [http : //www.ncnr.nist.gov/summerschool/ss04/information/lipids\\_s04.pdf](http://www.ncnr.nist.gov/summerschool/ss04/information/lipids_s04.pdf).
- [157] A. Glidle, P E. Pearson, E.L. Smith, J.M. Cooper, R. Cubitt, R.M. Dalgliesh, A. R. Hillman, and K. S. Ryder. Determining compositional profiles within conducting polymer films following reaction with vapour phase reagents. *The Journal of Physical Chemistry B*, 111(16):4043–4053, 2007. PMID: 17402770.

- [158] Mantid Project. Manipulation and analysis toolkit for instrument data. 2013. <http://dx.doi.org/10.5286/SOFTWARE/MANTID>.
- [159] O. Arnold. Mantid data analysis and visualization package for neutron scattering and sr experiments. *Nuclear Instruments and Methods in Physics Research*, Volume 764:156–166, 2014.
- [160] W. H. Press, S. A. Teukolsky, W. T. Vetterling, and B. P. Flannery. *Numerical Recipes in C: The Art of Scientific Computing*. Cambridge University Press, 1992. ISBN-10: 0521431085.
- [161] S. Kirkpatrick, C. D. Gelatt, and M. P. Vecchi. Optimization by simulated annealing. *Science*, 220(4598):671–680, 1983.
- [162] A. Nelson. Motofit - integrating neutron reflectometry acquisition, reduction and analysis into one, easy to use, package. *Journal of Physics: Conference Series*, 251(1):012094, 2010.
- [163] L.S White. Transport properties of a polyimide solvent resistant nanofiltration membrane. *Journal of Membrane Science*, 205(12):191 – 202, 2002.
- [164] L.E.M. Gevers, S. Aldea, I.F.J. Vankelecom, and P.A. Jacobs. Optimisation of a lab-scale method for preparation of composite membranes with a filled dense top-layer. *Journal of Membrane Science*, 281(12):741 – 746, 2006.
- [165] Crystran Ltd. Product data: Silicon (si) single crystal blocks. [http : //www.crystran.co.uk/optical – materials/silicon – si](http://www.crystran.co.uk/optical-materials/silicon-si).
- [166] A.H. Al-Bayati, K.G. Orrman-Rossiter, J.A. van den Berg, and D.G. Armour. Composition and structure of the native si oxide by high depth resolution medium energy ion scattering. *Surface Science*, 241(1-2):91 – 102, 1991.
- [167] M.H. Shirangi and B. Michel. *Moisture Sensitivity of Plastic Packages of IC Devices*. Number 2. Springer Science, 2010. 10.1007/978-1-4419-5719-1.
- [168] P. Bhargava, K.C. Chuang, K. Chen, and A. Zehnder. Moisture diffusion properties of hfpe-ii-52 polyimide. *Journal of Applied Polymer Science*, 102(4):3471–3479, 2006.
- [169] D.B. Asay, , and S.H. Kim. Evolution of the adsorbed water layer structure on silicon oxide at room temperature. *The Journal of Physical Chemistry B*, 109(35):16760–16763, 2005.
- [170] A. G. Erlat, R. J. Sponta, R. P. Clarke, T. C. Robinson, P. D. Haaland, Y. Tropsha, N. G. Harvey, , and E. A. Vogler. Siox gas barrier coatings on polymer substrates: Morphology and gas transport considerations. *The Journal of Physical Chemistry B*, 103(29):6047–6055, 1999.

- [171] W. How Koo, S. Moon Jeong, S. Hun Choi, , H. Koo Baik, S. Man Lee, and S. Jong Lee. Water vapor barrier properties of transparent  $snO_2 - SiO_x$  composite films on polymer substrate. *The Journal of Physical Chemistry B*, 108(49):18884 – 18889, 2004.
- [172] E. M. Flanigen, J. M. Bennett, R. W. Grose, J. P. Cohen, R. L. Patton, R. M. Kirchner, and J. V. Smith. Silicalite, a new hydrophobic crystalline silica molecular sieve. *Nature* 271, 271(5645):512–516, 1978.
- [173] B. Akhavan, K. Jarvis, and P. Majewski. Tuning the hydrophobicity of plasma polymer coated silica particles. *Powder Technology*, 249:403 – 411, 2013.
- [174] M.P. Weir, S.Y. Heriot, S.J. Martin, A.J. Parnell, S.A. Holt, J.R. P. Webster, and R.A.L. Jones. Voltage-induced swelling and deswelling of weak polybase brushes. *Langmuir*, 27(17):11000–11007, 2011. PMID: 21793596.
- [175] D. Kipping, R. Gähler, and K. Habicht. Small angle neutron scattering at very high time resolution: Principle and simulations of tisan. *Physics Letters A*, 372(10):1541 – 1546, 2008.
- [176] A. Wiedenmann, U. Keiderling, K. Habicht, M. Russina, and R. Gähler. Dynamics of field-induced ordering in magnetic colloids studied by new time-resolved small-angle neutron-scattering techniques. *Physics Review Letters*, 97:057202, Aug 2006.
- [177] T.R. Charlton, R.L.S. Coleman, R.M. Dalglish, C. J. Kinane, C. Neylon, S. Langridge, J. Plomp, N. G. J. Webb, and J. R. P. Webster. Advances in neutron reflectometry at isis. *Neutron News*, 22(2):15–18, 2011.
- [178] H. Yim, M.S. Kent, D.R. Tallant, M.J. Garcia, and J. Majewski. Hygrothermal degradation of (3-glycidoxypropyl)trimethoxysilane films studied by neutron and x-ray reflectivity and attenuated total reflection infrared spectroscopy. *Langmuir*, 2005. 10; 21(10) : 4382 – 92..
- [179] P.D. Topham, A. Glidle, D.T.W. Toolan, M.P. Weir, M.W.A. Skoda, R. Barker, and J.R. Howse. The relationship between charge density and polyelectrolyte brush profile using simultaneous neutron reflectivity and in situ attenuated total internal reflection ftir. *Langmuir*, 29(20):6068–6076, 2013. PMID: 23607484.
- [180] Linkam Scientific Instruments. <http://www.linkam.co.uk/products-page/>.
- [181] FemtoScale Inc. Patent: Technique and instrument for dew/frost point measuring using micro/nano-electro-mechanical resonators, ser.no.61,7patent :, 2013.
- [182] P. Saville. Polypyrrole - formation and use. *Defence Research and Development Canada*, 2005. Technical memo. <http://dtic.mil/get-tr-doc/pdf?AD=ada436284>.

- [183] G.E. Collinsa and L.J. Buckley. Conductive polymer-coated fabrics for chemical sensing. *Synthetic Metals*, 78(2):93, 1996.
- [184] E. Smela and N. Gadegaard. Volume change in polypyrrole studied by atomic force microscopy. *The Journal of Physical Chemistry B*, 105(39):9395–9405, 2001.
- [185] G. Eranna, B. C. Joshi, D. P. Runthala, and R. P. Gupta. Oxide materials for development of integrated gas sensors: A comprehensive review. *Critical Reviews in Solid State and Materials Sciences*, 29(3-4):111–188, 2004.
- [186] R. Kumar, O. Al-Dossary, G. Kumar, and A. Umar. Zinc oxide nanostructures for  $no_2$  gas-sensor applications: A review. *Nano-Micro Letters*, 7(2):97–120, 2015.
- [187] A. Tripathy, S. Pramanik, J. Cho, J. Santhosh, and N.A. Abu Osman. Role of morphological structure, doping, and coating of different materials in the sensing characteristics of humidity sensors. *Sensors*, 14(9):16343, 2014.
- [188] X. J. Gu. Raman spectroscopy and the effects of ultraviolet irradiation on polyimide film. *Applied Physics Letters*, 62(13):1568–1570, 1993.